Stability Analysis of Electromagnetically Supported Large Space Structures

Gwendolyn Vines Gettliffe, David W. Miller

February, 2016 SSL # 01-16

Stability Analysis of Electromagnetically Supported Large Space Structures

Gwendolyn Vines Gettliffe, David W. Miller

February, 2016 SSL # 01-16

This work is based on the unaltered text of the thesis by Gwendolyn Gettliffe submitted to the Department of Aeronautics and Astronautics in partial fulfillment of the requirements for the degree of Doctor of Philosophy at the Massachusetts Institute of Technology.

Stability Analysis of Electromagnetically Supported Spacecraft Structures

by
Gwendolyn Vines Gettliffe

Submitted to the Department of Aeronautics and Astronautics on September 18, 2015 in partial fulfillment of the requirements for the degree of Doctor of Philosophy in Aeronautics and Astronautics

Abstract

The high cost per unit mass of launch and the fixed envelope of a launch vehicle fairing respectively incentivize the reduction of spacecraft mass and stowed volume, while the performance boosts that come from an increase in spacecraft dimensions incentivize the maximization of spacecraft deployed size. Also, specific missions might benefit from a particular capability that represents a prohibitive addition of mass to the system or which may be performed inefficiently with current technology, and some missions cannot be accomplished without a capability that existing technologies cannot provide. New technologies, especially those that can contribute multiple capabilities that span the purviews of multiple subsystems, have the potential to enhance or even enable certain mission concepts.

This thesis introduces the concept of an electromagnetic subsystem which can provide both structural and ancillary capabilities to a large spacecraft, due to the tendency of two powered coils to exert forces and torques on one another, as well as several missions that would benefit from such a subsystem and in the process help to mature the technology.

As with any new technology, risks and challenges are identified as well as other enabling technologies which must be developed in parallel to make an electromagnetic subsystem possible. One major risk comes from the fact that the only stable configuration of two magnets is collocated and attracting at the origin. In repulsion, magnets are fundamentally unstable because they either diverge or rotate such that they attract and converge to the origin. Elastic hardware is added to the system to provide restorative forces and torques, but instability of the system remains a concern.

In this work, a validated methodology is developed for identifying pseudo-passive equilibria and classifying them as statically and dynamically stable or unstable and is applied to a series of electromagnetic structures of increasing realism and degrees of freedom to show that stable configurations can exist with appropriate boundary conditions. The methodology is later applied to a variety of systems, including a larger structure with more coils and connective hardware with different properties, to observe how stability conditions change with changes in assumptions or system size.

Thesis Supervisor: David W. Miller
Title: Professor of Aeronautics and Astronautics

Acknowledgements

This work was performed primarily under contract NNX12AQ59G with NASA as part of the NASA Innovative Advanced Concepts (NIAC) program. The work was also performed for Grant No. 1122374 with the National Science Foundation Graduate Research Fellowship, as well as fellowships from Linda and Arthur Gelb and Zonta International. The author gratefully thanks the sponsors for their generous support that enabled this research. The author also thanks her research advisor and committee chair Prof. David Miller; the rest of her doctoral committee, Prof. Karen Willcox, Prof. Raymond Sedwick and Dr. Rebecca Masterson; and her thesis readers, Prof. Enrico Lorenzini and Prof. Manuel Martinez-Sanchez.

Table of Contents

List of Figures

List of Tables

List of Acronyms

Acronym	Section Defined	Definition
EMIC	1.4.	Electromagnetic ion cyclotron
1DoF-T	1.4.	Single translational degree of freedom
1DoF-R	1.4.	Single rotational degree of freedom
2DoF	1.4.	Two degrees of freedom, one translational and one rotational when no modifier placed after the term
MAGESTIC	2.1.	Magnetically Enabled Structures Using Interacting Coils
LN2	2.1.1.	Liquid nitrogen
HTS	2.1.2.	High-temperature superconductor
MRI	2.1.2	Magnetic resonance imaging
EMFF	2.2.	Electromagnetic formation flight
MIT SSL	2.2.	Massachusetts Institute of Technology Space Systems Lab
RINGS	2.2.	Resonant Inductive Near-Field Generation System
ISS	2.2.	International Space Station
SPHERES	2.2.	Synchronized Position Hold Engage and Reorient Experimental Satellites
NIAC	2.2.	NASA Innovative Advanced Concepts
ConOps	2.3.1.	Concept of operations
SMES	2.3.2.	Superconducting magnetic energy storage
HTSSE-II	2.3.3.	High Temperature Superconducting Space Experiment II
EM	2.3.3.	Electromagnetic
AC	2.3.3.	Alternating current
EMI	2.3.3.	Electromagnetic interference
GEO	2.3.3.	Geostationary orbit
KET	2.3.4.	Key enabling technology
TRL	2.4.	Technology readiness level
LEO	2.4.	Low-Earth orbit
L2	2.4.	Second Earth-Sun Lagrangian point
AMP	2.4.	ARMADAS, MEDUSA, and PHOENIX, a collection of robotic assembly programs and technology
CMG	2.5.1.	Control moment gyro
ULF	2.5.1.	Ultra low frequency
VLF	2.5.1.	Very low frequency

DC	2.5.1.	Direct current
JWST	2.5.1.	James Webb Space Telescope
4DoF	6.1.	Four degree-of-freedom system
2DoF-T	6.1.	Two translational DoFs, used in three coil model when coils 2 and 3 each have 1DoF-T
2DoF-R	6.1.	Two rotational DoFs, used in three coil model when coils 2 and 3 each have 1DoF-R

A list of variables used in this thesis and their definitions will appear in Appendix A.

Chapter 1
Introduction

1.1. Motivation

The environment and logistics of getting to space present many challenges that directly and strongly guide the design of a spacecraft. For example, the enormous cost per unit mass to launch a spacecraft is so high that reducing both the dry and the wet mass of the spacecraft are key design objectives. At the same time, making the spacecraft dimensionally larger to reap the performance benefits of large spacecraft is another objective.

The competing objectives of mass minimization and size maximization can be captured in a general sense by a single objective minimizing the linear or areal density of a structure (the mass per unit length or area). A structural technology that can reduce the density of a structure would enable larger structures for the same mass as a traditional structure (and the same size structures for less mass). The two structural approaches to a lower-density spacecraft involve either creating a lower density structural material or system (inflatables, composites, isogrids, and tensegrity structures all pursue this approach) or a structural system capable of "ancillary" functions generally allocated to other subsystems, the latter of which would eliminate the need and the mass of additional hardware to provide those ancillary functions and capabilities.

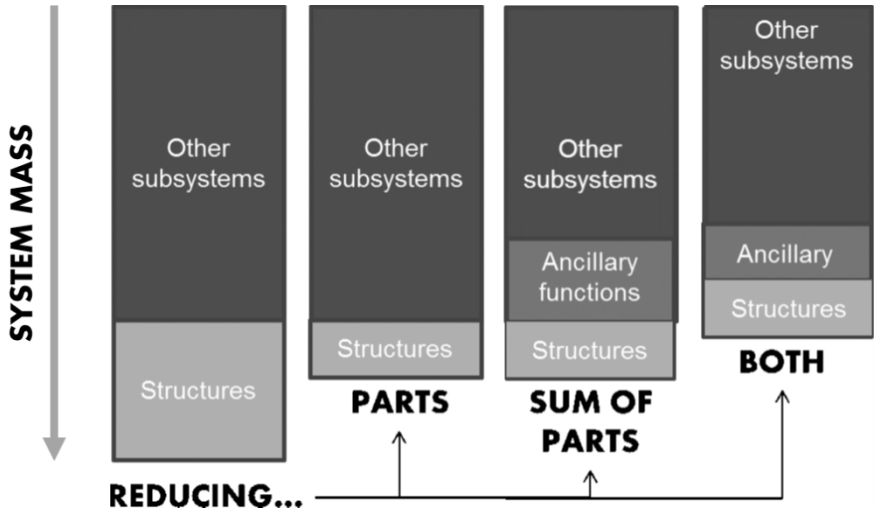

Figure 1: Visualization of approaches to reducing the mass of a space system

Figure 1 displays generalized approaches to reducing spacecraft mass: reducing the *parts* (for instance, decreasing the mass of the structural subsystem, which is on average 20% of spacecraft dry mass [1]),

reducing the *sum of the parts* (having one subsystem perform ancillary functions), or reducing *both* (decreasing subsystem mass while also having it perform ancillary functions).

This research proposes an electromagnetic subsystem that leverages the interaction of magnets with an external magnetic field to perform structural functions as well as some of the duties of other traditional spacecraft subsystems. Some unique capabilities also exist that can only be performed by an electromagnetic subsystem. However, new technologies come with unique challenges and risks that must be addressed and hopefully mitigated in the course of developing and maturing the technology. In the case of electromagnetic structures, their arguably greatest advantage (the ability of electromagnets to exert a force or torque at a distance without contact) also presents a severe risk of instability, because there is no point of equilibrium for a coil in an external magnetic field save for the origin without requiring other forces acting upon it. This innate instability is described by Earnshaw's Theorem, which stated simply says that "A body with steady charges, magnetization or currents placed in a steady electric or magnetic field cannot rest in stable equilibrium under the action of electric and magnetic forces alone [2]." The electromagnetic structures discussed in this thesis are magneto-elastic structures, meaning that they are both magnetically and elastically supported and constrained, the elastic components providing a potential means by which to achieve stability, but the risk still exists that such a structure might be statically unstable or easily made dynamically unstable by a small displacement or other injection of energy into the system.

The primary goals of this thesis are to present the concept of electromagnetic structures, place it in the context of previous and existing work, develop and describe a path to obtaining flight heritage and technological maturity, and identify risks inherent in the concept, addressing the most severe of them, stability. Another goal of this research, outside of the scope of this thesis, is to determine which of the three approaches in Figure 1 electromagnetic structures are capable of providing, such that electromagnetic structures can be traded against other structural technologies on common metrics like mass, density, power, and stiffness.

This introductory chapter discusses the nomenclature of stability and establishes the framework of the rest of the thesis, including the validated methodology that will be developed and presented in this work for determining the relative stability of magneto-elastic structures.

1.2. Stability Nomenclature

The systems studied in this thesis are conservative systems in that "work done by a force, or set of forces, is

1. Independent of path.
2. Equal to the difference between the final and initial values of an energy function.
3. Completely reversible [3]."

As there is no energy dissipation due to damping modeled in our springs nor resistive loss in the coils, our system is conservative of energy. A potential energy function can be determined for a conservative system [4], and the following definitions largely depend on the potential energy of our system.

1.2.1. Equilibrium

A system configuration in equilibrium, hereafter referred to as an *equilibrium*, is defined as one which satisfies the two necessary conditions of force balance and torque balance [5]. This is achieved when the respective vector sums of all forces ($\vec{F}_i$) and torques ($\vec{\tau}_i$) on each body in the system are zero, such that the forces and torque balances are satisfied for each body (coil) in the system, or

$$\sum_{i=1}^{n} \vec{F}_i = \vec{0},\ \sum_{i=1}^{m} \vec{\tau}_i = \vec{0}, \tag{1.1}$$

where n is the number of forces, m is the number of torques (including but not limited to those induced by forces), and i is the index used to sum over n and m. Linear and rotational momenta are conserved in the system. In this thesis, the word equilibrium refers to *static equilibrium*, wherein the linear and rotational momenta of the system are not only conserved but equal to zero.

If the system is described by a set of generalized coordinates X, such that

$$X = \{x_i : i \in S\}, where\ S = \{1 \dots n\},$$

where *n* is the cardinality of the set of generalized coordinates, then at an equilibrium,

$$all\left(\frac{\partial P}{\partial x_i}\right)_0 = 0, \tag{1.2}$$

where *P* is the potential energy of the system at the equilibrium, signified by the subscript 0 [6], and ∂x_i refers to the partial derivative with respect to a specific coordinate x_i. The relationship between Equation (1.1) and potential energy is described as follows, if $\{x_i : i \in S\} = \{x_{t,j}, x_{r,k}\}$, where $\{x_{t,j} : j \in S_t\}$, $S_t = \{1 \dots n_t\}$ are translational coordinates (represented by a *t*) and $\{x_{r,k} : k \in S_r\}$, $S_r = \{1 \dots n_r\}$ are rotational coordinates, represented by an *r*. n_t and n_r are the cardinalities of the sets of translational and rotational coordinates respectively, and $n = n_t + n_r$. This thesis will also use the vector $\vec{X}$ to refer to the

position of a system configuration in the generalized coordinates in which motion is permitted in that system, such that the previous equation can also be written as

$$\left(\frac{\partial P}{\partial \vec{X}}\right)_0 = \vec{0}, \tag{1.3}$$

The work $W_{t,j}$ done by a component of force $F_{tot,j}$ (or work $W_{r,k}$ done by torque $\tau_{tot,k}$) in the direction of a single translational coordinate $x_{t,j}$ (or rotational coordinate $x_{r,k}$) for an infinitesimal displacement $dx_{t,j}$ (or $dx_{r,k}$) is

$$W_{t,j} = F_{tot,j} dx_{t,j},$$

and

$$W_{r,k} = \tau_{tot,k} dx_{r,k}. \tag{1.4}$$

Since the work done by a force (or torque, in the case of rotational coordinates) is equal to the decrease of the system's potential energy [7] in the direction of $x_{t,j}$ due to that force, the work can be written as

$$W_{t,j} = -(dP)_{x_{t,j}},$$

and for rotational coordinates,

$$W_{r,k} = -(dP)_{x_{r,k}}, \tag{1.5}$$

such that if the force vector $\vec{F}_{tot} = [F_{tot,1} \dots F_{tot,n_t}]$ is compiled for all translational coordinates at equilibrium,

$$\vec{F}_{tot} = \left[\left(\frac{\partial W_{t,1}}{\partial x_{t,1}}\right)_0 \dots \left(\frac{\partial W_{t,n_t}}{\partial x_{t,n_t}}\right)_0\right] = -\left[\left(\frac{\partial P}{\partial x_{t,1}}\right)_0 \dots \left(\frac{\partial P}{\partial x_{t,n_t}}\right)_0\right] = \vec{0}, \tag{1.6}$$

and for rotational coordinates $x_{r,k}$,

$$\vec{\tau}_{tot} = \left[\left(\frac{\partial W_{r,1}}{\partial x_{r,1}}\right)_0 \dots \left(\frac{\partial W_{r,n_r}}{\partial x_{r,n_r}}\right)_0\right] = -\left[\left(\frac{\partial P}{\partial x_{r,1}}\right)_0 \dots \left(\frac{\partial P}{\partial x_{r,n_r}}\right)_0\right] = \vec{0}. \tag{1.7}$$

The principle of stationary potential energy states that a structure in static stability will have a stationary value of potential energy [8], meaning that the partial derivatives of potential energy in all directions at a static equilibrium position is zero. This statement is consistent with Equation (1.2). It will be seen in the dynamic stability sections in Chapters 3-5 that this corollary informs the later examination of potential energy curves and surfaces.

1.2.2. Stability

Once equilibria have been located, the *stability* of those equilibria, both *static* and *dynamic*, is of interest. In this work, stability is *pseudo-passive*, which in the context of this thesis means that no active control is being employed to ensure and maintain stability beyond the initial insertion of current through the electromagnets. In some works [9], *passive stability* refers to systems that are stable without requiring any addition of energy to the system in addition to no active control; the current in the electromagnets represents an addition of energy, and therefore electromagnetic structural systems do not fulfill that more restrictive criterion.

The principle of minimum potential energy states that "of all the displacements which satisfy the boundary conditions of a structural system, those corresponding to configurations of stable equilibrium make the total potential energy a relative minimum [8]." This statement refers in particular to *static stability*, which describes the behavior of the system forces and torques in response to a small displacement from equilibrium and is determined by examining the second derivative of the potential energy function.

Static Stability of Equilibrium

As stated by the principle of minimum potential energy, *statically stable* equilibria occur at relative minima of potential energy in all generalized coordinates being studied, or where

$$all \left(\frac{\partial^2 P}{\partial x_i^2}\right)_0 > 0, \qquad i = 1, 2 \dots n. \tag{1.8}$$

A displacement of a statically stable system from equilibrium results in a force and/or torque which tends to move the system back toward equilibrium [10].

Statically unstable equilibria occur at relative maxima of potential energy in any coordinate under study, or where

$$any \left(\frac{\partial^2 P}{\partial x_i^2}\right)_0 < 0, \qquad i = 1, 2 \dots n. \tag{1.9}$$

A displacement of a statically unstable system from equilibrium results in a force and/or torque in the same direction as the displacement that tends to increase the displacement [10].

Statically neutral equilibria occur at equilibria at which the potential energy function is essentially flat in any coordinate under study, or

$$any \left(\frac{\partial^2 P}{\partial x_i^2}\right)_0 = 0, \qquad i = 1, 2 \dots n. \tag{1.10}$$

At statically neutral equilibria, higher derivatives of potential energy are needed in order to determine the stability of the system [10], but a small displacement from equilibrium would not result in any significant forces or torques that would work to either increase or decrease the displacement. Figure 2 shows a representative potential energy curve in one dimension with the equilibria denoted with circles and classified as S/U/N for statically stable/unstable/neutrally stable respectively. The direction that the resultant force or torque from a perturbation would move the system is indicated by arrows.

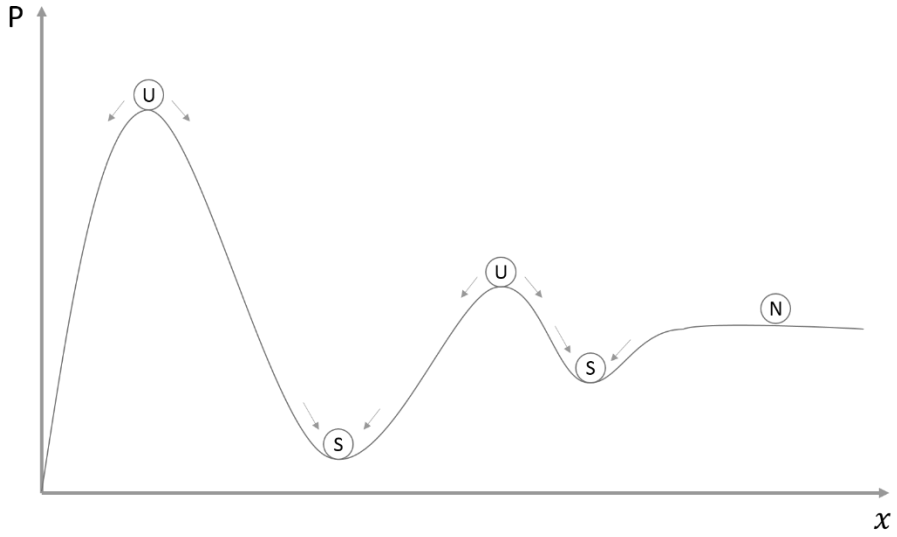

Figure 2: Representative potential energy curve in one dimension with equilibria located and labeled according to static stability

It is important to note that an equilibrium can be statically stable with respect to one coordinate but unstable with respect to another, such as that which occurs at a saddlepoint in a two or more dimension potential energy function. There are also inflection points in the potential energy function that, within the same coordinate, are stable with respect to motion in the positive direction but unstable with respect to the negative direction (or vice versa). In this thesis, equilibria are only called statically stable if they are stable with respect to all coordinates $\{x_i\}$ in all directions.

Dynamic Stability of Equilibrium

Hoff [11] proposes a general definition of structural stability as follows: "A structure is in a stable state if admissible finite disturbances of its initial state of static or dynamic equilibrium are followed by

displacements whose magnitudes remain within allowable bounds during the required lifetime of the structure." Phrased differently, if a certain equilibrium configuration is desired for operation of the structure, then it is considered to be *dynamically stable* in addition to being statically stable if small disturbances from equilibrium result in motion that remains bounded on either side of the equilibrium. It can be seen from this definition that dynamic stability is thus largely dependent on both the magnitude of *admissible finite disturbances* [11] as well as the *allowable bounds* [11] of resultant displacements, and so this definition will be explored below.

Because dynamic stability is related to the behavior of the system in motion around an equilibrium, it becomes necessary to include kinetic energy in our analysis. In a conservative system, the total energy E is a constant, such that

$$T + P = E, \tag{1.11}$$

where T is the kinetic energy and P is the potential energy of the system. When a system is at rest at an equilibrium point,

$$P_{eq} = E_{eq} \text{ and } T = 0, \tag{1.12}$$

where P_{eq} is at a minimum.

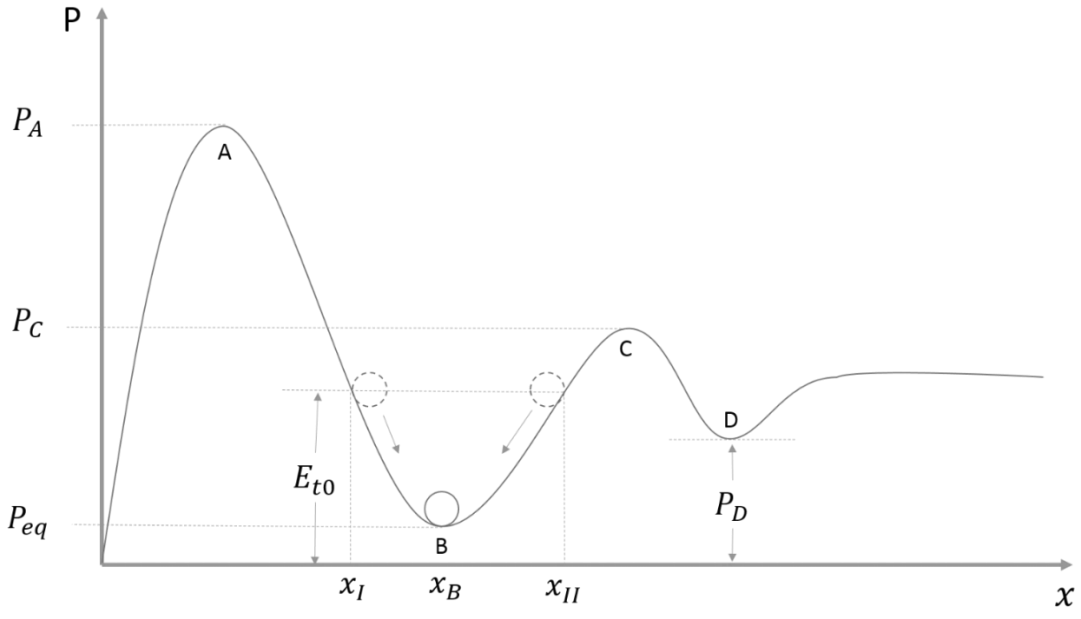

Figure 3: Energy curve showing relative energies and displacement bounds

Figure 3 shows the same energy curve as in Figure 2 with each of the (non-neutrally stable) static equilibrium positions labeled with a letter A through D and point B being the initial position of our system, such that

$$P_{eq} = P_B. \tag{1.13}$$

When an initial kinetic energy T_{t_0} (which is always positive) is added to the system at point B at the start of a dynamic simulation (defined by the subscript t_0) either by an external force or torque or by prescribing a small displacement from equilibrium, the new energy E_{t_0} is

$$E_{t_0} = P_{eq} + T_{t_0}, \tag{1.14}$$

such that

$$E_{t_0} > P_{eq}, \tag{1.15}$$

which means that the system after adding T_{t_0} has its greatest kinetic energy at the equilibrium position B because point B occurs at the minimum in the potential energy functional over the range considered. x_I and x_{II} represent the displacement bounds associated with an P_{t_0} that satisfies $P_{eq} < E_{t_0} < P_c$. At these bounds, the energy in the system is purely potential, and oscillation occurs between these bounds. This kind of bounded motion, where the initial point B is included in the path of motion, is often called *unbuckled motion* in the field of structural stability [12]. Figure 3's potential energies are equivalent to the total energy of the system when the kinetic energy of the system is zero at that point, such as if the system is at rest at equilibrium or when the system's motion reaches its bounds.

It can be seen from Figure 3 that $P_A > P_C$. In the case where T_{t_0} is large enough that

$$P_{eq} + T_{t_0} = P_C, \tag{1.16}$$

then "the system can reach point C with zero velocity (T = 0), and there exists a possibility of motion escaping (passing position C) or becoming unbounded. Such a motion is termed *buckled* motion [12]." This T_{t_0} is called the *critical initial kinetic energy* ($T_{t_0,crit}$) and corresponds to the maximum admissible finite disturbance mentioned earlier, whereas $x_I(P_c)$ and $x_{II}(P_c)$ represent the maximum allowable bounds. It is likely of interest to a system designer to operate with a margin of safety within the aforementioned categories.

Point B is observed to have a lower potential energy than point D, but because of the existence of the relative maximum at C, it is possible for a system to achieve unbuckled motion around both B and D, the magnitude and bounds of that motion being determined by the shape of the potential energy curve in its neighborhood. The type of system depicted in Figure 3 is not a *globally stable* [13] system because it is not an infinitely deep, well-shaped structure where the potential energy curve goes to positive infinity on either end of the x axis, which would thus ensure that the system is always resting at or oscillating around an equilibrium. Points B and D are referred to as *metastable* equilibria because there exists a disturbance for which the system motion escapes and does not return to the equilibrium [13].

From this discussion, it can be concluded that any statically stable equilibrium can be *dynamically stable*, so long as the critical initial kinetic energy for that point is not exceeded. If $T_{t_0,crit}$ is exceeded, then the system is *dynamically unstable* and experiencing buckled motion. One of the goals of this thesis is to explore how the critical initial kinetic energy changes with different choices of design variables.

1.3. Objectives

There are three primary questions that this thesis seeks to answer.

- **What applications would be enhanced or enabled by an electromagnetic subsystem and how?**
  An electromagnetic subsystem possesses a number of potential structural and ancillary capabilities, many of which could enhance or enable future space missions that require these capabilities. What missions could utilize electromagnets to achieve challenging requirements or enhance performance metrics? Several such missions are discussed in Chapter 2, along with a proposed pathway that uses three anchoring applications to drive maturation of the technology.

- **Is it possible for two or more connected electromagnetic coils in space to be pseudo-passively stable, both statically and dynamically?**
  In other words, does there exist at least *one* pseudo-passively stable system of connected electromagnetic coils? For a system to remain at rest in a configuration, it needs to be in equilibrium, with no resultant net forces or torques acting on its constituent bodies. Pseudo-passive stability, both static and dynamic, is evaluated about equilibrium points. This thesis attempts to answer this question by locating equilibrium points for a system and then evaluating stability around those points. The methods by which the work in this thesis accomplishes the aforementioned tasks are described generally in Section 1.4 and in more detail in each of Chapters 3, 4, and 5.

- **If so, what are the conditions on the design and operation of such a system to achieve and maintain stability?**
  If existence of a pseudo-passively stable configuration can be shown, what are the requirements on design parameters and system boundary conditions in order for stability to be achieved, and how sensitive to these parameters is the static and dynamic stability of an equilibrium point? This thesis answers this question symbolically for simple problems then uses these symbolic trends to inform the analysis of more complex problems for which symbolic insight is not as useful.

1.4. Thesis Overview and Approach

The physical fundamentals and capabilities of electromagnets, as well as their past and potential uses on spacecraft missions, are described in Chapter 2 in order to further motivate why electromagnetic structures are useful and why a method for determining the relative stability of electromagnetic structures is important for maturation and eventual implementation of the technology on a real mission.

Chapter 2 focuses on the structural capabilities of an electromagnetic subsystem but also introduces and discusses *ancillary capabilities* of such a subsystem. After these capabilities are broadly discussed, they are explored in the context of three selected applications that were selected to provide a maturation pathway for superconducting technology in space and to represent a cross-section of potential multi-functional allocation to the electromagnetic structure subsystem: torque coils for satellites in geostationary orbit, a large deployed loop antenna for precipitation of protons out of the inner Van Allen belt with electromagnetic ion cyclotron (EMIC) waves, and a next generation space-based observatory with electromagnetically deployed and formation flown elements. From there, the key enabling technologies and several risks are established, including the risk associated with instability of an electromagnetic structure.

In order to develop a validated and reliable method for finding and evaluating equilibria and their relative static and dynamic stability as per Section 1.2, this thesis takes a three–tier approach presented in Figure 4, progressively increasing the complexity of the system being studied while systematically validating each successive step using the last. These three tiers are presented with example problems in Chapters 3, 4, and 5 respectively.

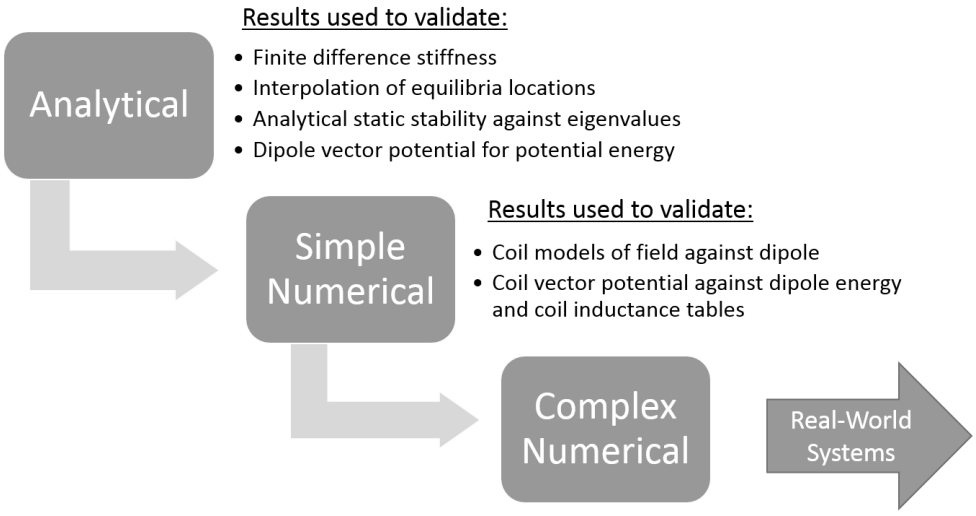

Figure 4: Three-tiered approach and validation steps

The simplest system considered can be described using closed-form, linearizable equations of motion that can be explored analytically and symbolically. The Analytical system uses what is known as the dipole

model, approximating the coils as point magnetic dipole moments, in order to calculate an approximate magnetic field and resultant forces and torques between the coils. The dipole model, which is more accurate at greater separation distances, is explained in more detail in Section 3.1. The stability of the Analytical system can be calculated classically, using linear algebra to examine for what design parameter values the eigenvalues of the system have no positive real parts. Chapter 3 presents the Analytical system.

The Simple Numerical system uses the same basic model as the Analytical system except instead of exploring stability analytically, the Simple Numerical system uses finite differencing and numerical simulation to locate equilibria and classify them as stable or unstable statically and dynamically. Because the system is still describable using linearizable equations, the results of the Simple Numerical system analyses should agree with those of the Analytical system, serving to validate the numerical approach to stability analysis. Chapter 4 presents the Simple Numerical System.

The Complex Numerical system uses the same numerical methods for assessing stability as does the Simple Numerical system, but it uses a more accurate model of the magnetic field of the coils, obeying the Biot-Savart law. The Biot-Savart law can be written in closed form but is not well suited to linearization, making it difficult to take an analytical approach to the resultant forces and torques. Because the same numerical methods are being used by both the Complex Numerical and the Simple Numerical systems, the results of the Simple Numerical system can be used to validate the Biot-Savart model in the region where the dipole model is most accurate as well as to investigate the impact of using the dipole model versus the Biot-Savart model at smaller separation distances. Chapter 5 presents the Complex Numerical System.

Once both the technique and the model used in the Complex Numerical system have been validated, it can be applied to more complicated and more realistic systems, referred to henceforth as “real-world systems”, which include but are not limited to three-dimensional motion, more than two coils, and coils in different configurations than straight masts.

Within each of the three tiers in Figure 4, three two-coil systems are studied: a single translational degree of freedom system (1DoF-T), a single rotational degree of freedom system (1DoF-R), and a combination of the two (2DoF). In addition, for each of these systems, three separate steps are taken: equilibrium identification, static stability analysis, and dynamic stability analysis. In order to organize all of the systems being studied and keep the reader oriented, Figure 5 shows the matrix format that will be repeated at the top of each subsection in Chapters 3, 4, and 5. The matrix will be highlighted each time it appears to indicate what system and step is currently in progress. Chapter 3’s subsections are shown as an example in Figure 5.

Chapter 6 uses the methodology and model developed in Chapters 3-5 to study different structural real-world problems and how changing assumptions affect the results of the methodology, including the addition of a third coil or the use of flexible tethers rather than springs. Finally, Chapter 7 includes a brief discussion of conclusions, contributions, future directions, and takeaways from this thesis.

	3. Analytical	4. Simple Numerical	5. Complex Numerical
Equilibrium Identification	Dipole force/torque balance equations	Dipole force/torque balance equations	Coil numerical force/torque balance
Static Stability	Dipole force/torque analytical derivatives and linearized eigenvalues	Finite difference stiffness matrix	Finite difference stiffness matrix
Dynamic Stability	Analytical formulation of potential energy	Numerical vector potential calculation of potential energy	Numerical vector potential calculation of potential energy

1 DoF – Translational	1 DoF – Rotational	2 DoF – Rotational & Translational
Equilibrium Identification	Equilibrium Identification	Equilibrium Identification
Static Stability	Static Stability	Static Stability
Dynamic Stability	Dynamic Stability	Dynamic Stability

Figure 5: Approach matrix to be followed throughout Chapters 3, 4, and 5

Chapter 2
Electromagnets in Space

The use of electromagnets in space for a variety of applications is motivated by characteristics of both the space environment and of the electromagnets themselves, individually as well as in interaction with each other. This chapter discusses these complimentary characteristics in general; reviews previous and existing uses of electromagnets in space specifically for actuation and support purposes; and then goes into depth on a maturation timeline for superconducting electromagnets in space, complete with three anchoring applications that motivate the development and advancement of this technology. Finally, the necessity of stability analysis for risk reduction purposes is discussed as well as how this thesis fits into the existing field of electromagnetic stability.[1] [2]

2.1. Fundamentals

Electromagnets and electromagnetic structures as spacecraft components are enabled by the fundamental physical principles of electromagnetism, superconductivity, and the unique features of the space environment. This section briefly describes the underlying principles that enable HTS structures, including:

1. The generation of Laplace forces via interaction of a magnetic field and current
2. Superconductivity
3. Enabling characteristics of the space environment (microgravity and vacuum)

The resultant magnetic field $\vec{B}_i$ at any point with respect to the ith current-carrying wire in a system can be described by the Biot-Savart law, integrating over the wire length (or coil circumference) with the differential length $d\vec{l}_i$ where I_i is a constant current through the ith wire, μ_0 is the magnetic constant, $4\pi \times 10^{-7} N/A^2$, and $\vec{r}_{ij}$ is the vector from each differential length element $d\vec{l}_i$ to the point where the field is being calculated:

$$\vec{B}_i = \frac{\mu_0}{4\pi} \int_{Coil\ i} \frac{I_i d\vec{l}_i \times \vec{r}_{ij}}{r_{ij}^3}. \tag{2.1}$$

[1] This chapter was adapted from an IAC 2014 paper: G. V. Gettliffe and D. W. Miller, "System Concept Development For Multifunctional Electromagnetically Actuated and Supported Space Structures," in *International Astronautical Congress*, Toronto, 2014. [63]

[2] The work in this chapter was largely done with the support of a NASA Innovative and Advanced Concepts (NIAC) Phase II grant ("MAGESTIC: Magnetically Enabled Structures Using Interacting Coils"), the final report of which [59] features many of the conclusions presented here.

The force on another (the jth, where $j \neq i$) current-carrying wire placed in the magnetic field of the first one is called the *Laplace force* and is described by the cross product of each of the second wire's differential current segments with the field of the first wire, integrated over the second wire or coil:

$$\vec{F}_{ij} = I_j \int_{Coil\ j} d\vec{l}_j \times \vec{B}_i. \tag{2.2}$$

Parallel currents cause attractive forces while opposite currents cause repulsive forces.

2.1.1. Superconductivity

Superconductors are materials that conduct electrical current losslessly when isothermalized below a critical temperature T_c. Superconductors have zero resistivity, with negligible quantities when approaching their T_c. Every superconductor has a critical temperature, external magnetic field strength, and current density above which superconductivity ceases, as shown graphically as the critical surface in Figure 6. The highest potential current density (while still remaining in the superconducting state) can be reached when the temperature and magnetic field are their lowest (though absolute zero is not quite possible) and so on for each of the three parameters. Superconductors enable HTS structures because they are able to generate much larger forces than regular conductor magnets can generate. The larger forces are due to the superconductor's much larger current carrying capacity when superconducting, which translates to a larger distance over which superconductors can act upon each other for the same amount of mass [14].

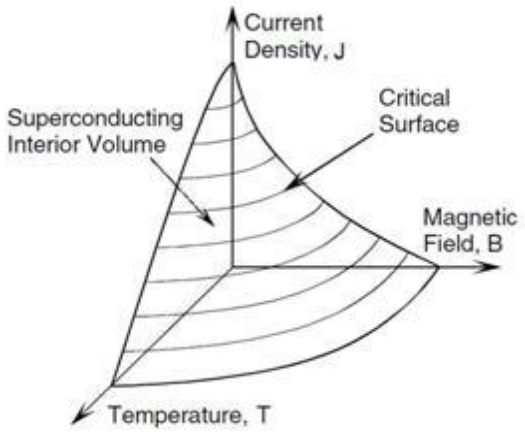

Figure 6: Critical surface for high-temperature superconductor [15] depicting the values of current density, magnetic field, and temperature for which superconductivity can be sustained

High-temperature superconductors, or HTSs, are those superconductors with T_cs above 77K, the boiling point of liquid nitrogen (LN2), enabling LN2 to be used as a coolant. The higher a superconductor's T_c, the less cooling it costs (in terms of power, storage, and consumables, for applications where a cryogen is not recycled).

2.1.2. Space Environment

On the Earth's surface, the strong unidirectional gravity vector as well as the cooling needs of superconductors make it difficult to use electromagnets as actuators or for continuous structural deployment. They are often used in maglev trains and magnetic resonance imaging (MRI) machines, but those devices use massive stationary superconducting magnets that require liquid helium for cooling. In the space environment, however, an electromagnet does not need an enormous magnetic field to actuate components, and there is no air transferring heat into the magnet by convection, making space a unique environment for the use of HTS structures.

The microgravity environment of space enables HTS structures because spacecraft elements can be actuated without needing to dominate strong gravitational forces. Only small forces are required to induce motion in microgravity, reducing the necessary size and current of electromagnets compared to what would be needed, for instance, to repel a coil upwards on the Earth's surface [16].

The vacuum of space is both beneficial and detrimental to the use of superconductors. If it can avoid radiated input from the sun or Earth or other bodies, a thermally isolated HTS subsystem can maintain temperature below its T_c without cryogens. However, it is difficult to remove heat from a system in a vacuum if it cannot be isolated from conductive or radiating heat sources.

2.2. Previous Work

The most extensive use of electromagnets in space to date has been magnetorquers, coils of wire used to torque a spacecraft against the Earth's geomagnetic field in order to dump momentum from the spacecraft's attitude control components (discussed in more detail in Section 2.5.1). With superconducting wire becoming cheaper, more flexible, and more manufacturable, the idea of using superconducting electromagnets for relative actuation of spacecraft and spacecraft elements became feasible.

Electromagnetic formation flight (EMFF) [17], [18], [19], [20], [21] is a concept that would use three orthogonal superconducting coils per vehicle to provide a fully steerable electromagnetic dipole that can actuate against the field from another such vehicle and dipole. A two-vehicle (3 degree-of-freedom each), liquid nitrogen-cooled air table testbed was created in 2003 by the MIT Space Systems Lab (MIT SSL) [18] to test the EMFF concept and develop controllers for such a system. Figure 7 shows one of the two testbed vehicles with subsystem labels. For reference, the diameter of the coils is 0.9m.

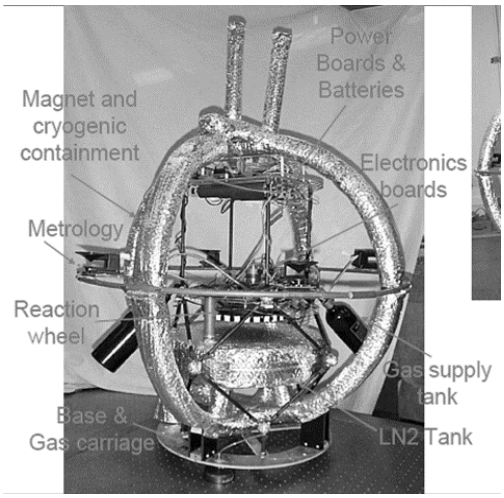

Figure 7: MIT SSL 3DOF EMFF testbed [18]

A microgravity EMFF testbed run by the University of Maryland and MIT SSL began operation on the International Space Station (ISS) in 2013-2014, called the Resonant Inductive Near-field Generation System (RINGS). RINGS used aluminum coils instead of superconducting coils and was limited to one coil per vehicle instead of three, using the thrusters of the Synchronized Position Hold Engage and Reorient Experimental Satellites (SPHERES) for steering of the vehicles' electromagnetic dipoles. Since the governing equations of electromagnetic force are not specific to the type of wire (as discussed further in the next section), both the air-table testbed and the RINGS testbed contribute to the maturation of the EMFF concept. Figure 8 shows one of the RINGS attached to a SPHERES unit on an air table.

EMFF and RINGS both used active control to reach and maintain relative position, and both were free-flying missions without connective hardware. Neither investigated pseudo-passive stability or integrated

elastic forces into their analyses, save for the use of elastic tethers to hold one RING to the wall of the ISS to fix its position.

Figure 8: A SPHERE outfitted with RINGS hardware in laboratory [16]

Electromagnetic tensioning of membranous or hollow structures has been proposed on multiple occasions, such as Zubrin's "magsail" concept in which a large plasma wind sail is supported using a flexible HTS perimeter to magnetically repel itself into a flat circle and keep the sail under tension. For the initial deployment of such a sail, Zubrin ultimately settled upon a non-magnetic rotating boom system to deploy the sail via centrifugal force, citing "reliable deployment" as a key issue for magsails [22]. A NIAC study by Powell et al. [23] discussed a "magnetically inflated cable" system for large space structures: flexible cables made of high-temperature superconducting wire expanding themselves magnetically, serving simultaneously as actuators, perimeter support, and standoff structures.

The latter work is the closest thing proposed to the electromagnetically actuated and supported systems discussed in this thesis, but the analysis was more qualitative and high-level. This work seeks to more quantitatively analyze the ability of electromagnets to support large space structures, as well as identify risks and other technologies that must be tackled for the technology to be feasible for use on future spacecraft. Reliable deployment of flexible coils is a risk that is discussed further later in this chapter, and the stability work in this thesis will inform future work on deployment dynamics as introduced in Gettliffe 2012 [16].

The stability of electromagnets in repulsion is a major concern of magnetic levitation systems, including but not limited to maglev trains and other hovering platforms in an environment with an established gravity vector [24] [25]. The use of stiffness and potential energy curves to study stability is well-established, most applicably in Moon [2] [25], wherein the concept of magnetic stiffness and of magnetoelasticity are introduced. His definition of magnetoelastic structures are those which experience

elastic deformation as a result of magnetic forces and torques, and though the systems studied in this thesis largely use rigid coils, the structure does experience elastic deformation as a result of magnetic effects. This work specifically applies these basic concepts to the new concept of space-based magneto-elastic systems in microgravity, establishing a non-dimensional stability evaluation methodology well suited to the needs of a spacecraft designer who may need to examine the relative stability of a number of systems and system configurations at once. The critical initial kinetic energy is a metric by which a designer can know the tolerance of a particular system for external perturbations. The methodology is applicable to a broad range of magneto-elastic structures. The applications discussed in this chapter include multiple electromagnet configurations, from single, rigid coils as in magnetorquers to flexible coils, from tethered coils to free-flying coils.

2.3. Capabilities, Risks, and Key Enabling Technologies

From the previous discussion, electromagnets are clearly capable of providing a number of capabilities to a spacecraft, both structural and otherwise. This section discusses some of these identified capabilities as well as several key enabling technologies that will be required to make such an electromagnetic subsystem a reality.

2.3.1. Structural Capabilities

Structural capabilities in this work are considered to be functions that traditionally fall to the structural subsystem to perform, such as deployment, support, and operational actuation functions. Electromagnetic coils can repel, attract, and even shear with respect to one another when energized, providing the forces and torques required for structural motion and support. Figure 9 shows seven structural functions that can be accomplished by electromagnetic coils depending on their boundary conditions, rigidity (a flexible coil's self-field exerts a force upon itself to flatten and tension the coil into a circular shape), and phase of deployment (either the *deployment* or the *operational* phase). The example structures studied in Chapters 3, 4, and 5 all utilize the Separate capability.

Table 1 (from Gettliffe 2013 [16]) describes the configurations shown in Figure 9 and some of their potential uses on a spacecraft.

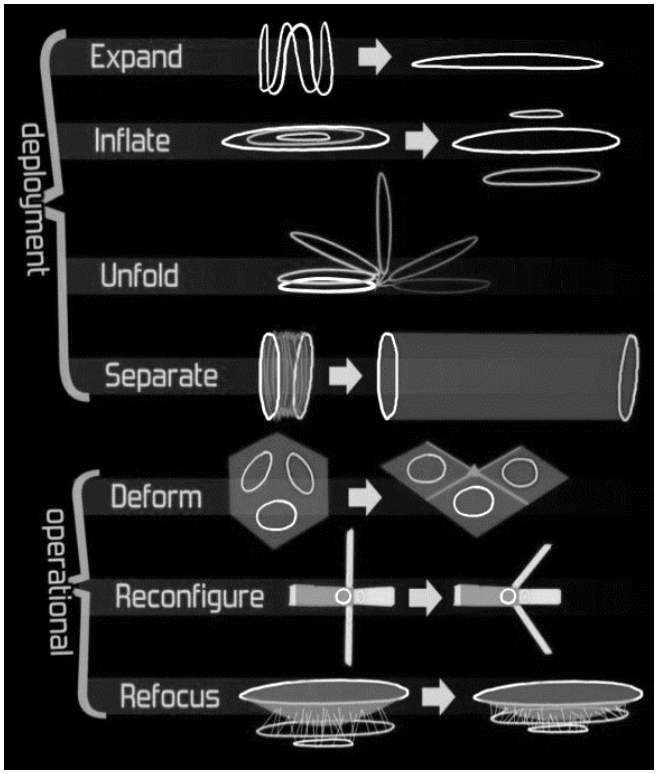

Figure 9: Electromagnetic structural functions and configurations [16]

Table 1: Descriptions and uses for electromagnetic structural configurations

Configuration	Description	Uses
Expand	A single, flexible HTS coil that is folded in its stowed position and uses its own magnetic field when current is run through it to expand to flat shape	To deploy and hold taut the perimeters of large membranous or flexible structures
Inflate	A 3D structure is built with two or more repelling coils in a configuration that creates a space between the two, inflating a structure (bounded by flexible walls or tethers)	To create a volume (such as a tank or toroidal perimeter) or to increase surface area (for solar cells)
Unfold	A series of coils embedded in or attached to a structure that is stowed folded and must be unfolded to become operational (folds can be hinges, springs, or couplings)	To deploy long, flat structures (like solar panels) or to take advantage of mechanical resistance at folds to create variable angles
Separate	Corollary of Inflate, in which two or more coils repel each other in series facing each other to separate two parts of a spacecraft; tethered or membranous structure connecting	To put large, controllable distance between two sensitive parts of spacecraft (such as a nuclear reactor, astronauts, optics, thrusters)
Deform	Two or more coils embedded in parts of the structure act magnetically on each other to temporarily deform or change the shape of the spacecraft	To reduce radar cross section (RCS) or adjust shape for avoidance of debris
Reconfigure	Corollary of Deform, except Reconfigured state is sustainable and lasting	To reduce drag profile or reconfigure satellite for different ConOps
Refocus	Two or more coils adjust their magnetic state such that an antenna or mirror is deformed to refocus it. Orientation of coils dependent on original shape of mirror or antenna.	To change focus lengths of mirrors and gains of antennas by reforming or moving their dishes, mirrors, or horns to Refocus them on a new target

2.3.2. Ancillary Capabilities

As described previously, ancillary capabilities or functions are those qualities that electromagnets naturally possess or provide which would normally be allocated to a (non-structural) subsystem or which will save mass from another subsystem. Some ancillary capabilities of superconducting electromagnetic coils in particular will be discussed here.

Strong quasi-controllable magnetic field: Superconducting electromagnets can carry large currents, translating to powerful magnetic fields. Because the current is controllable, the field strengths can be manipulated as well (unlike with permanent magnets). For applications that require deflecting particles (as in active radiation protection), such a manipulatable field would be desired.

Naturally circular deployed area and/or tensioned perimeter: A flexible current-carrying loop or coil, when folded, experiences magnetic forces due to the interaction of its current with its own magnetic field such that it expands and is tensioned into a flat, circular shape. There are some stowed configurations of such a flexible coil that will end up in a non-circular shape, such as a figure-8; but with planning, a large circular area with natural tensioning can be deployed from a stowed configuration. The self-force of such a flexible coil becomes weak at large sizes, so magnetic deployment can also be combined with strain energy or inflation to fully overcome any material resistance to deployment.

Consumable-free controllable actuation w.r.t non-contacting elements: Motion of spacecraft or spacecraft elements relative to one another is generally either a one-time only occurrence (pyrotechnics), requiring motors and other connective hardware, or thrusters, which consume propellant. With electromagnetic formation flight, spacecraft can move with respect to one another without touching and without consumables (only electrical power). Electromagnets can also provide an external torque on the spacecraft when interacting with an external magnetic field such as the Earth's geomagnetic field.

Lossless energy storage: Superconductors, when below their superconducting critical temperature, operate without resistive losses. Energy in an electromagnetic coil persists indefinitely (save for small losses in non-superconducting elements of the circuit if any exist), making superconducting magnetic energy storage (SMES) a possible alternative to batteries. The lossless nature of superconductors also means that superconducting magnets are very low-power compared to non-superconducting magnets (though this difference is made up at least in part by the power requirements of cryocoolers if such devices are needed to bring superconductors below their critical temperature).

Performs as well or better in cold environs: Superconductors can handle a larger amplitude current at lower temperatures, meaning that for missions to outer planets or cryogenic missions, a superconducting electromagnet can store more energy and produce a stronger field if desired.

Low exported vibration and heat transfer: Electromagnetically-supported structures (which have mostly empty space between them instead of solid structures) minimize the conductive pathways between spacecraft elements, enabling better thermal and vibrational isolation for sensitive components. If the

structures are formation flying (having no connective hardware), then heat transfer is completely limited to radiation.

Wireless power and/or data transfer: Exposure to a changing magnetic field induces a current in wire, which allows the power to be transferred wirelessly from coil to coil, as well as data if it is encoded within the signal.

In the following discussion of selected applications along the technology maturation pathway in Section 2.5, these ancillary capabilities will be referred to and their role in the application discussed.

2.3.3. Risks

Because the previous uses of superconductors on spacecraft have been limited to small electronic components within payloads, such as microwave circuits and antennas (see the High Temperature Superconducting Space Experiment II, or HTSSE-II [26]), a number of risks associated with (relatively) large superconducting magnets for structural or other applications have been identified. Some of the risks are related specifically to the lack of flight heritage or actually operating this technology in the space environment, while some are known challenges of superconducting magnets that require greater analysis or focused trade studies to reduce for a given application. Table 2 shows some of the identified risks, split into three categories based on what facet of an electromagnet subsystem they involve, as well as some possible strategies for mitigating the risk, either decreasing its likelihood or consequence or both.

Table 2: Risks associated with an electromagnetic subsystem and possible mitigation strategies

Category of Risk	Risk	Possible Mitigation Strategy
Electromagnets & Deployment	Uncompetitive performance/ cost	Create detailed model of an electromagnetic (EM) mast, calculate cost as compared to similar example structures
	Unknown stability of configuration	Design methodology for analyzing the static stability of EM structures of a range of sizes and field strengths
	Potential for no stable configs	Implement active control
	Disturbances (Cryocooler, solar , external mag. field)	Expand stability methodology to determine dynamic stability of statically stable configurations
	Inability of single expanding coil to deform itself plus attached equipment	Create multidisciplinary model of the field and self-forces of a flexible coil with mass and bending stiffness of itself and cooling equipment
	Losses prohibitive in AC applications, rectangular tape	Development of new winding patterns to further minimize the component of magnetic field perpendicular to the wire
Thermal Control	Power consumption of cooling system is prohibitively high	Development of better cryocoolers with lower power requirements for the same heat extraction
	Flexible cooling not available for flexible coil	Development of a flexible cooling system capable of reaching and maintaining a coil at temperatures $\leq$ 77K
	Leakage of coolant if thermal hardware broken/pierced	Investigate self-healing materials or a patching agent inserted into the coolant
Power Management & Control	Potential electromagnetic interference (EMI) between subsystems	Take into account field strengths from magnetic elements when selecting and positioning other components; use EMI or lack of it as a metric in trade studies
	Distributing power across coils inefficient or prohibitive	Consider flux pumping or individual batteries; model effects of attaching power cable to a tether
	Inadequate position accuracy and knowledge	Strategic placement of magnetometers and known structural dimensions and currents or infrared sensors could provide position information
	Do not have controllers for connected coils or GEO desat	Development of higher-fidelity magnetospheric models and robust controllers
	Do not have method for orthogonalizing coils	Find and develop strategies for orthogonalizing coil signals to reduce signal interference (time, frequency, etc)

2.3.4. Key Enabling Technologies

In the process of identifying the risks listed in Table 2, a number of key enabling technologies (KETs) were identified that, if developed, would reduce or even eliminate certain risks. Table 3 gives these key technologies and what risks they are associated with. Some KETs are required for certain electromagnetic capabilities to be made possible, whereas others make an electromagnetic subsystem less expensive to system budgets and therefore a more compelling option in trade studies. Some are active areas of research (such as more power efficient and lighter weight cryocoolers or a controller for desaturation in the GEO magnetic field) because they are necessary for other applications (lighter and lower power cryocoolers are beneficial to any spacecraft payload that requires one, and a controller for desaturation is necessary for GEO magnetorquers and already under work [27].)

Table 3: Key enabling technologies for mitigating risks listed in Table 2

Category of KET	KET	Associated risk mitigation
Electromagnets & Deployment	Striated superconductors for lower AC losses	Losses prohibitive in AC applications and rectangular tape
	Twisting tape stacks to reduce perpendicular magnetic field	Losses prohibitive in AC applications and rectangular tape
	HTS with higher critical temperature T_c	Uncompetitive performance/cost with other structural options
Thermal Control	Flexible cooling system for flexible HTS	Cooling not available for flexible coil
	More power efficient and lighter weight cryocoolers	Power consumption of cooling system is prohibitively high, and uncompetitive performance/cost with other structural options
	Self-healing materials for puncture mitigation	Leakage of coolant if thermal hardware broken/pierced
Power Management & Control	Controller for desaturation in GEO magnetic field	Do not have controllers for connected coils or GEO desat
	Phasing for 2+ matched sets of magnets w/out cross-interaction	Do not have method for orthogonalizing coils to reduce signal interference
	Controller for tethered or otherwise constrained magnets	Potential for no stable configurations

These KETs are provided so that mission planners interested in making use of an electromagnetic capability on their spacecraft are aware of preliminary investments of money and effort that may be required in order to make an electromagnetic subsystem possible.

2.4. Maturation Timeline

In order for electromagnetic structures to be implemented on real missions, the constituent technologies need to be matured significantly, both individually, through testing in increasingly relevant environments, and by gradual combination of technologies into increasingly complex systems. Figure 10 shows the maturation pathway that was proposed for high temperature superconducting electromagnetic coils cooled via a flexible forced vapor cooling system, starting from past single-technology laboratory testing and ending with far-future, fully-integrated operation on-orbit beyond geostationary orbit (GEO). The intermediary steps combine existing technologies into more complex systems and add some new technologies such that the final complex system, the observatory, is a combination of existing and new technologies.

Highlighted in red in Figure 10 are anchoring use-cases in the near-term, mid-term, and far-term. These use-cases provide mission pulls to support the technology push proposed in this work, and each use-case complements the focus of each of the aforementioned time periods:

Near-term spans the time period between now and five years from now with the goal of achieving Technology readiness Level (TRL) 5 for high-temperature superconducting electromagnets in orbit and proposing a demonstration mission for electromagnetic structures. The near-term is focused on building flight heritage and further maturation of the technology from Earth-based concept to a functioning system on orbit, and the anchoring application is GEO magnetorquers.

Mid-term spans the time period between five and fifteen years from now with the goal of enabling or enhancing new mission concepts that have heretofore been impossible or infeasible. The mid-term is focused on addressing technical feasibility barriers, starting with those associated with the anchoring application of a large deployed superconducting antenna.

Far-term spans the time period beyond fifteen years from now with the goal of using electromagnetic capabilities to imagine revolutionary mission concepts, reinventing how large spacecraft are imagined. Missions in the far-term, including the anchoring application of a large space-based observatory, will not just be enabled by but also be defined by their use of electromagnetic systems. Therefore, it will be important to focus in the far-term on addressing barriers to the integration and operation of sometimes several different electromagnetic subsystems with each other and the rest of the spacecraft.

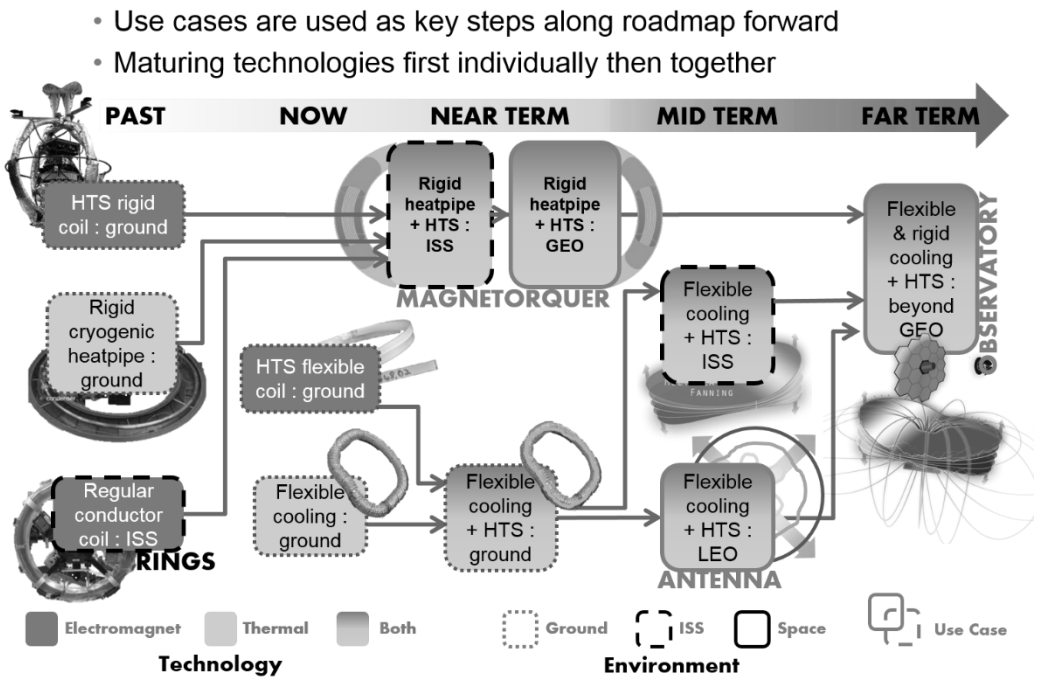

Figure 10: Technology maturation pathway with selected applications highlighted with grey borders and arrows connecting the individual electromagnet and thermal development paths

The environments of the steps in Figure 10 are also staged, such that the individual technologies are developed and tested in controlled laboratory settings on the ground, then combined and tested in a relevant but still controlled environment on the International Space Station (ISS), then the successively more difficult-to-reach free-flying environments of low Earth orbit (LEO), GEO, and the second Earth-Sun Lagrangian point (L2). Increasingly relevant environments are a requirement for increasing the TRL of a technology, and Figure 11 shows how each of the selected example missions increases and expands the number of environments in which superconductors and electromagnetic structures have been flown, while showcasing and maturing the three technology areas introduced in Section 2.3.3, Electromagnets and Deployment, Thermal Control, and Power Management and Control. (AMP refers to ARMADAS, MEDUSA, and PHOENIX, a collection of robotic assembly programs and technology that might be leveraged to help develop such a fractionated observatory.)

Given the difficulty of realistically testing the dynamics of a relatively low-stiffness structure in the presence of a strong directional gravity vector, as is present at the Earth's surface, other, more relevant environments are necessary for maturation of MAGESTIC and an increase in TRL of any MAGESTIC structure. The ISS presents a fundamental maturation environment for magnetic structures because the dynamic response of such structures in deployment is too long to effectively be studied in a parabolic flight, but the abilities that ISS presents to observe the dynamics, test many different system configurations and conditions, and reset if there are malfunctions are essential to the development of a broadly-applicable technology without one specific design. Flying a small satellite to test MAGESTIC deployment dynamics is very inefficient, given that the data that could be obtained from structural telemetry of one deployment (since there is no easy way to reset the system for another trial of the same or different configuration) is nowhere near as useful as being able to observe it with human eyes.

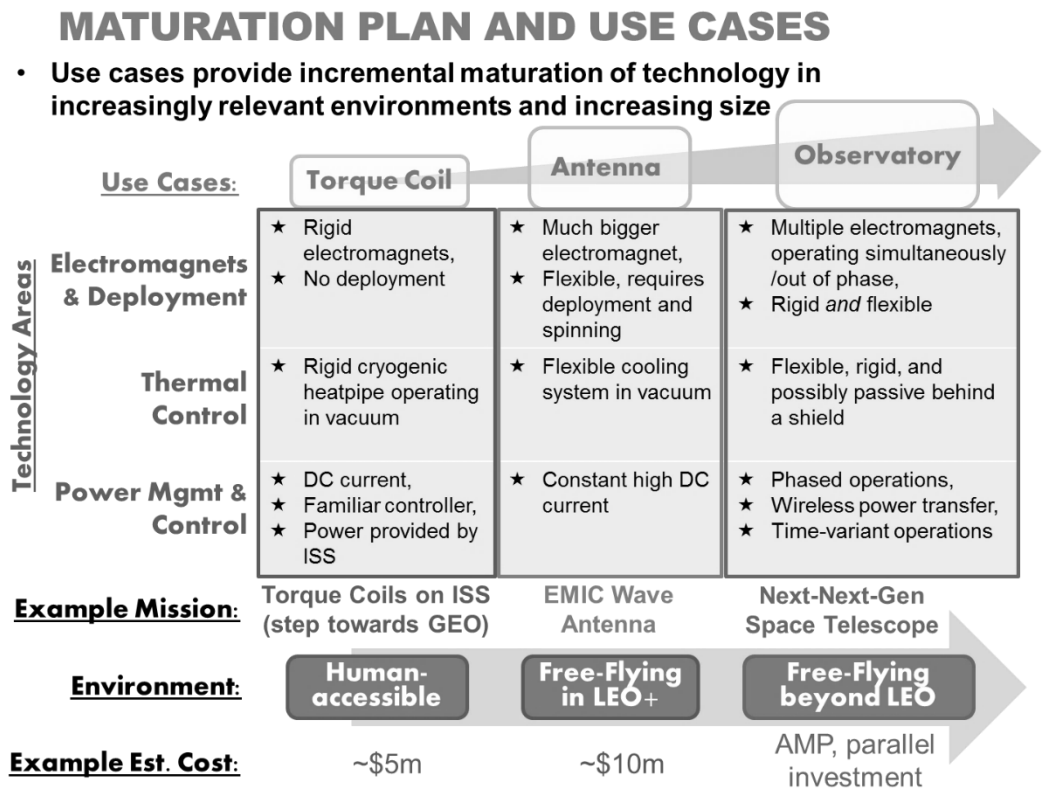

Figure 11: Selected use cases and the electromagnet, thermal, and power needs for each

2.5. Example Missions

In order to exhibit the capabilities of electromagnetic structures, Section 2.5.1 presents a more detailed description and analysis of the three applications selected to anchor the maturation timeline in each of the three epochs introduced in Section 2.4, followed by discussion in Section 2.5.2 of an application that could be necessary at any time without warning, a magnetic asteroid tug.

2.5.1. Selected Applications for Maturation Timeline

The following three subsections give preliminary analysis of the near-term, mid-term, and far-term anchoring applications on the maturation timeline presented in Figure 10.

Near-term: GEO Magnetorquer

Spacecraft in low-Earth orbit (LEO) typically use reaction wheels or control moment gyros (CMGs) for attitude control and magnetic torque coils, or magnetorquers, to desaturate their wheels or gyros by causing an external torque to act on the spacecraft (the magnetic torque induced by the interaction of the Earth's geomagnetic field with the magnetorquer). In GEO, spacecraft generally require the use of thrusters (also used for stationkeeping) for the desaturation of their reaction wheels and/or CMGs because the Earth's geomagnetic field is significantly weaker at GEO than at LEO. GEO satellites are typically lifetime-limited by their propellant, so a consumable-free desaturation method like magnetorquers would be hugely beneficial to GEO spacecraft lifetimes.

A quick way to approximate the strength of the Earth's geomagnetic field at a distance r from the center of the Earth is via the first-order dipole Earth model, wherein the field strength B_0 falls off proportional to $\frac{1}{r^3}$, or:

$$|B_0| = \mathrm{B_{surf}}\left(\frac{\mathrm{R_E}}{\mathrm{r}}\right)^3 \sqrt{1 + 3\cos^2\theta}, \tag{2.3}$$

where $\mathrm{B_{surf}}$ is the mean strength of the geomagnetic field on Earth's surface, $3.12 * 10^{-5}$ T, $\mathrm{R_E}$ is the radius of the earth, and θ is the co-latitude measured from the north magnetic pole. For comparison, the magnetic field strength at 42164 km from the center of the Earth (GEO) is 251.7 times weaker than the magnetic field strength at 6678.1km from the Earth's center (a 300km altitude orbit, LEO).

In addition to the weakness of the field at GEO, one thing the first-order Earth dipole model does not capture is the time-variance of the field at GEO, due to the interaction of the solar wind's interaction with the magnetosphere. Because the Earth dipole model does not capture this time-variance, it can only reliably be used to describe geomagnetic field strength out to about three Earth radii from the Earth's center [28].

This work focuses on one of these two barriers to the use of magnetorquers for desaturation at GEO; the issue of weak field strength can potentially be resolved via the use of superconductors. Prediction of the field strength over time is an active field of research for space weather scientists, and there exist several models for the geomagnetic and magnetospheric fields over time [28], [29], [30]. Another way of compensating for the uncertainty of the field is to design robust controllers for magnetorquers at GEO that can compensate for a lack of precise knowledge of the geomagnetic field strength at that location and time.

Magnetic torque $\vec{\tau}_{mag,i}$ on the ith current-carrying coil with magnetic moment $\vec{\mu}_i$ in an external magnetic field $\vec{B}$ is determined by

$$\vec{\tau}_{mag} = \vec{\mu}_i \times \vec{B}. \tag{2.4}$$

It can be seen from Equation (2.4) that the magnitude of magnetic torque is the product of the magnetic field strength and the strength of the magnetic moment of the coil; the same torque can be induced from a weak magnetic moment in a strong external field as can be induced by a strong magnetic moment in a weak external field. Since the field strength at GEO cannot be increased, the magnitude of the magnetic moment can instead be increased.

The magnetic moment $\vec{\mu}$ of an air-cored current-carrying coil of area A_{rea}, turns N and current I is as follows:

$$\vec{\mu} = NI\vec{A}_{rea}, \tag{2.5}$$

where the direction of $\vec{A}_{rea}$ is normal to the area enclosed by the coil, such that the current I is flowing counter-clockwise around $\vec{A}_{rea}$. According to Desiderio et al. [27], 3000-4000 Am^2 is a good estimate for the magnetic dipole moment needed from a torque coil for continuous magnetic momentum unloading for an average GEO spacecraft. A large magnetic moment can be provided with a) a large area, b) lots of turns, or c) a high current. Superconducting magnetorquers provide the latter.

Magnetorquers used on LEO spacecraft are typically wound with copper wire and are one of two form factors: large area, flat, air-cored coils (often wound around the perimeter of one of the spacecraft sides or solar arrays) or small area, tall, iron-cored coils (often called torque rods, with several placed orthogonally inside the spacecraft to provide desaturation in all axes). Ferromagnetic cores provide a stronger magnetic dipole than air-cores because the core acts to concentrate the magnetic field lines, but torque rods are typically reserved for spacecraft with larger mass budgets, due to the large mass of iron cores. This analysis focuses on large area, flat, air-cored torque coils wound with high-temperature superconducting (HTS) wire, but it would not be impossible to create an iron-cored HTS-wound torque rod.

Figure 12 shows for a given area of coil how many ampere-turns ($I * N$) are required to produce magnetic dipole strengths of 3000, 3500, and 4000 Am^2, while Figure 13 shows that for $5m^2$, the number of turns with a current of 150A is roughly 5 turns. The mass of a 150A coil (using the density of the 6mm Superpower HTS wire) is shown versus the coil area in Figure 14.

The knee in the curve is around $5m^2$ – larger areas do not save that many ampere-turns. $5m^2$ is also a reasonable area to assume that a GEO spacecraft can accommodate, so $5m^2$ will be used as an example coil area going forward. Figure 13 assumes that the wire is carrying 150A (the critical current for the commercially available 6mm wide SuperPower HTS wire [31]) and shows how many turns would then be required for the same magnetic dipole strengths as in Figure 12.

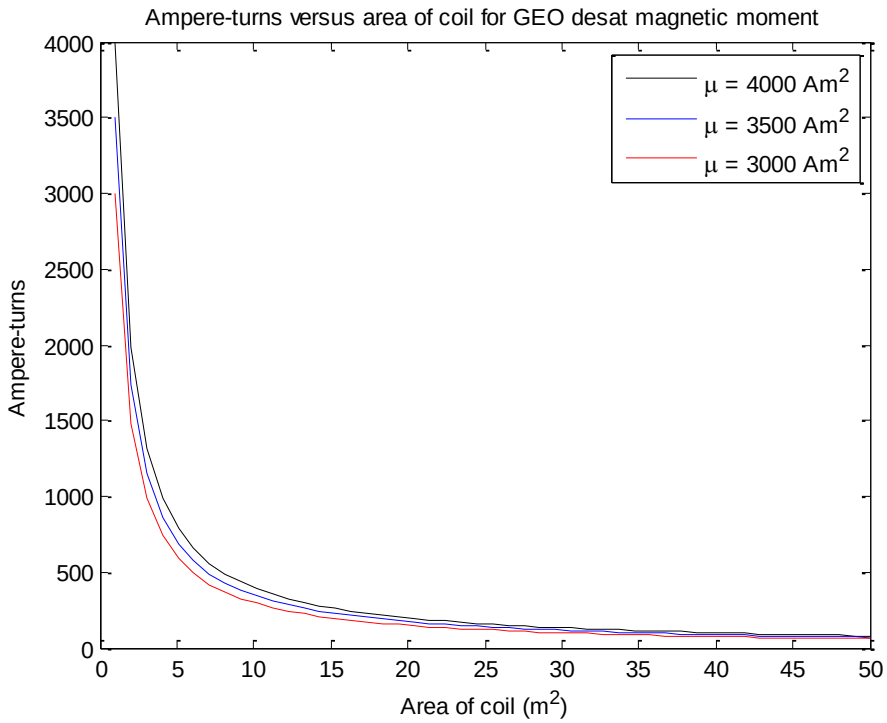

Figure 12: Ampere-turns versus area of coil required for several example magnetic moments

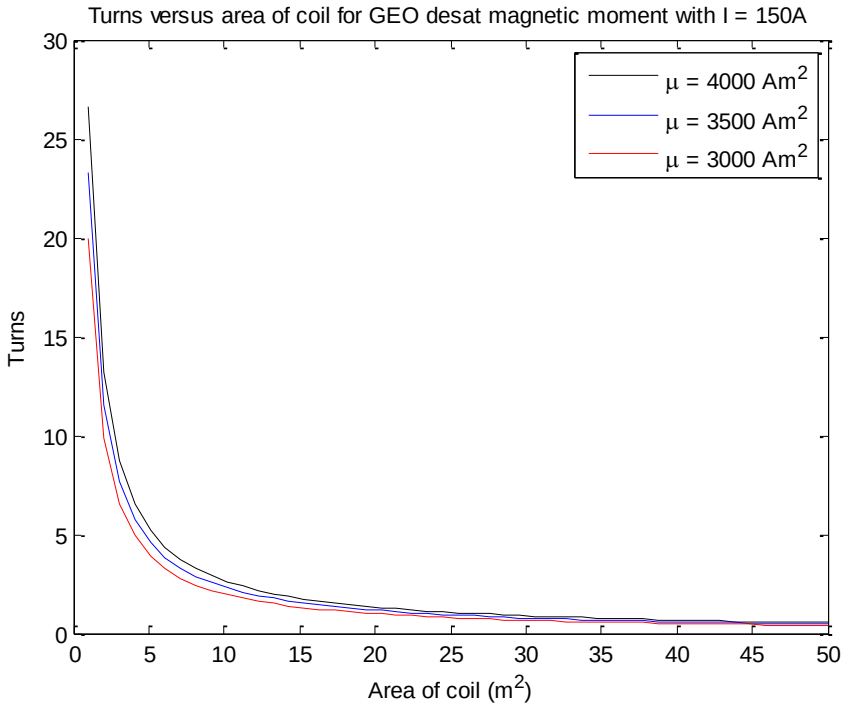

Figure 13: Turns versus area of coil required for several example magnetic moments

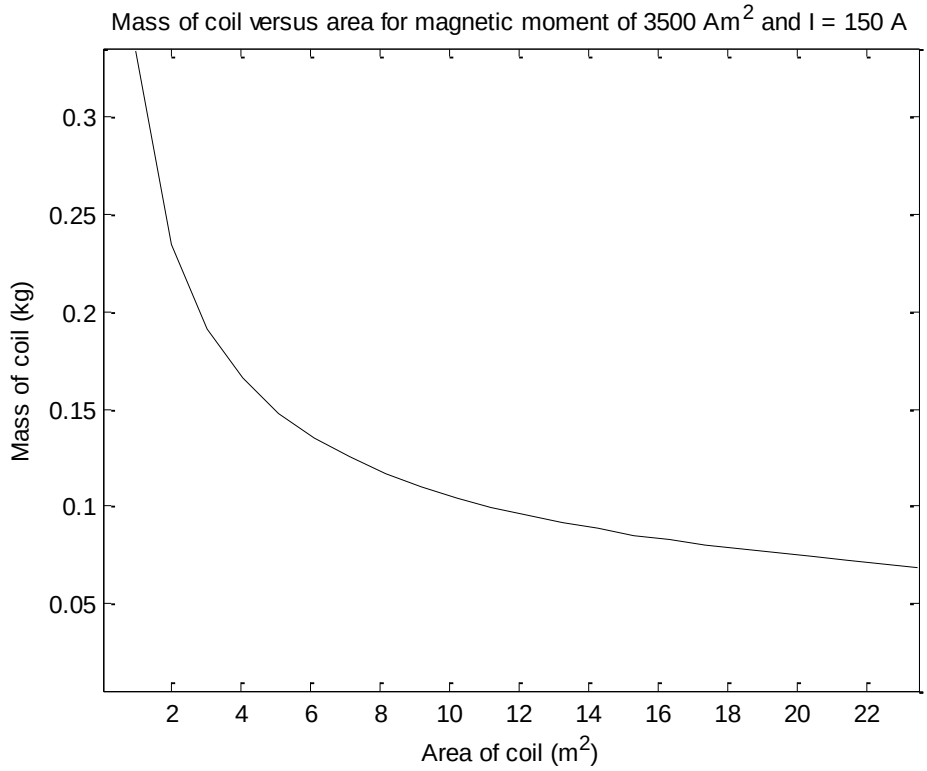

Figure 14: Mass versus area of coil required for a magnetic moment of 3500 AM^2

A mass of 0.14kg for a magnet capable of providing 3500Am^2 is very low. Note that this value does not account for the hardware required to cool the coil to 77K with liquid nitrogen, which will add significantly to the mass. Comparing a single turn coil of copper with one of HTS wire, both coils of the same mass and wire area, the HTS coil provides a magnetic dipole moment two orders of magnitude larger than that of the copper coil.

The copper versus HTS comparison is not just about mass of the coil, however, or many-turn copper magnetorquers would be used regularly at GEO. Even with heavy coils, the propellant savings would be still likely be worth the tradeoff. One of the defining characteristics of a superconductor is that when it is cooled below its superconducting temperature, the wire is lossless. This allows a high-amperage current to pass through an HTS wire without melting it or losing any energy to heat. In contrast, copper is resistive, and some of the electrical energy passed through it is converted to heat. Too many turns of copper (and no convection in the vacuum of space) would eventually heat a copper coil to its melting point. So, while a massive copper coil could theoretically provide the needed magnetic moment, it would require additional cooling hardware as well to evacuate the emitted heat, making adding extra propellant to the spacecraft the more reasonable of the two options for desaturation. Both HTS and copper coils requiring additional thermal hardware at GEO makes the choice between the two magnetorquer options simple.

Further work includes an analysis of how much less propellant would be required if magnetorquers were used on a GEO spacecraft as well as a more detailed thermal comparison of HTS and copper magnetorquers.

Mid-term: EMIC Wave Antenna

The Van Allen belts are regions encircling the Earth in which the Earth's geomagnetic field has trapped and concentrated energetic charged particles. The trapped particles come from cosmic rays, solar flares and storms, and other processes. There are two major Van Allen belts. The inner belt, which encompasses the equatorial region roughly between 0.2 and 2 Earth radii from the Earth's surface (1,000-6,000 km altitude), comprises electrons and protons; the outer belt spans 3 to 10 Earth radii from the Earth's surface (13,000-60,000 km) and comprises mainly electrons [32].

Charged particles are not healthy for spacecraft or humans as they can cause unwanted single event effects in spacecraft electronics and damage DNA in human cells, leading to cancer or other health concerns. Spacecraft in high LEO or highly elliptical orbits pass through the inner belt and are thus exposed to high dosages of radiation. Geostationary orbit is 35,786 km in altitude, so satellites in GEO are also constantly exposed to the particles trapped in the outer belt. A method for cleaning the trapped particles out of the Van Allen belts would reduce the radiation dosage to current and future space missions.

The charged particles in the Van Allen belts travel in helical paths around the geomagnetic field lines and bounce back and forth along the lines, reversing directions at mirror points along the field line where the angle, or *pitch angle*, between the helical path and the field line is 90 degrees. If the mirror points occur in atmosphere dense enough that the charged particles collide with atmospheric particles, then the charged particles are absorbed by the atmosphere and are no longer trapped. Particles with mirror points at low altitudes (and thus will precipitate into the atmosphere within a few cycles) have pitch angles that fall inside an altitude-defined *loss cone* around the field line during the middle of a bounce [33]. Particles with equatorial pitch angles outside of the loss cone stay trapped around the field line unless an external influence such as interaction with a plasma wave scatters their pitch angle into the loss cone.

It has been observed that ultra low and very low frequency waves (ULF and VLF) can scatter trapped particles into the loss cone, freeing them from the Van Allen Belts. Whistler waves (with frequencies of kHz) interact with electrons, while electromagnetic ion cyclotron (EMIC) waves (with frequencies less than 10 Hz) can interact with both protons and electrons, making them a good option for reducing the trapped radiation in the inner Van Allen belt [34]. A mission incorporating a large space-based antenna that could emit EMIC waves and begin precipitating inner belt protons would be both scientifically and economically valuable. This section will briefly discuss how superconducting electromagnets contribute to and enable the EMIC wave mission; for more in-depth analysis of the EMIC wave mission, antenna design and performance, see de Soria 2014 [34]. The following discussion includes a brief summary of the findings from the aforementioned paper.

A very large (30 m diameter) magnetic loop antenna was chosen for this application because of its very small radiation resistance in plasma compared to a linear dipole antenna. To prevent large voltages from forming across a static AC coil due to its enormous self-inductance, a rotating DC (direct current) coil was selected, which in the far field (5000 km or so away from the antenna) has a dipole component equivalent to two static orthogonal AC coils if the rotation rate of the coil matches the desired frequency of its signal. In order to make the spinning antenna gyroscopically stable, it would be necessary to design the spacecraft such that the antenna is spinning around a major axis of inertia. Figure 15 shows the basic concept of the rotating antenna in the frame of its orbit and the Earth's magnetic field (B_0) as well as a potential concept that splits the spacecraft into two buses to make the coil's spinning axis a major axis of inertia.

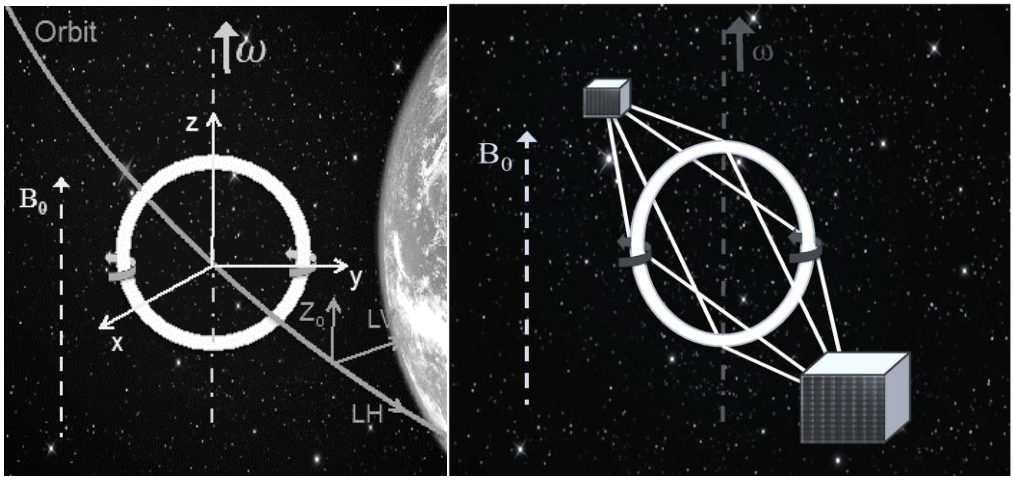

Figure 15: Concept EMIC-wave antenna in (a, left) orbit and (b, right) as a major-axis spinner [34]

In order to radiate the power necessary to detect whether the EMIC wave technique works (25W with a 30 m diameter coil), high-temperature superconductors were selected. Cooling superconductors to colder temperatures increases their performance, as previously stated, but then the cryocoolers necessary to achieve such temperatures demand more power and mass, so there is always a trade between power, mass, and performance when working with superconductors in space.

Additionally, a 30 m diameter antenna would not fit in a launch vehicle fairing and would need to be deployed somehow, likely via a combination of magnetic self-force, strain energy and inflation. Centrifugal force would not be ideal in the case of this antenna because it would mean inducing acceleration and motion around a different axis (normal to the plane of the coil) than the antenna should spin, which would stiffen it against efforts to spin it up around the correct axis (in the plane of the coil).

To date, only rigid heat pipes for the isothermalization of superconducting coils have been created [18]. A rigid heat pipe would not work for a coil large enough to need to be folded or otherwise stowed within a launch vehicle. In light of the difficulties of deployment and cooling, as part of our NIAC Phase II study, the University of Maryland Space Power and Propulsion Lab developed a flexible vapor-cooling system for

cooling superconducting coils to cryogenic temperatures. In addition, the cooling system uses strain energy (a compressed spring around the exterior of the tube) and inflation pressure (from the vapor) to assist deployment of a flexible coil.

A scientific proof-of-concept mission of the EMIC-wave antenna is possible with a smaller (5 m diameter coil) that doesn't require deployment and can be rigid. However, demonstrating a flexible cooling and deployment system would be a big step towards creating a mission that could start removing radiation in measurable quantities.

Far-term: Observatory

Space-based observatories are by necessity complex and precise structures. Each successive observatory has increasingly stringent requirements and the observatory's designers accommodate these requirements with often unique structures and solutions. Figure 16 depicts a notional "Next Next Generation Space Telescope" that incorporates many of the structural and ancillary capabilities mentioned in Section 2.3.

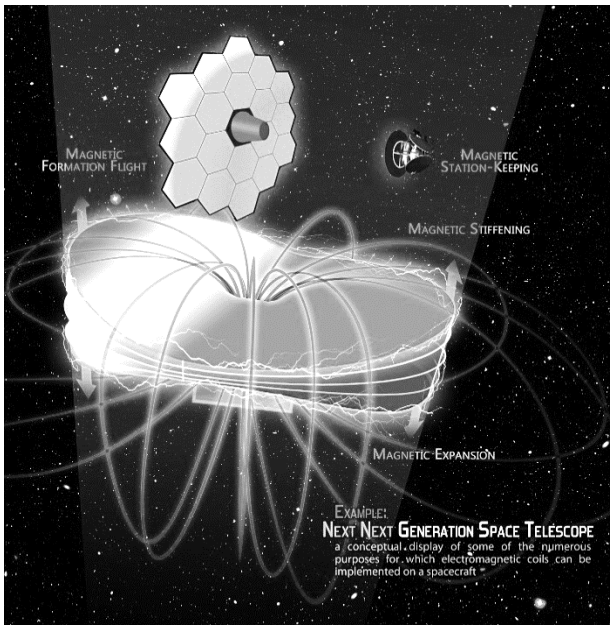

Figure 16: Notional depiction of a "Next Next Generation Space Telescope" incorporating many structural and ancillary electromagnetic functions [16]

Some of the uses incorporated in this futuristic observatory (or other variants upon it) are:

Sunshield/starshade separation and tensioning. Sunshields are structures found in cryogenic telescopes such as the James Webb Space Telescope (JWST), which has instruments that must be kept at cryogenic temperatures in order to observe in infrared. Figure 17 shows a multi-layered sunshield where superconducting coils around the perimeter of the layers are tensioning the layers radially as well as

repelling against each other to fan the layers apart. Referring back to the structural configurations shown in Figure 9, the sunshield depicted in Figure 17 includes both Expand and Separate.

Figure 17: Notional electromagnetically-tensioned multi-layer sunshield for a cryogenic telescope

In a telescope wherein some of the spacecraft is kept at cryogenic temperatures, the ancillary capability of a superconducting magnet to perform better in cold environments could also be leveraged.

For an occulting telescope like the proposed New Worlds Observer [35], a starshade might be used – an enormous flower-like membranous structure positioned great distances away from the telescope itself in order to occult a star and allow for study of a planetary system around said star. A starshade is also a structure that could benefit from electromagnetic perimeter tensioning or deployment.

Positioning of optics: Figure 16 shows a telescope in which multiple parts of the spacecraft are formation flying with each other without any physical contact. In particular, formation flying the secondary mirror with respect to the primary mirror eliminates the obscuration of a tower joining the two as well as takes advantage of the thermal and vibration isolation ancillary capabilities.

Using an example of a telescope positioned at GEO, the necessary strength can be explored of the magnetic dipoles on each of the primary and secondary mirrors to provide the required force to keep the two optics aligned. The primary mirror mass is assumed to be 100,000 kg (could also include the rest of the spacecraft) with a secondary mirror mass of 5,000 kg. The distance between the two is 150 m. The center of mass of the two-body system is along the orbit, aligned with the origin of the coordinate system seen in Figure 18 below.

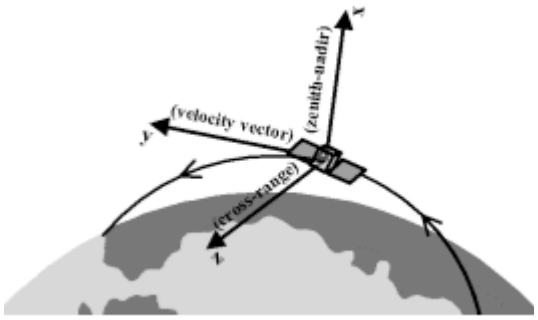

Figure 18: Coordinate system of formation flying optics example [36]

Of interest are the positions of the primary and secondary mirrors with respect to the center of mass of the system. Figure 19 shows the positions x_p and x_s of the primary and secondary mirrors respectively as well as the basic parameters of the problem.

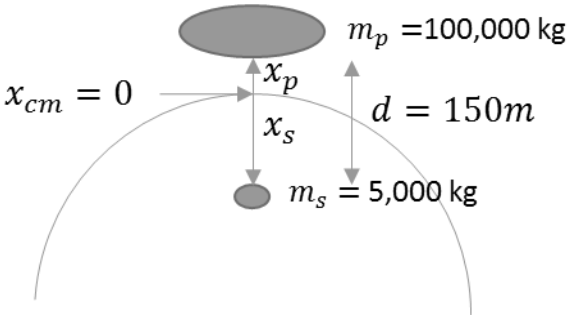

Figure 19: Orientation of primary and secondary mirrors if they are separated in the x direction

Assumed is a nominal orbit with no active orbit control, a spherical Earth (no J2 perturbation), and no-drag, magnetic or solar pressure perturbations. The frame origin/center of mass is in a circular orbit and rotates about the z-axis once per orbit.

The center of mass of the system is at

$$\frac{m_p x_p + m_s x_s}{m_p + m_s} = x_{cm} = 0, \tag{2.6}$$

so solving for x_p and x_s,

$$x_p = \frac{m_s}{m_p + m_s} d = 7.14 \text{ meters}, \tag{2.7}$$

and

$$x_s = -\frac{m_p}{m_p+m_s} d = -142.86 \text{ meters.} \tag{2.8}$$

Change x to y or z for cases where the mirrors are separated in those directions.

Considering the Hill's frame where n_{orb} is the orbital rate = 7.29 × 10^{-5} rad/s (GEO), and a_x, a_y, and a_z are accelerations:

$$\begin{aligned} \ddot{x} - 2n_{orb}\dot{y} - 3{n_{orb}}^2 x &= a_x \\ \ddot{y} + 2n_{orb}\dot{x} &= a_y \\ \ddot{z} + {n_{orb}}^2 z &= a_z \end{aligned} \tag{2.9}$$

If the mirrors are separated in x direction:

$$\ddot{x} = \ddot{y} = \ddot{z} = \dot{x} = \dot{y} = \text{z} = \text{y} = 0, \tag{2.10}$$

$$a_{x,s} = -3{n_{orb}}^2 x_s = 3{n_{orb}}^2 \left(\frac{m_p}{m_p+m_s} d\right),$$

and

$$F_{x,s} = m_s a_{x,s} = 3{n_{orb}}^2 \left(\frac{m_p m_s}{m_p+m_s} d\right) = -F_{x,p} = 0.0114 \text{ N (attraction).} \tag{2.11}$$

If mirrors are separated in z direction:

$$\ddot{x} = \ddot{y} = \ddot{z} = \dot{x} = \dot{y} = \text{x} = \text{y} = 0, \tag{2.12}$$

$$a_{z,s} = {n_{orb}}^2 z_s = -{n_{orb}}^2 \left(\frac{m_p}{m_p+m_s} d\right),$$

and

$$F_{z,s} = m_s a_{z,s} = -n^2 \left(\frac{m_p m_s}{m_p + m_s} d\right) = -F_{z,p} \tag{2.13}$$

$$= -0.0038 \text{ N (repulsion).}$$

If mirrors are separated in y direction:

$$\ddot{x} = \ddot{y} = \ddot{z} = \dot{x} = \dot{y} = \mathrm{x} = \mathrm{z} = 0, \tag{2.14}$$

$$a_{y,s} = 0 = F_{y,s} = F_{y,p}.$$

Separation in the x direction requires three times the force of separation in the z direction, but the x direction requires attraction, while z requires repulsion. Magnetic attraction is inherently more stable than repulsion, but it's likely that the orientation will depend on the mission objectives. It can be seen that there is no force required to keep the mirrors the desired distance apart when they are aligned along the velocity vector, which comes as no surprise.

The separation forces in x and z are small. The goal is therefore to determine how large and/or massive the magnets attached to the formation flying mirrors would need to be in order to achieve these forces.

When the coils are in the *far-field*, meaning at least 10 coil radii apart, they can be approximated as magnetic dipoles, for which the force between two parallel coils in repulsion or attraction is

$$|F| = \frac{3\mu_0\mu_1\mu_2}{2\pi d^4}, \tag{2.15}$$

where $\mu_0 = 4\pi * 10^{-7}\ \mathrm{N/A^2}$ as previously mentioned, and the magnetic moments of the two coils are , μ_1 and μ_2. Assuming that the two coils have the same magnetic moment, $\mu_1 = \mu_2 = \mu_{12}$, the magnitude of the force is therefore

$$|F| = \frac{6 * 10^{-7} * \mu_{12}^2}{d^4}. \tag{2.16}$$

Inserting the material density and dimensions of SuperPower wire and solving for the magnetic moment in terms of the mass and radius of a coil, the force of a SuperPower HTS-wound magnet is roughly

$$F_{SP} \sim \frac{128.3(mR)^2}{d^4}, \tag{2.17}$$

where m is the mass of a single coil in kg, and R is the radius of the coils in meters. Combining Equations (2.11), (2.13), and (2.17),

$$(mR)_x = \sqrt{\frac{0.0114*150^4}{128.3}} = 212.09 \text{ kg-m.} \tag{2.18}$$

and

$$(mR)_z = \sqrt{\frac{0.0038*150^4}{128.3}} = 122.45 \text{ kg-m.} \tag{2.19}$$

It can be seen that as the size of the coil on each of the optical elements is increased, the mass of the magnet decreases, making it clear that increasing the radius of the coil if possible is beneficial to the mass budget (but the maximum radius may be capped by launch vehicle parameters or other environmental constraints.) This analysis is valid for other formation flying elements, not just optical elements.

Formation flying sunshield with respect to primary mirror: Another possible advantage of formation flying within an observatory with a sunshield or something similarly large is that the orientation of the parts can be adjusted over time.

JWST's nominal lifetime is limited by its propellant supply. Barring another unexpected failure, the mission finishes when it runs out of fuel. The propellant is used for two purposes after the spacecraft reaches its operational destination of the Earth-Sun L2 point: stationkeeping in its halo orbit around the L2 point and desaturation of its reaction wheels. The reaction wheels on JWST saturate because of a net solar radiation pressure torque resulting from a center of pressure/center of mass offset on the spacecraft. Because JWST's sunshield is firmly attached to its primary mirror assembly, over the course of its orbit the offset varies but is not persistently zero. Figure 20 shows how disconnecting the optical assembly from the sunshield of our futuristic telescope and formation flying them allows for translational momentum exchange.

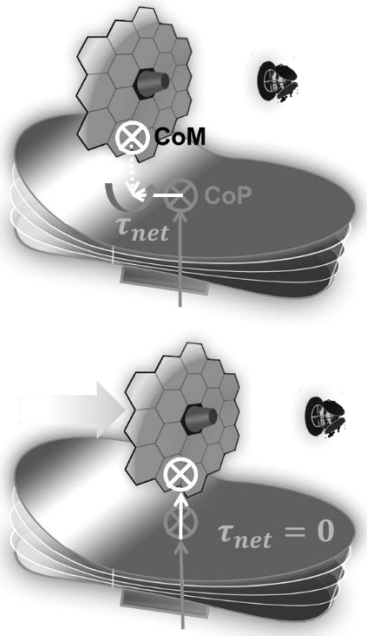

Figure 20: Reducing the center of pressure/center of mass offset of a cryogenic telescope at L2

By doing this, one is essentially "trimming" the sunshield over the course of the orbit to minimize the center of pressure/center of mass offset and therefore use less propellant for desaturation of the telescope. Enumerating the propellant that could be saved by such a technique is a task for future work.

2.5.2. Asteroid Tug

The anchoring applications discussed in the previous section are not the only applications enabled or enhanced by the use of electromagnetic coils and structures. Some other types of missions that could benefit from the structural and ancillary capabilities of an electromagnetic spacecraft are shape maintenance of a solar sail, angular or linear momentum control of objects such as astronauts, cargo, or asteroids, and magnetic shielding of a spacecraft or habitat from radiation using superconducting magnets, the latter of which is an active field of research [37], [38]. Using magnets to tug an asteroid is an application of particular interest, given the clear advantages over a traditional gravity tug approach.

A major potential application of electromagnetic coils on spacecraft that exists independent of a development timeline is a magnetic asteroid tug. Given that a dangerous asteroid could be detected at any time, it is crucial that a mitigation strategy not only exist but be ready for quick deployment. The faster a redirection technique can work, the larger the margin of safety that can be created. While gravitational asteroid tugs are frequently discussed for redirecting asteroids that pose a threat to the Earth, the force that a gravitational tug is able to exert on an asteroid is not only incredibly small (reducing the possible acceleration of the asteroid-spacecraft system), but also hinges on the mass of the spacecraft, which actively goes against the goal of minimizing mass to minimize cost. The dependence on mass also means that as fuel is expended, the force the tug exerts substantially decreases as well.

The force exerted by an electromagnetic tug equipped with a large, superconducting electromagnetic coil, however, would not rely on mass explicitly, but rather on electrical power and the size of the electromagnet. A magnetic tug is directly comparable to a gravitational tug, since both system concepts involve a vehicle that is not touching the asteroid but instead maintaining proximity and inducing some sort of force to pull the asteroid in a desired direction. For the same mass spacecraft, an electromagnetic tug could exert orders of magnitude more attractive force on the asteroid than a gravitational tug, depending upon the asteroid's magnetic and tumbling states.

The asteroid would need to be ferromagnetic and either not tumbling with an oriented magnetic dipole moment, or not already possessing an oriented magnetic dipole moment. A magnetic tug would be equipped with a strong directional HTS magnet that would either act to attract the magnet via its preexisting dipole moment or induce a time-variant alignment within the ferromagnetic core towards the HTS magnet. Further work is necessary to investigate how well the latter technique would work, but it is an application that is very much worth exploring in detail.

For a quick calculation of the ratio of force provided between magnetic and gravitational tugs of the same mass, this analysis uses the asteroid Vesta as an example and assumes that it is not spinning and will be being tugged in a direction along its magnetic dipole moment. This analysis also assumes that the minimum paleointensity at Vesta's surface is 2μT, based on meteorites found on Earth that likely sample Vesta's crust [39], and that the coil (not including thermal system) is 5% of the magnetic tug's mass, exploring later how changing that percentage changes the force ratio. The distribution of mass (including power, propellant, and thermal systems) is not otherwise specified.

The gravitational force between an asteroid and a spacecraft is

$$F_g = \frac{GM_A M_{sc}}{d^2},$$

where G is the gravitational constant ($6.67408 \times 10^{-11} \frac{m^3}{kg-s^2}$), M_A is the mass of the asteroid, and M_{sc} is the mass of the spacecraft. d is the distance between the asteroid and the spacecraft. The magnetic force between two aligned magnetic dipoles (using the dipole approximation for the magnetic moment of the coil, discussed in more detail in Chapter 3) is

$$F_m = \frac{3\mu_0 I_{eff} A_{rea} \mu_A}{2\pi d^4},$$

where N is the number of turns, A_{rea} is the area of the coil, d is the distance from the center of the coil to the center of the asteroid, I_{eff} is the effective current, or the current per turn I_{turn} times the number of turns N in the coil, μ_0 is the vacuum permeability, or $4\pi * 10^{-7} N/A^2$, and μ_A is Vesta's magnetic dipole.

To determine Vesta's magnetic dipole from an assumed 2μT surface field and the radius of the asteroid $r_{ast} \sim 260km$, one can use the formula for magnetic field at a distance r_{ast} along moment axis:

$$2\mu\mathrm{T} = \frac{\mu_0}{4\pi} * \frac{2\mu_A}{(260\ km)^3},$$

And therefore the magnetic dipole moment of the asteroid μ_A is

$$\mu_A = 1.7576 * 10^{17} Am^2.$$

The best approximation for Vesta's mass [40] is

$$M_A = 2.591 * 10^{20}\ kg.$$

The ratio x_f between the magnetic and gravitational forces is as follows:

$$x_f F_g = F_m, \qquad x_f = \frac{F_m}{F_g} = \frac{3\mu_0 I_{eff} A_{rea} \mu_A}{2\pi d^2 G M_A M_{sc}}.$$

The coil mass of a coil with radius R and number of turns N is assumed to be

$$0.05 M_{SC} = 2\pi RN * CSA * \rho_{HTS},$$

where CSA is wire cross-sectional area (m^2), and ρ_{HTS} is the density of the wire (kg/m^3) .

$$A_{rea} = \pi R^2.$$

Rearranging the above equation for coil mass in terms of N and multiplying by A_{rea},

$$NA_{rea} = N\pi R^2 = \frac{M_{SC} * R}{40 * CSA * \rho_{HTS}}.$$

Substituting known values into the equation for the ratio x_f,

$$x_f = \frac{3\mu_0 I_{turn}\mu_A M_{SC} R}{80CSA * \rho_{HTS}\pi d^2 G M_A M_{SC}} = \frac{3\mu_0 I_{turn}\mu_A R}{80CSA * \rho_{HTS}\pi d^2 G M_A} = \frac{3\mu_0 I_{turn}}{80CSA\rho_{HTS}\pi G} * \frac{\mu_A R}{d^2 M_A}.$$

The first term, called Z for reference, comprises constant terms (with a final unit of $\frac{kg}{Am}$, to avoid writing out all the units below), so its value can be determined as follows:

$$Z = \frac{3\mu_0 I_{turn}}{80CSA\rho_{HTS}\pi G} = \frac{3 * 4\pi * 10^{-7} * 150}{80 * 6 * 10^{-7} * 8583.33\pi * 6.67 * 10^{-11}} = (6.55013 * 10^6)\frac{kg}{Am}.$$

Inserting the properties of Vesta [39] gives

$$\frac{Z\mu_A}{M_A} = \frac{(6.55013 * 10^6)\frac{kg}{Am} * (1.7576 * 10^{17} Am^2)}{2.591 * 10^{20} kg} = 4443.27m,$$

$$x_f = \frac{Z\mu_A R}{d^2 M_A} = 4443.27m * \frac{R}{d^2}.$$

d depends largely on the optimal distance from the asteroid to both reduce plume impingement of the thrusters on the asteroid and use propellant most efficiently, if the thrusters are not aligned with the vector of movement. This high-level calculation gives an idea of how the ratio changes depending on how large the coil can be made and how closely the spacecraft can operate to the asteroid. Clearly, the larger radius the coil the better, the only drawback being that a larger coil would mean more mass dedicated to a thermal system (depending on where in the solar system the asteroid is located) and less to propellant, and deployment of that coil also becomes necessary when the radius exceeds that of the launch vehicle fairing. It is also worth noting that a larger force exerted on the asteroid allows faster movement.

How does this ratio change if more or less of the spacecraft mass is devoted to the naked coil? The effect of percentage of spacecraft mass dedicated to the coil can be found by multiplying Z by the multiplier between 5% and the desired mass percent. For example, if the coil is 50% of the mass of the spacecraft, $\frac{Z\mu_A}{M_A}$ = 10* 4443.27m = 44432.7 m.

It should be noted that this analysis *just* compares the relative forces, while an electromagnetic tug would *also* exert a gravitational force by virtue of its having mass, so at a given instant, an electromagnetic tug would exert $F_{tot,A} = F_g + F_m$ force on the asteroid, or

$$F_{tot,A} = F_g(1 + x_f),$$

which is by necessity no less than F_g. This analysis does not take into account a cooling system required for the superconducting magnet, fuel, mission lifetime or how including an EM coil might change those parameters, but it is clear that if an asteroid could possibly be or become magnetized, then an electromagnetic component to a tug would be a very useful option to explore.

2.5.3. Stability Significance

Though stability of elastically-connected electromagnet structures is the primary focus of this thesis, many of the applications discussed in this section do not fall into this category. While development of the specific stability methodology in this thesis will benefit the next-next-generation space observatory, which may have sun shields or long booms elastically connected and magnetically tensioned, the discussed applications all afford different insight into the problem of instability and/or suffer from the risk of instability in some way.

Magnetorquers: The development and deployment of HTS magnetorquers at GEO provides insight into the nature and strength of the perturbations to an electromagnet based on changes in the Earth's magnetic field at the location of the spacecraft. Whereas the methodology developed in this thesis provides a way of calculating the minimum kinetic energy that could made a statically stable equilibrium dynamically unstable, system designers also need data to inform their estimates of the perturbation energy that they should expect for their mission profiles.

EMIC-wave antenna: A spinning antenna presents a whole host of stability related issues, gyroscopic stability being the most significant. A spinning EMIC-wave antenna requires the spacecraft to be designed specifically for its stability, which may require going so far as to actually split the spacecraft into two buses, each kept at a distance from the spin axis to change the major axis of inertia for the system. A spinning magnetic moment in the Earth's magnetic field also imparts a constant magnetic torque that must be accounted for when studying the motion and precession stability of such a spacecraft [41].

Next-next-generation observatory: An observatory could feature a number of electromagnetic capabilities, structural or otherwise, as discussed earlier in this section. Stability in the context that it is discussed in this thesis is clearly applicable to any of the passive magnetic elements of the spacecraft that are elastically connected, but the potential energy curves contributed to by a number of spatially scattered electromagnets can also identified local potential energy minima as good locations for the positioning of active magnetic elements. Actively controlled magnetic elements could be elastically connected, for instance, if no pseudo-passive stable equilibria can be found for a specific set of requirements, but more likely they are disconnected and free-flying as in electromagnetic formation flight.

Asteroid tug: One of the reasons the asteroid tug is a "tug" and not a "shove" is that magnets are only stable in attraction, when they are aligned with an external magnetic field; trying to push an asteroid from behind could result in divergent behavior between the two, since the asteroid and spacecraft coil would want to rotate to align and attract. Such torques on the spacecraft could result in the best case in greater use of propellant for stationkeeping or worst case in the spacecraft colliding with the asteroid. Also, the gravitational attraction between the two would work in the opposite direction of what is desired in the pushing case.

Instability is clearly a major concern for any spacecraft application using electromagnets, and this work seeks to address some of the fundamental aspects of magnetic structural stability analysis and provide a foundational basis for such analyses going forward.

Chapter 3
Analytical Stability

Initial exploration of a topic is often done by starting with a simple system that can be described with simple equations and then adding complexity from there. This approach permits broad understanding of the concepts of interest and the impact of assumptions and design choices on results, as well as easy visualization of results. In this chapter, a simple magnetic structure is introduced for which analytical equations of motion and stability techniques are given and explored in a comprehensive way in order to be referenced in and used to validate later chapters.

Each of the three rows of the approach matrix from Figure 5 (equilibrium identification, static stability, and dynamic stability) are explicitly addressed in order for each of three systems: a translational single degree of freedom system, a rotational single degree of freedom system, and a two degree of freedom system that combines the previous two systems. Figure 21 depicts the three systems to be studied in this chapter and how they fit into the overall approach matrix as introduced in Figure 5 and will be used throughout this chapter with the relevant section highlighted to give the reader a visual guide through the analysis. Those sections that have already been addressed will be shaded with diagonal lines.

	3. Analytical	4. Simple Numerical	5. Complex Numerical
Equilibrium Identification	Dipole force/torque balance equations	Dipole force/torque balance equations	Coil numerical force/torque balance
Static Stability	Dipole force/torque analytical derivatives and linearized eigenvalues	Finite difference stiffness matrix	Finite difference stiffness matrix
Dynamic Stability	Analytical formulation of potential energy	Dipole vector potential calculation of potential energy	Coil (numerical) vector potential calculation of potential energy

1 DoF – Translational	1 DoF – Rotational	2 DoF – Rotational & Translational
Equilibrium Identification	Equilibrium Identification	Equilibrium Identification
Static Stability	Static Stability	Static Stability
Dynamic Stability	Dynamic Stability	Dynamic Stability

Figure 21: Three analytical systems to be studied in this chapter

Non-dimensionalization is an important part of this chapter. Dimensioned and dimensionless equations and calculations are presented side by side throughout the chapter to provide physical insight as well as generalizability of the analyses.

The results of the analytical assessment in this chapter are used to validate the model and approach used in the simple numerical problem of Chapter 3, which will in turn be used to validate the model and approach used in the more complex numerical problem of Chapter 5 such that the complex numerical model and approach can be used for a number of problems.

3.1. Dipole Model

As mentioned in Section 1.4, a simple model for the magnetic field at any point around a magnetic coil is to model the coil as a magnetic dipole moment. This model is henceforth called the dipole model. Figure 22a shows the magnetic moment of a coil based on its design parameters, pointing in the direction dictated by the direction of the current around the loop and the right hand rule. I_{eff} refers to the effective current through the coil, or the current through one turn I multiplied by the number of turns N.

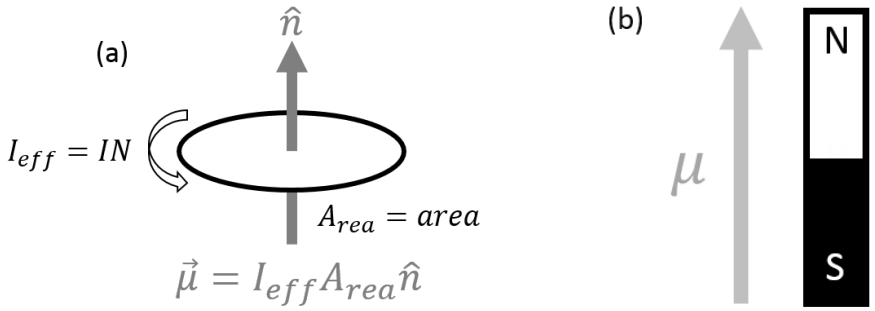

Figure 22: (a) Magnetic dipole moment of a current-carrying coil, (b) bar magnet aligned with magnetic moment

In this chapter, the system is graphically depicted using bar magnets as in Figure 22b, with the convention of pointing the north pole of the magnet in the direction of the magnetic moment. The following equation [20] for the dipole model gives the magnetic field vector at any point in space P_{oint} as a result of the magnetic moment $\vec{\mu}$ and a vector $\vec{r}$ pointing from the center of the dipole to P_{oint}, r being the distance between those points:

$$\vec{B}(\vec{r}) = \frac{\mu_0}{4\pi}\left[\frac{3(\vec{\mu}\cdot\vec{r})\vec{r}}{r^5} - \frac{\vec{\mu}}{r^3}\right]. \tag{3.1}$$

The forces and torques between two dipoles, μ_1 and μ_2, as shown in Figure 23 are given by Equations (3.2)-(3.4) [20], the magnet which the force or torque is acting on being denoted in the following equations with subscript 1 and 2 ($\vec{F}_{mag,1}$ is the magnetic force on dipole 1 from dipole 2, for example). The angles of magnets 1 and 2 (left and right) respectively around the z axis with respect to the x axis are α and β, and η and δ are the angles about the x axis with respect to the y axis. When α and $\beta = 0$, it can be seen that the dipoles are in a repelling (anti-aligned) configuration. The magnitude of the distance between the coils is given by x, with $\vec{r} = x\hat{\imath}$. μ_0 is the vacuum permeability coefficient, or $4\pi \times 10^{-7}\,\frac{N}{A^2}$.

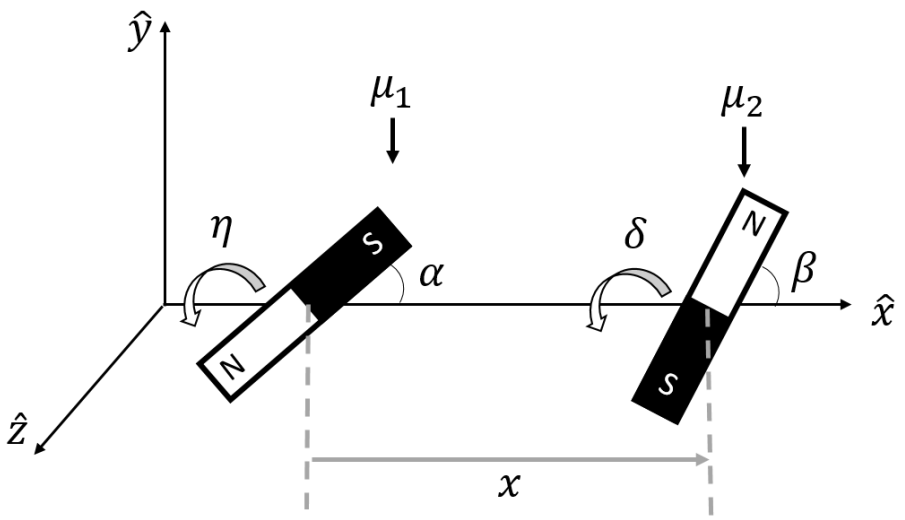

Figure 23: Two magnetic dipoles and the variables used to describe their configuration

$$\vec{F}_{mag,1} = -\frac{3\mu_0\mu_1\mu_2}{4\pi x^4}\begin{bmatrix} 2\cos\alpha\cos\beta - \sin\alpha\sin\beta\cos(\eta-\delta) \\ -\sin\alpha\cos\beta\cos\eta - \cos\alpha\sin\beta\cos\delta \\ -\sin\alpha\cos\beta\sin\eta - \cos\alpha\sin\beta\sin\delta \end{bmatrix} = -\vec{F}_{mag,2}, \tag{3.2}$$

$$\vec{\tau}_{mag,1} = \frac{\mu_0\mu_1\mu_2}{4\pi x^3}\begin{bmatrix} -\sin\alpha\sin\beta\sin(\eta-\delta) \\ -2\sin\alpha\cos\beta\sin\eta - \cos\alpha\sin\beta\sin\delta \\ 2\sin\alpha\cos\beta\cos\eta + \cos\alpha\sin\beta\cos\delta \end{bmatrix}, \tag{3.3}$$

and

$$\vec{\tau}_{mag,2} = \frac{\mu_0\mu_1\mu_2}{4\pi x^3}\begin{bmatrix} \sin\alpha\sin\beta\sin(\eta-\delta) \\ -\sin\alpha\cos\beta\sin\eta - 2\cos\alpha\sin\beta\sin\delta \\ \sin\alpha\cos\beta\cos\eta + 2\cos\alpha\sin\beta\cos\delta \end{bmatrix}. \tag{3.4}$$

The magnetic field resulting from a current carrying coil at a point in space as predicted by the dipole model is not very accurate to the true value except at distances d significantly larger than the radius R of the coil ($x \gg R$). This is because when a coil is close to a point of interest P_{oint} ($x \sim \mathcal{O}(R)$), such as point P_{oint} positioned along the axis of the coil in Figure 24a, the actual field observed at that point is the sum of the contributions to the field of each infinitesimal segment $d\vec{l}$ around the circumference of the coil, all of which are located a coil radius R from the center of the coil and therefore are a nonzero angle Θ from the axis of the coil. A better approximation of the coil magnetic field that sums contributions from numerically discretized elements is given by the Biot-Savart law, which was defined in Section 2.1.

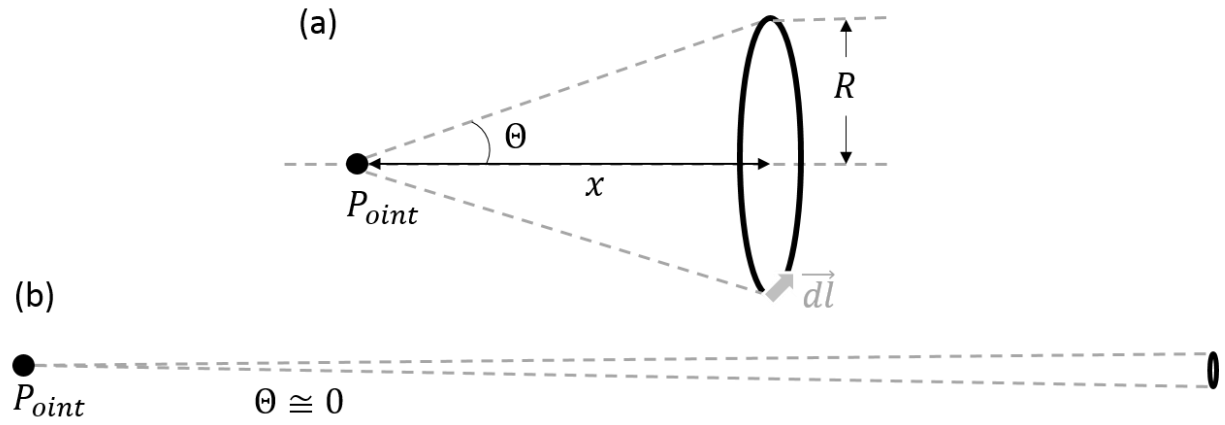

Figure 24: (a) Point in the near-field of a coil, (b) point in the far-field of a coil

As the coil gets farther away from point P, $(x > \mathcal{O}(R))$, as in Figure 24b, the angle subtended by the coil with respect to P becomes smaller and smaller until the coil effectively appears to be a dipole moment with no width. At distances this large, referred to henceforth in this work as the *far-field,* the dipole model has very small error as compared to the Biot-Savart model, because all contributions to the field come from the center of the coil in the dipole model. When $x \leq 10R$, the dipole model exhibits significant error as compared to the Biot-Savart model. Close proximity is henceforth called the *near-field.* The error is compounded by the selection of the point or points of interest when calculating forces and torques from the magnetic field approximation. When the second coil is approximated as a dipole moment, the magnetic field only needs to be calculated at the location of that dipole moment, versus at the center of every infinitesimally small current element around the circumference of the second coil, as it is done in the Biot-Savart model.

To give numerical scale to the near- and far-field, the following figures graphically depict the error between the two magnetic models. The axial dipole force and Biot-Savart force between magnets with the same magnetic moment are both plotted as a function of distance between the magnets in Figure 25, with two different axis scales. The ratio of the axial dipole force between two coils to the Biot-Savart force as a function of distance is shown in Figure 26, again with two different axis scales.

Figure 25 and Figure 26 show the significant overestimation of the magnetic force in the near-field by the dipole model. As the distance between the magnets goes to zero, the axial Biot-Savart force approaches zero as well, consistent with two coaxial, coplanar coils. The dipole force, however, goes to infinity, consistent with two bar magnets placed infinitely close together. It can be seen from Figure 26, especially Figure 26b, that the dipole force approaches the Biot-Savart force and is a good approximate of the magnetic force at $x > 10$ radii, at which point the dipole model has a $\sim 6\%$ error as compared to the Biot-Savart force.

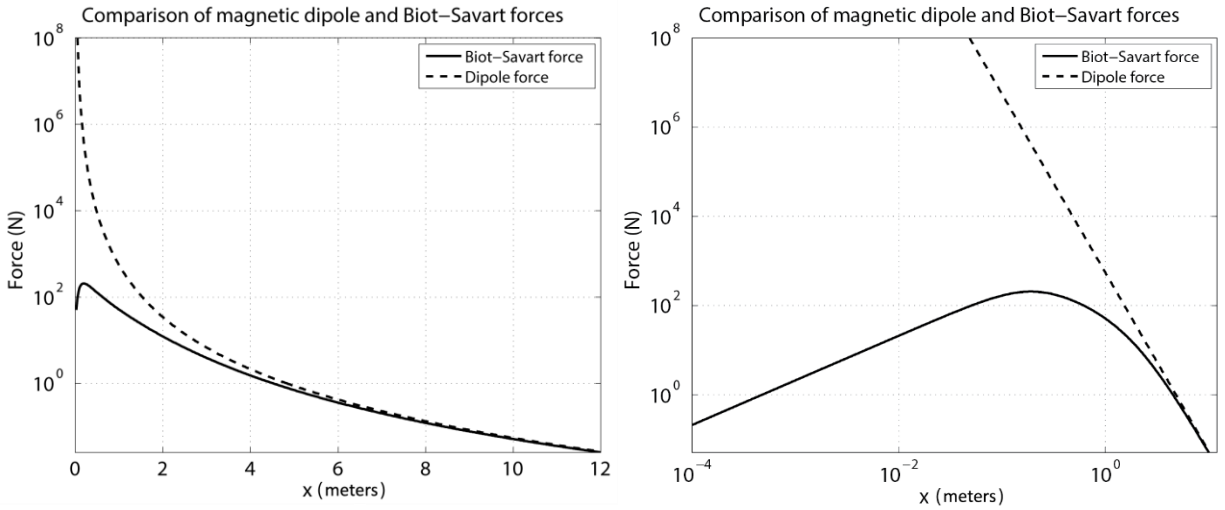

Figure 25: (a, left) Dipole and Biot-Savart forces versus distance with force on a logarithmic axis, (b, right) dipole and Biot-Savart forces versus distance, both logarithmic axes

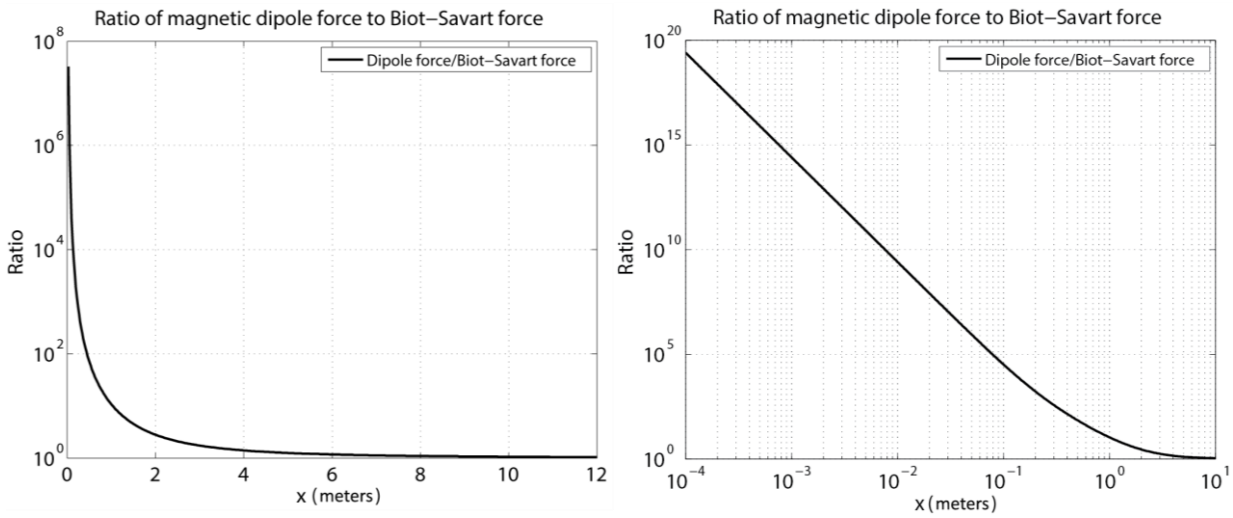

Figure 26: (a, left) Ratio of dipole to Biot-Savart force versus distance with force on a logarithmic axis, (b, right) ratio of dipole to Biot-Savart force versus distance, both logarithmic axes

From Figure 25 and Figure 26, it can be seen that the dipole model of magnetic force is most accurate the farther apart the coils are and increasingly less accurate as the coils move closer together. When the Biot-Savart model is introduced in greater detail and implemented in Chapter 4, the results of this chapter are used to validate the use of the Biot-Savart model in the far-field, wherein the two models should increasingly agree.

3.2. Dipole Boom Design and Assumptions

The general two-dimensional system being analyzed in this chapter is depicted in Figure 27, with the dipole moments visually represented as bar magnets following the aforementioned convention. The magnets are connected by a linear spring of spring constant k attached at the center of each magnet, with a torsional spring of spring constant k_r providing resistance around the z axis. R_1 and R_2 represent the radii of the coils being approximated by dipole moments and thus also contribute to the magnitude of dipole moments μ_1 and μ_2, where

$$\mu_i = \pi N_i I_i R_i^2, \qquad i = 1, 2. \tag{3.5}$$

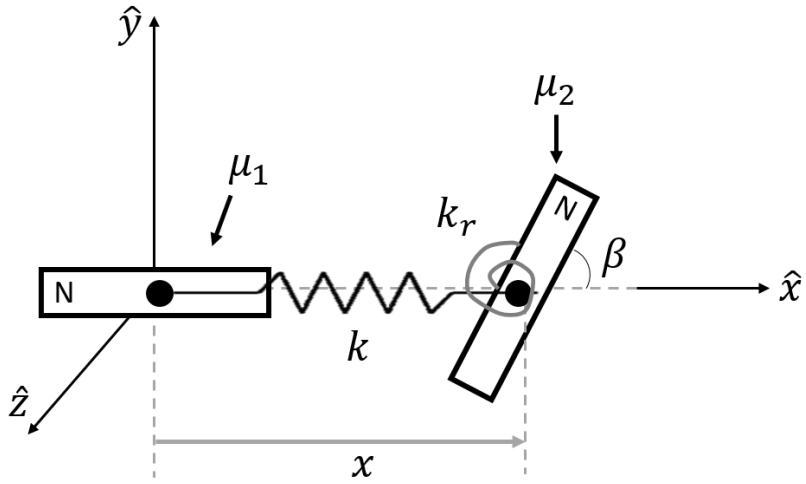

Figure 27: General dipole system with two degrees of freedom

Δx and β represent displacement in the two degrees of freedom that are permitted in this chapter – translation along the x axis and rotation about the z axis. Translation is studied first, followed next by rotation and finally by the combination of the two. The natural length of the linear spring is x_0, such that Δx is the distance the spring is stretched or compressed at location x, and

$$x = x_0 + \Delta x. \tag{3.6}$$

The springs in this work are all assumed to have constant spring constants that do not depend on the stretched or compressed distance. The left magnet/coil, magnet 1, is modeled as fixed in the inertial reference frame, not allowed to translate along or rotate around any axis. Only magnet 2 is allowed to move in the degree(s) of freedom designated. An alternative convention is one that fixes the center of mass of the system in the inertial frame, since no external forces are working to move the center of mass, and allows both coils to move about that point. This convention was not picked because it would either require twice the number of degrees of freedom with two coils moving or require only relative degrees of

freedom to be considered, which is acceptable and effectively identical for the translational degree of freedom but restricts the rotational degree of freedom to only those configurations where both coils are tilted the same but opposite angles with respect to the central axis. Since it was anticipated that a perturbation in a real system would likely affect a single coil, or at least not both coils in the same way, the single fixed coil convention was selected for study in this work.

The equations of motion and analyses are presented both dimensionally and non-dimensionally, the latter most notably performed by framing distance in terms of number of coil radii, based on the radius of coil 1.

The spring force and torque given by the linear and torsional springs respectively, with $k\ (N/m)$ being the linear spring constant and $k_r\ (N \cdot m/rad)$ being the torsional spring constant, are:

$$\vec{F}_{spr,2} = -k\Delta x\hat{\imath}, \tag{3.7}$$

and

$$\vec{\tau}_{spr,2} = -k_r\beta\hat{k}. \tag{3.8}$$

Because rotation about the x axis is not permitted in any of the three systems studied in this chapter, and magnet 1 is not allowed to rotate at all, $\alpha, \eta \text{ and } \delta = 0$. Therefore, Equations (3.2)-(3.4) simplify to the following:

$$\vec{F}_{mag,1} = -\frac{3\mu_0\mu_1\mu_2}{4\pi x^4}\begin{bmatrix} 2\cos\beta \\ -\sin\beta \\ 0 \end{bmatrix} = -\vec{F}_{mag,2}, \tag{3.9}$$

$$\vec{\tau}_{mag,1} = \frac{\mu_0\mu_1\mu_2}{4\pi x^3}\begin{bmatrix} 0 \\ 0 \\ \sin\beta \end{bmatrix}, \tag{3.10}$$

and

$$\vec{\tau}_{mag,2} = \frac{\mu_0\mu_1\mu_2}{4\pi x^3}\begin{bmatrix} 0 \\ 0 \\ 2\sin\beta \end{bmatrix}. \tag{3.11}$$

Equations (3.10) and (3.11) show that the magnetic torque on magnet 2 is twice that of the torque on magnet 1 under the assumptions given. This is not true for configurations with displacement in different degrees of freedom; there are some configurations in which the torque on magnet two is half that which acts on magnet 1. For any rotations allowed, the magnetic torques given in Equations (3.3) and (3.4) fulfill conservation of momentum [20]. Because there are no external forces and torques acting on the system, the total angular momentum is zero between the magnets such that

$$-\frac{\vec{x}}{2} \times \vec{F}_{mag,1} + \frac{\vec{x}}{2} \times \vec{F}_{mag,2} + \vec{\tau}_{mag,1} + \vec{\tau}_{mag,2} = [0]. \tag{3.12}$$

The first two terms in Equation (3.12) are the torques acting about the center of the system as a result of the magnetic forces on the system, where $\vec{x}$ is the vector from the center of magnet 1 to the center of magnet 2.

The analyses presented in this chapter are mostly symbolic, so it is not necessary to assign numerical values to the aforementioned variables until example systems are presented at the end of each section.

3.3. Translational Single Degree of Freedom

1 DoF – Translational	1 DoF – Rotational	2 DoF – Rotational & Translational
Equilibrium Identification	Equilibrium Identification	Equilibrium Identification
Static Stability	Static Stability	Static Stability
Dynamic Stability	Dynamic Stability	Dynamic Stability

The first analytical magnet system studied in this chapter is that which permits motion of magnet 2 translationally in the x direction, as shown in Figure 28. It is henceforth called the 1DoF-T system, with T standing for translational. The torsional spring has been removed from this diagram to reduce any potential confusion since rotation is not allowed, and therefore it does not act. In this diagram, the magnets are anti-aligned and thus repelling. This is called the *repulsive case* going forward. The *attractive case* refers to the flipping of the orientation of magnet 2 such that the dipole moments are now aligned.

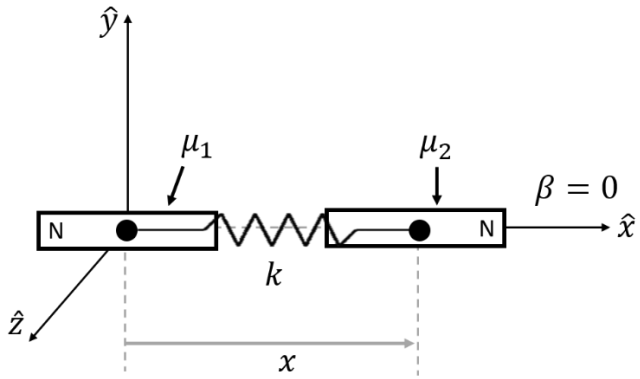

Figure 28: Translational single degree of freedom (1DoF-T) dipole system

3.3.1. Force Balance

A force balance is the first step to identifying equilibrium locations in the 1DoF-T system.

Equations (3.9)-(3.11) simplify when $\alpha, \beta = 0$ as in Figure 28 to

$$\vec{F}_{mag,1} = -\frac{3\mu_0\mu_1\mu_2}{4\pi x^4}\begin{bmatrix}2\\0\\0\end{bmatrix} = -\vec{F}_{mag,2},$$

$$\vec{F}_{mag,2} = \frac{3\mu_0\mu_1\mu_2}{2\pi x^4}\hat{\imath}, \tag{3.13}$$

$$\vec{\tau}_{mag,1} = \frac{\mu_0\mu_1\mu_2}{4\pi x^3}\begin{bmatrix}0\\0\\0\end{bmatrix} = [0], \tag{3.14}$$

and

$$\vec{\tau}_{mag,2} = \frac{\mu_0\mu_1\mu_2}{4\pi x^3}\begin{bmatrix}0\\0\\0\end{bmatrix} = [0]. \tag{3.15}$$

When the dipoles are oriented in opposite directions, the force between them is repulsive such that magnet 2 moves in the positive x direction, away from magnet 1. The spring attaching the coils exert a retracting force in the negative x direction on magnet 2, and thus the total force on magnet 2 is as follows:

$$\vec{F}_{2,rep} = \left(\frac{3\mu_0\mu_1\mu_2}{2\pi x^4} - k(x - x_0)\right)\hat{\imath}. \tag{3.16}$$

If the magnets are exerting an attractive magnetic force (oriented in the same direction), then the total force becomes

$$\vec{F}_{2,att} = \left(-\frac{3\mu_0\mu_1\mu_2}{2\pi x^4} - k(x - x_0)\right)\hat{\imath}. \tag{3.17}$$

Non-Dimensionalization of Force Balance Equations

Because of the large number of variables in Equations (3.16) and (3.17), non-dimensionalizing the equation to reduce the dimensionality of the variable space and thus reduce the number of plots necessary to explore that variable space is of interest. Three characteristic variables (one each of length, time, and mass) are selected to scale all other variables with dimensions of length, time, or mass. The radius of coil 1, R_1, is selected as the characteristic length variable. $\mathcal{T}$ is the characteristic time variable, and is selected based on the natural frequency of coil 2 attached to the linear spring, such that $\mathcal{T} = 1/\omega = \sqrt{m_2/k}$. The mass of coil 2, m_2, is chosen as the characteristic mass variable. Table 4 defines the dimensionless auxiliary variables, denoted by a tilde (~), that are used in the non-dimensionalization.

Table 4: Dimensionless variable definitions

Dimensionless variable	Variable definition
$\tilde{R}_1 \equiv \frac{R_1}{R_1} = 1$	Radius of coil/magnet *1*
$\tilde{R}_2 \equiv \frac{R_2}{R_1}$	Radius of coil/magnet *2*
$\tilde{R}_3 \equiv \frac{R_3}{R_1}$	Radius of coil/magnet *3* (relevant in Chapter 6)
$\tilde{x} \equiv \frac{x}{R_1}$	Distance from the center of coil *1* to the center of coil *2*
$\tilde{x}_0 \equiv \frac{x_0}{R_1}$	Natural length of the linear spring
$\tilde{t} \equiv \frac{t}{\mathcal{T}}$	Time
$\widetilde{m}_2 \equiv \frac{m_2}{m_2} = 1$	Mass of coil/magnet 2
$\widetilde{m}_3 \equiv \frac{m_3}{m_2} = \frac{\tilde{R}_3}{\tilde{R}_2}$	Mass of coil/magnet 3 (relevant in Chapter 6)

Substituting the above dimensionless variables into Equations (3.16) and (3.17) and replacing $F_{2,rep}$ and $F_{2,att}$ with mass multiplied by acceleration of magnet 2 yields the following general equations of motion, using Equation (3.5) for the magnetic moment definition:

Repulsive:

$$m_2\widetilde{m}_2\frac{d^2(R_1\tilde{x})}{d(\mathcal{T}\tilde{t})^2} = \left(\frac{3\pi\mu_0 I^2 N^2 \tilde{R}_2^2 \tilde{R}_1^2}{2\tilde{x}^4} - k(R_1\tilde{x} - R_1\tilde{x}_0)\right)\hat{\imath}, \tag{3.18}$$

and

Attractive:

$$m_2\widetilde{m}_2\frac{d^2(R_1\tilde{x})}{d(\mathcal{T}\tilde{t})^2} = \left(-\frac{3\pi\mu_0 I^2 N^2 \tilde{R}_2^2 \tilde{R}_1^2}{2\tilde{x}^4} - k(R_1\tilde{x} - R_1\tilde{x}_0)\right)\hat{\imath}. \tag{3.19}$$

Mass is a function of coil radius, and therefore it is necessary to expand out the mass term, where N is the number of turns in the coil, and ρ is the mass per unit length of wire:

$$m_2 = 2\pi\tilde{R}_2 R_1 N\rho.$$

Grouping all the constant terms, the following non-dimensional equations of motion are left:

Repulsive:

$$\widetilde{m}_2 \frac{d^2\tilde{x}}{d\tilde{t}^2} = \left(\left(\frac{3\mu_0 I^2 N\tilde{R}_2\tilde{R}_1^2\mathcal{T}^2}{4R_1^2\rho}\right)\frac{1}{\tilde{x}^4} - \frac{k\mathcal{T}^2}{2\pi\tilde{R}_2 R_1 N\rho}(\tilde{x}-\tilde{x}_0)\right)\hat{\imath}, \tag{3.20}$$

and

Attractive:

$$\widetilde{m}_2 \frac{d^2\tilde{x}}{d\tilde{t}^2} = \left(\left(-\frac{3\mu_0 I^2 N\tilde{R}_2\tilde{R}_1^2\mathcal{T}^2}{4R_1^2\rho}\right)\frac{1}{\tilde{x}^4} - \frac{k\mathcal{T}^2}{2\pi\tilde{R}_2 R_1 N\rho}(\tilde{x}-\tilde{x}_0)\right)\hat{\imath}. \tag{3.21}$$

From Equations (3.20) and (3.21), non-dimensional coefficients γ and k^* can be defined, both of which are always positive:

$$\gamma = \frac{3\mu_0 I^2 N\tilde{R}_2\tilde{R}_1^2\mathcal{T}^2}{4R_1^2\rho}, \tag{3.22}$$

and

$$k^* = \frac{k\mathcal{T}^2}{2\pi\tilde{R}_2 R_1 N\rho} = \frac{km_2}{km_2} = 1. \tag{3.23}$$

such that the equations simplify to

$$\tilde{\vec{F}}_{2,rep,ND} = \widetilde{m}_2 \frac{d^2\tilde{x}}{d\tilde{t}^2} = \left(\frac{\gamma}{\tilde{x}^4} - k^*(\tilde{x}-\tilde{x}_0)\right)\hat{\imath}, \tag{3.24}$$

and

$$\tilde{\vec{F}}_{2,att,ND} = \tilde{m}_2 \frac{d^2\tilde{x}}{d\tilde{t}^2} = \left(\frac{-\gamma}{\tilde{x}^4} - k^*(\tilde{x} - \tilde{x}_0)\right)\hat{\imath}. \tag{3.25}$$

The aforementioned equations and non-dimensional coefficients will be used in the rest of this section. As in the dimensional case, the term associated with the magnetic force switches signs between the repulsive and attractive cases. The left hand side of these equations, $\tilde{\vec{F}}_{2,rep,ND}$ and $\tilde{\vec{F}}_{2,att,ND}$, represent a non-dimensional total force, which will be what is plotted in future visualizations of these equations.

k^* can be seen in Equation (3.23) to equal 1 given the selected definition of $\mathcal{T}$. The rest of this chapter and others will continue to use k^* for generality in equations and plots because the terms do not cancel out in the same way in the rotational case (which uses a separate non-dimensional spring constant, k_r^*) or when more than 2 coils are being modeled. Because $k^* = 1$, however, additional values of k^* do not need to be explored in the two-coil case.

3.3.2. Equilibrium Identification

1 DoF – Translational	1 DoF – Rotational	2 DoF – Rotational & Translational
Equilibrium Identification	Equilibrium Identification	Equilibrium Identification
Static Stability	Static Stability	Static Stability
Dynamic Stability	Dynamic Stability	Dynamic Stability

As defined in Section 1.2.1, equilibrium is determined by finding where the net forces and/or torques are zero. Because magnet 1 is fixed in inertial space, the balances on coil 2 are used to satisfy the equilibrium criteria.

It should be noted that in the translational single degree of freedom (1DoF-T) problem, only a force balance is considered, since a torque imbalance would not result in rotation because rotation in this system is not permitted. It so happens that when $\beta = 0$, there is no torque between the two magnets (as shown by Equations (3.10) and (3.11)), and therefore there is always a torque balance in the 1DoF-T case.

In the rotational 1DoF (1DoF-R) case to be considered next, however, only a torque balance is considered, and a force balance is *not* otherwise satisfied by the conditions of the system. In the combined 2DoF case, both a force and torque balance will be required to achieve equilibrium.

The force balance in the repulsive case, and thus equilibrium in the x direction, occurs when Equation (3.16) is zero, or

$$\frac{3\mu_0\mu_1\mu_2}{2\pi x^4} = k(x - x_0). \tag{3.26}$$

Non-Dimensionalization of Equilibrium

The non-dimensional repulsive force balance occurs when Equation (3.24) equals zero, or

$$\frac{\gamma}{\tilde{x}^4} = k^*(\tilde{x} - \tilde{x}_0), \tag{3.27a}$$

and

$$\frac{\gamma}{k^*} = \tilde{x}^4(\tilde{x} - \tilde{x}_0). \tag{3.27b}$$

In the attractive case, the left side of Equations (3.26) and (3.27a) becomes negative.

Example Dimensioned Equilibrium Identification

The solutions to Equation (3.26) are best found by graphical examination. Figure 29a plots both sides of Equation (3.26) to examine for what values of x they intersect (which are equilibrium points) in the compressed regime ($x < x_0$, which occurs when the magnetic force is attractive). Figure 29b plots both sides of Equation (3.26) in the tensioned regime ($x > x_0$, which occurs when the magnetic force is repulsive). It should be noted that for this graphical examination and all the rest of the equilibrium identifications in this chapter, the step size for x is 0.02, meaning there is a point every 0.02 meters (or no units, in the dimensional case). In Chapter 4, smaller step sizes will be examined to determine how it affects the accuracy of equilibrium identification.

In order to plot Equation (3.26), some numerical values are required. Plotted in Figure 29 are the magnitude of the magnetic force between two magnetic moments of 25133 and 36191 Am^2 (based on 80 A and 100 turns in each coil, coil 1 with a radius of 1 m and coil 2 with a radius of 1.2 m) as well as several spring forces (each with a different value of k) against distance x. The natural length of each spring is assumed to be $x_0 = 2$ m. It should be noted that both magnetic moments are positive and that for the repulsive case, the negative sign that comes from the opposite direction current is pulled out and appears as appropriate; μ_1 and μ_2 are magnitudes.

In the compressed regime, the spring is compressed, and therefore the spring forces all act in the positive x direction. In order to compress the springs, an attractive magnetic force is required such that the magnetic dipole force on magnet 2 acts in the negative x direction. Therefore, anywhere that the spring force curves intersect with the dipole force curve, the total force is zero, making that point an equilibrium.

The same concept applies in the tensioned regime, wherein the spring forces are now negative, and the dipole force is now positive. The absolute values of each side of Equation (3.26) are plotted because of the logarithmic y axis. The numbered circles in each plot of Figure 29 represent an equilibrium point, and when they are detailed in Table 5, they are assigned as $x_{\#a}$ or $x_{\#b}$, where # is the number in the circle atop the equilibrium point, and a and b refer to the attractive and repulsive plots respectively.

Figure 29a has four equilibrium points, two on each of the two stiffest spring constants, k = 1000 and k = 10000. The more elastic spring constants plotted have no equilibria with the dipole force, which physically would mean that such a spring would be infinitely compressed to zero length as magnet 2 is pulled back to coincide with magnet 1. Equilibria 1a and 2a occur when the magnets are less than one coil radius apart (their associated x values indicated by x_{1a}, x_{2a}, and so forth in this section), and equilibria 3a and 4a occur very close to x_0, indicating only a small amount of compression. For the k=10000 spring, and similarly for the k = 1000 spring, when $x < x_{1a}$ and $x > x_{4a}$, the magnetic force is larger in magnitude than the spring force, and when $x_{1a} < x < x_{4a}$, the spring force dominates the magnetic force.

Figure 29b has a very different pattern of equilibria than Figure 29a; each spring force intersects once with the dipole force. The two stiffest springs have equilibria very close to x_0, indicating a small amount of stretching. The more elastic the spring, the more the spring is stretched at equilibrium, which is consistent with two magnets repelling against successively weaker springs. Table 5 gives the associated x values of the equilibria shown in Figure 29.

Table 5: x values of equilibria identified in Figure 29

Attractive			Repulsive		
Equilibrium ID	k value	x value at equilibrium	Equilibrium ID	k value	x value at equilibrium
x_{1a}	10000	0.4319	x_{1b}	10000	2.0037
x_{2a}	1000	0.8257	x_{2b}	1000	2.0320
x_{3a}	1000	1.9632	x_{3b}	100	2.2233
x_{4a}	10000	1.9964	x_{4b}	50	2.3549
			x_{5b}	20	2.5985
			x_{6b}	5	3.1329

The stability of these identified equilibria, both static and dynamic, will be explored in the rest of this section.

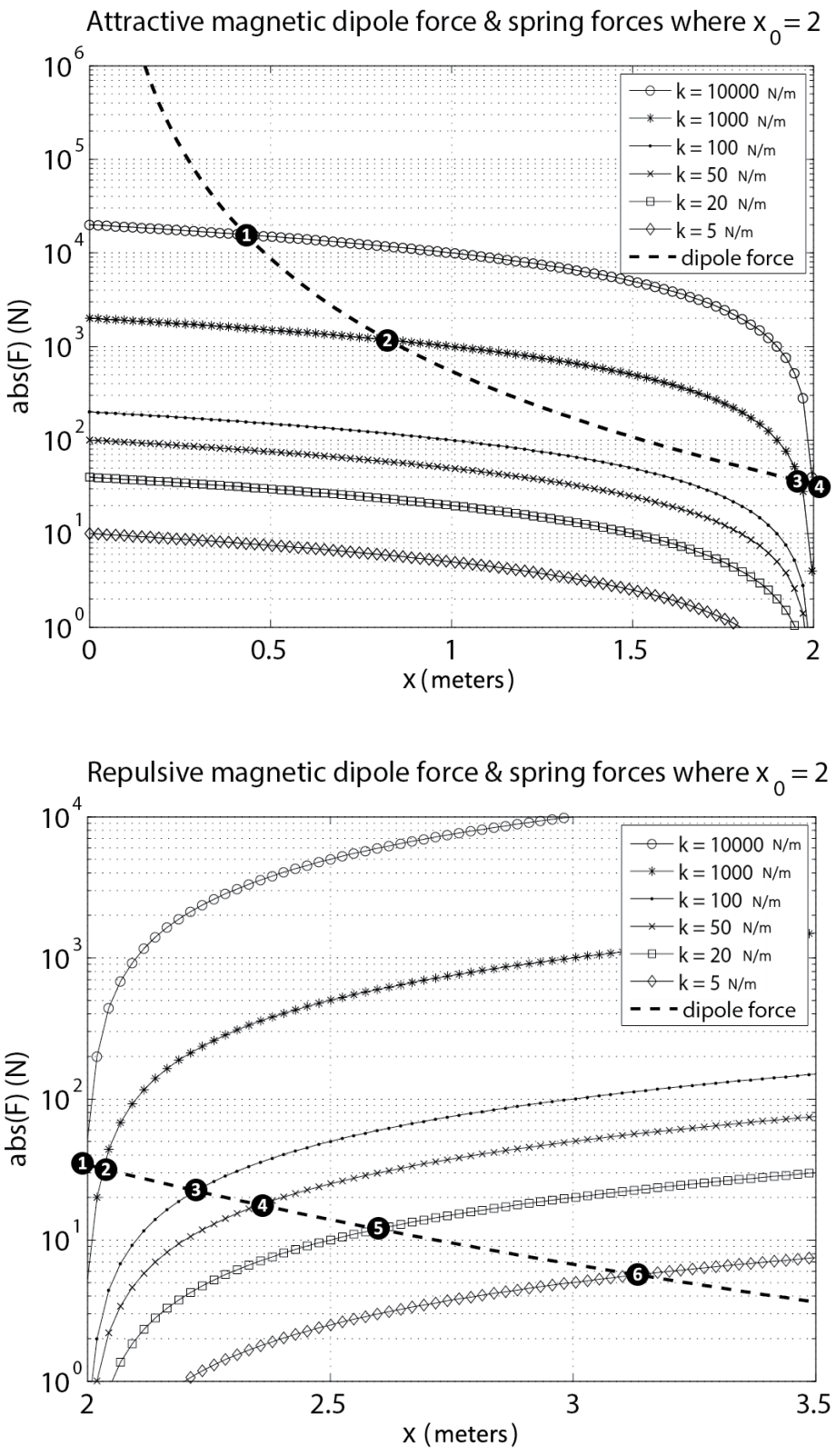

Figure 29: Absolute value of spring forces and (a, top) attractive magnetic dipole force or (b, bottom) repulsive magnetic dipole force, with 1DoF-T equilibrium points identified, from Equation (3.26)

Example Non-Dimensional Equilibrium Identification

The non-dimensional solutions to Equations (3.27) are best found by graphical examination. Figure 30a plots the absolute value of both sides of Equation (3.27b) to examine for what values of $\tilde{x}$ they intersect (which are equilibrium points) in the compressed regime ($\tilde{x} < \tilde{x}_0$, which occurs when the magnetic force is attractive). Figure 31b plots both sides of Equation (3.27b) in the tensioned regime ($\tilde{x} > \tilde{x}_0$, which occurs when the magnetic force is repulsive).

The reason for plotting Equation (3.27b) instead of Equation (3.27a) is that γ/k^* is the value that determines the equilibrium values of $\tilde{x}$, and condensing the two into one non-dimensional term reduces the number of lines that must be plotted, since $\tilde{x}^4(\tilde{x} - \tilde{x}_0)$ only depends on $\tilde{x}_0$, which is considered fixed for the sake of this chapter. Also, $k^* = 1$ in this particular system, so any variation in γ/k^* is attributable to variation in γ, which is linked to both magnetic design variables and the spring constant k. The plots look slightly different in shape from the dimensioned case and come with less physical intuition to the lines but more generalizability, such that the dimensioned and non-dimensioned sections of this chapter provide different insight on the same problem. Because the terms are rearranged, however, in this section the "left side" (γ/k^*) and "right side" ($\tilde{x}^4(\tilde{x} - \tilde{x}_0)$) are referred to rather than "magnetic" and "spring" forces.

As in the dimensioned case, in the compressed regime/attractive case, the right side is positive in $\tilde{x}$, and the left side is negative in $\tilde{x}$. In the tensioned regime/repulsive case, the right side is negative in $\tilde{x}$, and the left side is now positive in $\tilde{x}$. The absolute values of each side of Equation (3.27b) are plotted because of the logarithmic y axis. Anywhere that a horizontal left side line intersects with the right side curve, the equation balances, making that point an equilibrium. The numbered circles in each plot of Figure 30 represent an equilibrium point.

The same trends are visible in Figure 30 as in the previous section. The attractive case, shown in Figure 30a, shows that each left and right side combo has either zero or two equilibria. If the latter, then one exists very close to $\tilde{x} = 2$ and the other somewhere $\tilde{x} < 1$. If no equilibria exist, it is because the left side is larger than the right side, which corresponds with stronger magnetic moments and/or weaker springs. One can imagine a γ/k^* value expected to just barely intersect with the maximum absolute value of $\tilde{x}^4(\tilde{x} - \tilde{x}_0)$, or $\frac{\gamma}{k^*} = 2.621439$ at $\tilde{x}_{max} = 8/5$. This value is added to the table below for later study of its static and dynamic stability, since it represents a convergence of a statically stable and a statically unstable equilibrium.

The repulsive case, shown in Figure 30b, has exactly one equilibrium for every combination of left and right side, indicating that any value of γ/k^* could be chosen to result in a stable repulsive equilibrium. Larger values of γ/k^* result in a greater distance from $\tilde{x}_0$.

Table 6 gives the associated $\tilde{x}$ values of the equilibria shown in Figure 30, in the same format as the previous section.

Table 6: $\tilde{x}$ values of equilibria identified in Figure 30

Attractive			Repulsive		
Equilibrium ID	γ/k^*	$\tilde{x}$ value at equilibrium	Equilibrium ID	γ/k^*	$\tilde{x}$ value at equilibrium
$\tilde{x}_{1a}$	1	1.0001	$\tilde{x}_{1b}$	1	2.0563
$\tilde{x}_{2a}$	2	1.3003	$\tilde{x}_{2b}$	2	2.1028
$\tilde{x}_{3a}$	2	1.8159	$\tilde{x}_{3b}$	5	2.2098
$\tilde{x}_{4a}$	1	1.9269			
$\tilde{x}_{max}$	2.621439	$8/5$			

The stability of these identified equilibria, both static and dynamic, will be explored in the rest of this section.

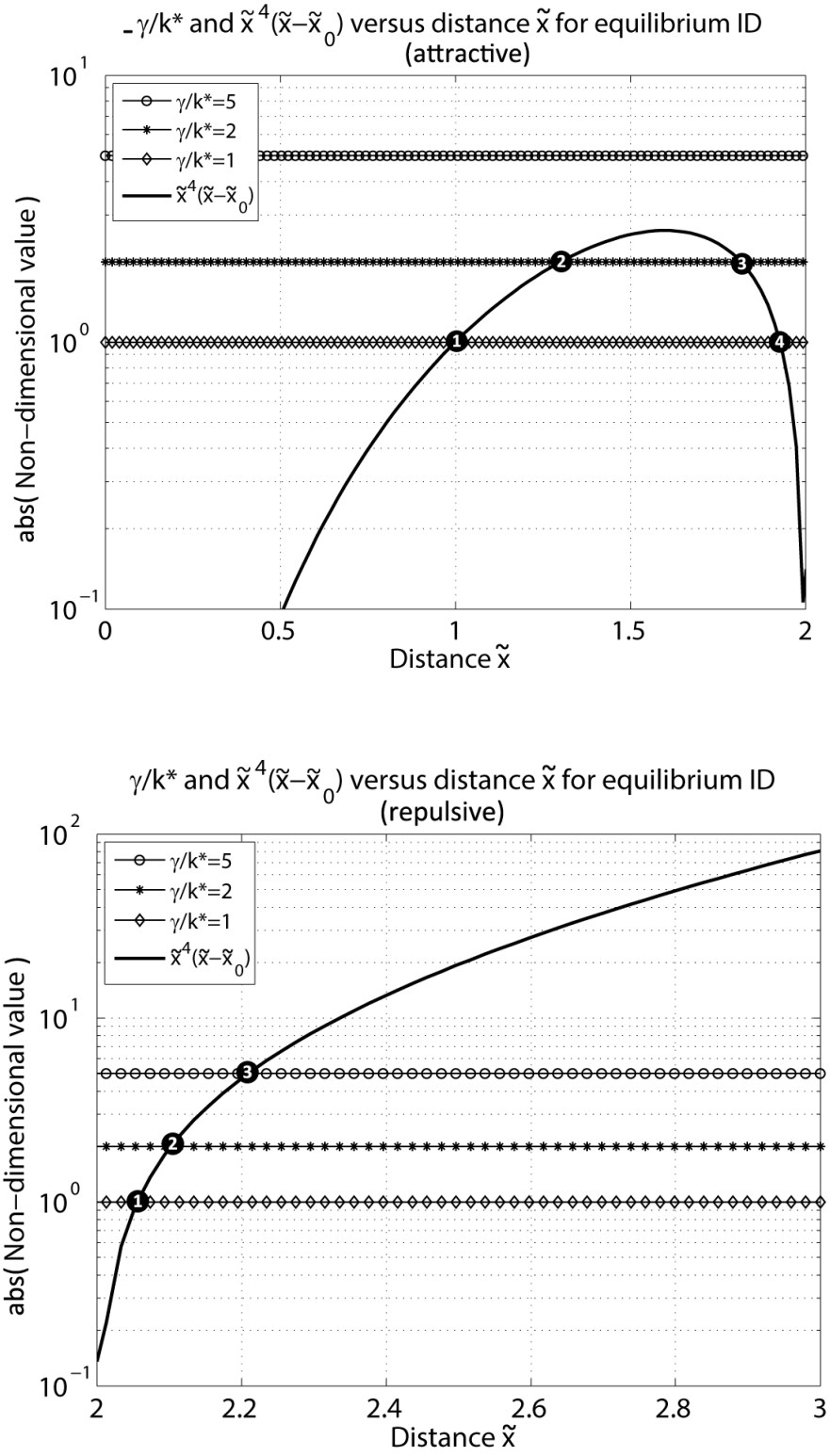

Figure 30: Absolute values of non-dimensional (ND) spring forces and absolute values of ND (a, top) attractive magnetic dipole force or (b, bottom) repulsive magnetic dipole force, with ND 1DoF-T equilibrium points identified, from Equation (3.27b)

3.3.3. Static Stability Classification

1 DoF – Translational	1 DoF – Rotational	2 DoF – Rotational & Translational
Equilibrium Identification	Equilibrium Identification	Equilibrium Identification
Static Stability	Static Stability	Static Stability
Dynamic Stability	Dynamic Stability	Dynamic Stability

In this section, the static stability of the 1DoF-T equilibria identified in the previous section is evaluated.

Stiffness Approach

Now that an equilibrium point has been identified, static stability at that point can be determined by looking at the sign of the *total stiffness* of the system. Stiffness in general is determined by the spatial derivative of a force or the change in the force due to a unit displacement [25]. Because the system under study has only one degree of freedom, there is only one generalized coordinate (x) in which force can cause motion in the system, and therefore the stiffnesses in this section are scalar values (rather than matrices). In the case of elastic, or spring, stiffness, the spring constant k is the stiffness of the spring, such that from Hooke's law, which says if Δx is measured from x_0,

$$F_{spring,x} = -k_{spring}\Delta x, \tag{3.28}$$

and because the spring stiffness is assumed to be constant and F_{spring} thus linear,

$$k_{spring} = -\left(\frac{dF_{spring,x}}{dx}\right)_{x=x_{eq}}, \tag{3.29}$$

where the derivative is calculated at $x = x_{eq}$.

It can be seen from Equation (3.29) that a positive stiffness means that the force is negative and thus restorative as the spring is stretched away from its natural length x_0. If only $F_{spring,x}$ is acting on the body, then positive stiffness means that the equilibrium is statically stable, a fact that makes easy conceptual sense since if no other forces are acting on the body, $x_{eq} = x_0$, and the spring remains undeformed and at rest.

Magnetic stiffness is defined similarly, according to Moon [25]:

$$k_{mag} = \left(\frac{dF_{mag,x}}{dx}\right)_{x=x_{eq}}, \tag{3.30}$$

with a negative k_{mag} representing a restorative force. In this work, however, the sign convention has been switched to allow combination of magnetic stiffness and spring stiffness into a total stiffness, such that

$$k_{mag} = -\left(\frac{dF_{mag,x}}{dx}\right)_{x=x_{eq}}, \tag{3.31}$$

and a positive stiffness entails a restorative force with a positive displacement away from equilibrium.

Total stiffness is therefore determined by the change in the total (elastic and magnetic) force due to a unit change in the position of the body in a specific generalized coordinate, or

$$\kappa_{tot} = -\left(\frac{dF_{tot,x}}{dx}\right)_{x=x_{eq}}, \tag{3.32}$$

where

$$(F_{tot})_{x=x_{eq}} = \left(F_{mag} + F_{spring}\right)_{x=x_{eq}}. \tag{3.33}$$

Therefore, if κ_{tot} is positive at the equilibrium location x, then the equilibrium is statically stable. It should be noted that if κ_{tot} is positive but very close to 0, the equilibrium may be essentially statically neutral, with higher derivatives required to more rigorously determine static stability [25].

In this chapter, an analytical formulation of stability is desired, so the derivative of Equation (3.16) is taken with respect to x:

$$\frac{d}{dx}\left(F_{2,rep,x}\right) = \frac{d}{dx}\left(\frac{3\mu_0\mu_1\mu_2}{2\pi x^4} - k(x - x_0)\right),$$

and (3.34)

$$\frac{d}{dx}\left(F_{2,rep,x}\right) = \frac{-6\mu_0\mu_1\mu_2}{\pi x^5} - k.$$

Similarly, the derivative of Equation (3.17) is

$$\frac{d}{dx}\left(F_{2,att,x}\right) = \frac{6\mu_0\mu_1\mu_2}{\pi x^5} - k. \tag{3.35}$$

Non-Dimensionalization of Stiffness

The non-dimensional version of each of Equations (3.34) and (3.35) are as follows from Equations (3.24) and (3.25):

Repulsive:

$$\frac{d}{d\tilde{x}}\left(\tilde{F}_{2,rep,ND,x}\right) = \frac{d}{d\tilde{x}}\left(\frac{\gamma}{\tilde{x}^4} - k^*(\tilde{x} - \tilde{x}_0)\right),$$

and

$$\frac{d}{d\tilde{x}}\left(\tilde{F}_{2,rep,ND,x}\right) = \frac{-4\gamma}{\tilde{x}^5} - k^*, \tag{3.36}$$

Attractive:

$$\frac{d}{d\tilde{x}}\left(\tilde{F}_{2,att,ND,x}\right) = \frac{d}{d\tilde{x}}\left(\frac{-\gamma}{\tilde{x}^4} - k^*(\tilde{x} - \tilde{x}_0)\right),$$

and

$$\frac{d}{d\tilde{x}}\left(\tilde{F}_{2,att,ND,x}\right) = \frac{4\gamma}{\tilde{x}^5} - k^*. \tag{3.37}$$

The dimensional derivatives are compared in the next subsection to another method of evaluating static stability via eigenvalue analysis.

Eigenvalue Approach

Another technique for evaluating the stability of a nonlinear system of equations is Jacobian linearization of a nonlinear system around an equilibrium [42], [43] followed by eigenvalue analysis of the Jacobian. This process involves first constructing a Jacobian matrix of the system at equilibrium points in order to approximate the system linearly. This linearization is done because "the eigenvalues of a system linearized around a fixed point can determine the stability behavior of a system around the fixed point. The particular stability behavior depends upon the existence of real and imaginary components of the eigenvalues, along with the signs of the real components and the distinctness of their values [44]."

This technique is focused on the transient response of a system, which refers to how the system response changes over time. As discussed in Section 1.2, static instability means dynamic instability and a divergent transient response in at least one generalized coordinate. Static stability can be dynamically stable, neutrally stable, or unstable, depending on the initial conditions of the system. If any of the eigenvalues of the system are in the right hand plane (RHP) of the complex plane, meaning that they have a positive real part, then the system is statically unstable and thus dynamically unstable. If all of the eigenvalues are in the left hand plane (LHP), meaning that they have negative real parts, then the system is statically stable, its dynamic stability yet to be determined. Repeated eigenvalues on the imaginary axis result in a statically unstable system [45].

A special case: If the system has non-repeated eigenvalues *on* the imaginary axis (meaning that those eigenvalues have no real parts), then it is statically stable and *neutrally dynamically stable*. A pair of eigenvalues on the imaginary axis of equal and opposite sign result in a constant oscillating response that neither decays nor increases in amplitude [45]. Because the systems investigated in this thesis are modeled with no energy dissipation mechanism, neutrally dynamically stable systems are accepted as dynamically stable, though in a real system, there would be energy dissipation that would factor into the eigenvalues.

The non-homogenous versions of the ODEs in Equations (3.16) and (3.17) are given by Equations (3.38) and (3.39) respectively, where m_2 is the mass of magnet 2:

$$m_2\ddot{x} = \left(\frac{3\mu_0\mu_1\mu_2}{2\pi x^4} - k(x - x_0)\right), \tag{3.38}$$

and

$$m_2\ddot{x} = \left(-\frac{3\mu_0\mu_1\mu_2}{2\pi x^4} - k(x - x_0)\right). \tag{3.39}$$

Each of the two second-order equations above can each be described with a system of two first-order equations. Equation (3.38) can be rewritten as follows, using y as a dummy variable to facilitate the split:

$$y = \dot{x},$$

and

$$\begin{cases} \dot{x} = f_{rep}(x, y) = y \\ \dot{y} = g_{rep}(x, y) = \dfrac{1}{m_2}\left(\dfrac{3\mu_0\mu_1\mu_2}{2\pi x^4} - k(x - x_0)\right), \end{cases} \tag{3.40}$$

and Equation (3.39):

$$\begin{cases} \dot{x} = f_{att}(x, y) = y \\ \dot{y} = g_{att}(x, y) = \dfrac{1}{m_2}\left(-\dfrac{3\mu_0\mu_1\mu_2}{2\pi x^4} - k(x - x_0)\right). \end{cases} \tag{3.41}$$

The Jacobian of Equation (3.40) calculated in general and not yet at a specific point, is

$$J_{rep} = \begin{bmatrix} \dfrac{\partial f_{rep}}{\partial x} & \dfrac{\partial f_{rep}}{\partial y} \\ \dfrac{\partial g_{rep}}{\partial x} & \dfrac{\partial g_{rep}}{\partial y} \end{bmatrix} = \begin{bmatrix} 0 & 1 \\ -\dfrac{6\mu_0\mu_1\mu_2}{m_2\pi x^5} - \dfrac{k}{m_2} & 0 \end{bmatrix}. \tag{3.42}$$

The eigenvalues of Equation (3.42) calculated by solving for where

$$\det\left(J_{rep} - \lambda_{rep}[I_n]\right) = 0, [46]$$

are as follows:

$$\lambda_{rep,1,2} = \pm\sqrt{-\frac{6\mu_0\mu_1\mu_2}{m_2\pi x^5} - \frac{k}{m_2}}. \tag{3.43}$$

Because the system modeled in this chapter does not include a damping or velocity-dependent term, both eigenvalues in Equation (3.43) are equal and of opposite sign. Real roots of opposite sign result in an unstable saddle node [44] because one eigenvalue thus has a positive real part. Therefore, the only way to ensure that the system is stable at any given equilibrium is to solve for where the formula inside the

radical is negative, as the square root of a negative number is necessarily imaginary and will therefore result in two purely imaginary eigenvalues:

$$-\frac{6\mu_0\mu_1\mu_2}{m_2\pi x^5}-\frac{k}{m_2}<0,$$

or, if m_2 is multiplied out,

$$-\frac{6\mu_0\mu_1\mu_2}{\pi x^5}-k<0. \tag{3.44}$$

Immediately, it can be seen that Equation (3.44) and Equation (3.35) represent the same equation:

$$\frac{d}{dx}\left(F_{2,rep,x}\right)=-\frac{6\mu_0\mu_1\mu_2}{\pi x^5}-k<0.$$

Because an equilibrium point requires positive stiffness (and thus a negative derivative of force) to be stable via the stiffness technique, both the stiffness and eigenvalue techniques reach the same conclusion, and thus the stiffness approach has been validated for future use in this chapter and future chapters.

Following the same process with the attractive case, the formula to be satisfied for purely imaginary eigenvalues is

$$\frac{6\mu_0\mu_1\mu_2}{\pi x^5}-k<0. \tag{3.45}$$

The first terms in each of Equations (3.44) and (3.45) are linked to the magnetic force and are indeed the derivatives of the magnetic force equation in each of the repulsive and attractive cases, respectively. μ_1 and μ_2 are dependent on the dimensions of, number of turns in, and the current through each of the two coils, and therefore as any of those three variables increases, the magnetic term increases as well. The second term is of course the derivative of the spring force, assumed linear in this work.

All of the coefficients involved in Equations (3.44) and (3.45) are positive, which means that the inequality in Equation (3.44) is always fulfilled for any equilibrium point, and therefore all equilibria should be statically stable in the repulsive case. Equation (3.45) is more interesting because if k is smaller than the first term, the inequality is not fulfilled. Thus, when the static stabilities of the equilibria identified in Figure 29 are calculated next, if there is a mix of stabilities in the attractive case, stability will occur for larger k values, and instability will occur for smaller k values.

Example Dimensional Stability Calculations

Table 7 shows Equation (3.34) or (3.35) (depending on whether the magnets are attracting or repelling) inserted into Equation (3.32) to obtain the stiffness κ_{tot} at each of the x values listed in Table 5 (basically just switching the signs on Equations (3.34) and (3.35)). The signs of the stiffnesses in Table 7 determine whether each equilibria is statically stable (positive) or unstable (negative). Statically stable equilibria are bolded.

Table 7: Stiffness values κ_{tot} at each equilibrium in Figure 29, with statically stable equilibria bolded

Attractive				Repulsive			
Equil. ID	k value (N-m)	x value at equilibrium (m)	κ_{tot} (N/m)	Equil. ID	k value (N-m)	x value at equilibrium (m)	κ_{tot} (N/m)
x_{1a}	10000	0.4319	-135250	$\boldsymbol{x_{1b}}$	**10000**	**2.0037**	**10068**
x_{2a}	1000	0.8257	-4690	$\boldsymbol{x_{2b}}$	**1000**	**2.0320**	**1063**
$\boldsymbol{x_{3a}}$	**1000**	**1.9632**	**930**	$\boldsymbol{x_{3b}}$	**100**	**2.2233**	**140**
$\boldsymbol{x_{4a}}$	**10000**	**1.9964**	**9930**	$\boldsymbol{x_{4b}}$	**50**	**2.3549**	**80**
				$\boldsymbol{x_{5b}}$	**20**	**2.5985**	**38**
				$\boldsymbol{x_{6b}}$	**5**	**3.1329**	**12**

From Table 7, it can be seen that all of the equilibria in the repulsive system are stable, as well as the equilibria that occur close to x_0 in the attractive system. If the system starts at one of these distances and is slightly displaced, the system experiences a force in the x direction towards the equilibrium. Those equilibria in the attractive system which occur within a distance of one coil radius (x_{1a} and x_{2a}) are statically unstable. If the system starts at either x_{1a} or x_{2a} and is slightly displaced, the system will experience a force increasing the distance from the equilibrium in the direction of the displacement

Example Non-dimensional Stability Calculations

Table 8 shows Equation (3.36) or (3.37) (depending on whether the magnets are attracting or repelling) inserted into Equation (3.32) to obtain the non-dimensional stiffness $\kappa_{tot,ND}$ at each of the $\tilde{x}$ values listed in Table 6 (basically just switching the signs on Equations (3.36) and (3.37)). The signs of the stiffnesses in Table 8 determine whether each equilibria is statically stable (positive) or unstable (negative). Statically stable equilibria are bolded.

As mentioned at the end of Section 3.3.3 for the dimensional case, all of the coefficients involved in Equations (3.36) and (3.37) are positive, which means that the repulsive stiffness is always positive, and therefore all repulsive equilibria should be statically stable. Equation (3.37) and the attractive case are more interesting, because if k^* is smaller than $4\gamma/\tilde{x}^5$, then a negative stiffness and instability results, such that stability requires

$$k^* > \frac{4\gamma}{\tilde{x}^5}.$$

k^* is known to be 1 by definition, so γ is therefore equal to γ/k^*.

Table 8: Non-dimensional stiffness values $\kappa_{tot,ND}$ at each equilibrium in Figure 30, statically stable equilibria bolded

Attractive					Repulsive				
Equil. ID	γ/k^*	γ	$\tilde{x}$ value	$\kappa_{tot,ND}$	Equil. ID	γ/k^*	γ	$\tilde{x}$ value	$\kappa_{tot,ND}$
$\tilde{x}_{1a}$	1	1	1.0001	-2.9980	$\boldsymbol{\tilde{x}_{1b}}$	**1**	**1**	**2.0563**	**1.1088**
$\tilde{x}_{2a}$	2	2	1.3003	-1.1521	$\boldsymbol{\tilde{x}_{2b}}$	**2**	**2**	**2.1028**	**1.1946**
$\boldsymbol{\tilde{x}_{3a}}$	**2**	**2**	**1.8159**	**0.5948**	$\boldsymbol{\tilde{x}_{3b}}$	**5**	**5**	**2.2098**	**1.3795**
$\boldsymbol{\tilde{x}_{4a}}$	**1**	**1**	**1.9269**	**0.8494**					
$\tilde{x}_{max}$	2.62144	2.62144	$8/5$	0.0001					

The two statically stable attractive equilibria near $\tilde{x} = 2$ are as expected, as are the two statically unstable equilibria for the same γ/k^* values closer to $\tilde{x} = 1$. Also, interestingly, $\tilde{x}_{max}$ is very close to 0 and effectively statically neutrally stable.

The above observations provoke another question: how much is a "slight" displacement, or how much can the system be displaced from each equilibrium before subsequent motion diverges from and no longer oscillates about the original equilibrium point? In other words, how much of a displacement can be tolerated before the system switches from dynamically stable to dynamically unstable? The next section addresses this question.

3.3.4. Dynamic Stability

1 DoF – Translational	1 DoF – Rotational	2 DoF – Rotational & Translational
Equilibrium Identification	Equilibrium Identification	Equilibrium Identification
Static Stability	Static Stability	Static Stability
Dynamic Stability	Dynamic Stability	Dynamic Stability

In this section, the dynamic stability of the 1DoF-T system equilibria is determined, this concluding the study of the system.

As introduced in Section 1.2.2, any statically stable equilibrium can be dynamically stable if the critical initial kinetic energy $T_{t_0,crit}$ for that point is not exceeded. In this section, the conditions for dynamic stability about an equilibrium are analytically determined.

In order to determine the critical initial kinetic energy, the potential energy of the system needs to be calculated. From Equation (1.6), it can be seen that force is the derivative of potential energy, and therefore by integrating the force over x, a relative potential energy function can be obtained.

Repulsive Case

In the repulsive case, Equation (3.16) is integrated in the generalized coordinate x to obtain potential energy (the subscript T referring to 1DoF-T):

$$P_{rep,T} = -\int F_{2,rep,x}\, dx = -\int \left(\frac{3\mu_0\mu_1\mu_2}{2\pi x^4} - k(x - x_0)\right) dx$$

$$= \frac{\mu_0\mu_1\mu_2}{2\pi x^3} + \frac{kx^2}{2} - kx_0x + C, \tag{3.46}$$

where C is a constant of integration that is unknown. C and what it represents will be discussed more in Section 5.3.4, but because $T_{t_0,crit}$ is calculated by examining the *difference* between the potential energy of two equilibria, C is assumed to be zero to begin with; however, nonzero values will be explored a little later in this section for plotting reasons.

Figure 31b shows Equation (3.46) plotted versus distance, with the locations of the equilibria seen in Figure 29b numbered. The black lines are where the potential energy is positive, and the grey lines are the absolute value of the negative valued potential energy. As such, statically stable equilibria occur at apparent local maxima in the grey lines, which are actually local minima in the potential energy functional.

The local maxima in Figure 31b are clear and straightforward, one per spring constant, at the same locations as the equilibria in Figure 29b.

It is interesting to note that since there are no unstable equilibria in the system within the domain plotted, any size perturbation from equilibrium will result in motion around the equilibrium; there is no critical initial kinetic energy, and therefore the equilibria in the 1DoF-T repulsive system are all globally stable because potential energy goes to positive infinity at $x = 0$ and $x = \infty$. Even if the potential energy were plotted beyond 5 radii, the potential energy functional remains monotonically increasing as $x \to \infty$.

Attractive Case

In the attractive case, Equation (3.17) is integrated in the generalized coordinate x to obtain potential energy:

$$P_{att,T} = -\int F_{2,att,x}\, dx = -\int \left(-\frac{3\mu_0\mu_1\mu_2}{2\pi x^4} - k(x - x_0)\right) dx$$

$$= -\frac{\mu_0\mu_1\mu_2}{2\pi x^3} + \frac{kx^2}{2} - kx_0x + C. \qquad (3.47)$$

Again, C is assumed to be zero. As in Figure 31b, Figure 31a uses grey lines to represent the absolute value of the negative valued potential energy functional, except this time for the attractive case.

It can be seen that the two unstable equilibria in the attractive case, located at x_{1a} and x_{2a} as shown in Table 8, occur at minima in the grey lines and thus at local maxima in the potential energy function. This is consistent with the definition of static instability as given by Equation (1.9). The two stable equilibria in the attractive case, occurring at x_{3a} and x_{4a}, occur at maxima in the grey lines and thus at local minima in the potential energy function, consistent with the definition of static stability in Equation (1.8). It can be seen that the global minimum in the potential energy function occurs when $x = 0$, but this is because the magnetic force goes to infinity at this point, not because there is an equilibrium at this point.

It can be seen that all of the more elastic springs (k = 5 to 100) are monotonically increasing in potential energy as x increases. There are no values of x for which the derivative of potential energy is zero, and therefore no equilibria exist in those systems, as shown also in Figure 29a.

The critical initial kinetic energy at each of the stable equilibria in Figure 31a is determined by the difference between $P_{att,T}(x_{3a})$ and $P_{att,T}(x_{2a})$ (for the equilibrium at x_{3a}) and the difference between $P_{att,T}(x_{4a})$ and $P_{att,T}(x_{1a})$ (for the equilibrium at x_{4a}). This is because there are two permissible directions for displacement, $+x$ and $-x$, and two local maxima in each direction (the unstable equilibria in the $-x$ direction and the monotonically increasing potential energy function in the $+x$ direction). The

unstable equilibria for each of $k = 10000\ N/m$ and $k = 1000\ N/m$ have lower potential energies than $P_{att,T}(x = 4)$ for both functions, and therefore they determine the critical initial kinetic energy of the stable equilibria.

In order to visualize the actual potential energy curves, C in Equations (3.46) and (3.47) are now assumed to be $10^{5.5}$, roughly the magnitude of the minimum potential energy observed in Figure 31 (though the actual minimum in Figure 31a is $-\infty$). This value of C is selected such that all data are positive and thus can be plotted on logarithmic axes without taking the absolute value of the data as in Figure 31. Equations (3.46) and (3.47) are plotted again in Figure 32 with the new value of C. It's not as easy to see the discrete lines plotted in Figure 32 as in Figure 31, but it can be seen more clearly that stiffer springs result in deeper valleys in the potential energy functional with steeper walls, which indicates greater dynamic stability (to be investigated in Section 3.3.4). It can also be seen that the only difference between the attractive and repulsive potential energy functions is the behavior of the curves approaching $x = 0$. In the attractive case, $P_{att,T} \to -\infty$ as $x \to 0$, and in the repulsive case, $P_{att,T} \to +\infty$ as $x \to 0$.

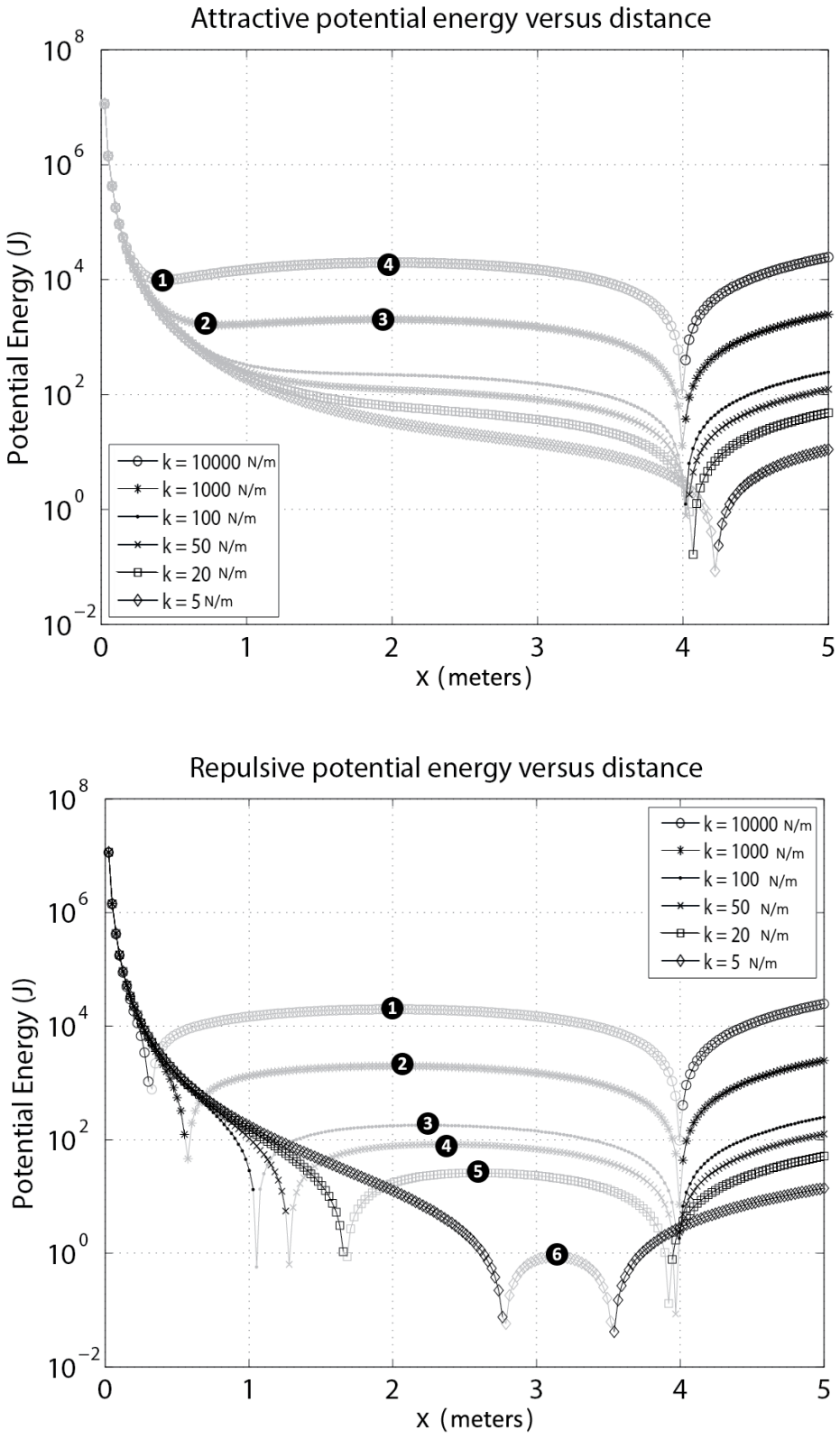

Figure 31: Potential energy versus distance in the (a, top) dimensioned attractive case, and the (b, bottom) dimensioned repulsive case, with grey lines being the absolute values of negative energies

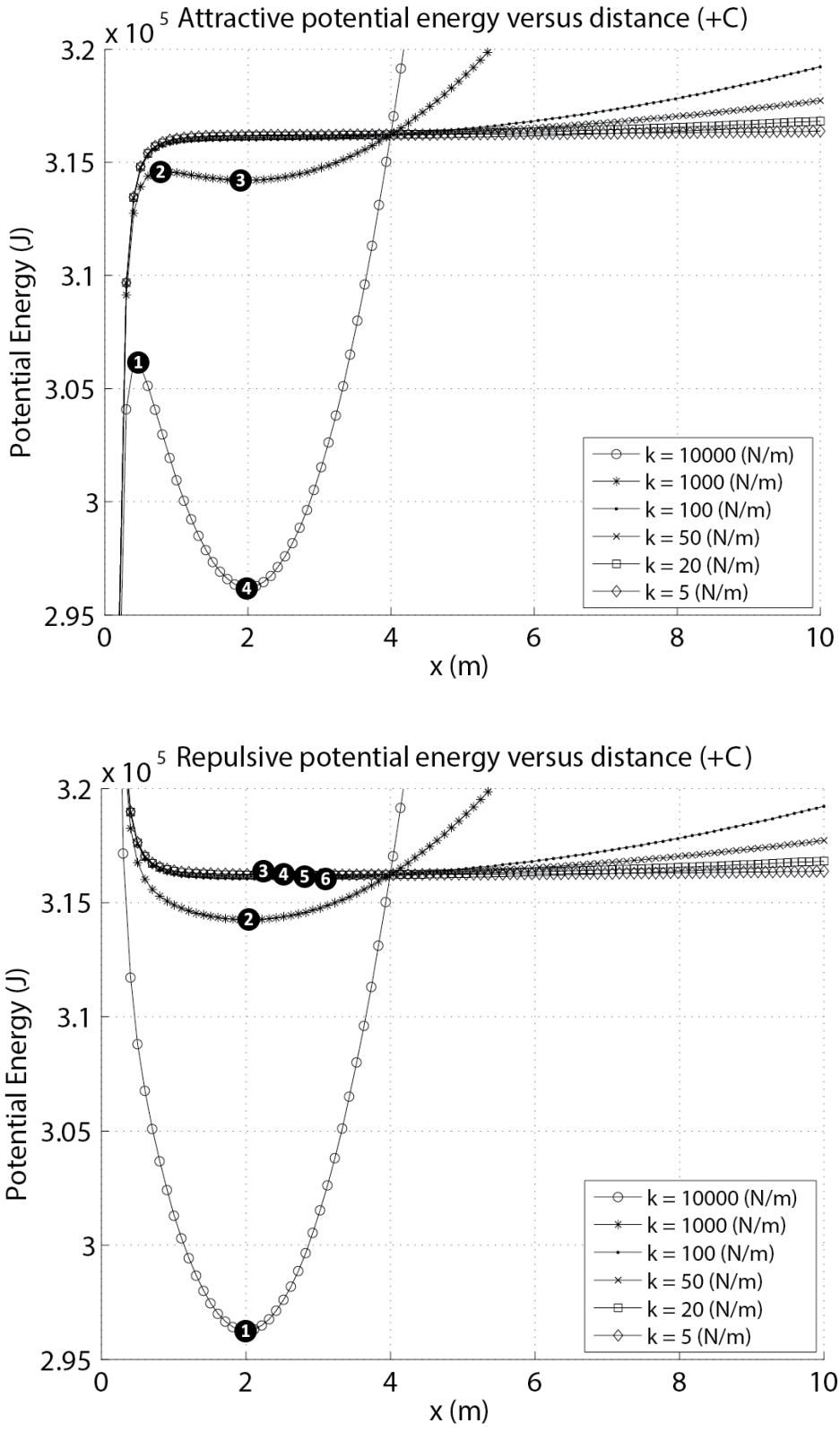

Figure 32: Potential energy versus distance in the (a, top) dimensioned attractive case, and the (b, bottom) dimensioned repulsive case, with $C = 10^{5.5}$ added to make values all positive

Non-Dimensionalization of Potential Energy

The nondimensional version of Equation (3.46), the repulsive potential energy, is calculated as follows:

$$\tilde{P}_{rep,T} = -\int \tilde{F}_{2,rep,ND,x}\, d\tilde{x} = -\int \left(\frac{\gamma}{\tilde{x}^4} - k^*(\tilde{x} - \tilde{x}_0)\right) d\tilde{x}$$

$$= \frac{\gamma}{3\tilde{x}^3} + \frac{k^*\tilde{x}^2}{2} - k^*\tilde{x}_0\tilde{x} + C. \qquad (3.48)$$

The nondimensional version of Equation (3.47), the attractive potential energy, is calculated as follows:

$$\tilde{P}_{att,T} = -\int \tilde{F}_{2,att,ND,x}\, d\tilde{x} = -\int \left(-\frac{\gamma}{\tilde{x}^4} - k^*(\tilde{x} - \widetilde{x_0})\right) d\tilde{x}$$

$$= \frac{-\gamma}{3\tilde{x}^3} + \frac{k^*\tilde{x}^2}{2} - k^*\tilde{x}_0\tilde{x} + C. \qquad (3.49)$$

Equations (3.48) and (3.49) are plotted in Figure 33a and Figure 33b respectively for the values of $k^* = 1$ and γ calculated from γ/k^* as given in Table 8. The three repulsive equilibria given in Table 8, $\tilde{x}_{1b}, \tilde{x}_{2b}, \text{and } \tilde{x}_{3b}$ are globally stable, since they are at the single minima of a potential energy wells that go to $+\infty$ on either side of the range of interest. The attractive equilibria, for the two lower values of γ, have one stable and one unstable equilibrium per line, as seen in the dimensional evaluation in the previous section. From Figure 33b it can clearly been be seen that, as expected, larger values of γ, associated with stronger magnetic moments, increase the distance $\tilde{x}$ at which the stable repulsive equilibrium is achieved.

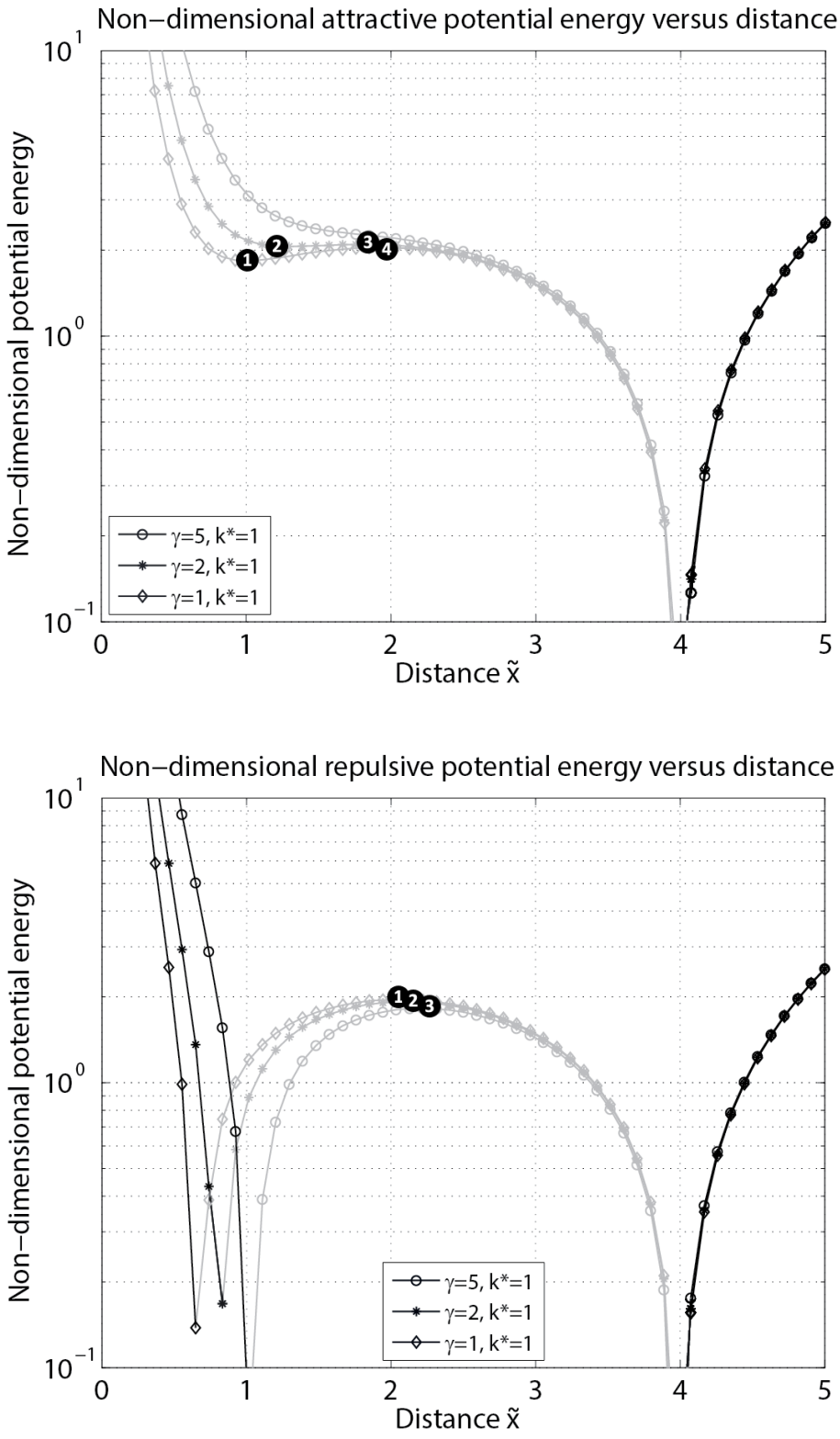

Figure 33: Non-dimensional potential energy versus distance in the (a, top) ND attractive case, and the (b, bottom) ND repulsive case, with grey lines being the absolute values of negative energies

Critical Dimensional Initial Kinetic Energy and Simulation

Only the attractive case has calculable critical initial kinetic energy for its stable equilibria, since for the attractive equilibria, there is actually the possibility of escaping, buckled motion over the unstable equilibrium on each line. The repulsive case's global stability means that there is no possibility of escaping motion.

Since the critical initial kinetic energy is determined by the difference between two potential energies, either Figure 31 or Figure 32 can be used. The former is selected to allow for finer evaluation of the energies at each point. From Figure 32a, it can be seen that the dimensional critical initial kinetic energies of the statically stable equilibria x_{3a} and x_{4a} are determined by the potential energy at each of the statically unstable equilibria x_{2a} and x_{1a}, respectively. For x_{3a},

$$T_{t_0,crit}(x_{3a}) = P_{att,T}(x_{2a}) - P_{att,T}(x_{3a}) = -10^{3.21317}J + 10^{3.30607}\,J,$$

and

$$T_{t_0,crit}(x_{3a}) = (x_{3a}) = 389.6540\,J. \tag{3.50}$$

For x_{4a},

$$T_{t_0,crit}(x_{4a}) = P_{att,T}(x_{1a}) - P_{att,T}(x_{4a}) = -10^{3.99847}\,J + 10^{4.30151}J,$$

and

$$T_{t_0,crit}(x_{4a}) = (x_{4a}) = 10057\,J. \tag{3.51}$$

It can be seen from Equations (3.50) and (3.51) that $T_{t_0,crit}(x_{4a}) > T_{t_0,crit}(x_{3a})$, meaning that the amount of energy that would need to be introduced to the system to make the k=10000 N/m equilibrium dynamically unstable is greater than that required to make the k = 1000 N/m equilibrium unstable. Therefore, the equilibrium at x_{4a} is more tolerant of perturbation than the equilibrium at x_{3a} and is therefore "more" dynamically stable. The takeaway is that larger spring constants result in larger critical initial kinetic energies.

Critical Non-Dimensional Initial Kinetic Energy and Simulation

Similar to the previous dimensional case, the critical initial kinetic energies of the statically stable non-dimensional equilibria at $\tilde{x}_{3a}$ and $\tilde{x}_{4a}$ are determined by the difference in non-dimensional potential energies with respect to $\tilde{x}_{2a}$ and $\tilde{x}_{1a}$, respectively. For $\tilde{x}_{3a}$:

$$\tilde{T}_{t_0,crit}(\tilde{x}_{3a}) = \tilde{P}_{att,T}(\tilde{x}_{2a}) - \tilde{P}_{att,T}(\tilde{x}_{3a}) = -10^{0.313541} + 10^{0.320977},$$

and

$$\tilde{T}_{t_0,crit}(\tilde{x}_{3a}) = 0.0355. \tag{3.52}$$

For x_{4a},

$$\tilde{T}_{t_0,crit}(\tilde{x}_{4a}) = \tilde{P}_{att,T}(\tilde{x}_{1a}) - \tilde{P}_{att,T}(\tilde{x}_{4a}) = -10^{0.263359} + 10^{0.310438},$$

and

$$\tilde{T}_{t_0,crit}(\tilde{x}_{4a}) = 0.2100. \tag{3.53}$$

As in Section 3.3.4, the curve with the smallest $\frac{\gamma}{k^*}$ value is more tolerant to perturbation.

3.3.5. Summary

In Section 3.3, a single translational degree of freedom spring-magnet system was presented and its equilibria identified and analyzed for their static and dynamic stability. It can be seen that the repulsive equilibria are all statically and dynamically stable, whereas attractive equilibria are a mix of statically stable and unstable and that dynamic stability is based upon the difference in potential energy between the stable and the unstable equilibria in systems with a spring constant large enough to have equilibria. The larger the spring constant, the higher the critical initial kinetic energy required to make the statically stable equilibrium dynamically unstable.

3.4. Rotational Single Degree of Freedom

1 DoF – Translational	1 DoF – Rotational	2 DoF – Rotational & Translational
Equilibrium Identification	Equilibrium Identification	Equilibrium Identification
Static Stability	Static Stability	Static Stability
Dynamic Stability	Dynamic Stability	Dynamic Stability

The second analytical magnet system studied in this chapter is that which permits motion of magnet 2 rotationally around the z axis, as shown in Figure 34. The linear spring has been replaced by a nonelastic massless rod since translation is not allowed in this system, and thus the linear spring experiences no deformation. Though force is not required to balance in this system, the two cases studied are still called the attractive and repulsive cases.

Figure 34 depicts the repulsive case, in which $\beta = 0$ corresponds to anti-aligned magnets and would result in repulsion if force were being considered. The attractive case refers to when the orientation of magnet 2 is flipped, and thus $\beta = 0$ corresponds to aligned magnets. β is positive in the $+z$ direction and will be studied over the range of $-\frac{\pi}{2} \leq \beta \leq \frac{\pi}{2}$. Referring to Figure 34, this range starts with the north pole of magnet 2 being pointed in the $-y$ direction, continues through being pointed in the $+x$ direction and ends with the north pole pointed in the $+y$ direction.

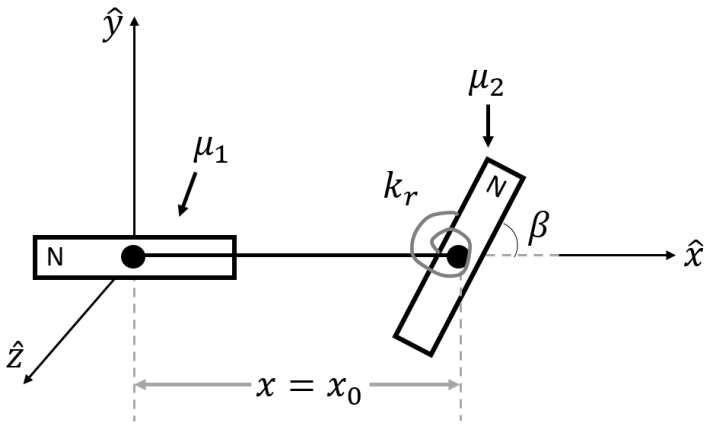

Figure 34: Rotational single degree of freedom (1DoF-T) dipole system

In the system above, x is constant and equivalent to the natural length of the spring, while the torsional spring stretches and compresses to provide an elastic torque on magnet 2.

3.4.1. Torque Balance

As mentioned in Section 3.3.1, a torque balance is the goal of this system, and whereas a torque balance was implicit in the 1DoF-T system, there is not a force balance in this (1DoF-R) system because the magnetic force is never equivalent to zero. Force will hereafter be ignored in this section because neither magnet is free to move translationally in response to a force.

Equations (3.9) - (3.11) simplify when $\alpha = 0$ and $x = x_0$ as in Figure 34 to

$$\vec{F}_{mag,2} = \frac{3\mu_0\mu_1\mu_2}{4\pi x^4}\begin{bmatrix} 2\cos\beta \\ -\sin\beta \\ 0 \end{bmatrix}, \tag{3.54}$$

$$\vec{\tau}_{mag,1} = \frac{\mu_0\mu_1\mu_2}{4\pi x_0^3}\begin{bmatrix} 0 \\ 0 \\ \sin\beta \end{bmatrix}, \tag{3.55}$$

and

$$\vec{\tau}_{mag,2} = \frac{\mu_0\mu_1\mu_2}{4\pi x_0^3}\begin{bmatrix} 0 \\ 0 \\ 2\sin\beta \end{bmatrix}. \tag{3.56}$$

Equation (3.55) is not used in this system since magnet 1 is not free to rotate or move in any way, so this section focuses on Equation (3.56). From Equation (3.8), the elastic torque about the z axis is given by

$$\vec{\tau}_{spr,2} = -k_r\beta\hat{k}, \tag{3.57}$$

and therefore the total torque on magnet 2 with $\beta = 0$ corresponding to anti-aligned magnets (repulsive case) is

$$\vec{\tau}_{2,rep} = \left(\frac{\mu_0\mu_1\mu_2}{2\pi x_0^3}\sin\beta - k_r\beta\right)\hat{k}. \tag{3.58}$$

The torque on magnet 2 in the attractive case is

$$\vec{\tau}_{2,att} = \left(-\frac{\mu_0\mu_1\mu_2}{2\pi x_0^3}\sin\beta - k_r\beta\right)\hat{k}. \tag{3.59}$$

Non-Dimensionalization of Torque Balance Equations

As in Section 3.3, a non-dimensionalization of the torque balance is of interest to reduce the dimensionality of the variable space. Substituting the same dimensionless auxiliary variables as defined in Table 4 into Equations (3.58) and (3.59) and replacing $\vec{\tau}_{2,rep}$ and $\vec{\tau}_{2,att}$ with mass moment of inertia multiplied by rotational acceleration of magnet 2 yields the following general equations of motion, using Equation (3.5) for the magnetic moment definition.

Repulsive:

$$I_z \frac{d^2(\beta)}{d(\mathcal{T}\tilde{t})^2} = \left(\frac{\pi \mu_0 I^2 N^2 \tilde{R}_2^2 \tilde{R}_1^2 R_1}{2 \tilde{x}_0{}^3} \sin\beta - k_r \beta \right) \hat{k}, \tag{3.60}$$

and attractive:

$$I_z \frac{d^2(\beta)}{d(\mathcal{T}\tilde{t})^2} = \left(-\frac{\pi \mu_0 I^2 N^2 \tilde{R}_2^2 \tilde{R}_1^2 R_1}{2 \tilde{x}_0{}^3} \sin\beta - k_r \beta \right) \hat{k}. \tag{3.61}$$

β is already dimensionless, so it does not require its own dimensionless variable, but it should be noted that the β values of the equilibria in the dimensional and non-dimensional cases will necessarily be different. The mass moment of inertia is

$$I_z = \frac{m_2 R_2^2}{2} = \frac{m_2 \tilde{m}_2 \tilde{R}_2^2 R_1^2}{2}.$$

So Equations (3.60) and (3.61) become, with the definition of m_2 substituted in as well,

Repulsive:

$$\frac{\tilde{m}_2 \tilde{R}_2^2}{2} \frac{d^2(\beta)}{d(\tilde{t})^2} \frac{d^2(\beta)}{d(\tilde{t})^2} = \left(\frac{\mu_0 I^2 N \tilde{R}_2 \tilde{R}_1^2 \mathcal{T}^2}{4 R_1^2 \rho \tilde{x}_0{}^3} \sin\beta - \frac{k_r \mathcal{T}^2}{2\pi \tilde{R}_2 R_1^3 N \rho} \beta \right) \hat{k}, \tag{3.62}$$

and attractive:

$$\frac{\tilde{m}_2 \tilde{R}_2^2}{2} \frac{d^2(\beta)}{d(\tilde{t})^2} = \left(-\frac{\mu_0 I^2 N \tilde{R}_2 \tilde{R}_1^2 \mathcal{T}^2}{4 R_1^2 \rho \tilde{x}_0{}^3} \sin\beta - \frac{k_r \mathcal{T}^2}{2\pi \tilde{R}_2 R_1^3 N \rho} \beta \right) \hat{k}. \tag{3.63}$$

From Equations (3.62) and (3.63), a non-dimensional magnetic torque coefficient ξ and spring torque coefficient k_r^* can be defined, both of which are always positive:

$$\xi = \frac{\mu_0 I^2 N \tilde{R}_2 \tilde{R}_1^2 \mathcal{T}^2}{4 R_1^2 \rho}, \tag{3.64}$$

and

$$k_r^* = \frac{k_r \mathcal{T}^2}{2\pi \tilde{R}_2 R_1^3 N \rho} = \frac{k_r}{k R_1^2}. \tag{3.65}$$

It can be noted from Equations (3.64) and (3.22) that

$$\xi = \frac{\gamma}{3} \tag{3.66}$$

such that the equations simplify to

$$\tilde{\vec{\tau}}_{2,rep,ND} = \frac{\widetilde{m}_2 \tilde{R}_2^2}{2} \frac{d^2(\beta)}{d(\tilde{t})^2} \frac{d^2(\beta)}{d(\tilde{t})^2} = \left(\frac{\gamma}{3 {\tilde{x}_0}^3} \sin\beta - k_r^* \beta \right) \hat{k}, \tag{3.67}$$

and

$$\tilde{\vec{\tau}}_{2,att,ND} \frac{\widetilde{m}_2 \tilde{R}_2^2}{2} \frac{d^2(\beta)}{d(\tilde{t})^2} = \left(-\frac{\gamma}{3 {\tilde{x}_0}^3} \sin\beta - k_r^* \beta \right) \hat{k}. \tag{3.68}$$

Note that ${\tilde{x}_0}^3$ was not included in ξ because Section 3.3 uses $\tilde{x}$ instead of $\tilde{x}_0$, and this avoids needing to define another variable. As in the dimensional case, the term associated with the magnetic torque switches signs between the repulsive and attractive cases. These equations and non-dimensional coefficients will be used in the rest of this section. The left hand side of these equations, $\tilde{\vec{\tau}}_{2,rep,ND}$ and $\tilde{\vec{\tau}}_{2,att,ND}$, represents a non-dimensional total torque, which will be what is plotted in future visualizations of these equations.

3.4.2. Equilibrium Identification

1 DoF – Translational	1 DoF – Rotational	2 DoF – Rotational & Translational
Equilibrium Identification	Equilibrium Identification	Equilibrium Identification
Static Stability	Static Stability	Static Stability
Dynamic Stability	Dynamic Stability	Dynamic Stability

In this section, 1DoF-R equilibria are identified in each of the repulsive and attractive cases.

In this section, a torque balance on magnet 2 about the z axis indicates an equilibrium point. The torque balance in the repulsive case occurs when Equation (3.58) equals zero, or

$$\frac{\mu_0\mu_1\mu_2}{2\pi x_0^3}\sin\beta = k_r\beta. \tag{3.69}$$

And in the attractive case, torque balance occurs when Equation (3.69) equals zero, or

$$-\frac{\mu_0\mu_1\mu_2}{2\pi x_0^3}\sin\beta = k_r\beta. \tag{3.70}$$

In order for the signs to be such that Equation (3.70) can be satisfied, either β must equal zero, or $\sin\beta$ needs to be the opposite sign of β, which does not occur within the range of $-\frac{\pi}{2} \leq \beta \leq \frac{\pi}{2}$. Thus, it can be predicted that the only equilibria possible in the attractive case would occur at $\beta = 0$, which corresponds to both a magnetic torque and a spring torque of zero.

However, it is possible for Equation (3.69) to be satisfied somewhere other than at $\beta = 0$, but it would require that

$$\frac{\mu_0\mu_1\mu_2}{2\pi k_r x_0^3} = \frac{\beta}{\sin\beta} = \varphi. \tag{3.71}$$

The constant term on the left hand side of Equation (3.69) is called φ for ease of reference.

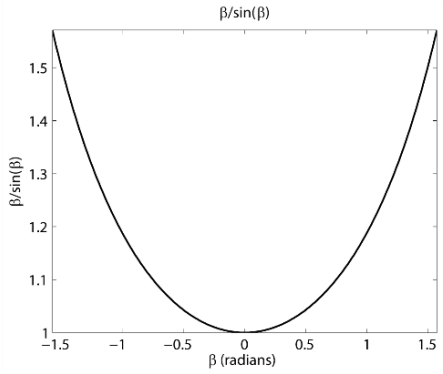

Figure 35: $\beta / \sin\beta$ versus β, showing that equilibria only exist when $1 \leq \frac{\mu_0\mu_1\mu_2}{2\pi k_s x_0^3} \leq \frac{\pi}{2}$

At some point over the range $-\frac{\pi}{2} \leq \beta \leq \frac{\pi}{2}$, Figure 35 shows that the acceptable range of values that φ can take to achieve an equilibrium is

$$1 \leq \varphi \leq \frac{\pi}{2}. \tag{3.72}$$

The next section selects some example variable values, at least one combination of which should produce non-zero equilibria in the repulsive case.

Non-Dimensionalization of Equilibrium

The non-dimensional repulsive torque balance occurs when Equation (3.67) equals zero, or

$$\frac{\gamma}{3\tilde{x}_0{}^3 k_r^*} = \frac{\beta}{\sin\beta} = \varphi,$$

and

$$\frac{\gamma}{k_r^*} = \frac{3\tilde{x}_0{}^3\beta}{\sin\beta}, \tag{3.73}$$

where

$$\frac{\gamma}{3\tilde{x}_0{}^3 k_r^*} = \frac{\pi\mu_0 I^2 N^2 \tilde{R}_2^2 \tilde{R}_1^2 R_1}{\tilde{x}_0{}^3 k_r}.$$

In the attractive case, the left sides of Equations (3.71) and (3.73) become negative.

Example Dimensional Equilibrium Identification

The same magnetic moment values ($\mu_1 = 25133\ Am^2$ and $\mu_2 = 36191\ Am^2$) studied in Section 3.3.2 are used in the example equilibrium identification for the 1DoF-R system. Again, these magnetic moments were calculated assuming that coil 1 has a radius of 1 m and coil 2 has a radius of 2 meters, with all other variables identical. Three torsional spring constants are examined ($k_r = 1, 5, 25\ N \cdot m/rad$), and the magnetic torque is calculated at two different x_0 values ($x_0 = 1.75, 3$). Figure 36a plots both sides of Equation (3.69) in the repulsive case; Figure 36b plots both sides of Equation (3.70) in the attractive case.

There are two line-types plotted in Figure 36: lines without symbols represent two different magnetic torques, based on each of the two different values of x_0, whereas the lines with symbols represent the spring torques. As in previous plots, the grey lines are the absolute values of negative values for each torque. Equilibria would occur anywhere a grey line and a black line of different line-types intersect.

It can be seen from both Figure 36a that, as expected, the only attractive equilibria occur at $\beta_{1,a} = 0$ and that there are 6 equilibria at that point (every combination of plotted magnetic and spring torque). Figure 36b is more interesting, as there are the six equilibria at $\beta_{3,b} = 0$ as well as several mirrored equilibria on either side of zero. These equilibria (at $\beta_{1,b}, \beta_{4,b}$ for $x_0 = 1.75$ and $k_r = 25 N \cdot m/rad$; $\beta_{2,b}, \beta_{5,b}$ for $x_0 = 3$ and $k_r = 5\ N \cdot m/rad$) exist because φ is within the prescribed bounds for nonzero equilibria.

Table 9 gives the locations of the equilibria from Figure 36 as well as the value of φ for each point. It can be seen that φ is within the prescribed bounds for all nonzero equilibria.

Table 9: β values for dimensional equilibria identified in Figure 36

Attractive			Repulsive			
Equilibrium ID	k_r, x_0 values ($\frac{Nm}{rad}$ & m)	β value at eq. (radians)	Equilibrium ID	k_r, x_0 values ($\frac{Nm}{rad}$ & m)	β value at eq. (radians)	φ
β_{1a-1}	1, 1.75	0	β_{1b}	25, 1.75	-1.3128	1.3577
β_{1a-2}	1, 3	0	β_{2b}	5, 3	-1.2975	1.3475
β_{1a-3}	5, 1.75	0	β_{3b-1}	1, 1.75	0	33.9436
β_{1a-4}	5, 3	0	β_{3b-2}	1, 3	0	6.7376
β_{1a-5}	25, 1.75	0	β_{3b-3}	5, 1.75	0	6.7887
β_{1a-6}	25, 3	0	β_{3b-4}	5, 3	0	1.3475
			β_{3b-5}	25, 1.75	0	1.3577
			β_{3b6}	25, 3	0	0.2695
			β_{4b}	25, 1.75	1.2975	1.3475
			β_{5b}	5, 3	1.3128	1.3577

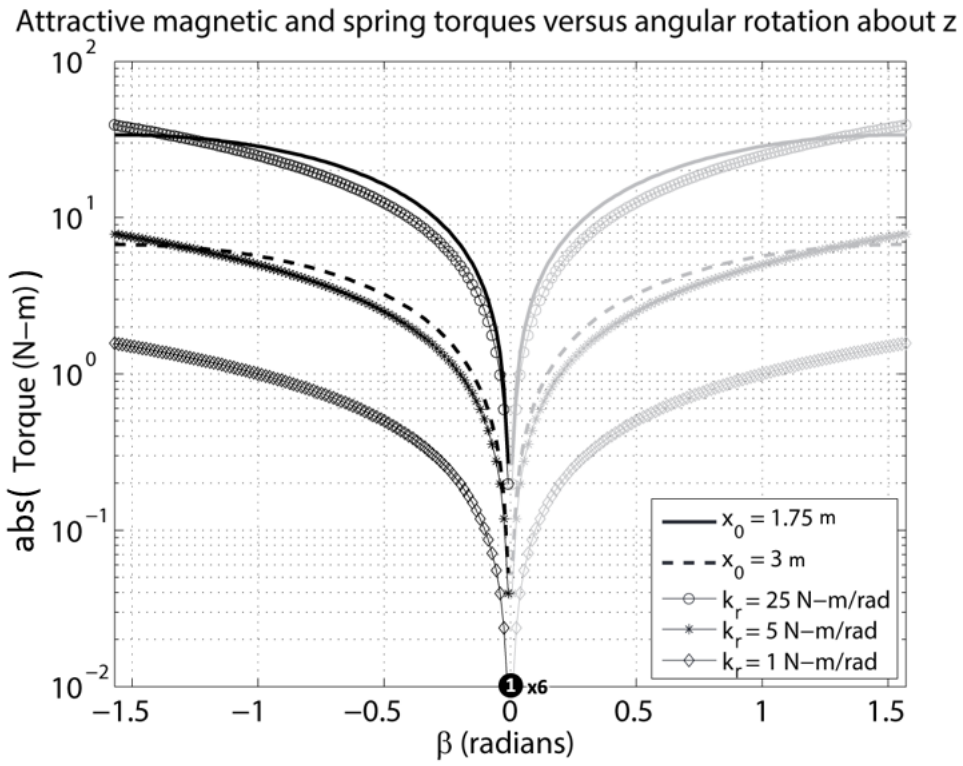

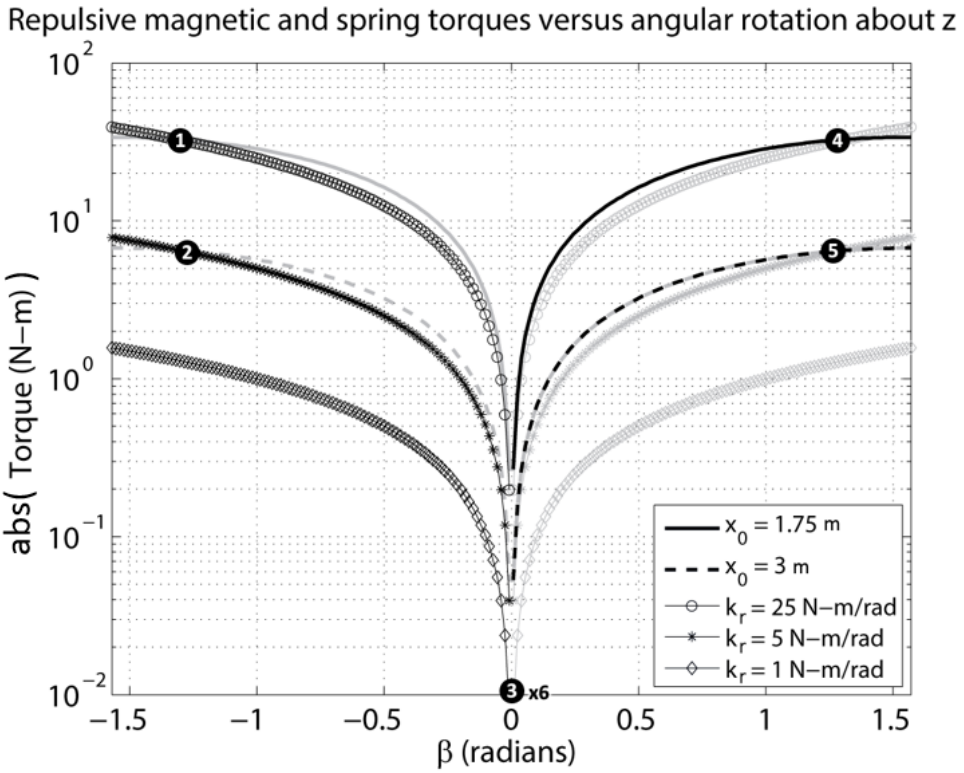

Figure 36: Spring torques and (a, top) attractive magnetic dipole torque or (b, bottom) repulsive magnetic dipole torque, with 1DoF-R equilibrium points identified

Example Non-Dimensional Equilibrium Identification

Figure 37 plots both sides of Equation (3.73) in both the attractive and repulsive cases for $\tilde{x}_0 = 2$ in order to determine for what values of β they intercept and thus are in equilibrium. Equation (3.73) is somewhat reorganized to reduce the number of variables being plotted, and therefore the conditions for equilibria are slightly different from the previous section: equilibria occur anywhere where two lines of the same sign/color intersect, versus in Figure 36 where equilibria occur at the intersection of dissimilar lines. It should be noted that Equation (3.67) (pre-reorganization) also balances when $\beta = 0$, as in the dimensional section, and thus every γ/k_r^* curve (three total in Figure 37) has an equilibrium at $\beta = 0$ in addition to those identified in Figure 37. The $\beta = 0$ equilibria are not visible in Figure 37, so they are represented in Table 10 by $\beta_{0a,ND-\#}$ or the attractive case, $\beta_{0b,ND-\#}$ for the repulsive case, where # is a number 1 through 3.

It can be seen from Figure 37 that an increase or decrease in $\tilde{x}_0$ will just shift the ${\tilde{x}_0}^3(\beta/\sin\beta)$ curve up or down respectively so that only one such curve is plotted. It can also be seen that larger values of γ/k_r^* result in non-zero equilibria closer to $\beta = \pm\pi/2$, since the magnetic force is large compared to the stiffness of the torsional spring, so the magnet can twist more before the spring provides a sufficient restorative torque to balance.

Table 10: β values for non-dimensional equilibria identified in Figure 37

Attractive			Repulsive		
Equilibrium ID	$\frac{\gamma}{k_r^*}$	β value at eq. (radians)	Equilibrium ID	$\frac{\gamma}{k_r^*}$	β value at eq. (radians)
$\beta_{0a,ND-1}$	35	0	$\beta_{1b,ND}$	35	-1.4472
$\beta_{0a,ND-2}$	30	0	$\beta_{2b,ND}$	30	-1.1311
$\beta_{0a,ND-3}$	25	0	$\beta_{3b,ND}$	25	-0.4929
			$\beta_{0b,ND-1}$	35	0
			$\beta_{0b,ND-2}$	30	0
			$\beta_{0b,ND-3}$	25	0
			$\beta_{4b,ND}$	35	1.4472
			$\beta_{5b,ND}$	30	1.1311
			$\beta_{6b,ND}$	25	0.4929

The stability of these identified rotational dimensional and non-dimensional equilibria, both static and dynamic, will be explored in the rest of this section.

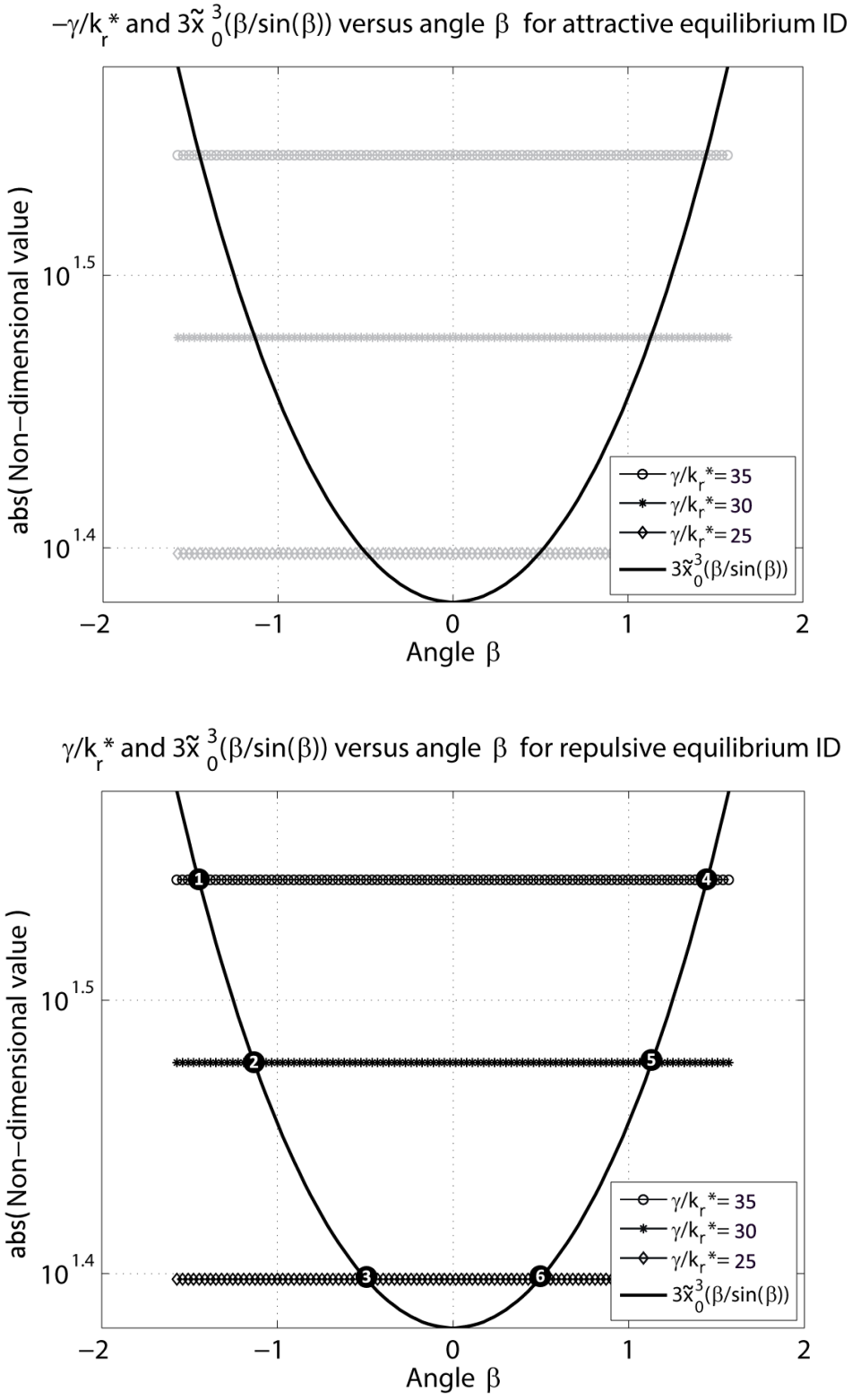

Figure 37: Non-dimensional (ND) right side of Equation (3.73) and several ND (a, top) absolute values of the attractive -γ/k_r^* or (b, bottom) absolute values of the repulsive γ/k_r^*, with ND 1DoF-R equilibrium points identified and $\tilde{x}_0$=2

3.4.3. Static Stability Classification

1 DoF – Translational	1 DoF – Rotational	2 DoF – Rotational & Translational
Equilibrium Identification	Equilibrium Identification	Equilibrium Identification
Static Stability	Static Stability	Static Stability
Dynamic Stability	Dynamic Stability	Dynamic Stability

In this section, the static stability of the 1DoF-R equilibria identified in the previous section is evaluated.

Examining the static stability of the 1DoF-R system is very similar to examining that of the 1DoF-T system, save for the use of torques instead of forces. This section uses the stiffness approach from Section 3.3.3, similar to in Equations (3.34) and (3.35). The derivative of torque about magnet 2 (Equation (3.58)) is taken with respect to the single generalized coordinate in which it is permissible to have motion:

$$\frac{d}{d\beta}\left(\tau_{2,rep}\right) = \frac{d}{d\beta}\left(\frac{\mu_0\mu_1\mu_2}{2\pi x_0^3}\sin\beta - k_r\beta\right),$$

and

$$\frac{d}{d\beta}\left(\tau_{2,rep}\right) = \frac{\mu_0\mu_1\mu_2}{2\pi x_0^3}\cos\beta - k_r. \tag{3.74}$$

Similarly, the derivative of Equation (3.59) is

$$\frac{d}{d\beta}\left(\tau_{2,att}\right) = -\frac{\mu_0\mu_1\mu_2}{2\pi x_0^3}\cos\beta - k_r. \tag{3.75}$$

Non-Dimensionalization of Stiffness

The nondimensional version of each of Equations (3.74) and (3.75) are as follows from Equations (3.67) and (3.68):

Repulsive:

$$\frac{d}{d\beta}\left(\tilde{\tau}_{2,rep,ND}\right) = \frac{d}{d\beta}\left(\frac{\gamma}{3\tilde{x}_0{}^3}\sin\beta - k_r^*\,\beta\right),$$

and

$$\frac{d}{d\beta}\left(\tilde{\tau}_{2,rep,ND}\right) = \frac{\gamma}{3\tilde{x}_0{}^3}\cos\beta - k_r^*\,, \tag{3.76}$$

Attractive:

$$\frac{d}{d\beta}\left(\tilde{\tau}_{2,att,ND}\right) = \frac{d}{d\beta}\left(-\frac{\gamma}{3\tilde{x}_0{}^3}sin\,\beta - k_r^*\,\beta\right),$$

and

$$\frac{d}{d\beta}\left(\tilde{\tau}_{2,att,ND}\right) = -\frac{\gamma}{3\tilde{x}_0{}^3}cos\,\beta - k_r^*\,. \tag{3.77}$$

Static stability results when the derivative of torque is negative (making the stiffness positive) [25], and therefore it is necessary for static stability that Equations (3.74)-(3.75) and (3.76)-(3.77) are less than zero for repulsive and attractive case equilibria respectively. Equation (3.78) gives the formula for rotational stiffness using either $\tau_{2,rep}$ or $\tau_{2,att}$ (or their non-dimensional equivalents) as τ_2:

$$\kappa_{tot,R} = -\left(\frac{d\tau_2}{d\beta}\right)_{\beta=\beta_{eq}}. \tag{3.78}$$

Example Dimensional Static Stability Evaluation

$\mathrm{Cos}\,\beta$ is positive over the range $-\frac{\pi}{2} \leq \beta \leq \frac{\pi}{2}$, and therefore, because all the constants in the torque formulations are positive, the attractive derivative of torque is always negative as in Equation (3.75). Hence, all six of the equilibria at β_{1a} are statically stable. This is consistent with the tendency of a magnetic pole to be attracted to the opposite pole and to return to the position where the two opposing poles are closest.

Table 11 is Table 9 with added stiffness values at the associated β values for each equilibrium. Equilibria that are statically stable are bolded within the table.

Table 11: Rotational stiffness values $\kappa_{tot,R}$ at each dimensional equilibrium in Figure 36, with statically stable equilibria bolded

Attractive				Repulsive			
Equil. ID	k_r, x_0 values ($\frac{Nm}{rad}$ & m)	β value at equil. (radians)	$\kappa_{tot,R}$ ($\frac{Nm}{rad}$)	Equil. ID	k_r, x_0 values ($\frac{Nm}{rad}$ & m)	β value at equil. (radians)	$\kappa_{tot,R}$ ($\frac{Nm}{rad}$)
$\boldsymbol{\beta_{1a-1}}$	**1, 1.75**	**0**	**34.9436**	$\boldsymbol{\beta_{1b}}$	**25, 1.75**	**-1.3128**	**16.3395**
$\boldsymbol{\beta_{1a-2}}$	**1, 3**	**0**	**7.7376**	$\boldsymbol{\beta_{2b}}$	**5, 3**	**-1.2975**	**3.1815**
$\boldsymbol{\beta_{1a-3}}$	**5, 1.75**	**0**	**38.9436**	β_{3b-1}	1, 1.75	0	-32.9436
$\boldsymbol{\beta_{1a-4}}$	**5, 3**	**0**	**11.7376**	β_{3b-2}	1, 3	0	-5.7376
$\boldsymbol{\beta_{1a-5}}$	**25, 1.75**	**0**	**58.9436**	β_{3b-3}	5, 1.75	0	-28.9436
$\boldsymbol{\beta_{1a-6}}$	**25, 3**	**0**	**31.7376**	β_{3b-4}	5, 3	0	-1.7376
				β_{3b-5}	25, 1.75	0	-8.9436
				$\boldsymbol{\beta_{3b-6}}$	**25, 3**	**0**	**18.2624**
				$\boldsymbol{\beta_{4b}}$	**25, 1.75**	**1.2975**	**16.3395**
				$\boldsymbol{\beta_{5b}}$	**5, 3**	**1.3128**	**3.1815**

It can be seen from Table 11 that all of the attractive equilibria are statically stable, as expected, and that all of the nonzero equilibria in the repulsive case are also statically stable. Interestingly enough, only one of the repulsive case $\beta = 0$ equilibria was stable, and that was β_{3b-6}, which had both the largest k_r and the largest x_0. It can be seen from Equation (3.74) that making both k_r and x_0 larger helps drive the equation towards a negative derivative and thus positive stiffness; this observation is most valuable conclusion that can be drawn from Table 11, especially since any operational system is going to be in repulsion and likely operating with large distances between the magnets in the system.

Example Non-Dimensional Static Stability Evaluation

As in the dimensional formulation, it can be seen from Table 12 that all of the attractive equilibria, all of which occur when $\beta = 0$, are stable. Again, k_r^* is assumed to be 1. In the repulsive case, the values of γ/k_r^* and $\tilde{x}_0$ result in purely unstable repulsive equilibria at $\beta_{0b,ND}$ and stable equilibria at non-zero equilibria. To further investigate this, Equation (3.76) is rearranged to determine when the derivative of torque is negative (making the stiffness positive):

$$\frac{\gamma}{k_r^*}\cos\beta < 3{\tilde{x}_0}^3.$$

Since $\cos\beta = 1$ at $\beta = 0$, stiffness is positive when

$$\frac{\gamma}{k_r^*} < 3{\tilde{x}_0}^3. \tag{3.79}$$

Since $\tilde{x}_0$=2 in this case, $\frac{\gamma}{k_r^*}$ just needs to be less than 24 to result in static stability. Because $\frac{\gamma}{k_r^*} = [35, 30, 25]$ in the example case, Equation (3.79) explains the unanimous static instability when $\beta = 0$. This inequality implies that as the distance between the coils increases, the magnetic to spring torque ratio can grow and still maintain static stability. Increasing k_r^* has a similar effect, allowing greater magnetic torque while maintaining static stability.

Table 12: Non-dimensional rotational stiffness values $\kappa_{tot,ND,R}$ at each ND equilibrium in Figure 38, with statically stable equilibria bolded

Attractive						Repulsive					
Equil. ID	$\frac{\gamma}{k_r^*}$	k_r^*	γ	β value at eq. (radians)	$\kappa_{tot,ND}$	Equil. ID	$\frac{\gamma}{k_r^*}$	k_r^*	γ	β value at eq. (radians)	$\kappa_{tot,ND,R}$
$\boldsymbol{\beta_{0a,ND-1}}$	**35**	**1**	**35**	**0**	**2.4583**	$\boldsymbol{\beta_{1b,ND}}$	**35**	**1**	**35**	**-1.4472**	**0.8202**
$\boldsymbol{\beta_{0a,ND-2}}$	**30**	**1**	**30**	**0**	**2.2500**	$\boldsymbol{\beta_{2b,ND}}$	**30**	**1**	**30**	**-1.1311**	**0.4679**
$\boldsymbol{\beta_{0a,ND-3}}$	**25**	**1**	**25**	**0**	**2.0417**	$\boldsymbol{\beta_{3b,ND}}$	**25**	**1**	**25**	**-0.4929**	**0.0823**
						$\beta_{0b,ND-1}$	35	1	35	0	-0.4583
						$\beta_{0b,ND-2}$	30	1	30	0	-0.2500
						$\beta_{0b,ND-3}$	25	1	25	0	-0.0417
						$\boldsymbol{\beta_{4b,ND}}$	**35**	**1**	**35**	**1.4472**	**0.8202**
						$\boldsymbol{\beta_{5b,ND}}$	**30**	**1**	**30**	**1.1311**	**0.4679**
						$\boldsymbol{\beta_{6b,ND}}$	**25**	**1**	**25**	**0.4929**	**0.0823**

3.4.4. Dynamic Stability

1 DoF – Translational	1 DoF – Rotational	2 DoF – Rotational & Translational
Equilibrium Identification	Equilibrium Identification	Equilibrium Identification
Static Stability	Static Stability	Static Stability
Dynamic Stability	Dynamic Stability	Dynamic Stability

In this section, the dynamic stability of the 1DoF-R system equilibria is determined, thus concluding the study of this system.

Determining the dynamic stability of the stable equilibria identified in Table 11 requires calculation of the potential energy functional for a rotational system, which is again comprised of two terms – a magnetic potential energy and an elastic potential energy. The moment from a torsional spring is given in Equation (3.57). "Work W_r done by the moment due to twisting through a very small angle $d\beta$ [47]" about the $+z$ axis is given by (in combination with Equation (3.57))

$$dW_r = -k_r\beta \cdot d\beta\hat{k}. \tag{3.80}$$

The elastic potential energy V_R of a torsional spring is "the negative of the total work done by the moment [47]" or

$$V_R = -\int -k_r\beta \cdot d\beta\hat{k} = \int k_r\beta \cdot d\beta\hat{k} = \frac{1}{2}k_r\beta^2 + C\,. \tag{3.81}$$

Repulsive Case

Using the same work-based approach as in Equation (3.81), the magnetic potential energy W_{rep} in the repulsive case can also be found with the negative integral of the work done by the magnetic dipole from 0 to β, using the repulsive magnetic moment given by Equation (3.56):

$$W_{rep} = -\int \tau_{2,rep} \cdot d\beta\hat{k} = -\int \frac{\mu_0\mu_1\mu_2}{2\pi x_0^3}\sin\beta \cdot d\beta = \frac{\mu_0\mu_1\mu_2}{2\pi x_0^3}\cos\beta + C. \tag{3.82}$$

As discussed previously, C in each of Equations (3.81) and (3.82) are unknown constants of integration that do not effect relative potential energy, so they are set to zero here. Equations (3.81) and (3.82)

combined are equivalent to the negative integral of Equation (3.58), the subscript R being used on potential energy because it is the 1DoF-R case:

$$P_{rep,R} = -\int \vec{\tau}_{2,rep,z}\, d\beta = -\int \left(\frac{\mu_0\mu_1\mu_2}{2\pi x_0^3}\sin\beta - k_r\beta\right)\hat{k}\, d\beta$$

$$= \frac{\mu_0\mu_1\mu_2}{2\pi x_0^3}\cos\beta + \frac{k_r\beta^2}{2} + C. \tag{3.83}$$

Figure 38b depicts the ten repulsive equilibria found in Section 3.4.2 with numbered circles on each plot, and it can be seen that the equilibria at β_{1b}, β_{2b}, β_{4b}, and β_{5b} all occur at local minima in their respective functions. Additionally, one of the equilibria at $\beta = 0$, the one associated with a k_r of 25 $N \cdot m/rad$ and an x_0 of 3, is in fact statically stable. All of these observations are consistent with the results in Table 11. It can be seen that at β_{3b}, wherein six equilibria occurred at $\beta = 0$, the equilibria are grouped by the value of x_0, with potential energy functions with an x_0 of 1.75 being about an order of magnitude higher at their equilibrium than those with an x_0 of 3.

Attractive Case

In the attractive case, (3.83) becomes

$$P_{att,R} = -\int \vec{\tau}_{2,att,z}\, d\beta = -\int \left(-\frac{\mu_0\mu_1\mu_2}{2\pi x_0^3}\sin\beta - k_r\beta\right)\hat{k}\, d\beta$$

$$= -\frac{\mu_0\mu_1\mu_2}{2\pi x_0^3}\cos\beta + \frac{k_r\beta^2}{2} + C. \tag{3.84}$$

Figure 38a identifies the six repulsive equilibria that are all located at $\beta = 0$. Similar to the plots in Figure 31, negative potential energy values are plotted as absolute values in grey, such that equilibria occurring at a plotted grey maxima are stable equilibria (since they are actually minima). These equilibria occur at a global minimum in the range plotted, but since the potential energy function does not go to $+\infty$ at $\beta = \pm\frac{\pi}{2}$, they are not globally stable (since motion could still escape).

Non-Dimensionalization of Potential Energy

The non-dimensional repulsive potential energy is equivalent to the negative integral of Equation (3.67):

$$\tilde{P}_{rep,R} = -\int \tilde{\tilde{\tau}}_{2,rep,ND,z}\, d\beta = -\int \left(\frac{\gamma}{3\tilde{x}_0{}^3}\sin\beta - k_r^*\,\beta\right)\hat{k}\, d\beta$$

$$= \frac{\gamma}{3\tilde{x}_0{}^3}\cos\beta + \frac{k_r^*\beta^2}{2} + C. \tag{3.85}$$

The non-dimensional attractive energy is equivalent to the negative integral of Equation (3.68):

$$\tilde{P}_{att,R} = -\int \tilde{\tilde{\tau}}_{2,att,ND,z} d\beta = -\int \left(-\frac{\gamma}{3\tilde{x}_0{}^3}\sin\beta - k_r^*\,\beta\right)\hat{k}\, d\beta$$

$$= -\frac{\gamma}{3\tilde{x}_0{}^3}\cos\beta + \frac{k_r^*\beta^2}{2} + C. \tag{3.86}$$

Figure 39 shows all of the equilibria identified in Table 12, with Figure 39a showing the statically stable attractive equilibria at $\beta = 0$ and Figure 39b showing the mix of repulsive equilibria. The attractive equilibria occur at a global minimum, but they are not globally stable for the same reasons that the dimensional attractive equilibria are not globally stable. Figure 39b illustrates the earlier discussion about how the $\beta_{0b,ND}$ equilibrium switches from statically unstable to stable when γ/k_r^* drops below 24; as γ decreases from 35 to 25, the ridge through $\beta = 0$ flattens out from a very unstable peak at $\gamma = 35$ to a shallower peak at $\gamma = 30$, to a very shallow peak at $\gamma = 25$, indicating that further reduction would combine the two stable and one stable equilibrium per line into a single stable equilibrium at $\beta = 0$.

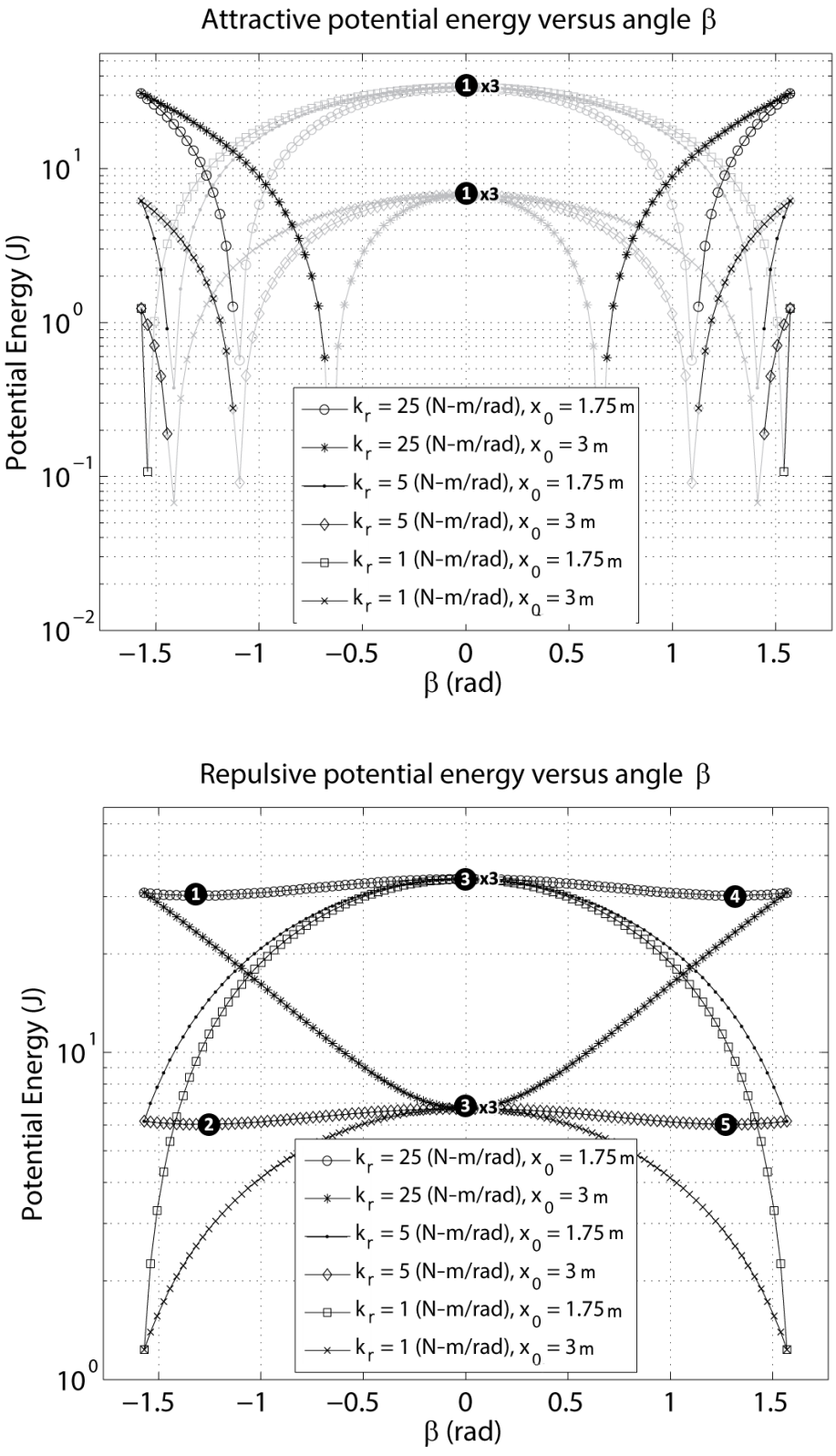

Figure 38: Potential energy curves for the (a, top) attractive and (b, bottom) repulsive cases, with grey lines being the absolute values of negative energies

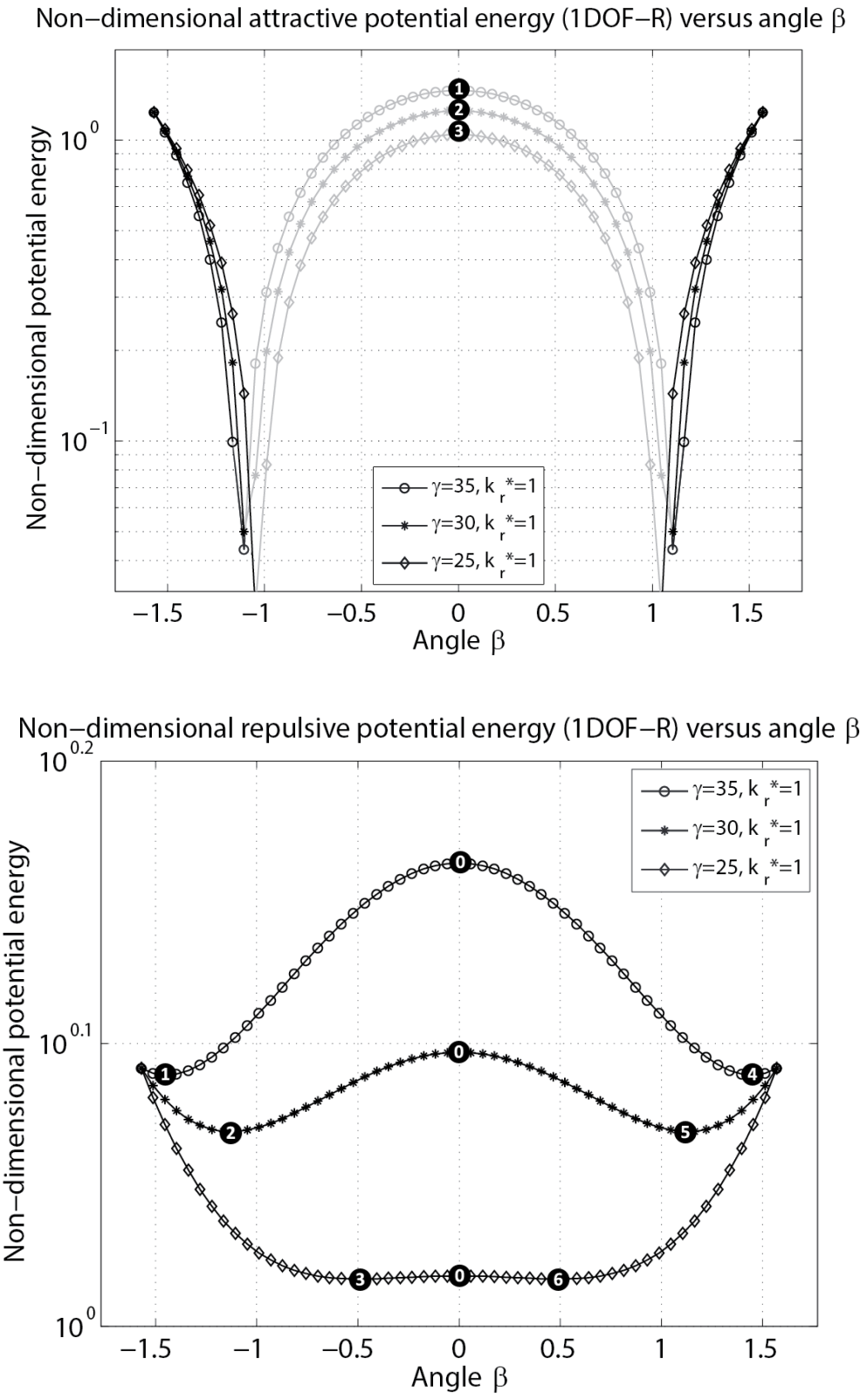

Figure 39: Non-dimensional potential energy curves for the (a, top) ND attractive and (b, bottom) ND repulsive cases, with $\tilde{x}_0$=2 and grey lines being the absolute values of negative energies

Critical Dimensional Initial Kinetic Energy and Simulation

Since the potential energy curves do not go to $+\infty$ on the edges of our range, it is of interest to examine what happens when β exceeds the range of $-\frac{\pi}{2} \leq \beta \leq \frac{\pi}{2}$ in either direction. Figure 40a shows the repulsive potential energy curve over the range $-\pi \leq \beta \leq \pi$ for the three example cases with $x_0 = 1.75$, and Figure 40b shows the repulsive potential energy curve over the same range for the three example cases with $x_0 = 3$. From these plots, it can be seen that for the four non-zero statically stable equilibria in the repulsive case, the critical initial kinetic energy is determined by the potential energy at $\beta = 0$ for each curve. For the two metastable equilibria β_{1b}, β_{4b} on the curve with $x_0 = 1.75, k = 25$,

$$T_{t_0,crit}(\beta_{1b}, \beta_{4b}) = P_{rep,R}(\beta_{3b-5}) - P_{rep,R}(|\beta_{1b}|) = 33.9436\,J - 30.2035\,J,$$

and

$$T_{t_0,crit}(\beta_{1b}, \beta_{4b}) = 3.7401\,J. \tag{3.87}$$

For the two metastable equilibria β_{2b}, β_{5b} on the curve with $x_0 = 3, k = 5$,

$$T_{t_0,crit}(\beta_{2b}, \beta_{5b}) = P_{rep,R}(\beta_{3b-4}) - P_{rep,R}(|\beta_{2b}|) = 6.7376\,J - 6.0273\,J,$$

and

$$T_{t_0,crit}(\beta_{2b}, \beta_{5b}) = 0.7103\,J. \tag{3.88}$$

It can be seen from Equations (3.87) and (3.88) that $T_{t_0,crit}(\beta_{1b}, \beta_{4b}) > T_{t_0,crit}(\beta_{2b}, \beta_{5b})$, meaning that the amount of energy that would need to be introduced to the system to make either equilibria on the curve $x_0 = 1.75, k = 25$ dynamically unstable is greater than that required to make either equilibria on the curve $x_0 = 3, k = 5$ unstable. Therefore, the equilibria at β_{1b} and β_{4b} are more tolerant of perturbation than the equilibria at β_{2b} and β_{5b} and are therefore better. As seen in Figure 40, noting that the $\beta = -\pi$ limit is the same point as $\beta = \pi$ and that the plot thus wraps around, the mode of instability on either curve is a switching from one equilibrium to the other, characteristic of metastable equilibria.

Critical Non-Dimensional Initial Kinetic Energy and Simulation

As in the previous section, the behavior of the system beyond the bounds of $-\frac{\pi}{2} \leq \beta \leq \frac{\pi}{2}$ is of interest. Figure 41 shows the non-dimensional repulsive potential energy curve over the range $-\pi \leq \beta \leq \pi$ for the three curves plotted in Figure 39. It can be seen that the two statically stable equilibria on each curve are metastable and that the mode of instability and escaping motion is switching from one equilibrium to the other. As in the dimensional case, the critical initial kinetic energy of the two statically stable equilibria on each of the three curves under study are determined by the difference in potential energy between the stable equilibrium and the unstable equilibrium at $\beta = 0$. For the two metastable equilibria $\beta_{1b,ND}, \beta_{4b,ND}$ on the curve with $\gamma = 35$,

$$\tilde{T}_{t_0,crit}(\beta_{1b,ND}, \beta_{4b,ND}) = \tilde{P}_{rep,R}(\beta_{0b,ND-1}) - \tilde{P}_{rep,R}(|\beta_{1b,ND}|)$$

$$= 10^{0.16386} - 10^{0.08884},$$

$$\tilde{T}_{t_0,crit}(\beta_{1b,ND}, \beta_{4b,ND}) = 0.2313. \tag{3.89}$$

For the two metastable equilibria $\beta_{2b,ND}, \beta_{5b,ND}$ on the curve with $\gamma = 30$,

$$\tilde{T}_{t_0,crit}(\beta_{2b,ND}, \beta_{5b,ND}) = \tilde{P}_{rep,R}(\beta_{0b,ND-2}) - \tilde{P}_{rep,R}(|\beta_{2b,ND}|)$$

$$= 10^{0.09691} - 10^{0.06890},$$

$$\tilde{T}_{t_0,crit}(\beta_{2b,ND}, \beta_{5b,ND}) = 0.0781. \tag{3.90}$$

For the two metastable equilibria $\beta_{3b,ND}, \beta_{6b,ND}$ on the curve with $\gamma = 25$,

$$T_{t_0,crit}(\beta_{3b,ND}, \beta_{6b,ND}) = \tilde{P}_{rep,R}(\beta_{0b,ND-3}) - \tilde{P}_{rep,R}(|\beta_{3b,ND}|)$$

$$= 10^{0.017729} - 10^{0.016689},$$

$$T_{t_0,crit}(\beta_{3b,ND}, \beta_{6b,ND}) = 0.0025. \tag{3.91}$$

It can be seen from Equations (3.89)-(3.91) that the larger the γ or γ/k_r^* value, the more energy that needs to be introduced to the system to make a statically stable equilibrium dynamically unstable.

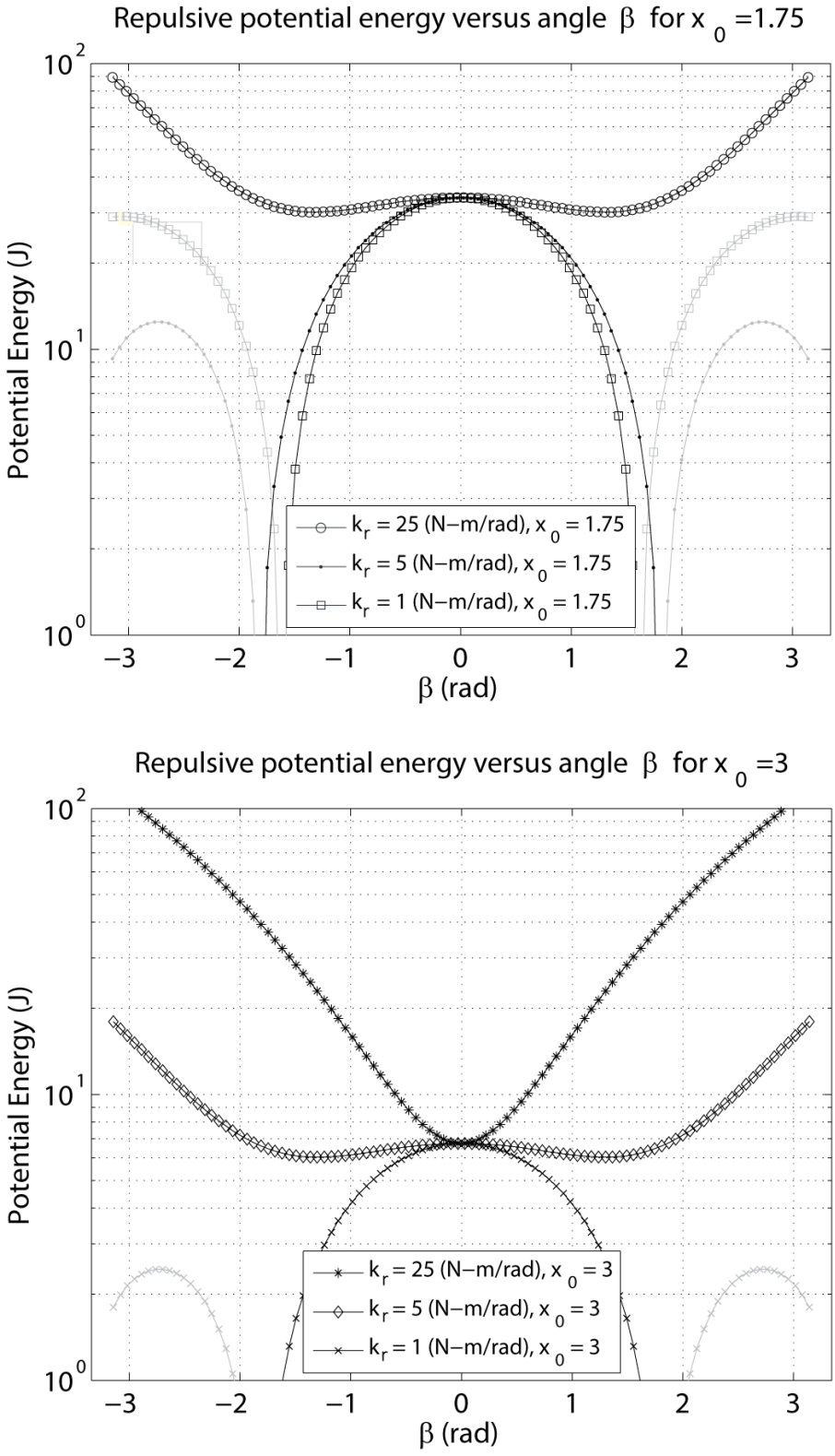

Figure 40: Potential energy curves for the repulsive case over the range $-\pi \leq \beta \leq \pi$ for (a,top) x_0 = 1.75 curves, and (b,bottom), x_0 = 3 curves

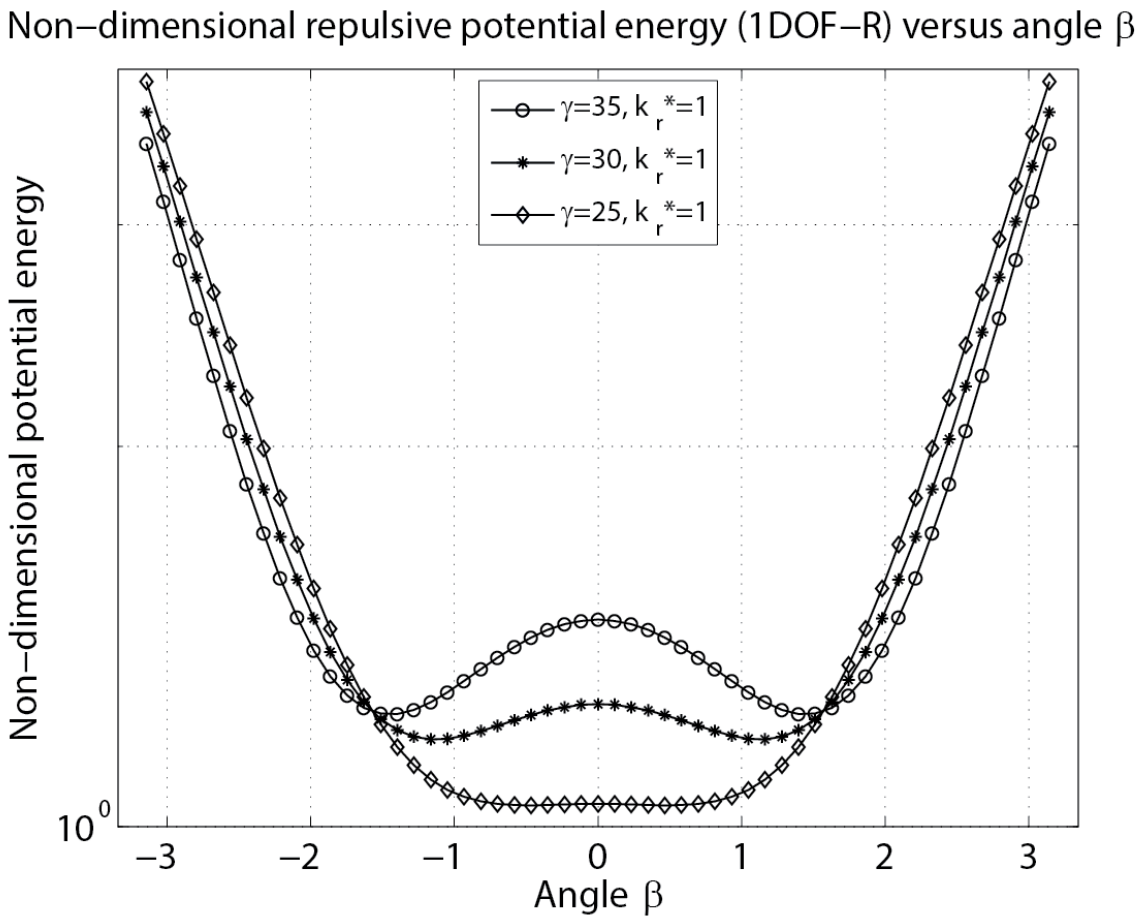

Figure 41: Non-dimensional potential energy curves for the repulsive case over the range $-\pi \leq \beta \leq \pi$

3.4.1. Summary

In Section 3.4, a single rotational degree of freedom spring-magnet system was presented; its equilibria were identified and analyzed for their static and dynamic stability. It can be seen that in the 1DoF-R system, in contrast to Section 3.3, the attractive equilibria are the ones that are all statically and dynamically stable, whereas repulsive equilibria are a mix of statically stable and unstable. Dynamic stability is based upon the difference in potential energy between the stable and the unstable equilibria in systems with a spring constant large enough to have equilibria. The larger the spring constant, the higher the critical initial kinetic energy required to make the statically stable equilibrium dynamically unstable.

3.5. Two Degrees of Freedom

1 DoF – Translational	1 DoF – Rotational	2 DoF – Rotational & Translational
Equilibrium Identification	Equilibrium Identification	Equilibrium Identification
Static Stability	Static Stability	Static Stability
Dynamic Stability	Dynamic Stability	Dynamic Stability

The third and final analytical magnet system studied in this chapter, depicted in Figure 42, permits motion in both a translational and a rotational degree of freedom, effectively combining the systems from Sections 3.3 and 3.4 into a two degree of freedom system. Both the linear and torsional springs are active in this system, since magnet 2 can move along the x axis and rotate around the z axis. As opposed to the previous two sections in this chapter, only the repulsive case (within the bounds $-\pi/2 < \beta < \pi/2$; outside of these bounds, the system becomes attractive) will be considered in this section to simplify visualization of the system and its results. Also, after the equilibrium identification step, all analysis will be non-dimensional to further reduce the complexity of the formulations for static and dynamic stability.

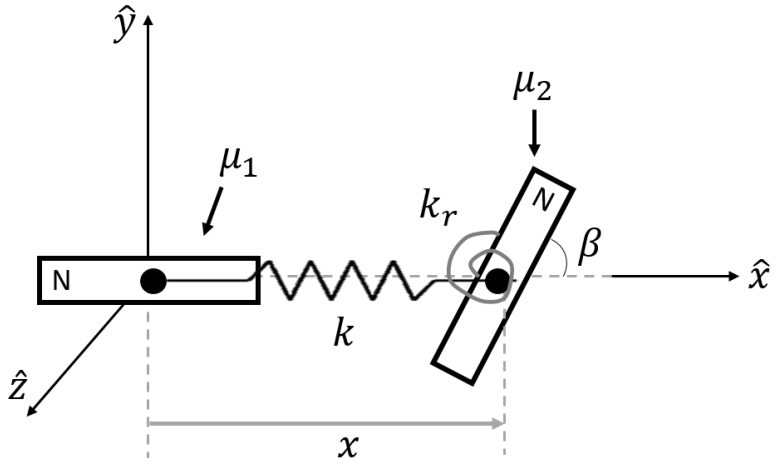

Figure 42: 2DoF (translational and rotational) system

3.5.1. Force and Torque Balance

In the 2DoF system, both a force and a torque balance are required for the system to be in equilibrium.

Equations (3.9)-(3.11) apply as is to the system as depicted in Figure 42, and the formulas that will be used in this section are repeated below for reference:

$$\vec{F}_{mag,2} = \frac{3\mu_0\mu_1\mu_2}{4\pi x^4}\begin{bmatrix} 2\cos\beta \\ -\sin\beta \\ 0 \end{bmatrix}, \tag{3.92a}$$

and

$$\vec{\tau}_{mag,2} = \frac{\mu_0\mu_1\mu_2}{4\pi x^3}\begin{bmatrix} 0 \\ 0 \\ 2\sin\beta \end{bmatrix}. \tag{3.92b}$$

Since only motion along the x axis is permitted, the y term in Equation (3.92a) is ignored going forward. Adding the linear spring force and torsional spring torque to Equations (3.92), respectively, the total force and torque are

$$\vec{F}_{2,rep} = \left(\frac{3\mu_0\mu_1\mu_2}{2\pi x^4}\cos\beta - k(x - x_0)\right)\hat{\imath}, \tag{3.93a}$$

and

$$\vec{\tau}_{2,rep} = \left(\frac{\mu_0\mu_1\mu_2}{2\pi x^3} sin\,\beta - k_r\beta\right)\hat{k}. \tag{3.93b}$$

Non-Dimensionalization of Force and Torque Balance Equations

Using the non-dimensional terms and forces and torques defined in Equations (3.22)-(3.25) and (3.64)-(3.68), the non-dimensional force and torque are

$$\tilde{\vec{F}}_{2,rep,ND} = \left(\frac{\gamma}{\tilde{x}^4}\cos\beta - k^*(\tilde{x} - \widetilde{x_0})\right)\hat{\imath}, \tag{3.94a}$$

and

$$\tilde{\vec{\tau}}_{2,rep,ND} = \left(\frac{\gamma}{3\tilde{x}^3}\sin\beta - k_r^*\,\beta\right)\hat{k}. \tag{3.94b}$$

Unlike in previous sections, Equations (3.93) and (3.94) are functions of two variables each, x (or $\tilde{x}$) and β. In the next subsection, equilibria are found that fulfill both a force and a torque balance with the above equations.

3.5.2. Equilibrium Identification

1 DoF – Translational	1 DoF – Rotational	2 DoF – Rotational & Translational
Equilibrium Identification	Equilibrium Identification	Equilibrium Identification
Static Stability	Static Stability	Static Stability
Dynamic Stability	Dynamic Stability	Dynamic Stability

Finding equilibria in two generalized coordinates is more complex than for one coordinate. First, both a force balance and a torque balance must be written by determining where Equations (3.93) equal zero. Equations (3.95) give the force and torque balance respectively:

$$\frac{3\mu_0\mu_1\mu_2}{2\pi x^4}\cos\beta = k(x - x_0), \tag{3.95a}$$

and

$$\frac{\mu_0\mu_1\mu_2}{2\pi x^3} sin\,\beta = k_r\beta. \tag{3.95b}$$

Immediately, it can be seen that (3.95b) is fulfilled when β=0, when zero torque is induced. At this point, the equilibrium x point is identical to that of the 1DoF-T case, which can be determined from graphical exploration of Equation (3.26), or Figure 29.

The analytical approach to determining points (x, β), where $\beta \neq 0$ and Equations (3.95) are both met is to solve Equation (3.95b) for x and then substitute it into (3.95a):

$$x^3 = \frac{\mu_0\mu_1\mu_2}{2\pi k_r\beta} sin\,\beta,$$

and

$$\frac{3\mu_0\mu_1\mu_2}{2\pi\left(\frac{\mu_0\mu_1\mu_2}{2\pi k_r\beta} sin\,\beta\right)^{\frac{4}{3}}}\cos\beta = k\left(\left(\frac{\mu_0\mu_1\mu_2}{2\pi k_r\beta} sin\,\beta\right)^{\frac{1}{3}} - x_0\right). \tag{3.96}$$

Equation (3.96) isn't very friendly looking, but it allows for similar analysis as in Sections 3.3 and 3.4; by plotting both sides of Equation (3.96) over the range $-\frac{\pi}{2} \leq \beta \leq \frac{\pi}{2}$ and finding intersections, the β

location of equilibria that satisfy both a force and torque balance can be found and then inserted into Equation (3.95b) to obtain the x coordinate.

Both sides of Equation (3.96) need to have the same sign. $\cos\beta$ and $\frac{sin\,\beta}{\beta}$ are each always positive over the range under study, both equaling 1 when $\beta = 0$ and $\cos\beta$ going to 0 at $\beta = \pm\frac{\pi}{2}$. All of the constants in the problem are positive, meaning that the left side of the equation is always positive or zero at the bounds. The right side is positive only if

$$\frac{\mu_0\mu_1\mu_2}{2\pi k_r\beta} sin\,\beta > x_0^3,$$

or, rearranged,

$$k_r < \frac{\mu_0\mu_1\mu_2}{2\pi\beta x_0^3} sin\,\beta.$$

The minimum value of $\frac{sin\,\beta}{\beta}, \frac{2}{\pi}$ occurs at the bounds, such that the most restrictive specification of k_r is

$$k_r < \frac{\mu_0\mu_1\mu_2}{\pi^2 x_0^3}. \tag{3.97}$$

Non-Dimensionalization of Equilibrium

The non-dimensional force and torque balances are met where Equations (3.94) equal zero, or, respectively

$$\frac{\gamma}{\tilde{x}^4}\cos\beta = k^*(\tilde{x} - \tilde{x}_0), \tag{3.98a}$$

and

$$\frac{\gamma}{3\tilde{x}^3}\sin\beta = k_r^*\,\beta. \tag{3.98b}$$

As in the dimensional case, (3.98b) is fulfilled when β=0, and zero torque is induced. At this point, the equilibrium x point is identical to that of the 1DoF-T non-dimensionalized case, which can be determined from graphical exploration of Equation (3.27a) as in Figure 30.

To determine points (x, β) where $\beta \neq 0$ and Equations (3.98) are met, Equation (3.98b) is solved for $\tilde{x}$ and then substituted into (3.98a):

$$\tilde{x}^3 = \frac{\gamma}{3k_r^*}\frac{sin\,\beta}{\beta},$$

and

$$\frac{\gamma}{\left(\frac{\gamma}{3k_r^*}\frac{sin\,\beta}{\beta}\right)^{4/3}}\cos\beta = k^*\left(\left(\frac{\gamma}{3k_r^*}\frac{sin\,\beta}{\beta}\right)^{\frac{1}{3}} - \tilde{x}_0\right). \tag{3.99}$$

Similarly to Equation (3.97), the left hand side of Equation (3.99) is always positive over the range in study, and therefore the right hand side also needs to be positive. From this observation, it can be seen that the most restrictive specification on k_r^* based on $\frac{sin\,\beta}{\beta} = \frac{2}{\pi}$ is

$$k_r^* < \frac{2\gamma}{3\pi{\tilde{x}_0}^3}. \tag{3.100}$$

In the next subsection, example values of the variables in Equation (3.99) are assigned such that the two sides of the equation can be plotted to observe for what values of β the non-dimensional forces intersect, indicating that the system is in equilibrium. The β locations can then be inserted into Equation (3.98b) to obtain the x coordinates of the 2DoF equilibria.

Example Non-Dimensional Equilibrium Identification

In this section, $\tilde{x}_0$ is assumed to be 2 radii, and a range of values of γ $(10, 20, 50)$ are studied. These values can be used in combination with Equation (3.100) to select k_r^* values that allow secondary equilibria in each case. However, for consistency of selection and a margin of safety, k_r^* is selected as a constant value based on $\gamma = 20$, taken to equal 90% of the upper boundary of Equation (3.100) , or

$$k_r^* = 0.9\frac{2\gamma}{3\pi{\tilde{x}_0}^3}. \tag{3.101}$$

When $\gamma = 20$, $k_r^* = 0.4775$. As such, it is expected that $\gamma = 10$ will *not* have secondary equilibria because the right side of Equation (3.99) will be negative. For $\gamma = 20$ and 50, the k_r^* condition is met but not sufficient for proving the existence of secondary equilibria.

Figure 43a plots the total non-dimensional force (the left side of Equation (3.99) minus the right side of (3.99)) against β with several different values of γ, such that zero crossings represent equilibria in both force and torque even though the y axis is non-dimensional force. Again, this is because the torque balance has been inserted into the force balance equation such that any force balance also guarantees a torque balance. Figure 43 only shows the non-zero equilibria.

Table 13 gives the β and $\tilde{x}$ values for each of the identified equilibria in Figure 43 as well as the equilibria at $\beta = 0$. It can be noted that every value of γ has a guaranteed equilibrium at $\beta = 0$ and that one of the three values of γ (the intermediate value) also has equilibria near $\beta = \pm\frac{\pi}{2}$.

Table 13: β and $\tilde{x}$ values for equilibria in Figure 43 as well as the equilibria at $\beta = 0$

- β				+ β				0			
Equil. ID	γ values	β	$\tilde{x}$	Equil. ID	γ values	β	$\tilde{x}$	Equil. ID	γ values	β	$\tilde{x}$
$\beta_{1,-}$	10	-	-	$\beta_{1,+}$	10	-	-	$\beta_{1,0}$	10	0	2.338
$\beta_{2,-}$	20	-1.445	2.1243	$\beta_{2,+}$	20	1.445	2.1243	$\beta_{2,0}$	20	0	2.508
$\beta_{3,-}$	50	-	-	$\beta_{3,+}$	50	-	-	$\beta_{3,0}$	50	0	2.809

Section 3.5.3 evaluates the static stability of each equilibrium point.

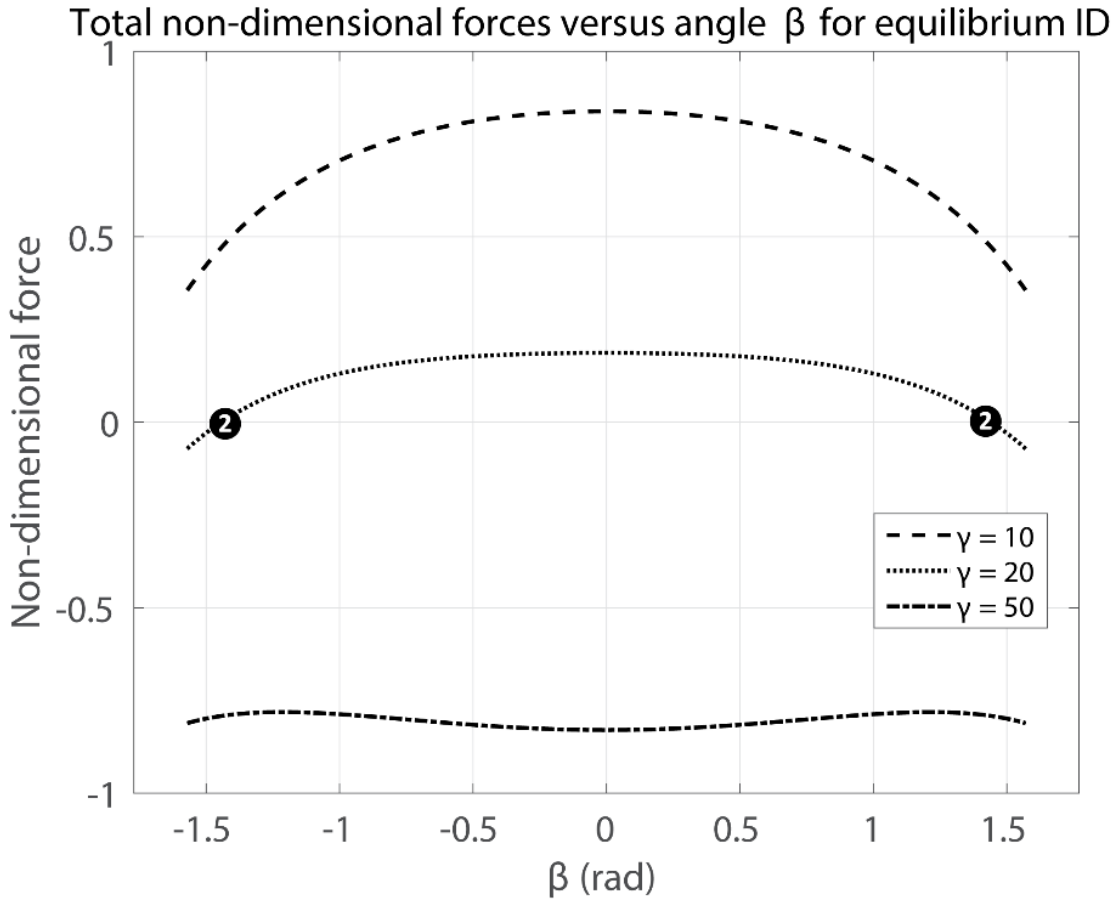

Figure 43: Total non-dimensional forces of Equation (3.99) (left side minus the right side) for various values of γ and $\tilde{x}_0$=2 shown for full range of $-\frac{\pi}{2} \leq \beta \leq \frac{\pi}{2}$. It can be seen that secondary equilibria only occur for $\gamma = 20$.

3.5.3. Static Stability Classification

1 DoF – Translational	1 DoF – Rotational	2 DoF – Rotational & Translational
Equilibrium Identification	Equilibrium Identification	Equilibrium Identification
Static Stability	Static Stability	Static Stability
Dynamic Stability	Dynamic Stability	Dynamic Stability

In this section, the static stability of the 2DoF equilibria identified in the previous section is evaluated.

In Sections 3.3.3 and 3.4.3, the single degree of freedom meant that only one stiffness value needed to be calculated to evaluate static stability. Now that motion in two generalized coordinates is allowed, a stiffness *matrix* must be calculated such that the real part of the eigenvalues of the stiffness matrix must all be positive for static stability (any zero eigenvalues indicate statically neutral stability in the direction of the associated eigenvector, and any negative eigenvalues indicate static instability in the direction of the associated eigenvector) [48]. Negative eigenvalues are possible because the electromagnets represent negative stiffness elements in the system. Equation (3.102) gives the structure of the stiffness matrix. It should be noted that the aforementioned stability convention corresponds to the eigenvalues of the stiffness matrix on its own, not the state-space displacement coefficient matrix. If the latter were being used, the convention would switch signs for static stability and instability [48].

$$[K_{ND}] = -\begin{bmatrix} \dfrac{\partial \tilde{F}_2}{\partial \tilde{x}} & \dfrac{\partial \tilde{F}_2}{\partial \beta} \\ \dfrac{\partial \tilde{\tau}_2}{\partial \tilde{x}} & \dfrac{\partial \tilde{\tau}_2}{\partial \beta} \end{bmatrix}. \tag{3.102}$$

Inserting the partial derivatives of Equations (3.94) into Equation (3.102), the non-dimensional stiffness matrix is

$$[K_{ND}] = \begin{bmatrix} \dfrac{4\gamma}{\tilde{x}^5}\cos\beta + k^* & \dfrac{\gamma}{\tilde{x}^4}\sin\beta \\ \dfrac{\gamma}{\tilde{x}^4}\sin\beta & -\dfrac{\gamma}{3\tilde{x}^3}\cos\beta + k_r^* \end{bmatrix}. \tag{3.103}$$

While Equation (3.103) seems deceptively simple, its eigenvalues require Mathematica to find:

$$\lambda_{1,2} = \frac{k^* + k_r^*}{2} + \gamma\cos\beta\left[\frac{2}{\tilde{x}^5} - \frac{1}{6\tilde{x}^3}\right] \pm$$

$$\pm\frac{\sqrt{4\left[(k^* + k_r^*)\tilde{x}^5 + \left(4 - \frac{\tilde{x}^2}{3}\right)\gamma\cos\beta\right]^2 - 8\tilde{x}^2\left[2k^*k_r^*\tilde{x}^8 - \frac{7\gamma^2}{3} + \left(8k_r^*\tilde{x}^3 - \frac{2k^*\tilde{x}^5}{3}\right)\gamma\cos\beta - \frac{\gamma^2}{3}\cos 2\beta\right]}}{4\tilde{x}^5}. \tag{3.104}$$

Given the complexity of Equation (3.104), Table 14 gives the eigenvalues for the equilibria in Table 13 as calculated by Equation (3.104), double checked by MATLAB's *eig* command on the stiffness matrix in Equation (3.103).

Table 14: 2DoF stiffness matrix eigenvalues $\lambda_{1,2}$ at each equilibrium in Figure 43, statically stable equilibria bolded

- β					
Equil. ID	γ	β	$\tilde{x}$	λ_1	λ_2
$\beta_{1,-}$	10	-	-	-	-
$\beta_{2,-}$	20	-1.445	2.1243	1.8725	-0.2502
$\beta_{3,-}$	50	-	-	-	-
+ β					
Equil. ID	γ	β	$\tilde{x}$	λ_1	λ_2
$\beta_{1,+}$	10	-	-	-	-
$\beta_{2,+}$	20	1.445	2.1243	1.8725	-0.2502
$\beta_{3,+}$	50	-	-	-	-
β = 0					
Equil. ID	γ	β	$\tilde{x}$	λ_1	λ_2
$\beta_{1,0}$	**10**	**0**	**2.338**	**1.5726**	**0.2167**
$\beta_{2,0}$	**20**	**0**	**2.508**	**1.8062**	**0.0549**
$\beta_{3,0}$	50	0	2.809	2.1436	-0.2745

From Table 14, it can be seen that the only statically stable equilibria (with two positive eigenvalues) are two of the three equilibria that occur at $\beta = 0$, those for which $\gamma = 10, 20$, as expected. The eigenvalue that tends to be negative is that eigenvalue where the ± is negative in Equation (3.104). Unlike in the one dimensional problems earlier in this chapter, it is much more difficult to determine from Equation (3.104) the requirements on the 2DoF system for static stability. Going forward with more complex systems, a less complicated calculation of the static stability of a list of equilibria is desirable. Chapter 4 investigates a numerical method for static stability evaluation and uses the results of this section to validate that method. The next section uses the stable equilibria that have been identified to investigate dynamic stability in two degrees of freedom.

3.5.4. Dynamic Stability

1 DoF – Translational	1 DoF – Rotational	2 DoF – Rotational & Translational
Equilibrium Identification	Equilibrium Identification	Equilibrium Identification
Static Stability	Static Stability	Static Stability
Dynamic Stability	Dynamic Stability	Dynamic Stability

In this section, the dynamic stability of the system equilibria is determined, this concluding the study of this system as well as the analytical step of the three-step approach.

Again, the potential energy is used to determine the dynamic stability of the statically stable equilibria identified in the previous section. However, because the system under study allows motion in two degrees of freedom, the potential energy functional is a three-dimensional surface rather than a two-dimensional curve. The resulting increase in complexity will make the calculation of critical initial kinetic energy more challenging.

In Sections 3.3.4 and 3.4.4, potential energy is calculated by integrating the force equation with respect to x (or $\tilde{x}$) or by integrating the torque equation with respect to angle β. In the two degree of freedom system, calculation of potential energy can be done either way in order to get the same result. Jackson [49] explains that "the potential energy of a permanent magnetic moment (or dipole) in an external magnetic field can be obtained from either the force or the torque", so it is shown below that the magnetic potential energy calculated from both force and torque are the same.

In order to show that the magnetic potential energy calculated from both force and torque are the same, both are given below (in the repulsive case) and then compared along with the definitions of γ and ξ from Equations (3.22) and (3.64) to show that they are identical:

$$\tilde{P}_{mag,T} = -\int \tilde{\vec{F}}_{2,rep,mag,x}\, d\tilde{x} = -\int \left(\frac{\gamma}{\tilde{x}^4}\cos\beta\right)\hat{\imath}\, d\tilde{x}$$

$$= \frac{\gamma}{3\tilde{x}^3}\cos\beta + C,$$

and (3.105)

$$\tilde{P}_{mag,R} = -\int \tilde{\vec{\tau}}_{2,rep,mag,z}\, d\beta = -\int \left(\frac{\gamma}{3\tilde{x}^3} sin\,\beta\right)\hat{k}\, d\beta \quad (3.106)$$

$$= \frac{\gamma}{3\tilde{x}^3} cos\,\beta + C.$$

It can easily be seen that Equations (3.105) and (3.106) are identical. The elastic potential energies for the linear and torsional springs are as follows, denoted by $\tilde{V}_T$ and $\tilde{V}_R$ for the translational and rotational energies respectively:

$$\tilde{V}_T = -\int \tilde{\vec{F}}_{spr,lin} = -\int -\left(k^*(\tilde{x} - \tilde{x}_0)\right) \hat{\imath}\, d\tilde{x} = \frac{k^*\tilde{x}^2}{2} - k^*\tilde{x}_0\tilde{x} + C,$$

and (3.107)

$$\tilde{V}_R = -\int \tilde{\vec{\tau}}_{spr,lin} = -\int -(k_r^*\beta)\, \hat{k}\, d\beta = \frac{k_r^*\beta^2}{2} + C, \quad (3.108)$$

such that the total non-dimensional repulsive potential energy in the 2DoF system is

$$\tilde{P}_{2DoF} = \tilde{V}_T + \tilde{V}_R + \tilde{P}_{mag,T}$$

$$= \frac{\gamma}{3\tilde{x}^3}\cos\beta + \frac{k^*\tilde{x}^2}{2} + \frac{k_r^*\beta^2}{2} - k^*\tilde{x}_0\tilde{x} + C. \quad (3.109)$$

The physical meaning of the value of C is something that will be investigated in the next chapter, but for now, the potential energy values calculated in Equations (3.106)-(3.109) are sufficient to study relative potential energies. C is taken to be the magnitude of the minimum value of Equation (3.109) for each configuration such that all the potential energy values in the range under study are positive and thus can be plotted logarithmically. In the nine configurations explored, C is roughly 10^2.

Because the plot of the potential energy functional in Equation (3.109) is three dimensional/a surface, the parameters and potential energy of each of the three systems presented in Table 14 are plotted in the three contour plots of Figure 44 respectively, with γ increasing from left to right. The potential energy values shown along the colorbar are actually log10($\tilde{P}_{2DoF}$). Equilibria are indicated by numbered dots corresponding to the equilibrium IDs in Table 14. The distance range plotted in Figure 44 is $1.5 \leq \tilde{x} \leq 3.5$, allowing for finer contouring of the plots in the regions of interest.

A trend can be observed: as γ increases, the potential energy around the $\beta = 0$ equilibrium goes from a deep well to a shallower, narrower well (spawning two saddle points on either side at the statically unstable secondary equilibria), to a saddlepoint, meaning that for large γ, there are no statically stable equilibria.

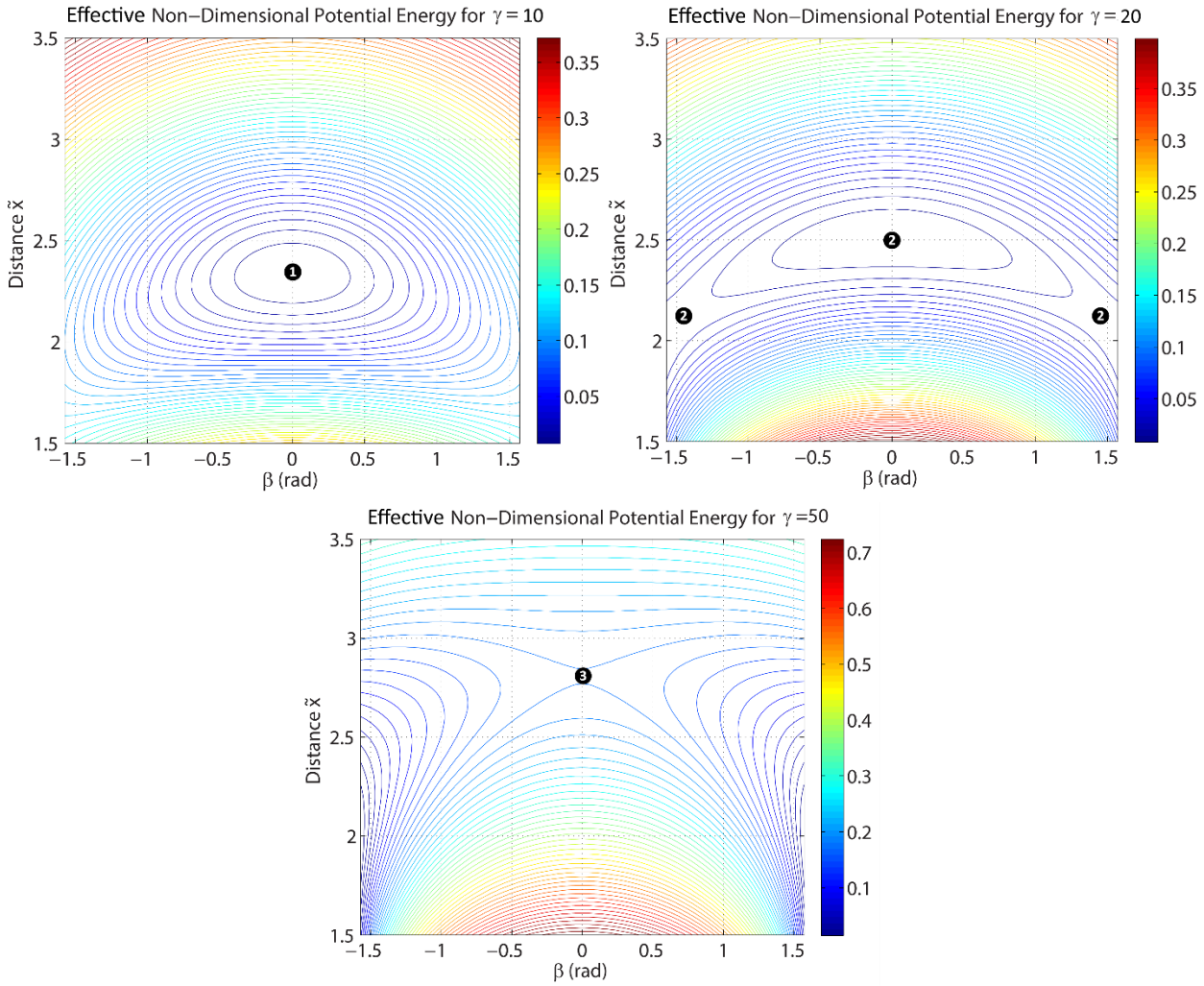

Figure 44: Zoomed-in potential energy contours ($1.5 \leq \tilde{x} \leq 3.5$*) and equilibria (identified with dots and numbered according to Table 14) for the 2DoF system. Colorbar values are log10(*$\tilde{P}_{2DoF}$*).*

As γ increases for a fixed k^* and k_r^*, the $\beta = 0$ equilibrium increases in the $\tilde{x}$ direction away from the natural spring length, as expected for stronger magnetic forces.

It is interesting to note that an injection of kinetic energy into the system in the right direction could result in an orbiting of the system around a statically stable equilibrium, so long as the kinetic energy is less than the critical initial kinetic energy of that equilibrium. Bounded motion is not limited to one generalized coordinate in the 2DoF system. The next section presents a table of the numerical values of potential energy for comparison and calculation of the critical initial kinetic energy.

Critical Non-Dimensional Initial Kinetic Energy and Simulation

To directly compare the energy of the equilibria depicted in Figure 44 in order to compute the critical initial kinetic energy, Table 15 gives the potential energy values (without the constant of integration C added) for each of the equilibria in Table 14.

Table 15: 2DoF potential energy at each equilibrium in Figure 44 with $\tilde{T}_{t_0,crit}$ for statically stable (bolded) equilibria

- β					
Equil. ID	γ	β	$\tilde{x}$	$\tilde{P}_{2DoF}$	$\tilde{T}_{t_0,crit}$
$\beta_{1,-}$	10	-	-	-	-
$\beta_{2,-}$	20	-1.445	2.1243	-1.4065	-
$\beta_{3,-}$	50	-	-	-	-
+ β					
Equil. ID	γ	β	$\tilde{x}$	$\tilde{P}_{2DoF}$	$\tilde{T}_{t_0,crit}$
$\beta_{1,+}$	10	-	-	-	-
$\beta_{2,+}$	20	1.445	2.1243	-1.4065	-
$\beta_{3,+}$	50	-	-	-	-
β = 0					
Equil. ID	γ	β	$\tilde{x}$	$\tilde{P}_{2DoF}$	$\tilde{T}_{t_0,crit}$
$\boldsymbol{\beta_{1,0}}$	10	**0**	**2.338**	**-1.6817**	**0.3367**
$\boldsymbol{\beta_{2,0}}$	20	**0**	**2.508**	**-1.4483**	**0.0418**
$\boldsymbol{\beta_{3,0}}$	50	0	2.809	-0.9211	**-**

From Table 15, it can be seen that the critical initial kinetic energy of the $\beta = 0$ equilibrium decreases as γ increases. The $\tilde{T}_{t_0,crit}$ values are calculated the same way as in the 1DoF-T and 1DoF-R systems, by taking the difference between the potential energy at the stable equilibrium and the nearest unstable equilibrium (or when $\gamma = 10$, the lowest energy at the bounds of the system due to the lack of secondary unstable equilibria). In the case of the configurations modeled in Figure 44, the closest (and only) unstable equilibria to a stable equilibrium are symmetric about $\beta = 0$ and thus have the same potential energy as each other. Because they have identical potential energies, the critical initial kinetic energies are calculated against the $+\beta$ unstable equilibrium for convention.

For $\gamma = 10$, $\tilde{T}_{t_0,crit}$ is

$$\tilde{T}_{t_0,crit}(\beta_{1,0}) = \min(\tilde{P}_{2DoF}(bounds)) - \tilde{P}_{2DoF}(\beta_{1,0}) = -1.3449 + 1.6817,$$
$$\tilde{T}_{t_0,crit}(\beta_{1,0}) = 0.3367; \tag{3.110}$$

and for $\gamma = 20$:

$$\tilde{T}_{t_0,crit}(\beta_{2,+}, \beta_{2,0}) = \tilde{P}_{2DoF}(\beta_{2,+}) - \tilde{P}_{2DoF}(\beta_{2,0}) = -1.4065 + 1.4483,$$
$$\tilde{T}_{t_0,crit}(\beta_{2,+}, \beta_{2,0}) = 0.0418. \quad (3.111)$$

3.6. Summary

From the calculations in the previous section and Table 15, $\tilde{T}_{t_0,crit}$ decreases with increasing γ, indicating that the dynamic stability of a statically stable equilibrium decreases as the magnets get stronger. Though the spring strength is fixed in this study, it can be seen that an increase in spring strength would increase the range of γ values which result in a staticallys table equilibrium at $\beta = 0$.

This section showed a combination of a translational and a rotational degree of freedom into a 2DoF system, and that equilibria could be identified and their static and dynamic stability calculated analytically within the assumptions of the model described in Section 3.2.

This chapter in general provides a thorough exploration of the thesis approach in the context of a simple analytical model, with dimensional and non-dimensional analysis and comparison throughout. The results of this chapter also are used to validate the methods introduced in the next chapter for problems of escalating complexity, given that analytical solutions are cumbersome or unobtainable for more accurate approaches to magneto-elastic stability.

Chapter 4
Simple Numerical Stability

In this chapter, the simple magnetic structure introduced in Chapter 3 is studied using numerical rather than analytical techniques. This chapter is a bridge between the simple structure and the more complex structure explored in Chapter 5. The analysis herein is used to validate numerical methods for calculating static and dynamic stability on a system with known, analytical stability formulations before applying it to a new structure with more complicated models for the magnetic field, forces, and torques.

The structure being studied is the same as that which was presented in Section 3.2, using bar magnets and the associated dipole model of the magnetic field in order to represent the coils. The general structure is repeated below for reference:

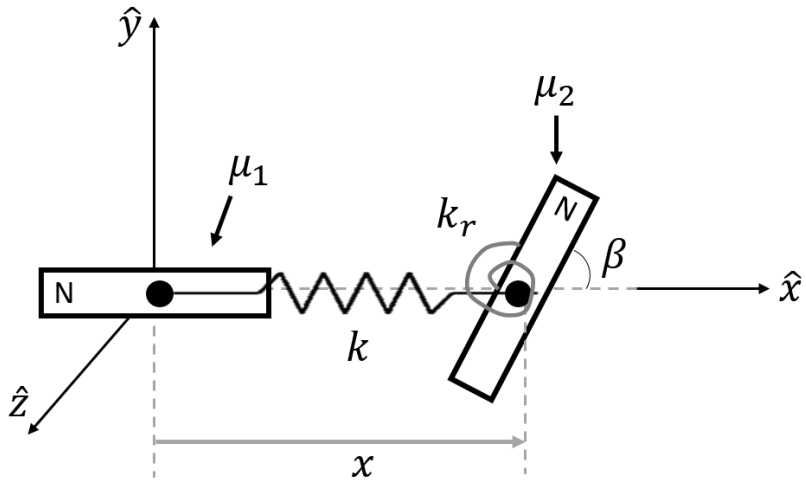

Figure 45: General dipole system with two degrees of freedom

Because the model for magnetic field (and resultant force and torque) is identical to that in Chapter 3, the equilibria in this chapter are the same as those presented in the previous chapter and will be re-copied here where appropriate for reference. The two differences between the previous chapter and this chapter are the methods by which the static and the dynamic stability are calculated. In Chapter 3, analytical differentiation of force and torque was used to calculate the stiffness value or matrix in order to determine if an equilibrium was statically stable or unstable. In this chapter, finite differencing is used to calculate the stiffness value, validated by the analytical results. In Chapter 3, analytical integration of force and torque was used to calculate the potential energy of magnet configurations in order to determine the bounds of dynamic stability for a statically stable equilibrium. In this chapter, the vector potential of a magnetic dipole is instead used to determine potential energy, and then the results of the previous chapter are used to validate this approach.

	3. Analytical	4. Simple Numerical	5. Complex Numerical
Equilibrium Identification	Dipole force/torque balance equations	Dipole force/torque balance equations	Coil numerical force/torque balance
Static Stability	Dipole force/torque analytical derivatives and linearized eigenvalues	Finite difference stiffness matrix	Finite difference stiffness matrix
Dynamic Stability	Analytical formulation of potential energy	Numerical vector potential calculation of potential energy	Numerical vector potential calculation of potential energy

1 DoF – Translational	1 DoF – Rotational	2 DoF – Rotational & Translational
Equilibrium Identification	Equilibrium Identification	Equilibrium Identification
Static Stability	Static Stability	Static Stability
Dynamic Stability	Dynamic Stability	Dynamic Stability

Figure 46: Three analytical systems to be studied in this chapter

Figure 46 shows this chapter in the overall approach framework presented in Section 1.4. Each of the 1DoF-T, 1DoF-R, and 2DoF systems will be discussed in this chapter using the new methods discussed above.

Going forward, only repulsive, non-dimensional formulations will be considered, now that the relationships between the dimensional and non-dimensional equations for equilibrium, static stability, and dynamic stability are well-understood from Chapter 3 and because repulsive systems are those that are of primary interest in spacecraft applications.

4.1. Translational Single Degree of Freedom

1 DoF – Translational	1 DoF – Rotational	2 DoF – Rotational & Translational
Equilibrium Identification	Equilibrium Identification	Equilibrium Identification
Static Stability	Static Stability	Static Stability
Dynamic Stability	Dynamic Stability	Dynamic Stability

Again, the same system as in Chapter 3 is used in this chapter, so the 1DoF-T magnetic structure from Figure 28 is replicated below in Figure 47:

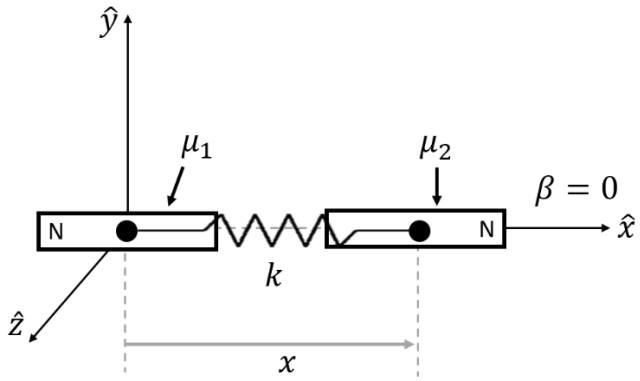

Figure 47: Translational single degree of freedom (1DoF-T) dipole system

The force balance is the same as that given by Equation (3.24), or

$$\tilde{\vec{F}}_{2,rep,ND} = \tilde{m}_2 \frac{d^2\tilde{x}}{d\tilde{t}^2} = \left(\frac{\gamma}{\tilde{x}^4} - k^*(\tilde{x} - \tilde{x}_0)\right)\hat{\imath}. \tag{4.1}$$

4.1.1. Equilibrium Identification

1 DoF – Translational	1 DoF – Rotational	2 DoF – Rotational & Translational
Equilibrium Identification	Equilibrium Identification	Equilibrium Identification
Static Stability	Static Stability	Static Stability
Dynamic Stability	Dynamic Stability	Dynamic Stability

As in Section 3.3.2, equilibrium occurs when the force balance equals zero, or

$$\frac{\gamma}{\tilde{x}^4} = k^*(\tilde{x} - \tilde{x}_0), \tag{4.2}$$

and

$$\frac{\gamma}{k^*} = \tilde{x}^4(\tilde{x} - \tilde{x}_0). \tag{4.3}$$

With an analytical formulation for the force balance, equilibrium points could be found through solving for $\tilde{x}$. Without an analytical solution, the force will be approximated at each of a discrete number of sample points, and the equilibria will either need to be found through graphical observation or by interpolation between two points. In this chapter and the next chapter, the location of an equilibrium is found by linearly interpolating between two adjacent points with opposite signs to find the zero crossing. In practice, this is done using a custom MATLAB function, *crossing.m* [50], which locates sets of points between which intersections occur and linearly interpolates to return the approximated value of $\tilde{x}$ (or β, in later sections) at the equilibrium as well as the indices between which the crossing occurs.

Clearly the mesh size (the frequency of samples) affects the accuracy of the approximation, since linear interpolation is more accurate over smaller portions of the function, but too small of a grid size requires the function to be evaluated at more points than are necessary, increasing the computational cost, especially in the next chapter where the calculation of force or torque at each point is more computationally intensive than calculating the analytical solution. In Chapter 3, a mesh size of 0.02 was used for the plots from whence equilibria locations were derived, and it will be examined in this chapter how that mesh size may have affected the accuracy of equilibrium identification.

The particular value of the discretization size is now selected by a grid refinement study. In this chapter, the mesh size is progressively decreased until the solution does not change from one grid level to the next. The tolerance for acceptable deviation from the exact solution is taken to be ± 0.0001, such that the magnitude of the pointwise maximum change in the $\tilde{x}$ values of equilibria at each equilibrium point is ≤ 0.0001, selected because that is the smallest level of change detectable within the number of decimal

places given for $\tilde{x}$ in the following table. The tolerance may be reduced in the next chapter due to the Biot-Savart model being very computationally intensive, and a sampling of thousands of points in one or two dimensions may be unacceptably time consuming, so the following table will show the approximations of some example sample sizes in comparison to the exact equilibrium to observe how the predictions change and to inform an initial choice in the next chapter.

Table 16, replicated from Table 6 in the previous chapter, gives the associated $\tilde{x}$ values of the 1DoF-T equilibria shown in Figure 30:

Table 16: $\tilde{x}$ values of equilibria identified in Figure 30b

Repulsive			Approximate $\tilde{x}$ value		
Equilibrium ID	γ/k^*	$\tilde{x}$ value at equilibrium	$\Delta\tilde{x}$=0.1	$\Delta\tilde{x}$=0.05	$\Delta\tilde{x}$=0.01
$\tilde{x}_{1b}$	1	2.0563	2.0563	2.0560	2.0560
$\tilde{x}_{2b}$	2	2.1028	2.1024	2.1024	2.1024
$\tilde{x}_{3b}$	5	2.2098	2.2100	2.2098	2.2097

It can be seen that the maximum deviation is within the tolerance given between the equilibrium locations predicted by $\Delta\tilde{x}$=0.05 and $\Delta\tilde{x}$=0.01, and therefore $\Delta\tilde{x}$=0.05 is an acceptable grid size. It can also be seen that the interpolation method converges to a slightly different solution than the graphical identification in Chapter 3, even though the grid size used in those graphs was finer than the one converged to in this section. That's because in the previous chapter, intersections between *two* discretized functions determined equilibrium, not where one discretized function crossed zero. Since plotting requires discretization of the function, and between each sample point the function is linearly interpolated, there's two sources of discretization error in the plots rather than the singular one here.

Because the stability values in the previous chapter are based off of the equilibria identified therein, the rest of this section will use those original equilibria and their static and dynamic stability assessments to validate the numerical approaches to be used in the next chapter rather than the new equilibria locations converged to in the table above. This still validates the methods for static and dynamic stability because those values were calculated explicitly for the equilibria in Chapter 3, and the numerical methods in this chapter can converge to the exact values of stiffness and potential energy, the former because it is just approximating the derivative at a point (which doesn't depend on it being an exact equilibrium, just a point with a smooth function), and the latter because the new approach for dynamic stability is described purely symbolically in this chapter. For this reason, in the 1DoF-R and 2DoF cases, the previous equilibrium locations are used without doing the above convergence analysis.

4.1.2. Static Stability Classification

1 DoF – Translational	1 DoF – Rotational	2 DoF – Rotational & Translational
Equilibrium Identification	Equilibrium Identification	Equilibrium Identification
Static Stability	Static Stability	Static Stability
Dynamic Stability	Dynamic Stability	Dynamic Stability

In the previous chapter, static stability of the 1DoF-T system was determined by examining the sign of the analytical derivative of the force at an equilibrium point. A negative force derivative (or positive stiffness) indicates static stability. In this section, the derivative of force will be taken numerically using finite differencing and compared to the analytical derivative to show that the two methods result in similar derivatives. There will be some error because the finite differencing approach (described below) relies on a finite number of samples to create a discrete solution of a derivative versus the exact, continuous solution as in the analytical case; however, the most important thing to validate is that the sign of the derivative is determined correctly each time, since the sign determines stability, not the exact value of the stiffness.

The finite difference approach is based on the "standard definition of the derivative in elementary calculus [51]," or

$$u'(x) = \lim_{\Delta x \to 0} \frac{u(x + \Delta x) - u(x)}{\Delta x}.$$

In a discrete numerical approximation of a function, the grid size is positive ($\Delta x > 0$), and therefore the "definition of the derivative in the continuum can be used to approximate the definition of the derivative in the discrete case [51]," using a "finite set of discrete points x_i where the function is known":

$$u'(x_i) \approx \frac{u(x_i + \Delta x) - u(x_i)}{\Delta x} = \frac{u_{i+1} - u_i}{\Delta x}.$$

The above approximation is "known as a forward Euler approximation since it uses forward differencing." Another approach uses central differencing to bracket the point where the derivative is of interest:

$$u'(x_i) \approx \frac{u(x_i + \Delta x) - u(x_i - \Delta x)}{2\Delta x} = \frac{u_{i+1} - u_{i-1}}{2\Delta x}.$$

The central difference method has a truncation error of $O(\Delta x^2)$, which is better than the truncation error of the forward (or backward) differencing methods (which have a truncation error of $O(\Delta x)$ [51]), and therefore that method is the one that will be used going forward, dependent on validation.

In this section, the function of interest is force at the location of an equilibrium $\tilde{x}_i = \tilde{x}_{eq}$; and therefore the finite difference approximation is given by

$$\left(\frac{d\tilde{F}_{2,rep,ND}}{d\tilde{x}}\right)_{\tilde{x}=\tilde{x}_{eq}} \approx \frac{\tilde{F}_{2,rep,ND}(\tilde{x}_{eq}+\Delta\tilde{x}) - \tilde{F}_{2,rep,ND}(\tilde{x}_{eq}-\Delta\tilde{x})}{2\Delta\tilde{x}}, \tag{4.4}$$

and stiffness at a given equilibrium is thus approximated by

$$\kappa_{tot,ND,num,T} = -\left(\frac{d\tilde{F}_{2,rep,ND}}{d\tilde{x}}\right)_{\tilde{x}=\tilde{x}_{eq}}. \tag{4.5}$$

Example Stability Calculations

From Section 3.3.3, the stiffness values of the equilibria in Table 16 as determined from Equation (3.36) are replicated below in Table 17, with an extra column for the finite difference calculation of the stiffness as given by Equation (4.5).

Since the derivative is only important around a handful of selected points rather than the full function, a very small $\Delta\tilde{x}$ can be selected without significantly increasing computational cost, though it is good practice to not increase the fidelity more than is necessary for the application. The particular value of the discretization size is selected by a grid refinement study, with a tolerance of ± 0.0001, such that the magnitude of the pointwise maximum change in the values of stiffness at each equilibrium point is ≤ 0.0001. The value of $\Delta\tilde{x}$ is selected by this method to be 0.01, and it can be seen from Table 17 that this mesh size also adequately approximates the "exact" stiffness $\kappa_{tot,ND}$ within an error tolerance of 0.0001. As such, the static stability and stiffness of the 1DoF-T equilibria can be approximated very well using a central finite difference approach.

Table 17: Non-dimensional stiffness values $\kappa_{tot,ND}$ at each equilibrium in Figure 30b, with statically stable equilibria bolded

Repulsive						
Equil. ID	γ/k^*	k^*	γ	$\tilde{x}$ value	$\kappa_{tot,ND}$	$\kappa_{tot,ND,num}$
$\tilde{x}_{1b}$	**1**	**1**	**1**	**2.0563**	**1.1088**	**1.1088**
$\tilde{x}_{2b}$	**2**	**1**	**2**	**2.1028**	**1.1946**	**1.1946**
$\tilde{x}_{3b}$	**5**	**1**	**5**	**2.2098**	**1.3795**	**1.3796**

4.1.3. Dynamic Stability

1 DoF – Translational	1 DoF – Rotational	2 DoF – Rotational & Translational
Equilibrium Identification	Equilibrium Identification	Equilibrium Identification
Static Stability	Static Stability	Static Stability
Dynamic Stability	Dynamic Stability	Dynamic Stability

In the previous chapter, dynamic stability of the 1DoF-T equilibria was determined by analytically calculating the potential energy as the spatial integral of the force. Going forward into more complex problems, having a formulation that depends less on having a simple analytical expression of force is advantageous. In the next chapter, the coils are no longer approximated as magnetic dipole moments but rather as loops of current. This section investigates a technique for calculating the potential energy of a system using the magnetic dipole vector potential and validates it against the analytical integration method. When the coils are no longer being approximated as dipole moments in the next chapter, the general magnetic vector potential will be used. The magnetic vector potential is a quantity that can be used to calculate a magnetic field and can be less cumbersome than the magnetic field representation, depending on the system.

Given that the currents in this problem are assumed constant, the laws of magnetostatics apply, including Gauss's law for magnetism, which says that the divergence of $\vec{B}$ is taken to be zero [49], or

$$\vec{\nabla} \cdot \vec{B} = 0. \tag{4.6}$$

As such, then the magnetic field $\vec{B}$ must be equivalent to the curl of a vector field $\vec{A}$, henceforth known as the magnetic vector potential:

$$\vec{B} = \vec{\nabla} \times \vec{A}. \tag{4.7}$$

It can be shown, by substituting this identity for $\vec{B}$ into Maxwell's equations, that "instead of solving Maxwell's equations for the magnetic field intensity and the electric field intensity we can solve for the magnetic vector potential and then obtain the magnetic and electric field intensities as well as flux densities from the magnetic vector potential [52]."

The magnetic vector potential $\vec{A}$ for a current carrying loop centered at the origin is calculated as

$$\vec{A}(\vec{x}) = \frac{\mu_0}{4\pi} \int \frac{\vec{J}(\vec{x}')}{|\vec{x} - \vec{x}'|} \, d^3x', \tag{4.8}$$

where $\vec{x}'$ is the coordinates of the current carrying element, and $\vec{x}$ is the coordinates of the point where the vector potential is being computed, with $\vec{J}(\vec{x}')$ the current density of the element at $\vec{x}'$. This formula, relevant simplifications, and its numerical implementation will be discussed in more detail in the next chapter when the magnets are modeled more realistically as current-carrying coils.

The magnetic *dipole* vector potential is given by Jackson as

$$\vec{A}_1(\vec{x}) = \frac{\mu_0}{4\pi}\frac{\vec{\mu}_1 \times \vec{x}}{|\vec{x}|^3}, \tag{4.9}$$

where $\vec{x}$ is the vector from the center of the magnetic dipole $\vec{\mu}_1$ to the point where the vector potential is being calculated.

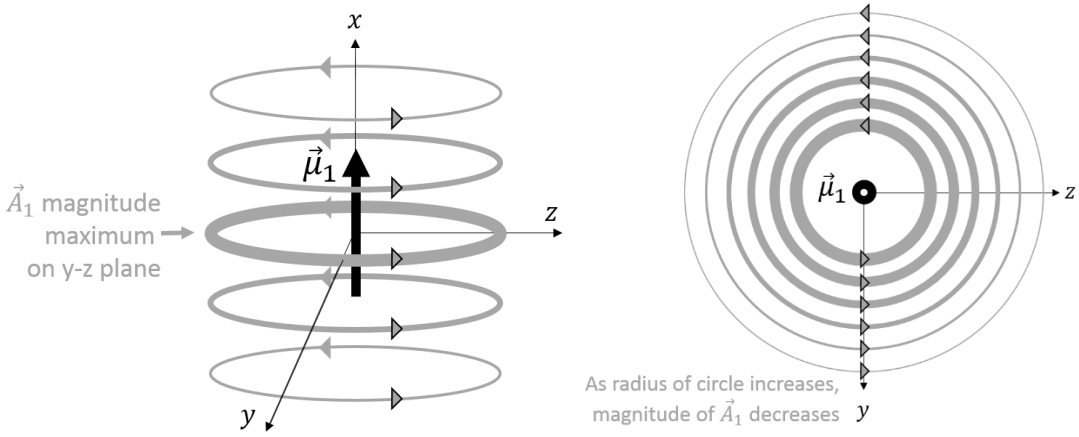

Figure 48: Magnetic dipole vector potential (a, left) from side and (b, right) from top, in the y-z plane

It can be seen from Equation (4.9) and the illustration in Figure 48a that the vector potential at point $\vec{x}$ is directed azimuthal to the dipole moment if viewed from the top, as in Figure 48b. The magnitude of the vector potential decreases in the x,y, and z directions if the dipole is positioned at the origin, but at all places, the direction remains azimuthal to the direction of the magnetic dipole. The vector potential of a current carrying circular coil also is oriented in a direction azimuthal to the normal of the coil. At any point off of the axis of magnet 1, the magnetic dipole vector potential can be calculated from Equation (4.9). Since magnet 2 is indeed positioned along the axis of magnet 1, the cross product $\vec{\mu}_1 \times \vec{x} = 0$. However, if the objective is to calculate $\vec{B}_1$ using $\vec{A}_1$, if Equation (4.9) is inserted into Equation (4.7), it can be seen that [53]:

$$\vec{B}_1 = \vec{\nabla} \times \vec{A}_1 = \frac{\mu_0}{4\pi}\left[\vec{\nabla} \times \frac{\vec{\mu}_1 \times \vec{x}}{|\vec{x}|^3}\right] \tag{4.10}$$

$$= \frac{\mu_0}{4\pi}\left[\vec{\mu}_1\left(\vec{\nabla}\cdot\frac{\vec{x}}{|\vec{x}|^3}\right) - (\vec{\mu}_1\cdot\vec{\nabla})\left(\frac{\vec{x}}{|\vec{x}|^3}\right)\right] = \frac{\mu_0}{4\pi|\vec{x}|^3}\left[\frac{3(\vec{\mu}_1\cdot\vec{x})\vec{x}}{|\vec{x}|^2} - \vec{\mu}_1\right].$$

The above formulation is identical to that of Equation (3.1) and is in fact how the earlier equation was derived. So, as long as the vector potential is used to calculate $\vec{B}$, it can be used for axially aligned dipoles such as the system under study. Along the axis of a dipole, this formula simplifies to

$$\vec{B}_1 = \frac{\mu_0\mu_1}{2\pi|\vec{x}|^3}.$$

The magnetic energy of a dipole moment in an external magnetic field (in this case taken to be the dipole moment of magnet 2 in the magnetic field created by magnet 1) is given by Jackson [49] as

$$W_{1DoF,T} = \frac{1}{2}\int_{V_1} \overrightarrow{M_2}\cdot\overrightarrow{B_1}\,dxdydz, \tag{4.11}$$

where $\vec{M}_2$ is the magnetization of the dipole (defined as the dipole per unit volume of the magnet), and $\vec{B}_1$ is the initial magnetic field at the point before the dipole is placed there, which in this case is the magnetic field created by magnet 1. The volume integral of the magnetization of dipole 1 is actually equivalent to the magnetic moment $\vec{\mu}_2$:

$$\vec{\mu}_2 = \int_{V_2} \vec{M}_2\,dxdydz,$$

such that

$$W_{1DoF,T} = \frac{1}{2}\int_{V_2} \vec{M}_2\cdot\vec{B}_1\,dxdydz = \frac{B_1(\vec{x})\mu_2\cos\theta_m}{2} = \frac{\mu_0\mu_1\mu_2\cos\theta_m}{4\pi x^3}. \tag{4.12}$$

Comparing $W_{1DoF,T}$ to the magnetic part of $P_{rep,T}$ from Equation (3.46) and inserting $\theta_m = 0$, where θ_m is the angle between the magnetic moment and the external field,

$$P_{rep,mag,T} = \frac{\mu_0\mu_1\mu_2}{2\pi x^3} = 2W_{1DoF,T}.$$

The reason $W_{1DoF,T}$ needs to be multiplied by 2 to match the potential energy derived from the integral of force is that $W_{1DoF,T}$ only calculates the energy associated with magnet 2 in the magnetic field of

magnet 1 and not the energy associated with magnet 1 being in the field of magnet 2. Therefore, $W_{1DoF,T}$ needs to be doubled to account for the total magnetic energy due to the interaction of the magnets.

In order to obtain the non-dimensional $\widetilde{W}_{1DoF,T}$ formulation, it is noted that 1 Joule is equivalent to 1 $N \cdot m$ or 1 $\frac{kg \cdot m^2}{s^2}$, and therefore the dimensionless variables in Table 4 can be used to create a scaling term in $\frac{s^2}{kg \cdot m^2}$ that will non-dimensionalize $W_{1DoF,T}$:

$$\frac{\mathcal{T}^2}{m_2 R_1^2}.$$

Multiplying both sides of Equation (4.12) by this scaling term, expanding μ_1, μ_2 and m_2, and using the non-dimensional distance and radius definitions $\tilde{x}$ and $\widetilde{R}_2$, gives the following comparison to the magnetic portion of $\widetilde{P}_{rep,T}$ from Equation (3.48) when $\theta_m = 0$:

$$\begin{aligned} \widetilde{W}_{1DoF,T} = W_{1DoF,T}\left(\frac{\mathcal{T}^2}{m_2 R_1^2}\right) = \frac{\mu_0 \mu_1 \mu_2 \cos\theta_m \mathcal{T}^2}{4\pi x^3 m_2 R_1^2} = \frac{\mu_0 N I^2 \tilde{R}_2 \cos\theta_m \mathcal{T}^2}{8\tilde{x}^3 R_1^2 \rho} = \frac{\gamma \cos\theta_m}{6\tilde{R}_1^2 \tilde{x}^3} \\ = \frac{\tilde{P}_{rep,mag,T}}{2\tilde{R}_1^2}. \end{aligned} \tag{4.13}$$

Since $\tilde{R}_1 = 1$, $\widetilde{W}_{1DoF,T} = (1/2)\, \tilde{P}_{rep,mag,T}$ in the same way that $W_{1DoF,T} = (1/2)\, P_{rep,mag,T}$. Therefore, the magnetic vector potential approach is a valid way to calculate the magnetic potential energy that results from the interaction between two magnets. The formulas for W and $\vec{A}_1(\vec{x})$ change slightly in the next chapter with coils instead of dipole moments (and require the vector potential and not just the magnetic field, which is why the vector potential has been introduced here), but the general approach is physically valid. The potential energy due to the linear spring force can then be added and does not require a different approach to calculate.

Because this approach analytically agrees with that of the previous chapter, the potential energies and critical initial kinetic energies won't be recalculated here.

4.1.4. Summary

In this section, it was shown that for the 1DoF-T case, the stiffness can be determined in a straightforward manner via centered finite differencing and that the magnetic vector potential can also be used to calculate the magnetic potential energy of two interacting magnets. In the next section, efforts will be made to draw the same conclusions for the 1DoF-R by again validating these approaches with the results of Chapter 3.

4.2. Rotational Single Degree of Freedom

1 DoF – Translational	1 DoF – Rotational	2 DoF – Rotational & Translational
Equilibrium Identification	Equilibrium Identification	Equilibrium Identification
Static Stability	Static Stability	Static Stability
Dynamic Stability	Dynamic Stability	Dynamic Stability

The 1DoF-R magnetic structure from Figure 34 is replicated below in Figure 49:

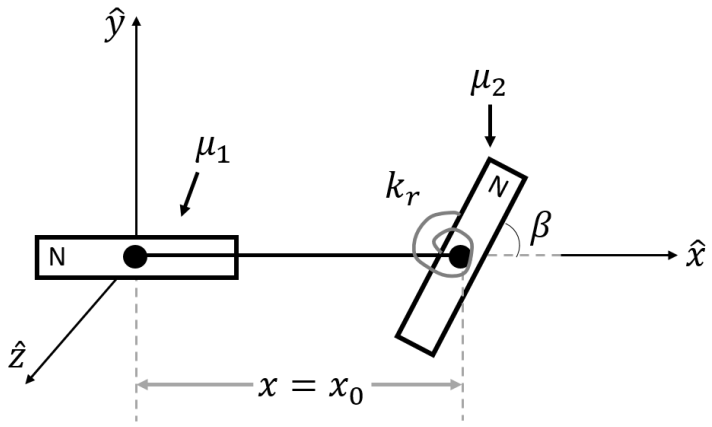

Figure 49: Rotational single degree of freedom (1DoF-T) dipole system

The torque balance is therefore the same as that given by Equation (3.67), or

$$\tilde{\vec{\tau}}_{2,rep,ND} = \left(\frac{\gamma}{3\tilde{x}_0{}^3}\sin\beta - k_r^*\,\beta\right)\hat{k}. \tag{4.14}$$

4.2.1. Equilibrium Identification

1 DoF – Translational	1 DoF – Rotational	2 DoF – Rotational & Translational
Equilibrium Identification	Equilibrium Identification	Equilibrium Identification
Static Stability	Static Stability	Static Stability
Dynamic Stability	Dynamic Stability	Dynamic Stability

As in Section 3.4.2, equilibrium occurs when the torque balance equals zero, or

$$\frac{\gamma}{k_r^*} = \frac{3\tilde{x}_0{}^3\beta}{\sin\beta}. \tag{4.15}$$

Table 18, replicated from Table 10 in the previous chapter, gives the associated β values of the ND 1DoF-R equilibria shown in Figure 37 (and those that occur at $\beta = 0$):

Table 18: β values for non-dimensional equilibria identified in Figure 37

Repulsive		
Equilibrium ID	$\frac{\gamma}{k_r^*}$	β value at eq. (radians)
$\beta_{1b,ND}$	35	-1.4472
$\beta_{2b,ND}$	30	-1.1311
$\beta_{3b,ND}$	25	-0.4929
$\beta_{0b,ND-1}$	35	0
$\beta_{0b,ND-2}$	30	0
$\beta_{0b,ND-3}$	25	0
$\beta_{4b,ND}$	35	1.4472
$\beta_{5b,ND}$	30	1.1311
$\beta_{6b,ND}$	25	0.4929

The stability of these identified equilibria, both static and dynamic, will be explored numerically in the rest of this section.

4.2.2. Static Stability Classification

1 DoF – Translational	1 DoF – Rotational	2 DoF – Rotational & Translational
Equilibrium Identification	Equilibrium Identification	Equilibrium Identification
Static Stability	Static Stability	Static Stability
Dynamic Stability	Dynamic Stability	Dynamic Stability

In this section, static stability will be approached using finite differencing of the torque on magnet 2, similar to how finite differencing was performed on the force in the 1DoF-T case in Section 4.1.2. As such, Equation (4.4) with torque as the function being approximated is

$$\frac{d\tilde{\vec{\tau}}_{2,rep,ND}}{d\beta_{eq}} \approx \frac{\tilde{\vec{\tau}}_{2,rep,ND}(\beta_{eq}+\Delta\beta)-\tilde{\vec{\tau}}_{2,rep,ND}(\beta_{eq}-\Delta\beta)}{2\Delta\beta}, \tag{4.16}$$

and rotational stiffness is thus approximated by

$$\kappa_{tot,ND,num,R} = -\frac{d\tilde{\vec{\tau}}_{2,rep,ND}}{d\beta_{eq}}. \tag{4.17}$$

4.2.2.1. Example Stability Calculations

The rotational stiffness values of the repulsive equilibria in Table 12 as determined by Equation (3.78) are replicated below in Table 19, with an extra column for the finite difference calculation of the stiffness as given by Equation (4.17).

Similar to the selection of $\Delta\tilde{x}$, $\Delta\beta$ can be made very small without seriously increasing computational cost because the derivative of torque is only being taken at a handful of points from the exact solution for torque. Using the same approach of a grid refinement study with a maximum pointwise change tolerance of $\pm 0.0001, \Delta\beta$ is selected to be 0.02. The selection of step size will be more important computationally in the next chapter, wherein the step size is used to discretize the translational or the rotational variable over a range and will thus affect the calculation of equilibrium as well as both static and dynamic stability (as was already seen in Section 4.1.2.)

Table 19: Non-dimensional rotational stiffness values $\kappa_{tot,ND}$ at each ND equilibrium in Figure 37, with statically stable equilibria bolded

Repulsive						
Equil. ID	$\frac{\gamma}{k_r^*}$	k_r^*	γ	β value at eq. (radians)	$\kappa_{tot,ND}$	$\kappa_{tot,num}$
$\boldsymbol{\beta_{1b,ND}}$	**35**	**1**	**35**	**-1.4472**	**0.8202**	**0.8202**
$\boldsymbol{\beta_{2b,ND}}$	**30**	**1**	**30**	**-1.1311**	**0.4679**	**0.4680**
$\boldsymbol{\beta_{3b,ND}}$	**25**	**1**	**25**	**-0.4929**	**0.0823**	**0.0824**
$\beta_{0b,ND-1}$	35	1	35	0	-0.4583	-0.4582
$\beta_{0b,ND-2}$	30	1	30	0	-0.2500	-0.2499
$\beta_{0b,ND-3}$	25	1	25	0	-0.0417	-0.0416
$\boldsymbol{\beta_{4b,ND}}$	**35**	**1**	**35**	**1.4472**	**0.8202**	**0.8202**
$\boldsymbol{\beta_{5b,ND}}$	**30**	**1**	**30**	**1.1311**	**0.4679**	**0.4680**
$\boldsymbol{\beta_{6b,ND}}$	**25**	**1**	**25**	**0.4929**	**0.0823**	**0.0824**

From Table 19, it can be seen that the numerical stiffness calculation is identical to the exact stiffness value, so centered finite differencing continues to be an acceptable numerical approach for calculating static stability.

4.2.3. Dynamic Stability

1 DoF – Translational	1 DoF – Rotational	2 DoF – Rotational & Translational
Equilibrium Identification	Equilibrium Identification	Equilibrium Identification
Static Stability	Static Stability	Static Stability
Dynamic Stability	Dynamic Stability	Dynamic Stability

It was shown in Section 4.1.3 that the magnetic vector potential can be used to calculate the potential energy of the interaction of two magnetic dipoles. Equation (4.12) and Equation (4.13) for the calculation of W and $\widetilde{W}$ respectively can be used for the 1DoF-R case as well as the previous 1DoF-T case (and the combination of the two in the 2DoF case), except $\theta_m = \beta$ rather than 0 and $x = x_0$ in the 1DoF-R case, such that

$$W_{1DoF,R} = \frac{\mu_0 \mu_1 \mu_2 \cos\beta}{4\pi x_0^3} = \frac{P_{rep,mag,R}}{2}, \tag{4.18}$$

and

$$\widetilde{W}_{1DoF,R} = \frac{\mu_0 N I^2 \tilde{R}_2 \cos\theta_m \mathcal{T}^2}{8{\tilde{x}_0}^3 R_1^2 \rho} = \frac{\gamma \cos\beta}{6\tilde{R}_1^2 {\tilde{x}_0}^3} = \frac{\tilde{P}_{rep,mag,R}}{2\tilde{R}_1^2}, \tag{4.19}$$

and the magnetic vector potential approach to potential energy calculation is validated for the 1DoF-R case as well, with the note made that, again, $W_{1DoF,R}$ and $\widetilde{W}_{1DoF,R}$ are one half their respective P values because the vector potential approach only calculates the energy of one magnet in the other's magnetic field and not vice-versa. The potential energy due to the spring torque can then be added and does not require a different approach to calculate.

4.2.4. Summary

In this section, it was shown that for the 1DoF-R case, the stiffness can also be determined in a straightforward manner via centered finite differencing and that the magnetic vector potential is a valid means of calculating the magnetic potential energy of two interacting magnets with a single rotational degree of freedom. In the next and final section of this chapter, efforts will be made to draw the same conclusions for the 2DoF system by again validating these approaches with the results of Chapter 3.

4.3. Two Degrees of Freedom

1 DoF – Translational	1 DoF – Rotational	2 DoF – Rotational & Translational
Equilibrium Identification	Equilibrium Identification	Equilibrium Identification
Static Stability	Static Stability	Static Stability
Dynamic Stability	Dynamic Stability	Dynamic Stability

The 2DoF magnetic structure from Figure 42 is replicated below in Figure 50:

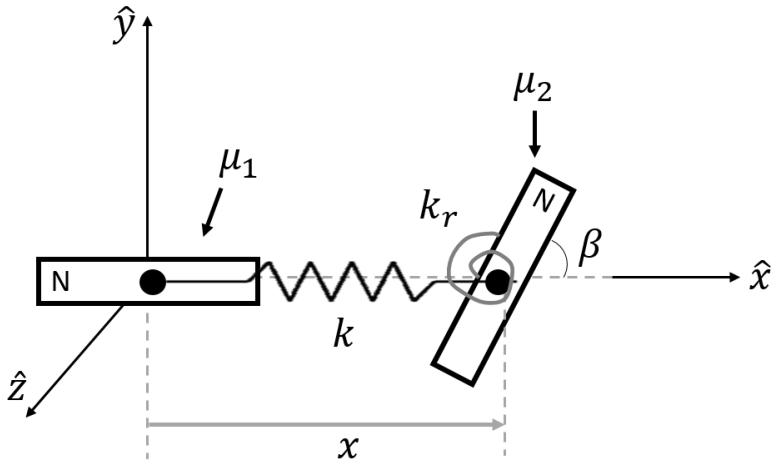

Figure 50: 2DoF (translational and rotational) system

The force and torque balances that need to be fulfilled are therefore the same as that given by Equations (3.94), or

$$\tilde{\vec{F}}_{2,rep,ND} = \left(\frac{\gamma}{\tilde{x}^4}\cos\beta - k^*(\tilde{x} - \tilde{x}_0)\right)\hat{\imath}, \tag{4.20a}$$

and

$$\tilde{\vec{\tau}}_{2,rep,ND} = \left(\frac{\gamma}{3\tilde{x}^3}\sin\beta - k_r^*\,\beta\right)\hat{k}. \tag{4.20b}$$

4.3.1. Equilibrium Identification

1 DoF – Translational	1 DoF – Rotational	2 DoF – Rotational & Translational
Equilibrium Identification	Equilibrium Identification	Equilibrium Identification
Static Stability	Static Stability	Static Stability
Dynamic Stability	Dynamic Stability	Dynamic Stability

As described and explored in Section 3.5.2, equilibrium in both translational and rotational coordinates occurs when both the force and torque balance are zero, which occurs when

$$\tilde{x}^3 = \frac{\gamma}{3k_r^*}\frac{sin\,\beta}{\beta},$$

and

$$\frac{\gamma}{\left(\frac{\gamma}{3k_r^*}\frac{sin\,\beta}{\beta}\right)^{4/3}}\cos\beta = k^*\left(\left(\frac{\gamma}{3k_r^*}\frac{sin\,\beta}{\beta}\right)^{\frac{1}{3}} - \tilde{x}_0\right). \tag{4.21}$$

Table 20, replicated from Table 13 in the previous chapter, gives the associated β and $\tilde{x}$ values of the 2DoF equilibria shown in Figure 43 (and those that occur at $\beta = 0$):

Table 20: β and $\tilde{x}$ values for equilibria in Figure 43 as well as the equilibria at $\beta = 0$

- β				+ β				0			
Equil. ID	γ values	β	$\tilde{x}$	Equil. ID	γ values	β	$\tilde{x}$	Equil. ID	γ values	β	$\tilde{x}$
$\beta_{1,-}$	10	-	-	$\beta_{1,+}$	10	-	-	$\beta_{1,0}$	10	0	2.338
$\beta_{2,-}$	20	-1.445	2.1243	$\beta_{2,+}$	20	1.445	2.1243	$\beta_{2,0}$	20	0	2.508
$\beta_{3,-}$	50	-	-	$\beta_{3,+}$	50	-	-	$\beta_{3,0}$	50	0	2.809

The stability of these identified equilibria, both static and dynamic, will be explored numerically in the rest of this section.

4.3.2. Static Stability Classification

1 DoF – Translational	1 DoF – Rotational	2 DoF – Rotational & Translational
Equilibrium Identification	Equilibrium Identification	Equilibrium Identification
Static Stability	Static Stability	Static Stability
Dynamic Stability	Dynamic Stability	Dynamic Stability

In this section, static stability needs to be calculated in two different coordinates, and therefore not one but four finite differences need to be taken in order to fill out the stiffness matrix such that the numerical approximation of Equation (3.102) becomes

$$\left[K_{tot,ND,num}\right] = -\begin{bmatrix} \dfrac{\widetilde{F}_{2,rep,ND}(\tilde{x}_i+\Delta\tilde{x})-\widetilde{F}_{2,rep,ND}(\tilde{x}_i-\Delta\tilde{x})}{2\Delta\tilde{x}} & \dfrac{\widetilde{F}_{2,rep,ND}(\beta_i+\Delta\beta)-\widetilde{F}_{2,rep,ND}(\beta_i-\Delta\beta)}{2\Delta\beta} \\ \dfrac{\tilde{\tau}_{2,rep,ND}(\tilde{x}_i+\Delta\tilde{x})-\tilde{\tau}_{2,rep,ND}(\tilde{x}_i-\Delta\tilde{x})}{2\Delta\tilde{x}} & \dfrac{\tilde{\tau}_{2,rep,ND}(\beta_i+\Delta\beta)-\tilde{\tau}_{2,rep,ND}(\beta_i-\Delta\beta)}{2\Delta\beta} \end{bmatrix}. \quad (4.22)$$

The eigenvalues of $\left[K_{tot,ND,num}\right]$ can then be calculated at each equilibrium $\beta_i, \tilde{x}_i$ in Table 20 and their signs evaluated to determine the static stability.

4.3.2.1. Example Stability Calculations

The eigenvalues of the repulsive 2DoF equilibria from Table 14 as determined by Equation (3.104) are replicated below in Table 21, with extra columns for the numerical calculations of the eigenvalues via the finite difference stiffness matrix as given by Equation (4.22). From the grid refinement approach discussed previously, (keeping $\Delta\tilde{x}$ and $\Delta\beta$ the same size for simplicity), a mesh size of $\Delta\tilde{x} = \Delta\beta = 0.001$ was selected such that the change in eigenvalue solution from the previous mesh size was within the tolerance of ± 0.0001. This mesh size is roughly an order of magnitude smaller than the 1DoF mesh sizes, likely both because four different derivatives are being approximated instead of just one and because in this problem the eigenvalues are the desired solution and not just the individual stiffness values, and eigenvalues involve an extra layer of operations on the base derivative approximations that could amplify a small error.

Table 21: 2DoF stiffness matrix eigenvalues $\lambda_{1,2}$ and numerically calculated eigenvalues $\lambda_{1,2_{num}}$ at each equilibrium in Figure 44, with statically stable equilibria bolded

- β							
Equil. ID	γ	β	$\tilde{x}$	λ_1	λ_2	$\lambda_{1_{num}}$	$\lambda_{2_{num}}$
$\beta_{1,-}$	10	-	-	-	-	-	-
$\beta_{2,-}$	20	-1.445	2.1243	1.8725	-0.2502	1.8725	-0.2502
$\beta_{3,-}$	50	-	-	-	-	-	-
+ β							
Equil. ID	γ	β	$\tilde{x}$	λ_1	λ_2	λ_1	λ_2
$\beta_{1,+}$	10	-	-	-	-	-	-
$\beta_{2,+}$	20	1.445	2.1243	1.8725	-0.2502	1.8725	-0.2502
$\beta_{3,+}$	50	-	-	-	-	-	-
β = 0							
Equil. ID	γ	β	$\tilde{x}$	λ_1	λ_2	λ_1	λ_2
$\beta_{1,0}$	**10**	**0**	**2.338**	**1.5726**	**0.2167**	**1.5726**	**0.2167**
$\beta_{2,0}$	**20**	**0**	**2.508**	**1.8062**	**0.0549**	**1.8062**	**0.0549**
$\beta_{3,0}$	50	0	2.809	2.1436	-0.2745	2.1436	-0.2745

It can be seen from Table 21 that the finite differencing approach also obtains good estimates of the exact solution, within an error tolerance of ± 0.0001.

4.3.3. Dynamic Stability

1 DoF – Translational	1 DoF – Rotational	2 DoF – Rotational & Translational
Equilibrium Identification	Equilibrium Identification	Equilibrium Identification
Static Stability	Static Stability	Static Stability
Dynamic Stability	Dynamic Stability	Dynamic Stability

As shown in Section 3.5, the 2DoF magnetic potential energy can be calculated either from the magnetic torque or the magnetic force between dipoles and is thus the most general case of the three studied in this and the previous chapter. The 2DoF magnetic potential energy is identical to the 1DoF-T magnetic potential energy when $\cos\beta$ hasn't been cancelled out or the 1DoF-R magnetic potential energy when $\tilde{x}_0$ is replaced with the more general $\tilde{x}$, such that

$$W_{2DoF} = \frac{\mu_0\mu_1\mu_2\cos\beta}{4\pi x^3} = \frac{P_{rep,mag,2DoF}}{2}, \tag{4.23}$$

and

$$\widetilde{W}_{2DoF} = \frac{\mu_0 N I^2 \tilde{R}_2 \cos\theta_m \mathcal{T}^2}{8\tilde{x}^3 R_1^2 \rho} = \frac{\gamma\cos\beta}{6\tilde{R}_1^2\tilde{x}^3} = \frac{\tilde{P}_{rep,mag,2DoF}}{2\tilde{R}_1^2}. \tag{4.24}$$

Again, $\tilde{R}_1 = 1$, so the 2DoF magnetic vector potential approach also gives half that of the analytical approach, just like for the 1DoF-T and 1DoF-R cases and can thus be used going forward into more complex models.

4.3.4. Summary

In this chapter, it was shown that the magnetic stiffness can be numerically approximated very well using a centered finite difference approach, providing a technique for evaluating static stability in systems without analytical solutions, such as that which will be introduced and used in the next chapter. It was also shown that the magnetic potential energy can be calculated by using the magnetic vector potential, a useful approach for determining the dynamic stability of equilibria when the magnetic field formulation is not as clean and simple as that for the dipole model.

Chapter 5
Complex Numerical Stability

While Chapter 3 provided symbolic context for the concepts of static and dynamic stability in a simple magnetic system, Chapter 0 introduced and validated an approach for numerically identifying equilibria in three distinct systems as well as for evaluating static and dynamic stability of those equilibria. The numerical approach can be used upon either the simple magnetic system of Chapter 3, against which it was validated, or upon the more complex magnetic system that is introduced and explored in this chapter that uses current-carrying coils instead of magnetic dipoles. As in the previous two chapters, the 1DoF-T, 1DoF-R, and 2DoF systems are each assessed non-dimensionally as per the methods listed for each of equilibrium identification, static stability, and dynamic stability in Figure 51.

	3. Analytical	4. Simple Numerical	5. Complex Numerical
Equilibrium Identification	Dipole force/torque balance equations	Dipole force/torque balance equations	Coil numerical force/torque balance
Static Stability	Dipole force/torque analytical derivatives and linearized eigenvalues	Finite difference stiffness matrix	Finite difference stiffness matrix
Dynamic Stability	Analytical formulation of potential energy	Numerical vector potential calculation of potential energy	Numerical vector potential calculation of potential energy

1 DoF – Translational	1 DoF – Rotational	2 DoF – Rotational & Translational
Equilibrium Identification	Equilibrium Identification	Equilibrium Identification
Static Stability	Static Stability	Static Stability
Dynamic Stability	Dynamic Stability	Dynamic Stability

Figure 51: Three analytical systems to be studied in this chapter

This chapter's system and results are more applicable to an actual magneto-elastic structure than Chapters 3 and 0, but they involve more approximation and numerical computation. The previous two chapters are intended to support the results of the analyses in this chapter, which in turn will support the evaluation of increasingly applicable "real-world problems" with more degrees of freedom or more magnetic bodies.

5.1. Biot-Savart and Vector Potential Models

Section 2.1 briefly introduced the Biot-Savart law, which provides a means of calculating the magnetic field at any point in space around a current-carrying wire. The Biot-Savart law is replicated below:

$$\vec{B}(\vec{r}) = \frac{\mu_0}{4\pi}\int_{coil}\frac{I\overrightarrow{dl}\times\overrightarrow{r'}}{\left|\overrightarrow{r'}\right|^3}, \tag{5.1}$$

where $\overrightarrow{dl}$ is the length of the infinitesimally small differential element around the coil in the direction of the current I, and $\overrightarrow{r'}$ is the vector from the center of the differential element to the point where $\vec{B}$ is being calculated. Coil 1 is assumed to be centered at the origin and lying flat in the x-y plane, whereas coil 2 is placed some distance from coil 1 along the x axis, as in Figure 52 in the next section.

The integration in Equation (5.1) is around the circumference of the coil to sum the contributions to the magnetic field from each individual differential element around the coil. This magnetic field formulation can be compared to the dipole magnetic field formulation of Equation (3.1), and it can be seen that while the dipole model is a single calculation to achieve the relevant magnetic field value, the Biot-Savart model requires integration around the circumference of the coil, which entails as many calculations as there are differential elements.

However, using the knowledge from Section 4.1.3 that the magnetic field is derivable from the magnetic vector potential resulting from a magnet or coil, it's possible to obtain a closed-form solution using the complete elliptic integrals $E(k^2)$ and $K(k^2)$ that allows a single calculation of the magnetic field at a point resulting from the contributions of the entire coil of radius a.

The discussion and calculation of the magnetic vector potential $\vec{A}$ will be saved for the potential energy discussion in Section 5.3.4, but Simpson et al. [54] give the magnetic field components in Cartesian coordinates as

$$B_x = \frac{C_0 xz}{2\alpha^2\eta\upsilon^2}[(a^2+r^2)E(k^2)-\alpha^2K(k^2)],$$

$$B_y = \frac{C_0 yz}{2\alpha^2\eta\upsilon^2}[(a^2+r^2)E(k^2)-\alpha^2K(k^2)] = \frac{y}{x}B_x, \tag{5.2}$$

and

$$B_z = \frac{C_0}{2\alpha^2\eta}[(a^2 - r^2)E(k^2) + \alpha^2 K(k^2)],$$

where

$$v^2 = x^2 + y^2,$$
$$r^2 = x^2 + y^2 + z^2,$$
$$\alpha^2 = a^2 + r^2 - 2av,$$
$$\eta^2 = a^2 + r^2 + 2av,$$
$$k^2 = 1 - \frac{\alpha^2}{\eta^2},$$

and

$$C_0 = \frac{\mu_0 NI}{\pi}.$$

The magnetic field at a point of interest at a vector $\vec{r}$ away from the coil can therefore be calculated using

$$\vec{B} = B_x\hat{\imath} + B_y\hat{\jmath} + B_z\hat{k}.$$

Since our system places the coil flat in the y-z plane rather than the x-y plane, some of the definitions change, such that

$$v^2 = y^2 + z^2,$$

and Equation (5.2) becomes

$$B_x = \frac{C_0}{2\alpha^2\eta}[(a^2 - r^2)E(k^2) + \alpha^2 K(k^2)],$$

$$B_y = \frac{C_0 xy}{2\alpha^2\eta v^2}[(a^2 + r^2)E(k^2) - \alpha^2 K(k^2)], \tag{5.3}$$

and

$$B_z = \frac{C_0 xz}{2\alpha^2\eta v^2}[(a^2 + r^2)E(k^2) - \alpha^2 K(k^2)] = \frac{z}{y}B_y.$$

The next step is to determine the forces and torques as a result of the interaction between coil 2 and the magnetic field from coil 1. While the magnetic field formulation has a closed form solution, an integration is still required around the circumference of coil 2. This is because the magnetic force on coil 2 is calculated via the Laplace force, or

$$\vec{F}_{2,mag,coil} = I_2 N_2 \int_{coil\ 2} d\vec{l}_2 \times \vec{B}_1. \tag{5.4}$$

The Laplace force is calculated upon every differential element $d\vec{l}_2$ and then summed to obtain the resultant net force vector on coil 2. The torque upon coil 2 in the presence of the magnetic field of coil 2 is also calculated using the individual differential force vectors on each element by taking the cross product of the forces with the vector $\vec{R}_2$ from the center of the coil to the element in question, or

$$\vec{\tau}_{2,mag,coil} = I_2 N_2 \int_{coil\ 2} \vec{R}_2 \times \left(d\vec{l}_2 \times \vec{B}_1\right). \tag{5.5}$$

As discussed in Section 3.1, the Biot-Savart model as calculated by Equation (5.1) is closely approximated by the dipole model in the far-field. In order to ensure that the dipole model in the far-field also closely approximates the closed form solution in Equation (5.3), the two calculations of $\vec{B}$ from Equations (5.1) and (5.2) are compared to make sure they agree. Each of the aforementioned equations are used to calculate the resultant force on coil 2 when the coils are parallel ($\beta = 0$), and the results are shown in Table 22. The forces are purely in the x direction when the coils are parallel, so the values in the table are the scalar magnitudes of $\vec{F}_{2,mag,coil,x}$.

Table 22: Magnitude of magnetic force $\vec{F}_{2,mag,coil,x}$ as determined by Equations (5.1) and (5.2) and the difference $\Delta\vec{F}_{2,mag,coil,x}$ between the calculations

$\tilde{x}$	$\vec{F}_{2,mag,coil,x}$ from (5.1)	$\vec{F}_{2,mag,coil,x}$ from (5.2)	$\Delta\vec{F}_{2,mag,coil,x}$
1	51.1928	50.7891	0.4037
2	12.2087	12.1124	0.0963
3	3.8852	3.8546	0.0306
4	1.5232	1.5112	0.0120

Because the two force calculations agree within a small margin of error that is attributable to the discretization in Equation (5.1), the magnetic field equations from (5.1) and (5.3) therefore agree, which makes the previous validation against the dipole model extend to the new formulation of magnetic field. The error is higher the closer together the coils are, an effect which is described further in Section 5.3. Since Equation (5.3) has a smaller computational cost, it will be used going forward in this chapter.

5.2. Coil Boom Design and Assumptions

The largest difference between the system studied in this chapter and the one studied in Chapters 3 and 0 is that the system in this chapter models the magnets as coils rather than magnetic dipoles or bar magnets. Figure 52 shows the general two-dimensional coil system being analyzed in this chapter. The magnets are connected as in the dipole system by a linear spring of spring constant k attached at the center of each magnet and a torsional spring of spring constant k_r that provides resistance around the z axis. R_1 and R_2 are the radii of the coils, and I_1 and I_2 are the currents through a single turn of the coil (multiplied by N_1 or N_2 respectively gives the effective current in the coil), the associated arrows showing the direction of the current. It can be seen when compared to the general dipole model that the right hand rule with the currents shown in Figure 52 gives magnetic moments pointing in the same direction as the north pole on the bar magnets.

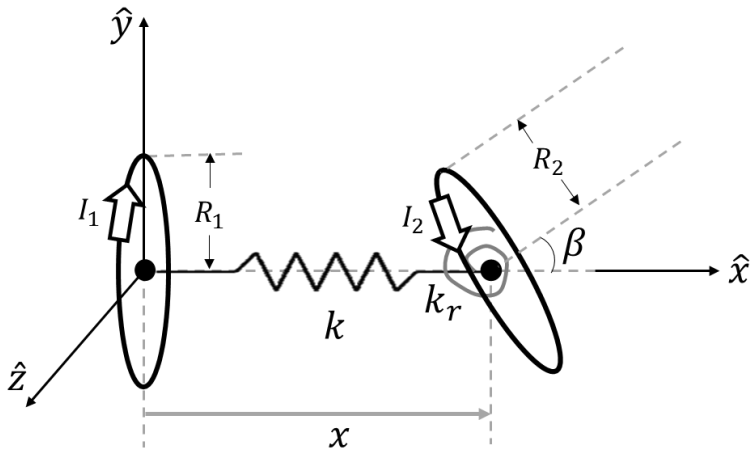

Figure 52: General coil system with two degrees of freedom

As in Chapters 3 and 0, Δx and β represent displacement in the two degrees of freedom that are permitted in this chapter – translation along the x axis and rotation about the z axis. Translation is studied first, followed by rotation and then the combination of translation and rotation. All of the same assumptions as in Section 3.2 apply in this system: coil 1 remains fixed at the origin of the inertial reference frame in all degrees of freedom, and no external forces or torques are acting on the system. The primary difference in this chapter is the magnetic forces and torques. In this chapter, for simplicity, only the repulsive, non-dimensional case is considered.

5.3. Translational Single Degree of Freedom

1 DoF – Translational	1 DoF – Rotational	2 DoF – Rotational & Translational
Equilibrium Identification	Equilibrium Identification	Equilibrium Identification
Static Stability	Static Stability	Static Stability
Dynamic Stability	Dynamic Stability	Dynamic Stability

In this section, the coil-based single translational degree of freedom (or 1DoF-T) system is studied. The system is depicted in Figure 53.

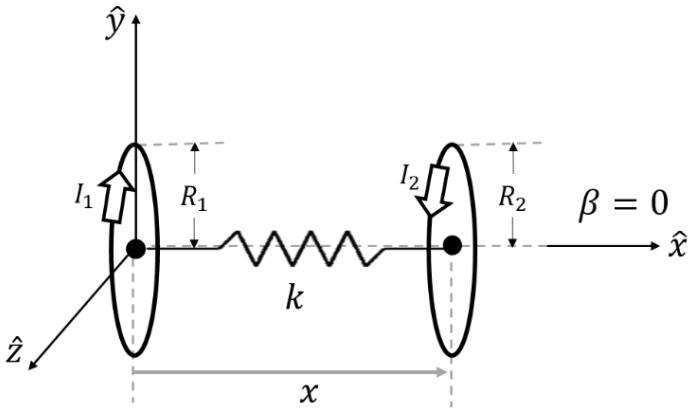

Figure 53: Translational single degree of freedom (1DoF-T) coil system

The number of segments that the coil perimeter will be discretized into is based on Figure 2-3 in Buck [55], which shows the change in vector norm of the magnetic force and torque as the discretization increases from n to n+1 segments, assuming that the number of segments is kept the same across both coils. From those plots, it can be seen that unless the coils are operating in the extreme near-field (<1 radius apart), the error decreases very little for segments beyond 50, both when the coils are in an axial configuration ($\beta = 0$) and when they are in the shear configuration ($\beta = \pm\pi/2$). The shear case is more limiting (higher change in vector norm for the same number of segments), and the error does not decrease much with added segments in the extreme near-field; therefore, 50 segments are selected as a relatively conservative discretization. This is the same number of segments used in the validation in Section 5.1.

5.3.1. Force Balance

The force balance is less simple to write analytically with the more complex coil-based system. The non-dimensional force provided by the spring is still

$$\tilde{\vec{F}}_{spring} = -k^*(\tilde{x} - \tilde{x}_0)\hat{\imath},$$

but the magnetic force can only effectively be written as a cross product, with Equation (5.3) inserted into Equation (5.4), with the assumption that coil 1 and coil 2 have the same number of turns N and current $|I_1| = |I_2| = I$ and the realization that $a = R_1$,

$$\vec{F}_{2,mag,coil} = I_2 N_2 \int_{coil\ 2} d\vec{l}_2 \times \vec{B}_1,$$

and the same force can be calculated with the vector potential approach as follows:

$$\vec{F}_{2,mag,coil} = -\frac{\mu_0 N^2 I^2}{2\pi} \int_{coil\ 2} d\vec{l}_2 \times \frac{1}{\alpha^2 \eta v^2} \begin{bmatrix} v^2 \left[\left({R_1}^2 - r^2 \right) E\left(k^2\right) + \alpha^2 K\left(k^2\right) \right] \\ xy \left[\left({R_1}^2 + r^2 \right) E\left(k^2\right) - \alpha^2 K\left(k^2\right) \right] \\ xz \left[\left({R_1}^2 + r^2 \right) E\left(k^2\right) - \alpha^2 K\left(k^2\right) \right] \end{bmatrix}.$$

The subscript adds the word coil to reflect that this is the magnetic force as calculated using the magnetic field from a coil-based model, not the dipole model. The force has a negative sign to account for the currents being in opposite directions (repulsive). In order to get dimensionless force, the above formula is multiplied on both sides by the scaling factor ($\mathcal{T}^2/m_2 R_1$), and all of the variables with units of length are scaled by R_1, such that the above formula becomes

$$\tilde{\vec{F}}_{2,mag,coil} = -\frac{\mu_0 N I^2 \mathcal{T}^2}{4\pi^2 \tilde{R}_2 \rho R_1^2} \int_{coil\ 2} \widetilde{d\vec{l}_2} \times \frac{1}{\tilde{\alpha}^2 \tilde{\eta} \tilde{v}^2} \begin{bmatrix} \tilde{v}^2 \left[\left({\tilde{R}_1}^2 - \tilde{r}^2 \right) E\left(k^2\right) + \tilde{\alpha}^2 K\left(k^2\right) \right] \\ \tilde{x}\tilde{y} \left[\left({\tilde{R}_1}^2 + \tilde{r}^2 \right) E\left(k^2\right) - \tilde{\alpha}^2 K\left(k^2\right) \right] \\ \tilde{x}\tilde{z} \left[\left({\tilde{R}_1}^2 + \tilde{r}^2 \right) E\left(k^2\right) - \tilde{\alpha}^2 K\left(k^2\right) \right] \end{bmatrix}. \quad (5.6)$$

To simplify the above formula, the following non-dimensional term is defined:

$$\chi = \frac{\mu_0 N I^2 \mathcal{T}^2}{4\pi^2 \tilde{R}_2 \rho R_1^2}. \quad (5.7)$$

The force balance therefore occurs when

$$\tilde{\vec{F}}_{spring} + \tilde{\vec{F}}_{mag,coil} = [0],$$

or

$$\tilde{F}_{tot,x} = \tilde{F}_{spring} + \tilde{F}_{2,mag,coil,x} = 0, \tag{5.8}$$

since the forces are purely in the x direction.

5.3.2. Equilibrium Identification

1 DoF – Translational	1 DoF – Rotational	2 DoF – Rotational & Translational
Equilibrium Identification	Equilibrium Identification	Equilibrium Identification
Static Stability	Static Stability	Static Stability
Dynamic Stability	Dynamic Stability	Dynamic Stability

Finding equilibrium will be done in this section via the interpolation technique discussed in Section 4.1.1, by using *crossing.m* to find where $\tilde{F}_{2,mag,coil,x} + \tilde{F}_{spring}$ crosses zero. In order to combine non-dimensional terms into a single term χ/k^*, both sides of Equation (5.8) are divided by k^*, such that

$$\frac{\tilde{F}_{total}}{k^*} = 0. \tag{5.9}$$

Example Equilibrium Identification

Table 23 gives the interpolated $\tilde{x}$ value at equilibrium for a range of χ/k^* based on a $\Delta\tilde{x}$ of 0.01. The equilibrium IDs are written with a subscript BS to indicate that they are related to the Biot-Savart formulation versus the dipole formulation. This convention is used through the rest of the chapter.

Table 23: Equilibrium locations in the 1DoF-T complex case for a range of values of χ/k^* with $\tilde{R}_2 = 1.2$ and $\tilde{x}_0 = 2$

Equilibrium ID	χ/k^*	$\tilde{x}$ value at equilibrium
$\tilde{x}_{coil,1}$	1	2.5114
$\tilde{x}_{coil,2}$	10	3.6322
$\tilde{x}_{coil,3}$	100	5.5959
$\tilde{x}_{coil,4}$	1000	8.7320

Figure 54 shows the left side of Equation (5.9) plotted against distance $\tilde{x}$, with the grey lines representing the absolute value of negative forces as in Chapter 3 and the equilibria numbered as they are in Table 23.

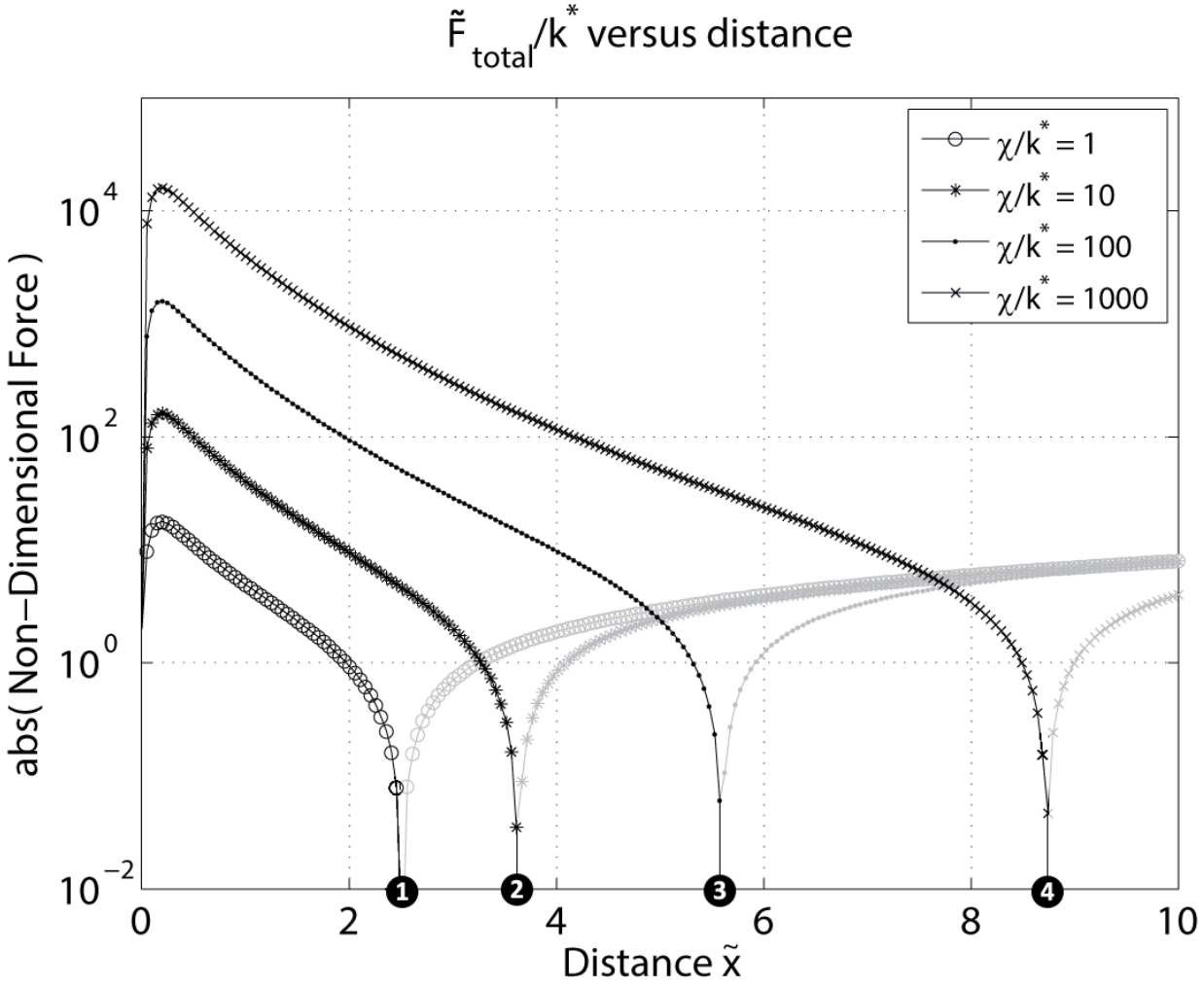

Figure 54: Equilibrium positions in the 1DoF-T coil system with $\tilde{R}_2 = 1.2$ and $\tilde{x}_0 = 2$, where the grey lines are the absolute values of negative forces

It can be seen that for larger values of χ/k^*, the equilibrium is farther from the natural length of the linear spring (still taken to be $\tilde{x}_0 = 2$), which is as expected for a stronger magnet (large χ) and/or a weaker spring (small k^*). Compared to the dipole system, the major observable difference is that, whereas the dipole force goes to $+\infty$ as $\tilde{x}$ goes to 0, the coil force goes to 0 as $\tilde{x}$ goes to 0, which is in agreement with Figure 25. The next section discusses the static stability of these equilibria.

5.3.3. Static Stability Classification

1 DoF – Translational	1 DoF – Rotational	2 DoF – Rotational & Translational
Equilibrium Identification	Equilibrium Identification	Equilibrium Identification
Static Stability	Static Stability	Static Stability
Dynamic Stability	Dynamic Stability	Dynamic Stability

In this section, the static stability of the 1DoF-T equilibria identified in the previous section is evaluated.

As mentioned in Section 4.1.2, the static stability for each of the coil model equilibria will be determined using centered finite differencing to approximate the derivative of the total force at each of the equilibria, remembering that a negative force derivative or positive stiffness means static stability.

Example Stability Calculations

Table 24 gives the stiffnesses of the equilibria identified in the previous section as calculated by finite differencing, with the statically stable (positive stiffness) rows bolded.

Table 24: Stiffness values at equilibria of the 1DoF-T complex case for a range of values of χ/k^*

Equilibrium ID	χ/k^*	$\tilde{x}$ value at equilibrium	$\kappa_{tot,ND,coil,T}$
$\tilde{\boldsymbol{x}}_{\boldsymbol{coil,1}}$	**1**	**2.5114**	**1.5827**
$\tilde{\boldsymbol{x}}_{\boldsymbol{coil,2}}$	**10**	**3.6322**	**2.4867**
$\tilde{\boldsymbol{x}}_{\boldsymbol{coil,3}}$	**100**	**5.5959**	**3.3514**
$\tilde{\boldsymbol{x}}_{\boldsymbol{coil,4}}$	**1000**	**8.7320**	**3.9673**

All the equilibria in Table 24 are statically stable (similar to the 1DoF-T repulsive equilibria in the dipole case), and it can furthermore be seen that the stiffness magnitude increases with larger values of χ/k^*, implying that such systems are less deformed by small external perturbations.

5.3.4. Dynamic Stability

1 DoF – Translational	1 DoF – Rotational	2 DoF – Rotational & Translational
Equilibrium Identification	Equilibrium Identification	Equilibrium Identification
Static Stability	Static Stability	Static Stability
Dynamic Stability	Dynamic Stability	Dynamic Stability

In this section, the dynamic stability of a 1DoF-T coil system is evaluated, using the magnetic vector potential of a single coil in order to calculate the potential energy of a two coil system.

Effective Potential Energy

Before diving into the vector potential, it is valuable to discuss the energies in the system that compose the overall effective potential energy and how they are combined. Moon [2] describes the "effective potential energy" P_{tot} of a system as being

$$P_{tot} = V_{tot} + (-W_{tot}),$$

where V_{tot} is the total elastic potential energy, and W_{tot} is the formulation of the total magnetic energy of the system based on the currents in the coils (as will be used in this chapter) instead of the flux. The magnetic energy based on the flux would have been added in the positive to obtain the effective potential energy, but the switch in sign convention is due to a Legendre transformation from the flux-based potential energy formulation [2]. Non-dimensionally, the above formulation becomes

$$\tilde{P}_{tot} = \tilde{V}_{tot} - \widetilde{W}_{tot}. \tag{5.10}$$

The negative of $\widetilde{W}_{mag}$ is summed with $\tilde{V}$ instead of the positive of $\widetilde{W}_{mag}$ as would typically be expected in a simple summation of potential energies because the definition of magnetic energy with respect to the current in each coil as will be performed in this chapter is as follows:

$$\vec{\tilde{F}}_{mag} = \left(\frac{\partial \widetilde{W}_{tot}}{\partial \vec{\tilde{x}}_t}\right)_0 \text{ [2]}. \tag{5.11}$$

In contrast, it can be recalled that the calculation of magnetic potential energy via integration of the force or torque, as was performed in Chapter 3, obeyed Equation (1.6) copied below and modified for non-dimensionality, wherein the sign is negative instead of positive as in Equation (5.11):

$$\vec{\tilde{F}}_{tot} = -\left[\left(\frac{\partial \widetilde{P}}{\partial \tilde{x}_{t,1}}\right)_0 \dots \left(\frac{\partial \widetilde{P}}{\partial \tilde{x}_{t,n_t}}\right)_0\right],$$

Hence, maxima in the $\widetilde{W}_{tot}$ represent static stability rather than minima as in $\tilde{V}_{tot}$, and therefore in order to be comparing apples to apples, $-\widetilde{W}_{tot}$ needs to be added to $\tilde{V}_{tot}$. In the next subsection wherein the inductance formulation for magnetic energy is described, this will be quickly verified.

Component Energies (Elastic and Magnetic) in 1DoF-T System

$\tilde{V}_T$, the elastic potential energy of the stretched linear spring, is simple to calculate, as the spring force formulation hasn't changed between the dipole system and the coil system:

$$\tilde{V}_T = \frac{k^*\tilde{x}^2}{2} - k^*\tilde{x}_0\tilde{x} + \frac{k^*{\tilde{x}_0}^2}{2}. \tag{5.12}$$

${\tilde{x}_0}^2$ was lumped in as part of the $+C$ integration constant in the previous analysis but is included here because the integration constant will be further defined in the discussion of inductance below.

$\widetilde{W}_{tot}$ is a bit more complex. In general, the total magnetic energy can be given in terms of self- and mutual inductances of the two coils, such that

$$W_{tot} = \frac{1}{2}\sum_{i=1}^{2}\sum_{j=1}^{2} L_{ij}I_iI_j = \frac{1}{2}L_{11}I_1^2 + \frac{1}{2}L_{12}I_1I_2 + \frac{1}{2}L_{21}I_2I_1 + \frac{1}{2}L_{22}I_2^2, \tag{5.13}$$

and

$$\frac{1}{2}L_{ij}I_iI_j = \frac{1}{2}\int \vec{J}_j \cdot \vec{A}_i \, dxdydz = \frac{N_jI_j}{2}\int \vec{A}_i \cdot d\vec{l}_j, \tag{5.14}$$

because

$$\vec{J}_j \, dxdydz = J_j d\vec{l}_j \cdot A_{CS} = N_jI_j d\vec{l}_j,$$

where A_{CS} is the cross-sectional area of the coil through which current flows, $\overrightarrow{J_j}$ is the current density vector, and L_{ij} is the inductance of a coil (self-inductance if $i = j$, mutual inductance between two coils if $i \neq j$). The sign of W_{tot} can be verified with the above definitions; inductances are always positive, but the mutual inductance decreases as distance between the coils increases (in the direction of the magnetic force on a coil being repelled). The self-energy terms are always positive because the currents are squared, but the opposing currents make the mutual energy negative. So, as the coils get farther apart, W_{tot} increases, meaning that force acts in the direction of a positive change in magnetic potential energy, consistent with Equation (5.11).

The self-inductance terms in Equation (5.13) (those that include L_{11} and L_{22}, for coil 1 or coil 2 respectively) are actually configuration independent and only depend on that coil's design parameters, not on its proximity or orientation with respect to the other coil. As such, the self-inductance terms remain constant even as $\tilde{x}$ (and/or β, in the rest of this chapter) changes. Self-inductance refers to the energy inside a current-carrying coil. These self-inductance energy terms are therefore part of what comprise the magnetic energy contribution to the integration constant C in Chapter 3's analytical determination of potential energy, Equation (3.48).

The mutual inductance energy term represents the energy of one coil in the magnetic field of the other, multiplied by two to account for the reverse situation (similar to how the magnetic potential energy in Chapter 0 needed to be multiplied by 2 as well). The magnetic potential energy calculated in Chapter 3 is thus synonymous with $L_{12}I_1I_2$ and can be calculated as follows:

$$\frac{1}{2}L_{12}I_1I_2 = \frac{I_2N_2}{2}\int \vec{A}_1 \cdot d\vec{l}_2,$$

where $\vec{A}_1$ is purely azimuthal as discussed in Section 4.1.3, such that

$$\vec{A}_1(r,\theta,\phi) = A_\phi(r,\theta) * d\hat{l}_1(\phi),$$

where r and θ are the magnitude of the distance vector from the center of coil 1 to the point of interest $P(r,\theta,\phi)$ and the angle of that distance vector with respect to the x axis respectively, as per Figure 55. θ is the coil analogy to θ_m in the dipole case.

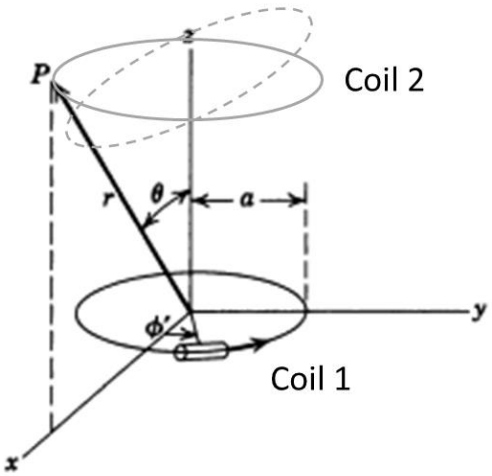

Figure 55: Variables for calculation of the magnetic vector potential of coil 1 at points P around the circumference of coil 2 (From Figure 5.5 in Jackson [49]), the solid grey line representing the coil position in the 1DoF-T case, the dotted grey line representing a rotation as in the 1DoF-R case

The magnitude of the vector potential at the point $P(r,\theta,\phi)$ is as follows:

$$A_\phi(r,\theta) = \frac{\mu_0 NIR}{\pi\sqrt{R^2+r^2+2Rr\sin\theta}}\left[\frac{(2-k^2)K(k^2)-2E(k^2)}{k^2}\right] = \frac{\mu_0 NIR}{\pi\sqrt{R^2+r^2+2Rr\sin\theta}}H,$$

where R is the radius of the coil in question, H represents the non-dimensional term in brackets, and $K(k^2)$ and $E(k^2)$ are the complete elliptic integrals [56], using as their argument

$$k^2 = \frac{4R_1 r\sin\theta}{R_1^2+r^2+2R_1 r\sin\theta}.$$

The magnitude $A_\phi(r,\theta)$ then must be multiplied by the unit vector $d\hat{l}_1(\phi)$ to make the magnetic vector potential azimuthal to coil 1. Then, the dot product of the magnetic vector potential and the differential length element $d\vec{l}_2$ are taken for each element around coil 2 and summed then multiplied by the effective current I_2N_2 to get the energy associated with coil 2 in the field of coil 1 and vice versa as per Equation (5.14).

It can be seen that in the 1DoF-T case when coil 2 is parallel to coil 1, the magnetic vector potential is always parallel with the differential length elements around coil 2. As it rotates, the dot product gets smaller and smaller until it's virtually non-existent when $\beta = \pm\frac{\pi}{2}$. This observation is consistent with the physical meaning of the mutual inductance energy term being linked to how much magnetic flux from one magnet goes through the enclosed area of the other, which is maximized when $\beta = 0$ (and increases as the coils move closer together) [57]. It can also be noted that when the coils are repelling, I_1 and I_2 have opposite signs, and therefore $L_{12}I_1I_2$ is negative, whereas the self-inductance energy terms are positive, meaning that a higher mutual inductance results in a lower total magnetic potential energy (but a higher effective potential energy).

Non-Dimensional Magnetic Energy

The non-dimensional $\widetilde{W}_{tot}$ is obtained by multiplying both sides of Equation (5.13) by $\mathcal{T}^2/m_2R_1^2$, pulling the constants out of $A_\phi(r,\theta)$, and assuming $N_1 = N_2 = N$ and $|I_1| = |I_2| = I$ (but inserting a negative sign where the two are multiplied together):

$$\begin{aligned}\widetilde{W}_{tot} &= W_{tot}\left(\frac{\mathcal{T}^2}{m_2R_1^2}\right)\\ &= \chi\left[\int \frac{\widetilde{H}_{11}d\hat{l}_1(\phi)\cdot d\tilde{\vec{l}}_1}{\sqrt{1+\tilde{r}_{11}{}^2+2\tilde{r}_{11}\sin\theta_{11}}} - \int \frac{\widetilde{H}_{12}d\hat{l}_1(\phi)\cdot d\tilde{\vec{l}}_2}{\sqrt{1+\tilde{r}_{12}{}^2+2\tilde{r}_{12}\sin\theta_{12}}}\right.\\ &\left. - \tilde{R}_2\int \frac{\widetilde{H}_{21}d\hat{l}_2(\phi)\cdot d\tilde{\vec{l}}_1}{\sqrt{\tilde{R}_2^2+\tilde{r}_{21}{}^2+2\tilde{R}_2\tilde{r}_{21}\sin\theta_{21}}} + \tilde{R}_2\int \frac{\widetilde{H}_{22}d\hat{l}_2(\phi)\cdot d\tilde{\vec{l}}_2}{\sqrt{\tilde{R}_2^2+\tilde{r}_{22}{}^2+2\tilde{R}_2\tilde{r}_{22}\sin\theta_{22}}}\right],\end{aligned} \tag{5.15}$$

where $\widetilde{H}_{1x}$ is calculated using

$$\tilde{k}_{1x}{}^2 = \frac{4\tilde{r}\sin\theta}{1+\tilde{r}^2+2\tilde{r}\sin\theta},$$

$\widetilde{H}_{2x}$ is calculated using

$$\tilde{k}_{2x}{}^2 = \frac{4\tilde{r}\tilde{R}_2\sin\theta}{\tilde{R}_2^2+\tilde{r}^2+2\tilde{r}\,\tilde{R}_2\sin\theta},$$

and all the length terms ($\tilde{r}, \overrightarrow{\tilde{d}\tilde{l}}, \tilde{R}_2$) have been divided by R_1.

Self-Inductance Terms ($\frac{1}{2}L_{11}I_1^2$ and $\frac{1}{2}L_{22}I_2^2$)

When $\tilde{k}^2$ is found for the self-inductance energy terms, $\theta = 0$, and thus for coil 1 (and coil 2 when $R_2 = R_1$), $\tilde{k}^2$ is 1. When $\tilde{k}^2$ approaches unity, $K(\tilde{k}^2) \to \infty$, so the vector potential cannot be directly formulated at $\tilde{r} = R_1$ or R_2. In order to avoid this artificial divergence, the modulus $\tilde{k}_{11}{}^2$ is calculated at a small distance ϵ from $\tilde{r}$. In order to approximate the vector potential at the center of the coil bundle ($\tilde{r} = R_1$ or R_2), it is of interest to calculate $\widetilde{H}_{11}/\sqrt{1+\tilde{r}_{11}{}^2+2\tilde{r}_{11}\sin\theta_{11}}$ or $\widetilde{H}_{22}/\sqrt{\tilde{R}_2^2+\tilde{r}_{22}{}^2+2\tilde{R}_2\tilde{r}_{22}\sin\theta_{22}}$ on the outer or inner radius of the coil ($\tilde{r} = R_{1\,or\,2} \pm \epsilon$), as seen in Figure 56, and average the two.

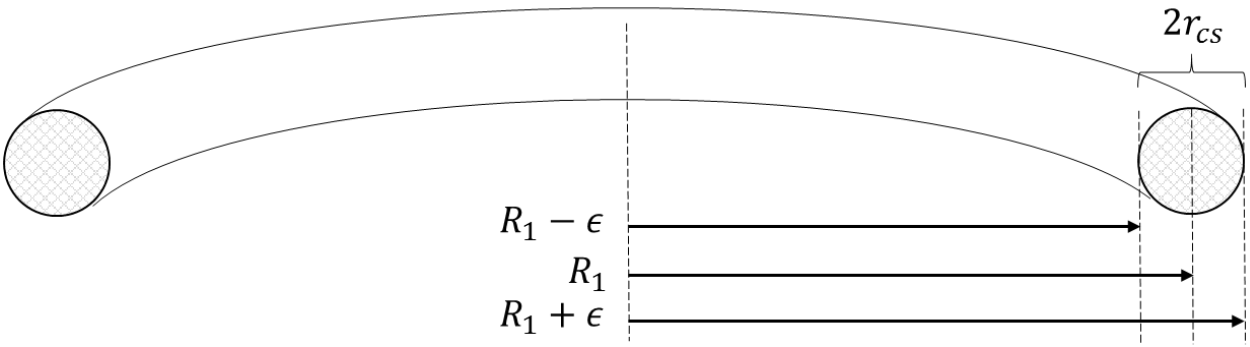

Figure 56: Representational cross-sectional view of coil 1, with the inner and outer radii indicated, as well as the wire bundle's effective cross-sectional radius. Wire bundle cross section is not circular in reality because the wire has a rectangular profile, but this figure represents the effective dimensionality of the coil.

The size of epsilon only matters in terms of how accurate the estimate at R_1 is, similar to how smaller grid sizes result in more accurate solution estimates, since $\tilde{k}^2$ can be calculated at any point that is not exactly R_1. ϵ is thus taken as the non-dimensional effective cross-sectional radius of the coil bundle, $\tilde{r}_{CS}$, or 4mm by 0.1mm, assuming the SuperPower 2G HTS wire [31] times the number of turns of wire N, divided by R_1. For the purposes of this chapter, N is assumed to be 100, and $R_1 = 1m$. Therefore,

$$\epsilon = \tilde{r}_{CS} = 4 \times 10^{-5}.$$

The average value of the $\tilde{r}$-dependent self-inductance terms for coil 1 are calculated as follows:

$$\frac{\widetilde{H}_{11}}{\sqrt{1 + \tilde{r}_{11}{}^2 + 2\tilde{r}_{11}\sin\theta_{11}}} \approx \frac{1}{2}\left[\frac{\widetilde{H}_{11+\epsilon}}{\sqrt{1 + (\tilde{r}_{11}+\epsilon)^2 + 2(\tilde{r}_{11}+\epsilon)\sin\theta_{11}}} + \frac{\widetilde{H}_{11-\epsilon}}{\sqrt{1 + (\tilde{r}_{11}-\epsilon)^2 + 2(\tilde{r}_{11}-\epsilon)\sin\theta_{11}}}\right].$$

For coil 2,

$$\frac{\widetilde{H}_{22}}{\sqrt{\tilde{R}_2^2 + \tilde{r}_{22}{}^2 + 2\tilde{R}_2\tilde{r}_{22}\sin\theta_{22}}} \approx \frac{1}{2}\left[\frac{\widetilde{H}_{22+\epsilon}}{\sqrt{\tilde{R}_2^2 + (\tilde{r}_{22}+\epsilon)^2 + 2\tilde{R}_2(\tilde{r}_{22}+\epsilon)\sin\theta_{22}}} + \frac{\widetilde{H}_{22-\epsilon}}{\sqrt{\tilde{R}_2^2 + (\tilde{r}_{22}-\epsilon)^2 + 2\tilde{R}_2(\tilde{r}_{22}-\epsilon)\sin\theta_{22}}}\right].$$

Another Method for Estimating Self-Inductance

In addition to the above vector potential method, Jackson gives an estimation [49] of the self-inductance energy values, which can be compared to the values as calculated by the vector potential method to ensure that the latter are of the correct order of magnitude:

$$\frac{1}{2}L_{11}I_1^2 \approx \frac{\mu_0 R_1 I_1^2 N^2}{4}\left[\ln\left(\frac{0.373\pi}{\tilde{r}_{CS}^2}\right)+\frac{1}{2}\right],$$

where $\tilde{r}_{CS}$ is the effective radius of the cross section of the coil bundle. In order to non-dimensionalize the self-inductance energies such that they can be combined with the vector potential calculations for the mutual inductance energy terms, the previous equation is multiplied by $\mathcal{T}^2/m_2R_1^2$ to get

$$\widetilde{W}_{11} = \frac{1}{2}L_{11}I_1^2\left(\frac{\mathcal{T}^2}{m_2R_1^2}\right) \approx \frac{\mu_0 N I_1^2 \mathcal{T}^2}{8\pi\tilde{R}_2 R_1^2\rho}\left[\ln\left(\frac{0.373\pi}{\tilde{r}_{CS}^2}\right)+\frac{1}{2}\right] \approx \frac{\chi\pi}{2}\left[\ln\left(\frac{0.373\pi}{\tilde{r}_{CS}^2}\right)+\frac{1}{2}\right]. \tag{5.16}$$

Additionally, for coil 2,

$$\begin{aligned}\widetilde{W}_{22} = \frac{1}{2}L_{22}I_2^2\left(\frac{\mathcal{T}^2}{m_2R_1^2}\right) &\approx \frac{\mu_0 N I_2^2 \mathcal{T}^2}{8\pi R_1^2\rho}\left[\ln\left(\frac{0.373\pi\tilde{R}_2^2}{\tilde{r}_{CS}^2}\right)+\frac{1}{2}\right] \\ &\approx \frac{\chi\pi\tilde{R}_2}{2}\left[\ln\left(\frac{0.373\pi\tilde{R}_2^2}{\tilde{r}_{CS}^2}\right)+\frac{1}{2}\right].\end{aligned} \tag{5.17}$$

Example Dynamic Stability Calculations

Equations (5.10), (5.12), and (5.15) can be combined to calculate the non-dimensional formulation for 1DoF-T effective potential energy that will be used going forward in Equation (5.18). The non-dimensional effective potential energy will be calculated using Equation (5.18) for each of the equilibria found in Section 5.3.2 to determine their dynamic stability conditions:

$$\begin{aligned}\tilde{P}_T = \tilde{V}_T - \widetilde{W}_{tot} = \frac{k^*\tilde{x}^2}{2} &- k^*\tilde{x}_0\tilde{x} + \tilde{x}_0{}^2 \\ &- \chi\left[\int \frac{\widetilde{H}_{11}d\hat{l}_1(\phi)\cdot d\tilde{\vec{l}}_1}{\sqrt{1+\tilde{r}_{11}{}^2+2\tilde{r}_{11}\sin\theta_{11}}} - \int \frac{\widetilde{H}_{12}d\hat{l}_1(\phi)\cdot d\tilde{\vec{l}}_2}{\sqrt{1+\tilde{r}_{12}{}^2+2\tilde{r}_{12}\sin\theta_{12}}}\right. \\ &\left. - \tilde{R}_2\int \frac{\widetilde{H}_{21}d\hat{l}_2(\phi)\cdot d\tilde{\vec{l}}_1}{\sqrt{\tilde{R}_2^2+\tilde{r}_{21}{}^2+2\tilde{R}_2\tilde{r}_{21}\sin\theta_{21}}} + \tilde{R}_2\int \frac{\widetilde{H}_{22}d\hat{l}_2(\phi)\cdot d\tilde{\vec{l}}_2}{\sqrt{\tilde{R}_2^2+\tilde{r}_{22}{}^2+2\tilde{R}_2\tilde{r}_{22}\sin\theta_{22}}}\right]\end{aligned} \tag{5.18}$$

It is important to note that the formulation for magnetic potential energy in Equation (5.15) is applicable to any of the three systems, 1DoF-T, 1DoF-R, and 2DoF, since the mutual inductance energy terms accommodate rotations and displacements within their integrals, and will therefore be referred back to throughout this chapter when example dynamic stability calculations are made at identified equilibria. Only $\tilde{V}$ changes between the aforementioned systems, from $\tilde{V}_T$ to $\tilde{V}_R, to\ \tilde{V}_{tot}$ respectively.

The calculation of Equation (5.18) is done in MATLAB, by defining the positions of the coils in space and then calculating the vector potential of one coil at the center of each element around the coil in question. Then, the dot product of the potential with the differential length element vector is calculated and then summed around the second coil to get the magnetic energy term relating to that particular pair of coils.

Verification and Validation Steps

After the four magnetic inductance energy terms have been calculated, there are a few ways to verify that the code to calculate the vector potential energy terms is functioning correctly and to validate the results.

Mutual inductance V&V: The inductance tables in Grover [57] allow calculation of the mutual inductance and thus the full energy associated with the interaction of two coils; however, interpolation of the data tables is required for the specific coil configuration, which entails some degree of error. The vector potential results can be compared to the Grover results once non-dimensionalized to validate that the MATLAB code is coming up with the same or similar value of energy. Whereas Chapter 0's specific results could be validated by those of Chapter 3, this external validation is necessary because the coil model and the dipole model are not comparable in the near-field, and thus the results of this chapter are not directly comparable to the results from Chapters 3 and 0.

It is expected that $L_{12} = L_{21}$ due to the reciprocity theorem [58], which would then make the two middle terms in the brackets in Equation (5.15) equal. This equality will be verified in this section. Also expected is that the Grover results are the sum of the individual mutual inductance energy terms in Equation (5.18), which would make the Grover results twice as large if indeed $L_{12} = L_{21}$.

Table 25 shows the mutual inductance energy terms from Equation (5.18) calculated when the coils are parallel for a few sample values of $\tilde{x}$ and χ and then compared to the Grover calculations. In order to use Grover's formulas, it is necessary to first pick a value of $\tilde{R}_2$, which was selected as 0.9218, a legacy value from early dimensional exploration of Grover's formulas.

Table 25: Mutual inductance energy terms when coils are parallel as calculated by vector potential and Grover's inductance tables

$\tilde{x}$	χ	$\widetilde{W}_{12}$	$\widetilde{W}_{21}$	$\widetilde{W}_{Grover}$
1	1	1.1118	1.1118	2.2241
2	1	0.3111	0.3111	0.6224
3	1	0.1190	0.1190	0.2379
1	10	11.1181	11.1181	22.2411
2	10	3.1115	3.1115	6.2238
3	10	1.1895	1.1895	2.3794

It can be seen from Table 25 that, as expected, $\widetilde{W}_{12} = \widetilde{W}_{21}$ and can therefore be combined into $2\widetilde{W}_{12}$ from here onward. Additionally, the calculation of mutual inductance energy with the non-dimensional Grover mutual inductance energy estimate is equal to $2\widetilde{W}_{12}$, which is as expected.

Self-inductance V&V: The estimates given by Equations (5.16) and (5.17) can be used to validate the self-energy of the coils as calculated with the vector potential, though both are estimates and therefore aren't expected to be as close in value as the mutual inductance calculations mentioned above. Luckily, any error in calculation here is less important than error in the mutual inductance terms. This is because dynamic stability is determined by the relative potential energy across configurations, and as such, the constant self-inductance terms in Equation (5.15) do not contribute to a *difference* in potential energy between different points in $\tilde{x}$ for the same coils. That means that the self-inductance terms do not impact the critical initial kinetic energy of the system equilibria. However, it is of interest to include the constant terms to study how different design parameters change the energy stored in a coil (expressed in the 1DoF problem by χ).

Table 26 shows the self-inductance energy terms from Equation (5.18) calculated for a few different χ and $\tilde{R}_2$ values, compared to the Jackson estimates from Equations (5.16) and (5.17).

Table 26: Self-inductance energy terms as calculated by vector potential and Jackson estimates

χ	$\tilde{R}_2$	$\widetilde{W}_{11}$	$\widetilde{W}_{Jackson,11}$	$\widetilde{W}_{22}$	$\widetilde{W}_{Jackson,22}$	% error b/w $\widetilde{W}_{Jackson,22}$ and $\widetilde{W}_{22}$
1	.75	32.0630	32.8482	23.3695	23.9583	0.9754
1	1.5	32.0630	32.8482	50.0050	51.1830	0.9770
1	3	32.0630	32.8482	106.5412	108.8988	0.9784
10	.75	320.6301	328.4820	233.6949	239.5831	0.9754
10	1.5	320.6301	328.4820	500.0497	511.8301	0.9770
10	3	320.6301	328.4820	1065.4116	1088.9879	0.9784

It can be seen from Table 26 that the magnetic vector potential approach and the Jackson estimates for the self-inductance energy terms are very close and that the percent error between the two decreases as the radius of the coil in question gets larger.

From the previous verification and validation steps, confidence has been established in the vector potential method for determining magnetic energy, and it can be used going forward in this work. Figure 57 plots the effective potential energy curves as given by Equation (5.18) over the range of distance $0 \leq \tilde{x} \leq 10$ for each of $\chi = [1, 10, 100, 1000]$ (with k^* assumed to be 1) and labels the equilibria from Table 24 accordingly. The raw formulation of Equation (5.18) returned purely negative values of effective potential energy even with the constant terms included, but any constant can be added to a potential field to shift it upwards or downwards, so the minimum potential energy for each curve was added to the curve to boost its minima to $\tilde{P} = 0$. Zeroing all of the equilibria allows comparative study of how the potential energy slope changes between curves but not direct comparison of values.

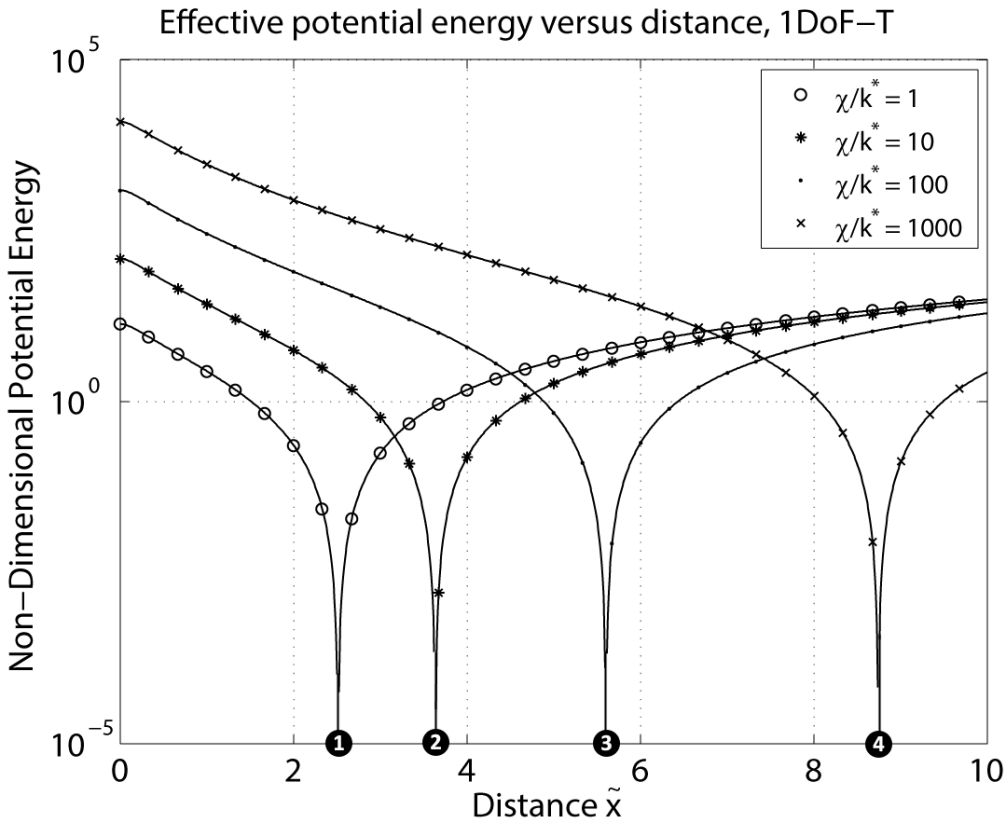

Figure 57: Effective potential energy curves of the 1DoF-T complex numerical case for $\chi = [1, 10, 100, 1000]$

Figure 57 bears strong similarity to Figure 54, except for the behavior near $\tilde{x} = 0$, where the total force decreases quickly when the coils are in the extreme near-field, but the potential energy is at a maximum. In the potential energy case, this is because the effective potential energy subtracts $\widetilde{W}_{tot}$, and $\widetilde{W}_{tot}$ is at a minimum and $\tilde{V}_T$ a maximum at $\tilde{x} = 0$. All four of the equilibria are clearly at the only minima on their curves and are thus incapable of escaping motion or dynamic instability if a constraint is assumed that says that coil 2 cannot pass "through" coil 1 into negative $\tilde{x}$, since the potential energy continues to increase infinitely beyond $\tilde{x} = 10$. As such, there is no critical initial kinetic energy to calculate for the complex 1DoF-T case. This figure primarily differs from Figure 33b (besides being entirely positive-valued) by the behavior near $\tilde{x} = 0$, which goes to $+\infty$ in the 1DoF-T dipole case shown in Figure 33b but not in the case studied in this section.

5.3.5. Summary

In this section, the techniques for identifying equilibria and determining their static and dynamic stability were implemented for the complex numerical coil system. This process required the derivation, non-dimensionalization, and verification/validation of several of the formulas that will be used throughout the rest of this chapter. The major difference between the results of the complex numerical 1DoF-T system and the analytical and simple numerical 1DoF-T systems is the behavior of the system in the extreme near-field ($\tilde{x} < 1$).

5.4. Rotational Single Degree of Freedom

1 DoF – Translational	1 DoF – Rotational	2 DoF – Rotational & Translational
Equilibrium Identification	Equilibrium Identification	Equilibrium Identification
Static Stability	Static Stability	Static Stability
Dynamic Stability	Dynamic Stability	Dynamic Stability

In this section, the coil-based single rotational degree of freedom (or 1DoF-R) system is studied. The system is depicted in Figure 58, with the torsional spring providing resistance to motion away from $\beta = 0$.

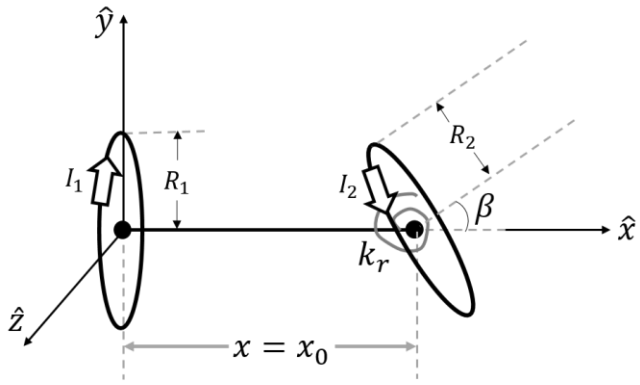

Figure 58: Rotational single degree of freedom (1DoF-R) coil system

5.4.1. Torque Balance

As in the 1DoF-T case, the torque balance in the coil-based system is less simple to write analytically than that of the dipole-based system. The non-dimensional torque provided by the torsional spring is still

$$\tilde{\vec{\tau}}_{2,spring} = -k_r^* \beta \hat{k},$$

but the magnetic torque is expressed instead as a cross product, with Equation (5.3) inserted into Equation (5.5) and non-dimensionalized the same way as in Equation (5.6), except with a scaling factor of $(\mathcal{T}^2/m_2 R_1^2)$. The same assumptions stand about currents and number of turns being the same across the two coils, such that

$$\tilde{\vec{\tau}}_{2,mag,coil} = \frac{\mu_0 N I^2 \mathcal{T}^2}{4\pi^2 \widetilde{R}_2 \rho R_1^2} \int_{coil\ 2} \tilde{\vec{R}}_2 \times \left(\overrightarrow{d\tilde{l}_2} \times \frac{1}{\tilde{\alpha}^2 \tilde{\eta} \tilde{v}^2} \begin{bmatrix} \tilde{v}^2 \left[\left(\widetilde{R}_1{}^2 - \tilde{r}^2 \right) E(k^2) + \tilde{\alpha}^2 K(k^2) \right] \\ \tilde{x}\tilde{y} \left[\left(\widetilde{R}_1{}^2 + \tilde{r}^2 \right) E(k^2) - \tilde{\alpha}^2 K(k^2) \right] \\ \tilde{x}\tilde{z} \left[\left(\widetilde{R}_1{}^2 + \tilde{r}^2 \right) E(k^2) - \tilde{\alpha}^2 K(k^2) \right] \end{bmatrix} \right). \quad (5.19)$$

It can be seen from the above formula that the non-dimensional term outside the parentheses is indeed χ.

The torque balance therefore occurs when

$$\tilde{\vec{\tau}}_{2,spring} + \tilde{\vec{\tau}}_{2,mag,coil} = [0],$$

or

$$\tilde{\tau}_{2,tot} = \tilde{\tau}_{2,spring} + \tilde{\tau}_{2,mag,coil} = 0, \quad (5.20)$$

since the torques all act about the z axis.

5.4.2. Equilibrium Identification

1 DoF – Translational	1 DoF – Rotational	2 DoF – Rotational & Translational
Equilibrium Identification	Equilibrium Identification	Equilibrium Identification
Static Stability	Static Stability	Static Stability
Dynamic Stability	Dynamic Stability	Dynamic Stability

Equilibrium identification will be performed for the 1DoF-R case via the interpolation technique discussed in the previous chapter and used already in the previous system in this chapter, using *crossing.m* to find where $\tilde{\tau}_{2,mag,coil} + \tilde{\tau}_{spring}$ crosses zero. Combining non-dimensional terms by dividing by k_r^*, the new torque balance formula is

$$\frac{\tilde{\tau}_{total}}{k_r^*} = 0,$$

and the points where the above equation is met are equilibria.

Example Equilibrium Identification

Table 27 gives the interpolated β values at equilibrium for a range of χ/k_r^* selected to show different behavior, with the interpolation based on a $\Delta\beta$ of 0.01. k_r^* is assumed to be 1 (which only impacts the stability values in the next section, not the location of equilibria), $\tilde{R}_2 = 1.2$, and $\tilde{x} = \tilde{x}_0 = 2.5$.

Table 27: Equilibrium locations in the non-dimensional 1DoF-R complex case for a range of values of $\frac{\chi}{k_r^*}, \tilde{R}_2 = 1.2, and\ \tilde{x} = \tilde{x}_0 = 2.5$

- β		
χ/k_r^*	Equil. ID	β
.1	—	-
10	$\beta_{ND,coil,1}$	-0.4844
100	—	-
$\beta = 0$		
χ/k_r^*	Equil. ID	β
.1	$\beta_{ND,coil,2-1}$	0
10	$\beta_{ND,coil,2-2}$	0
100	$\beta_{ND,coil,2-3}$	0
+β		
χ/k_r^*	Equil. ID	β
.1	—	-
10	$\beta_{ND,coil,3}$	0.4844
100	—	-

The equilibrium values above can be seen in Figure 59. As always, the grey lines represent the absolute value of negative non-dimensional torque, and it can be seen that at every equilibrium, each curve switches signs, indicating a crossing at zero or equilibrium.

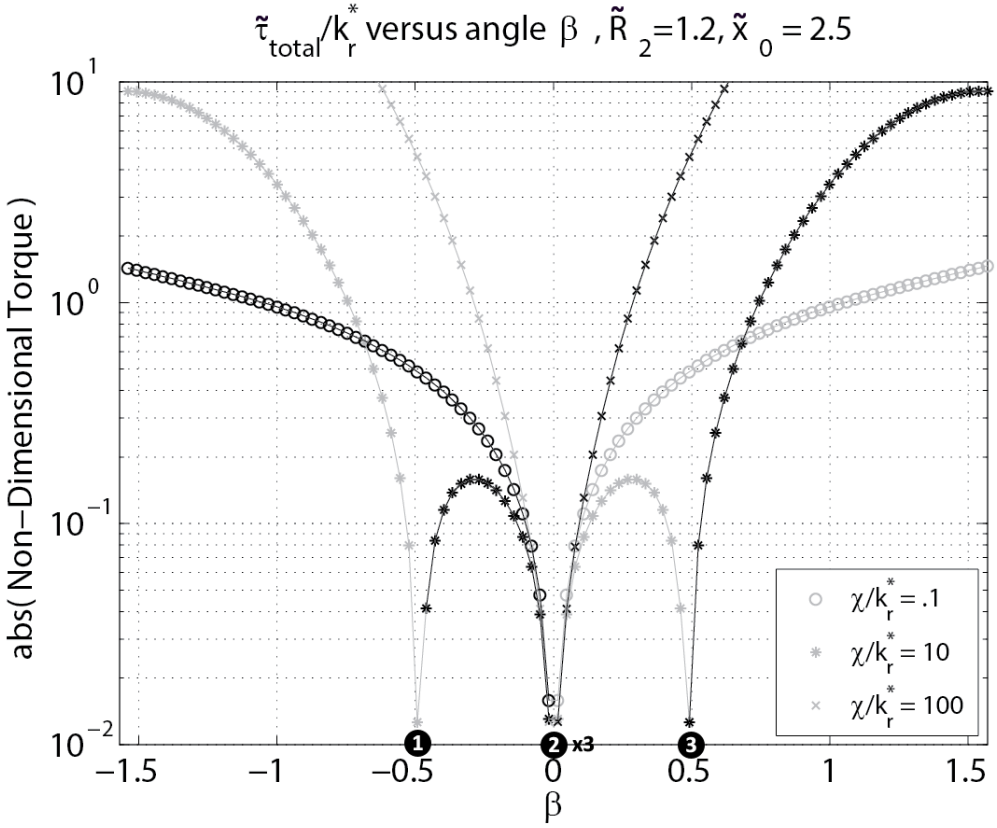

Figure 59: Equilibrium identification for the 1DoF-R coil model for $\tilde{x}_0 = 2.5$ and $\tilde{R}_2 = 1.2$, where grey lines represent the absolute value of the non-dimensional torque

It can be seen that every curve has an equilibrium at $\beta = 0$, and that the lowest χ/k_r^* curve is dominated by the spring restorative spring torque, meaning that the torque is negative for positive β and vice versa, while the highest χ/k_r^* curve dominates the spring torque for any $\beta \neq 0$ and works in the direction that the dipole torques do. However, the medium χ/k_r^* curve also has equilibria near $\beta = 0.5$. This feature in the coil model plot (resulting from what will henceforth be called the "proximity effect") results from the perimeter of coil 2 coming closer to the perimeter of coil 1 when the coil is tilted, which causes for positive β a strong restorative torque from the top element of coil 1 but an almost-as-strong divergent torque from the bottom of coil 1. The bottom of coil 2 moves farther away when β is positive (and its net torque is divergent), so it is the torque on the top of coil 2 versus the spring torque that determines the secondary equilibrium for the medium χ/k_r^* case. For the largest χ/k_r^* case, the net divergent torque on the bottom of coil 2 is large enough to dominate the spring torque on its own. In the dipole case, there is no closer or farther portion of the coil, so the net torque is immediately divergent and secondary equilibria do not appear until closer to $\beta = \pm\pi/2$, where the spring torque is finally large enough to counter the magnetic torque.

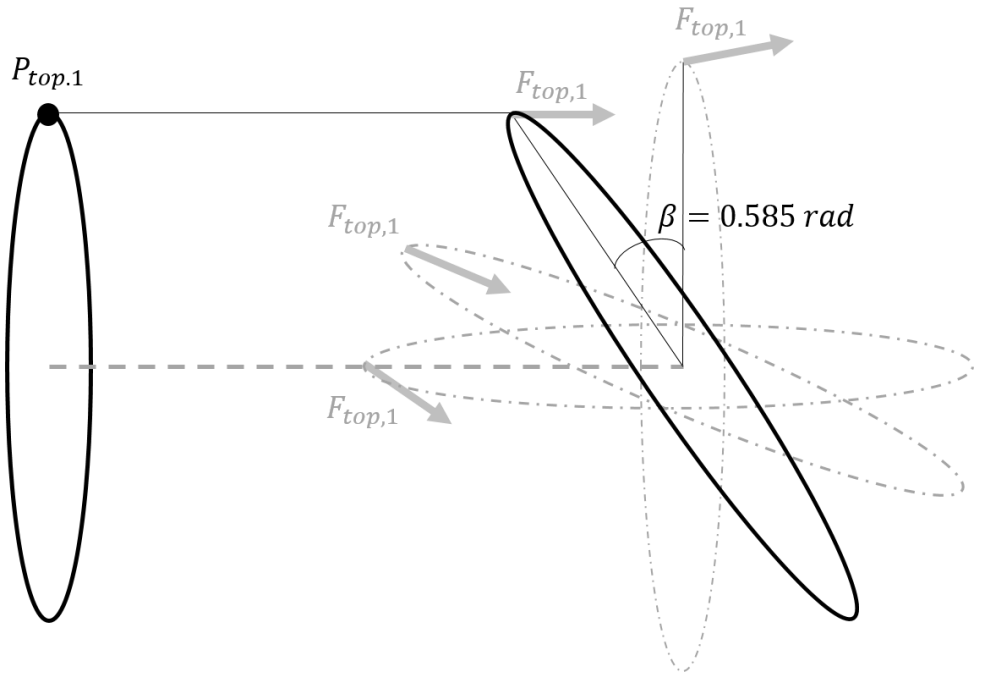

Figure 60: Geometry of proximity effect and the forces from the top element of coil 1 on the top element of coil 2 for a repulsive 1DoF-R system with $\tilde{x}_0 = 2.5$ and $\tilde{R}_2 = 1.2$

Figure 60 shows the geometry of the system plotted in Figure 59 for a positive rotation in β, along with the direction of the magnetic forces from the top element of coil 1 on the top element of coil 2. At first, the restorative torque on the top of coil 2 dominates the divergent torque on the bottom of coil 2 (not shown for simplicity), but the restorative torque on the top of coil 2 reduces as it is redirected into the plane of coil 2 as β grows. Once the coil rotates to some equilibrium magnitude of β (in the case of Figure 59 , $\beta \approx \pm 0.5$ radians), then the net divergent torque dominates the restorative torque. As such, $\beta_{ND,coil,2-1}$ is expected to be stable, since the spring torque dominates at the equilibrium, as well as $\beta_{ND,coil,2-2}$, due to the restorative effect of the proximity effect, while $\beta_{ND,coil,2-3}$, $\beta_{ND,coil,1}$, and $\beta_{ND,coil,3}$ are expected to be unstable. It can be noted that with a different selection of $\tilde{R}_2$ and $\tilde{x}_0$, the β at which the proximity effect occurs would change. In the far-field, as the coil is more closely approximated by a point dipole, these proximity effects would disappear.

5.4.3. Static Stability Classification

1 DoF – Translational	1 DoF – Rotational	2 DoF – Rotational & Translational
Equilibrium Identification	Equilibrium Identification	Equilibrium Identification
Static Stability	Static Stability	Static Stability
Dynamic Stability	Dynamic Stability	Dynamic Stability

In this section the static stability of the non-dimensional 1DoF-R equilibria identified in the previous section is presented, calculated from the coil model via the central finite difference method.

5.4.3.1. Example Stability Calculations

Table 28 gives the stiffnesses of the equilibria identified in the previous section as calculated by finite differencing, with the statically stable (positive stiffness) rows bolded.

Table 28: Stiffness values for the non-dimensional 1DoF-R coil model equilibria for $\tilde{x}_0 = 2.5$ and $R_2 = 1.2$„ with the statically stable equilibria bolded

- β			
χ/k_r^*	Equil. ID	β	$\kappa_{tot,ND,coil,R}$
.1	—	-	-
10	$\beta_{ND,coil,1}$	-0.4844	-1.7285
100	—	-	
$\beta = 0$			
χ/k_r^*	Equil. ID	β	$\kappa_{tot,ND,coil,R}$
.1	$\boldsymbol{\beta_{ND,coil,2-1}}$	**0**	**1.0082**
10	$\boldsymbol{\beta_{ND,coil,2-2}}$	**0**	**0.8236**
100	$\beta_{ND,coil,2-3}$	0	-0.8546
+β			
χ/k_r^*	Equil. ID	β	$\kappa_{tot,ND,coil,R}$
.1	—	-	-
10	$\beta_{ND,coil,3}$	0.4844	-1.7285
100	—	-	

It can be seen from Table 28 that the expected stabilities from the previous section's analysis are correct, with the smallest χ/k_r^* exhibiting a single stable equilibrium, the intermediate χ/k_r^* exhibiting an unstable equilibrium at the origin and two unstable secondary equilibria, and the bigger χ/k_r^* having one unstable equilibrium at that origin.

5.4.4. Dynamic Stability

1 DoF – Translational	1 DoF – Rotational	2 DoF – Rotational & Translational
Equilibrium Identification	Equilibrium Identification	Equilibrium Identification
Static Stability	Static Stability	Static Stability
Dynamic Stability	Dynamic Stability	Dynamic Stability

In this section, the dynamic stability of a 1DoF-R coil system is evaluated, using the magnetic vector potential subtracted from the elastic potential energy of a torsional spring in order to calculate the potential energy of a system with one rotational degree of freedom:

$$\tilde{P}_R = \tilde{V}_R - \widetilde{W}_{tot} = \frac{k_r^* \beta^2}{2} - \frac{1}{2} L_{11} I_1^2 + L_{12} I_1 I_2 - \frac{1}{2} L_{22} I_2^2. \tag{5.21}$$

The $\beta \neq 0$ magnetic energies have also been validated against the tables in Grover to make sure that they get the same values for the more complicated calculations.

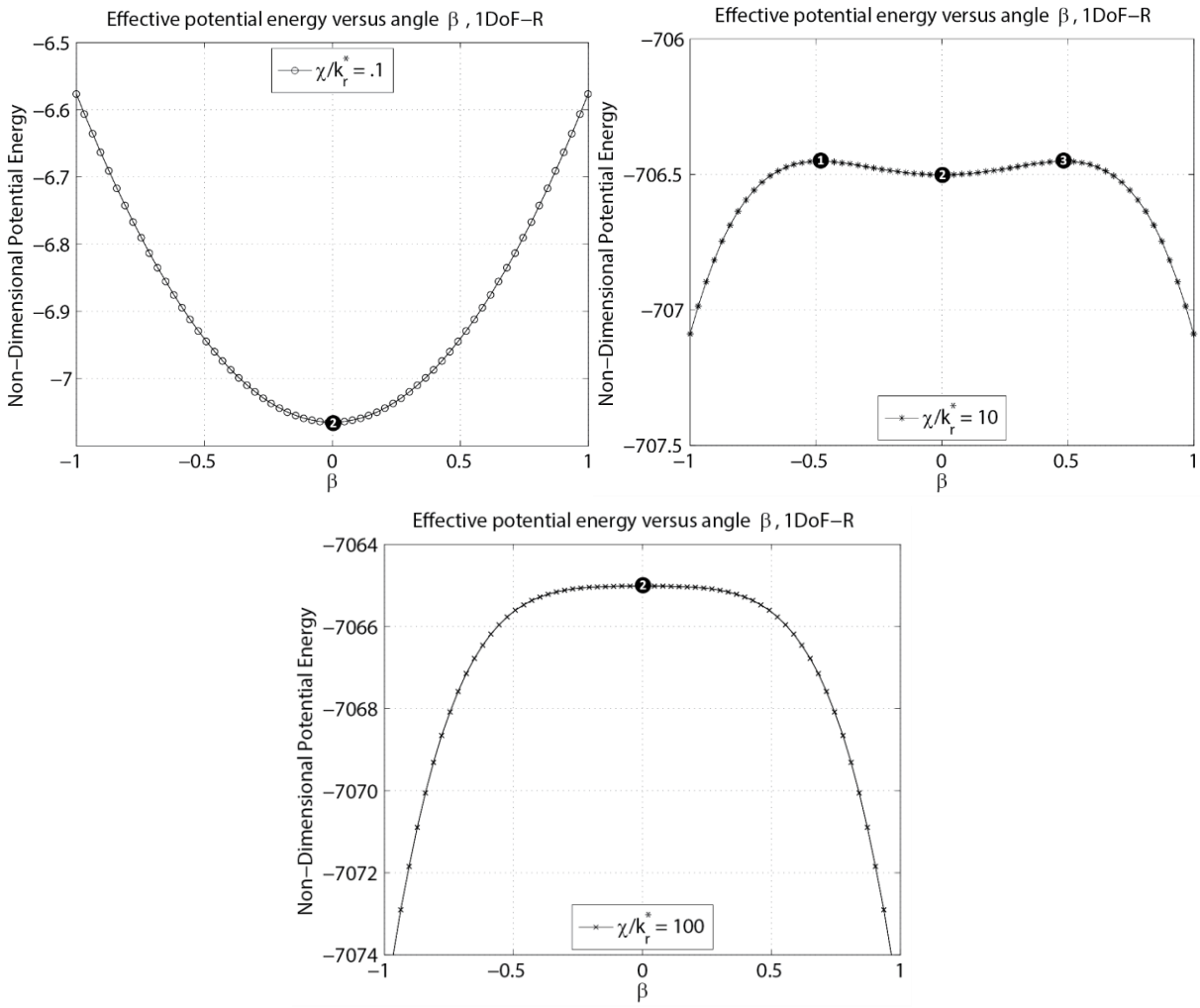

Figure 61: Effective potential energy for the 1DoF-R case, $\tilde{x}_0 = 2.5$ *and* $\tilde{R}_2 = 1.2$ *and (a, left)* $\frac{\chi}{k_r^*} = 0.1$ *(b, right)* $\frac{\chi}{k_r^*} = 10$ *(c, bottom)* $\frac{\chi}{k_r^*} = 100$*, shown for* $-1 \leq \beta \leq 1$ *to emphasize the behavior around the equilibria*

Figure 61 agrees with the results of Section 5.4.3.1. Figure 61a has a clear minimum in potential energy at $\beta_{ND,coil,2-1}$, rendering it stable, while Figure 61c has a clear maximum at $\beta_{ND,coil,2-3}$, rendering it unstable. Figure 61b has three equilibria, a stable central one at $\beta = 0$ and two unstable ones on either side of the central one, making $\frac{\chi}{k_r^*} = 10$ the only curve for which a critical initial kinetic energy can be calculated in the next section.

It makes intuitive sense that a stronger magnet/weaker spring (small $\frac{\chi}{k_r^*}$) would result in an unstable equilibrium, since a strong enough divergent magnetic torque would dominate even the proximity effect; on the other hand, an intermediate $\frac{\chi}{k_r^*}$ has enough divergent torque to allow equilibria away from $\beta = 0$, but the proximity effect makes the region in between $\beta = 0$ and the other equilibria stable. At greater distances $\tilde{x}_0$, the curves all have a single stable equilibrium at $\beta = 0$ because the magnetic torque drops off with increased distance, but the spring torque does not.

5.4.4.1. Critical Initial Kinetic Energy and Simulation

Only equilibrium $\beta_{ND,coil,2-2}$ has a critical initial kinetic energy beyond which motion can escape.

$$\tilde{T}_{t_0,crit}(\beta_{ND,coil,2-2}) = \tilde{P}_R(\beta_{ND,coil,1}) - \tilde{P}_R(\beta_{ND,coil,2-2})$$

$$= -706.4520 + 706.5020,$$

$$\tilde{T}_{t_0,crit}(\beta_{ND,coil,2-2}) = 0.05. \quad (5.22)$$

This is a fairly small critical energy, so it would take relatively little to make the system leave the small potential well between the unstable equilibria of $\beta_{ND,coil,1}$ and $\beta_{ND,coil,3}$. As $\tilde{x}_0$ decreases, the potential well (if one exists) around $\beta = 0$ deepens, and thus the critical initial kinetic energy increases. For example, at $\tilde{x}_0 = 1.5$, both $\frac{\chi}{k_r^*} = 10$ and 100 have the three equilibria, and in that case, $\tilde{T}_{t_0,crit}\left(\frac{\chi}{k_r^*} = 10, \beta = 0\right) = 2.60$ and $\tilde{T}_{t_0,crit}\left(\frac{\chi}{k_r^*} = 100, \beta = 0\right) = 22.80$, which shows that when three equilibria exist in a system, the initial critical kinetic energy is higher for a higher $\frac{\chi}{k_r^*}$ value.

5.4.5. Summary

Every combination of non-dimensional design variables results in an equilibrium at $\beta = 0$ in the 1DoF-R case. For smaller values of $\frac{\chi}{k_r^*}$, that zero equilibrium tends to be the only equilibrium and stable because the magnet is dominated by the restorative spring torque. At intermediate values of $\frac{\chi}{k_r^*}$, the zero equilibrium tends to be stable and bracketed symmetrically by two unstable equilibria that result from the proximity effect. At large values of $\frac{\chi}{k_r^*}$, the zero equilibrium tends to be not only the only equilibrium, but also unstable because the magnetic torque dominates. As $\tilde{x}_0$ increases, the central equilibrium tends toward stability. For two systems with three equilibria each and the same $\tilde{x}_0$, the system with the higher $\frac{\chi}{k_r^*}$ will have the higher critical kinetic energy.

5.5. Two Degrees of Freedom

1 DoF – Translational	1 DoF – Rotational	2 DoF – Rotational & Translational
Equilibrium Identification	Equilibrium Identification	Equilibrium Identification
Static Stability	Static Stability	Static Stability
Dynamic Stability	Dynamic Stability	Dynamic Stability

In this section, the two degree-of-freedom case (one translational, one rotational) will be discussed, with equilibria locations identified and classified as statically and dynamically stable and unstable. Figure 63 depicts the 2DoF, two coil system:

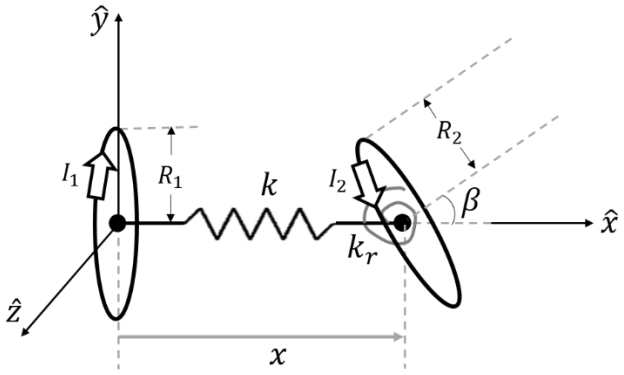

Figure 62: Two degree of freedom (2DoF) coil system

5.5.1. Force and Torque Balance

In the 2DoF case, as discussed in Section 3.4.1, both the force and torque equations as given in Equations (5.6), (5.8), (5.19), and (5.20) must sum to zero. In the 1DoF-T case, β was fixed as zero, and therefore the torque balance was automatically satisfied. As such, it is expected that the force balance along $\beta = 0$ will be the same in the 2DoF case as in the 1DoF-T case. The same is not true for the 1DoF-R case; $\tilde{x}$ in that case was fixed and was not selected to satisfy the force balance across the range of β values.

5.5.2. Equilibrium Identification

1 DoF – Translational	1 DoF – Rotational	2 DoF – Rotational & Translational
Equilibrium Identification	Equilibrium Identification	Equilibrium Identification
Static Stability	Static Stability	Static Stability
Dynamic Stability	Dynamic Stability	Dynamic Stability

Rather than solving for $\tilde{x}$ in terms of β as in the analytical case of Chapter 3, the numerical model will individually identify where total torque and force sum to zero and then determine for what values of $(\beta, \tilde{x})$ there is both a force balance *and* a torque balance. The plots in the next section identify where the sum of the torques equals zero with green circles, where the sum of the forces is zero with red circles, and where both the forces and torques are zero with black circles. This process is performed by calculating the force and torque at every discrete point in the domain and then using *crossing.m* to identify where the force and torque change signs/ cross zero in either β or $\tilde{x}$. The circles are plotted at the index before the crossing, which is why the plots are not perfectly symmetrical even though the system is symmetrical in actuality.

5.5.2.1. Example Equilibrium Identification

In this example 2DoF equilibrium identification, $\tilde{x}_0 = 2$ and each of $\frac{\chi}{k_r^*} = [0.1, 1, 10]$ are studied. Figure 63 shows the locations of the force (red) and torque (green) equilibria as well as where they overlap (black). Numbered dots are used for ease of reference to the black mutual equilibria on each diagram, either directly atop the mutual equilibrium if there is a clear singular point or next to it if there are a few. The numbering is only done on the left half of each diagram because, as has been shown in previous sections and chapters, the plots are symmetric, both in equilibrium location as well as stability, so only one of the two halves needs to be discussed.

The locations where a few points occur are due to one of several reasons. First, there are some portions of the graph (near $\beta_{4,1}$ in plot Figure 63b, for instance) where several mutual equilibria occur with close proximity to each other. In the studies of stability going forward, only one of these will be selected, since they all have similar stability conditions.

Second, around $\tilde{x} \approx 0.6$ in the following plots, a large number of force and/or torque equilibria can be observed for $|\beta| > 0.5$. The first thing to notice about this trend is that there are force equilibria in a repulsive system at $\tilde{x} < \tilde{x}_0$. That in itself can only happen when the magnetic force goes from positive (repulsive) to negative (attractive). This switching is a result of the coils actually coinciding at a certain angle (an extreme case of the proximity effect), wherein the edge of coil 2 basically touches the edge of coil 1 at $\beta = 0.5236$ when $\tilde{R}_2 = 1.2$ and $\tilde{x} = 0.6$. For $\beta > 0.5236$, the edge of coil 2 has actually swung behind the edge of coil 1, and thus the proximity effect contributes a dominating negative force. The torque due to the proximity effect also switches signs past that overlap point, which can create a torque equilibrium if the magnetic torque dominates the spring torque.

Finally, because the algorithm searches for crossings in both dimensions $(\beta, \tilde{x})$, sometimes the same equilibrium is identified by a circle before the equilibrium in β and a separate circle in $\tilde{x}$, leading to multiple circles representing the same equilibrium. As such, the discussion in the rest of this section and chapter will focus on the general trends of equilibria displayed in Figure 63 rather than analyzing every black circle.

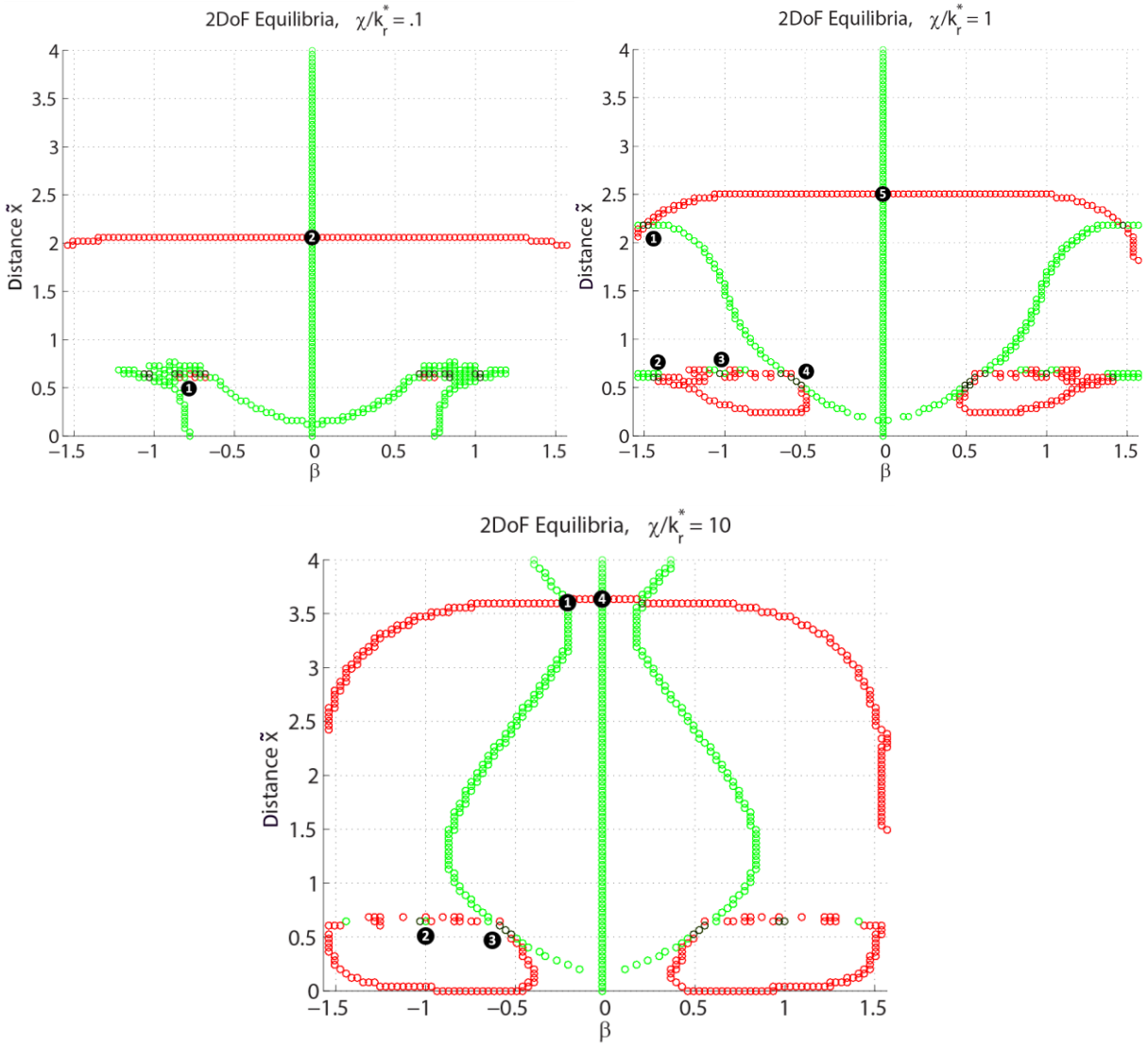

Figure 63: 2DoF equilibrium locations, red being force equilibria, green being torque equilibria, and black being equilibria in both. Only one of each mirrored pair of secondary equilibria is numbered, since they are symmetric and have the same stiffness and energy values. (a, left) $\frac{\chi}{k_r^*} = 0.1$*, (b, right)* $\frac{\chi}{k_r^*} = 1$*, and (c, bottom)* $\frac{\chi}{k_r^*} = 10$

Figure 63 displays some interesting trends. In Figure 63a, it can be seen that the $\beta = 0$ force equilibria (and those force equilibria bracketing it on either side) are very close to $\tilde{x}_0$ because of the small $\frac{\chi}{k_r^*}$ value; the spring does not stretch very much. As such, the curve of red circles is relatively flat. In Figure 63b and Figure 63c, the equivalent curves are more pronounced as the magnetic force falls off as β moves away from 0.

The torque curves are also interesting; in each of the three plots in Figure 63, there exist the expected $\beta = 0$ torque equilibria, but also a secondary concave up curve of torque equilibria. For $\frac{\chi}{k_r^*} = 0.1$, this secondary torque curve does not extend over the full range of $\tilde{x}$, just over small values of $\tilde{x}$. Remembering back to the 1DoF-R case, the secondary torque curve corresponds with secondary statically unstable

equilibria bracketing a central stable equilibrium. In the $\frac{\chi}{k_r^*} = 0.1$ case, these secondary torque equilibria only appear for small values of $\tilde{x}$, and none of them are mutual equilibria in force as well. For the intermediate $\frac{\chi}{k_r^*} = 1$ case, the secondary torque curve extends up to the main force equilibrium curve, where two secondary mutual equilibria can be seen. For the large $\frac{\chi}{k_r^*} = 10$ case, the secondary torque curve closes in on itself somewhat, drawing the secondary equilibria back towards $\beta = 0$. These observations indicate that a value of $\frac{\chi}{k_r^*}$ between 1 and 10 could be selected to result in secondary mutual equilibria at an angle anywhere in $0 \leq |\beta| \leq \pi/2$, though the resultant equilibrium distance $\tilde{x}$ would depend on that desired angle. It is also very likely from the 1DoF-R analysis that these secondary equilibria are statically unstable, a prediction that will be addressed in the next section.

Another topic of interest is what exactly is going on at the equilibria around $\tilde{x} \approx 0.6$.

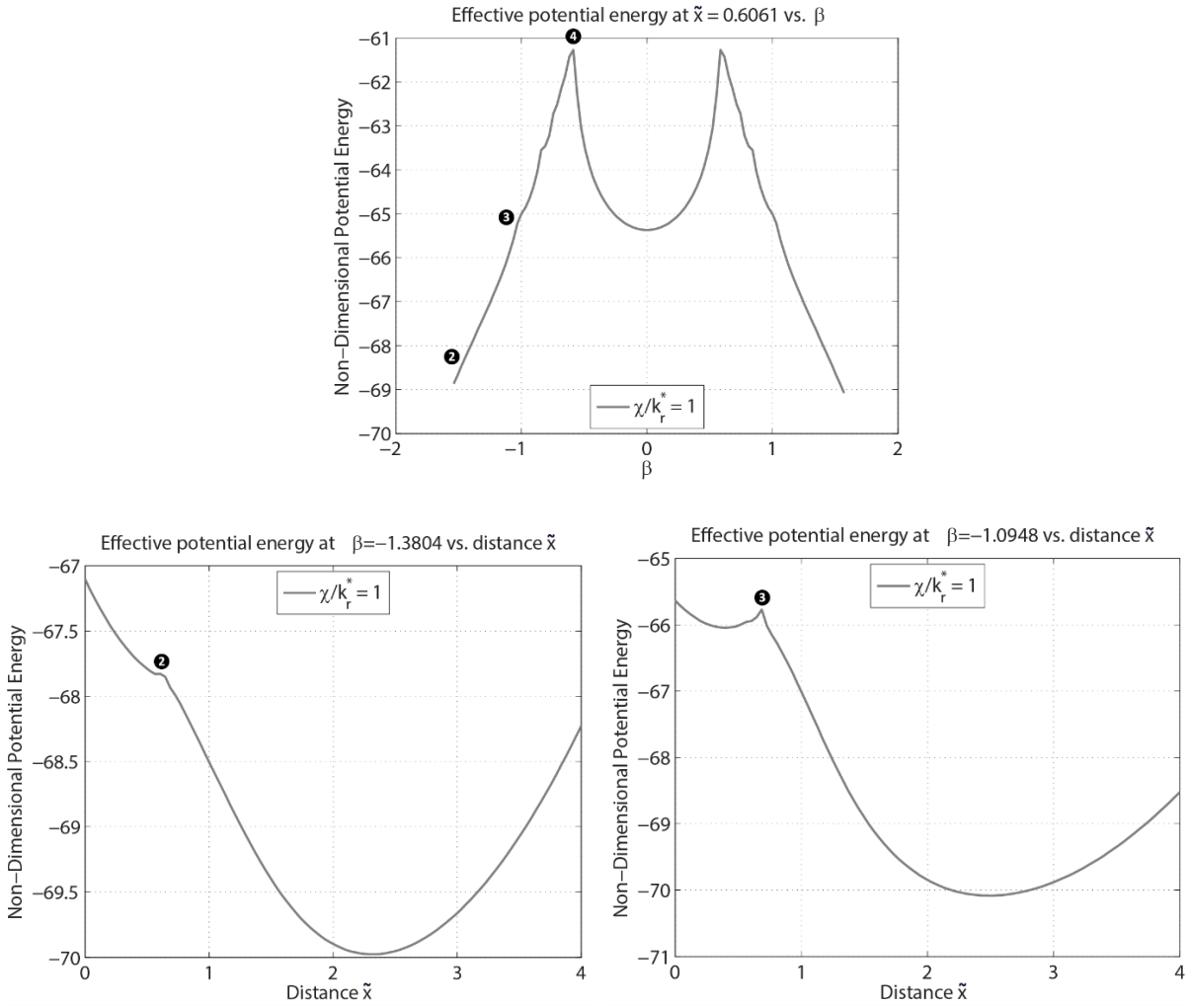

Figure 64: Cross-sectional view of potential energy curve at the $\frac{\chi}{k_r^*} = 1$ equilibria around $\tilde{x} \approx 0.6$, showing how equilibria $\beta_{2,1}$ and $\beta_{3,1}$ occur at local maxima in one direction ($\tilde{x}$, bottom two plots) but not in another direction (β, top plot).

Figure 64 focuses on equilibria $\beta_{2,1}$ and $\beta_{3,1}$ in the $\frac{\chi}{k_r^*} = 1$ case by presenting the cross-sectional views of the potential energy curve, showing that the equilibria occur at local maxima when viewed in one direction ($\tilde{x}$, bottom two plots), but not at a local extrema in another direction (β, top plot). The peaks in the bottom two plots in Figure 64 quickly disappear for points on either side of the equilibria, smoothing down to a monotonically decreasing functional. Figure 64 presents a graphical view of how static stability requires stability in all directions, not just one.

5.5.3. Static Stability Classification

1 DoF – Translational	1 DoF – Rotational	2 DoF – Rotational & Translational
Equilibrium Identification	Equilibrium Identification	Equilibrium Identification
Static Stability	Static Stability	Static Stability
Dynamic Stability	Dynamic Stability	Dynamic Stability

In this section, the static stability of the equilibria identified in Section 5.5.2, and Figure 63 will be calculated. As in Section 3.5.3, the stiffness is not a scalar but a 2x2 matrix in the 2DoF case, replicated below from Equation (3.102):

$$\left[K_{tot,ND}\right] = -\begin{bmatrix} \frac{\partial \tilde{F}_2}{\partial \tilde{x}} & \frac{\partial \tilde{F}_2}{\partial \beta} \\ \frac{\partial \tilde{\tau}_2}{\partial \tilde{x}} & \frac{\partial \tilde{\tau}_2}{\partial \beta} \end{bmatrix}.$$

For each of the numbered equilibria in Figure 63 (with a representative value picked from the clusters of mutual equilibria, or two if there's a difference in stability within a cluster), the stiffness matrix is constructed using centered finite differencing, and the eigenvalues of the stiffness matrix are calculated numerically, using MATLAB's eig() function. The eigenvalues are then given in Table 29, with the lines that have two positive eigenvalues (and are thus statically stable) bolded.

Table 29: Stiffness matrix eigenvalues for the 2DoF equilibria shown in Figure 63, with statically stable equilibria bolded

Equil. ID	$\frac{\chi}{k_r^*}$	β	$\tilde{x}$	λ_1	λ_2
$\beta_{1,0.1-1}$	0.1	-1.0661	0.6586	-52.77	54.70
$\boldsymbol{\beta_{1,0.1-2}}$	**0.1**	**-1.0409**	**0.6426**	**98.56**	**9.46**
$\boldsymbol{\beta_{2,0.1}}$	**0.1**	**0**	**2.0606**	**1.1221**	**1.0273**
$\beta_{1,1}$	1	-1.4756	2.1818	2.89	-1.45
$\beta_{2,1}$	1	-1.4194	0.6265	-93.0	25.0
$\beta_{3,1}$	1	-1.0313	0.6465	-51.39	-366.21
$\beta_{4,1}$	1	-0.5553	0.5657	49.12	-321.13
$\boldsymbol{\beta_{5,1}}$	**1**	**0**	**2.5051**	**1.61**	**0.99**
$\beta_{1,10}$	10	-0.2380	3.5960	2.6	-0.1
$\beta_{2,10}$	10	-1.0313	0.6465	-523	-3671.2
$\beta_{3,10}$	10	-0.5553	0.5657	482.1	-3220.4
$\boldsymbol{\beta_{4,10}}$	**10**	**0**	**3.6364**	**2.5**	**0.1**

From Table 29, it can be seen that all of the $\beta = 0$ equilibria are statically stable, and all other equilibria except for one of the secondary ones are statically unstable. These observations are consistent with predictions and the results from the 1DoF-T and 1DoF- R cases. The next section investigates the dynamic stability conditions on these statically stable equilibria.

5.5.4. Dynamic Stability

1 DoF – Translational	1 DoF – Rotational	2 DoF – Rotational & Translational
Equilibrium Identification	Equilibrium Identification	Equilibrium Identification
Static Stability	Static Stability	Static Stability
Dynamic Stability	Dynamic Stability	Dynamic Stability

In this section, the dynamic stability of the statically stable equilibria in the 2DoF complex numerical case is investigated, concluding the study of this system and drawing to a close the methodology development process.

The potential energy is once again used to explore the dynamic stability of the statically stable equilibria. As in the other dynamic stability analyses in this chapter, the magnetic potential energy is calculated by the vector potential method and subtracted from the elastic potential energy to obtain the effective potential energy of the system. In the 2DoF case, the elastic potential energy is given as the combination of contributions from both the linear and the torsional spring, or

$$\tilde{V}_{tot} = \tilde{V}_R + \tilde{V}_T = \frac{k_r^* \beta^2}{2} + \frac{k^* \tilde{x}^2}{2} - k^* \tilde{x}_0 \tilde{x} + \frac{k^* {\tilde{x}_0}^2}{2}. \tag{5.23}$$

The magnetic potential energy is the same as calculated in Section 5.3.4, with both the mutual inductance energy terms as well as the constant self-inductance energy terms for each configuration in β and $\tilde{x}$. Figure 65 shows the potential energy contours overlaid upon the equilibrium points from Figure 63 such that it can be seen that the $\beta = 0$ equilibria are at potential energy minima in each plot, with the statically unstable secondary equilibria occurring at saddle points in the potential energy curve. These conclusions are supported by the static stability analysis from the stiffness matrices in the previous section.

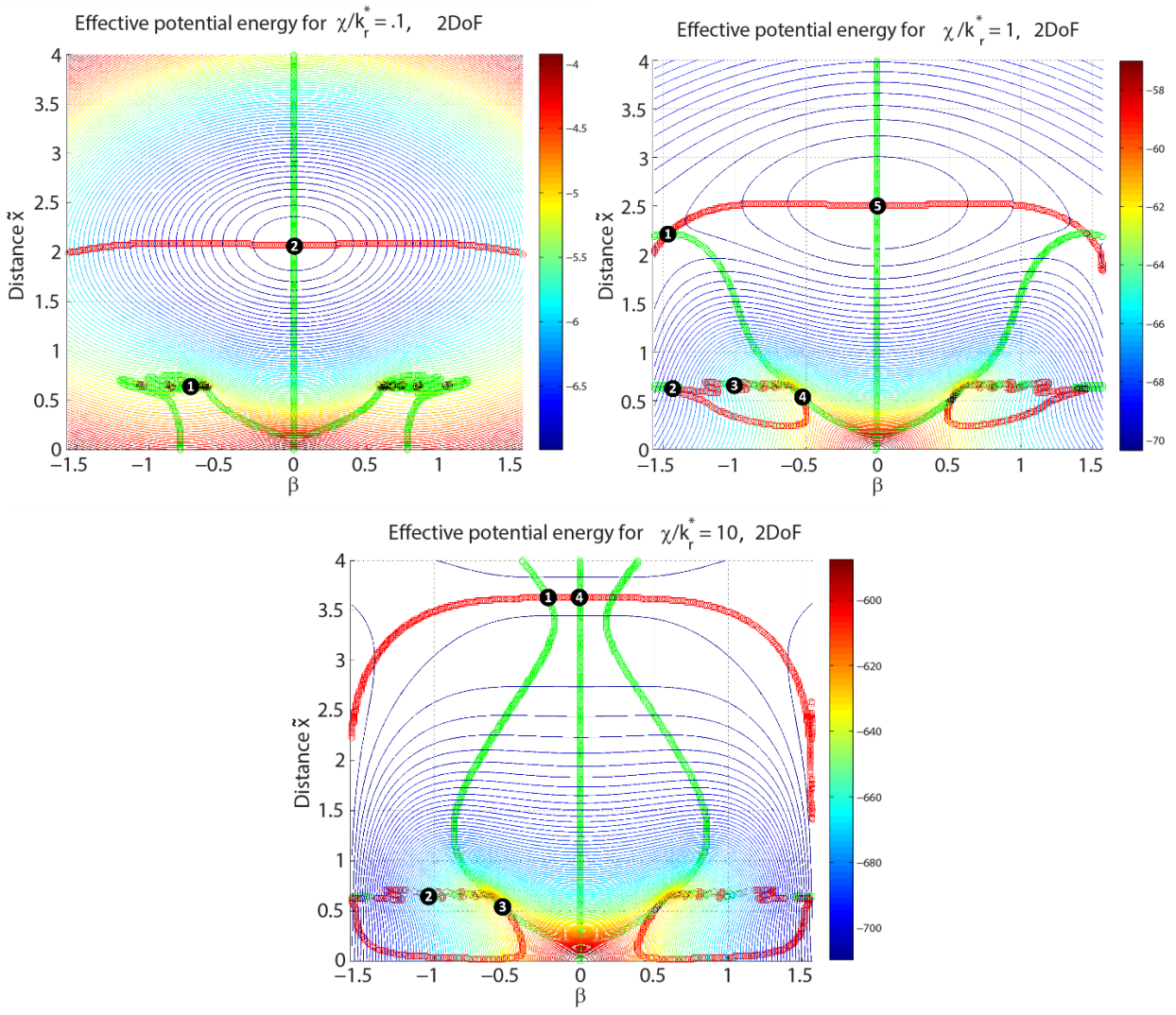

Figure 65: Potential energy contours for the 2DoF complex numerical case, overlaid upon the 2DoF equilibria in force, torque, or both; (a, left) $\frac{\chi}{k_r^*} = 0.1$*, (b, right)* $\frac{\chi}{k_r^*} = 1$*, and (c, bottom)* $\frac{\chi}{k_r^*} = 10$

The next section explores how the value of $\frac{\chi}{k_r^*}$ affects the critical initial kinetic energy of the system.

Critical Initial Kinetic Energy and Simulation

It can be seen from Figure 65 that the critical initial kinetic energies of the $\beta = 0$ equilibria are determined by the relative energies of the secondary equilibria along the upper force equilibrium curve, as motion in $\tilde{x}$ tends to increase the potential energy to a much higher level ($+\infty$ in the $+\tilde{x}$ direction and a peak at $\tilde{x} = 0$). Table 30 gives the critical initial kinetic energy for each of the $\beta = 0$ equilibria. In the case of Figure 65a or $\frac{\chi}{k_r^*} = 0.1$, the lack of a secondary equilibria along the upper force curve means that the limiting potential energy is taken as the potential energy at the ends of the upper force curve, at $\beta = \pi/2$, $\tilde{x} = 2$. It is possible that the potential energy continues to increase beyond $\beta = \pm\pi/2$ due to the elastic

potential energy increasing, but the magnetic potential energy begins to grow beyond $\beta = \pm\pi/2$ as the magnetic torque switches signs, thus reducing the effective potential energy.

Table 30: Critical initial kinetic energy for the 2DoF statically stable equilibria with the potential energy curves as seen in Figure 65

Equil. ID	$\frac{\chi}{k_r^*}$	β	$\tilde{x}$	λ_1	λ_2	$\tilde{T}_{t_0,crit}$
$\beta_{1,0.1-1}$	0.1	-1.0661	0.6586	-52.77	54.70	-
$\boldsymbol{\beta_{1,0.1-2}}$	**0.1**	**-1.0409**	**0.6426**	**98.56**	**9.46**	**0.0129**
$\boldsymbol{\beta_{2,0.1}}$	**0.1**	**0**	**2.0606**	**1.1221**	**1.0273**	**1.1016**
$\beta_{1,1}$	1	-1.4756	2.1818	2.89	-1.45	-
$\beta_{2,1}$	1	-1.4194	0.6265	-93.0	25.0	-
$\beta_{3,1}$	1	-1.0313	0.6465	-51.39	-366.21	-
$\beta_{4,1}$	1	-0.5553	0.5657	49.12	-321.13	-
$\boldsymbol{\beta_{5,1}}$	**1**	**0**	**2.5051**	**1.61**	**0.99**	**0.5553**
$\beta_{1,10}$	10	-0.2380	3.5960	2.6	-0.1	-
$\beta_{2,10}$	10	-1.0313	0.6465	-523	-3671.2	-
$\beta_{3,10}$	10	-0.5553	0.5657	482.1	-3220.4	-
$\boldsymbol{\beta_{4,10}}$	**10**	**0**	**3.6364**	**2.5**	**0.1**	**0.0027**

For $\frac{\chi}{k_r^*} = 1$, the limiting unstable equilibrium that determines the critical initial kinetic energy ends up being $\beta_{1,1}$ (with a potential energy of -69.9699) instead of $\beta_{4,1}$ (with a potential energy of -61.7432).

5.5.5. Summary

This chapter was the last step in a tiered and successively validated approach to evaluating the static and dynamic stability of a multi-coil constrained electromagnetic structure. Stable configurations have been found within the assumptions and constraints levied on the system, and the approaches for calculating static and dynamic stability are valid in any number of degrees of freedom. Now that it has been validated in many ways against a tractable two-coil, 2DoF problem, the approach developed over the last three chapters can be expanded to evaluate problems with more degrees of freedom or different assumptions, such as the example real-world problems discussed in the next chapter.

Chapter 6
Application to Real-World Problems

The three primary goals of the methodology presented in Chapters 3, 4, and 5 are to be (1) useful, (2) scalable, and (3) plausible. Now that the methodology has been validated and nondimensionalized, making it useful to spacecraft designers, it can be expanded to investigate other structures with more degrees of freedom (scalability) and how changing the assumptions affects the results of the analysis (plausibility). The numerical methods for finding equilibria, determining their static stability via stiffness, and calculating the potential energy functional to examine dynamic stability, are all extensible to models with more degrees of freedom or changes in design variables.

This chapter presents two "real-world problems" that represent scalability and plausibility of the methodology respectively: adding a third coil to the previously two-coil system and noting trends or features that persist in such systems beyond two coils, as well as exploring how using different elastic connecting hardware such as tethers changes the stability of the system. The former will be investigated much like the two-coil system by starting with a single degree of freedom in translation for each of the second and third coils then investigating a single degree of freedom in rotation for each of the second and third coils, both of which are 2DoF problems. The equilibria will be identified, and their static and dynamic stabilities evaluated. The analysis of how using tethers instead of springs to connect the coils affects the assumptions and results will be performed on the already established two-coil system after the three-coil analysis.

6.1. Three Coils

As in the two coil case, the three coil system is modeled as a boom, with each coil centered along the x axis. Each is connected by a linear spring to the one directly adjacent to it, and coils 2 and 3 have torsional springs that provide resistance to rotation around the z axis. In this model, the torsional spring torque is proportional to the angle with respect to the x axis, not with respect to the angle of the coil adjacent to it. Figure 66 shows the degrees of freedom of the three coil system featured in this chapter, where β_3 is the angle of rotation of coil 3 around the z axis, and the distances between adjacent coils are x_2 and x_3. Coil 3 is assumed to have the same radius as coil 2 unless otherwise specified in order to reduce the number of unique parameters in the problem. Also, $|I_1| = |I_2| = |I_3|$, and I_1 and I_3 run in the same direction, such that coils 1 and 2 repel, and coils 2 and 3 repel, though there is an attractive force between coils 1 and 3. The natural length of each of the two linear springs are assumed to be equal and equivalent to $\tilde{x}_0 = 2$, and the spring constants are considered to all be equal to one another.

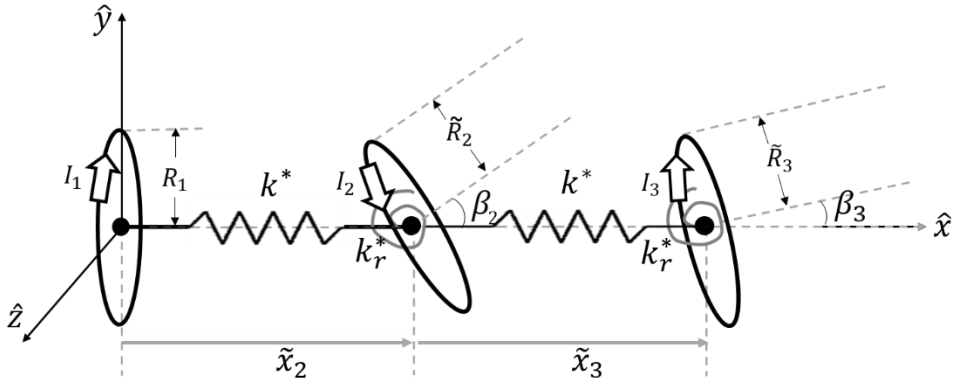

Figure 66: General four degree of freedom (4DoF) three-coil system

Two systems will be examined: 2DoF-T (both coils 2 and 3 translating) and 2DoF-R (both coils 2 and 3 rotating). It is not particularly worthwhile to examine a three-coil system with one rotational and one translational degree of freedom, since one or more of the coils would not be in a force and/or torque balance as the other moves.

6.1.1. 2DoF Translation

When both coils 2 and 3 are allowed to translate, a system of two equations must be solved to find the equilibrium positions of each of coils 2 and 3 with respect to the origin, one for each of coils 2 and 3. Figure 67 shows the non-dimensional 2DoF-T three-coil system being explored in this section.

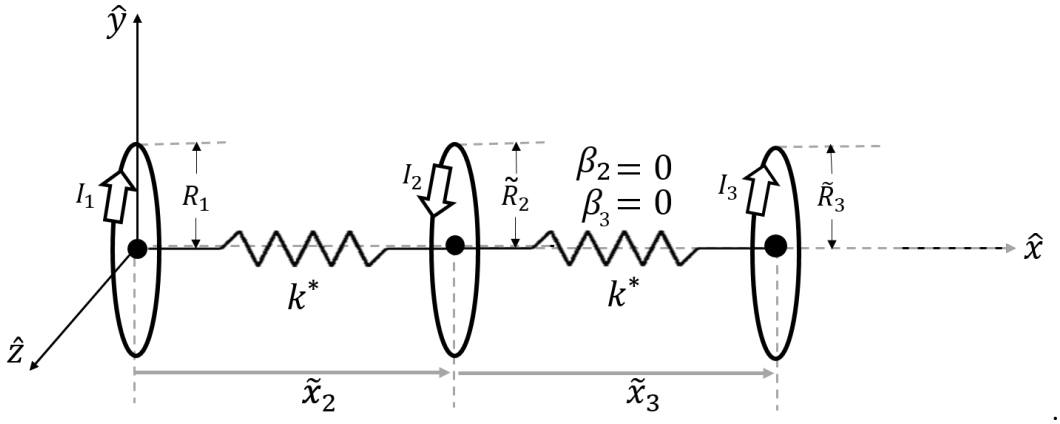

Figure 67: 2DoF-T three-coil system

In a three coil system, there is a magnetic interaction between each discrete pair of coils (1 and 2, 1 and 3, and 2 and 3) based on the distance apart ($\tilde{x}_2, \tilde{x}_2 + \tilde{x}_3$ and $\tilde{x}_3$ respectively), as well as an elastic force between each adjacent pair of coils (1 and 2 or 2 and 3) based on the distances between adjacent coils (x_2 and x_3 respectively). The two non-dimensional translational equations that must be satisfied along the x axis for equilibrium are

$$\tilde{F}_{total,2} = \tilde{F}_{spring,21} + \tilde{F}_{spring,23} + \tilde{F}_{mag,21} + \tilde{F}_{mag,23} = 0, \tag{6.1}$$

and

$$\tilde{F}_{total,3} = \tilde{F}_{spring,32} + \tilde{F}_{mag,31} + \tilde{F}_{mag,32} = 0. \tag{6.2}$$

However, with the spring forces substituted in and reducing the number of magnetic forces by substituting in negatives where applicable,

$$-k^*(\tilde{x}_2 - \tilde{x}_0) + k^*(\tilde{x}_3 - \tilde{x}_0) + \tilde{F}_{mag,21} - \tilde{F}_{mag,32} = 0, \tag{6.3}$$

and

$$-k^*(\tilde{x}_3 - \tilde{x}_0) + \tilde{F}_{mag,31} + \tilde{F}_{mag,32} = 0, \tag{6.4}$$

since $\tilde{R}_2 = \tilde{R}_3$, $\tilde{F}_{mag,21}$ and $\tilde{F}_{mag,31}$ are calculated as in Equation (5.6). $\tilde{F}_{mag,32}$ is calculated slightly differently but with similar definitions as in Equation (5.6), because it is based on the magnetic field from coil 2 instead of coil 1, such that

$$\tilde{\vec{F}}_{mag,32} = -\frac{\mu_0 N I^2 \mathcal{T}^2}{4\pi^2 \tilde{R}_2 \rho R_1^2} \int_{coil\ 3} d\tilde{\vec{l}}_3 \times \tilde{\vec{B}}_2, \tag{6.5}$$

where

$$\tilde{\vec{B}}_2 = \frac{1}{\tilde{\alpha}^2 \tilde{\eta} \tilde{v}^2} \begin{bmatrix} \tilde{v}^2 \left[\left(\tilde{R}_2{}^2 - \tilde{r}^2 \right) E(k^2) + \tilde{\alpha}^2 K(k^2) \right] \\ \tilde{x}\tilde{y} \left[\left(\tilde{R}_2{}^2 + \tilde{r}^2 \right) E(k^2) - \tilde{\alpha}^2 K(k^2) \right] \\ \tilde{x}\tilde{z} \left[\left(\tilde{R}_2{}^2 + \tilde{r}^2 \right) E(k^2) - \tilde{\alpha}^2 K(k^2) \right] \end{bmatrix}.$$

Before scaling each by R_1 or R_1^2, the other variables appearing in the previous equation are

$$a = \tilde{R}_2,$$

$$v^2 = y^2 + z^2,$$

$$r^2 = x^2 + y^2 + z^2,$$

$$\alpha^2 = a^2 + r^2 - 2av,$$

$$\eta^2 = a^2 + r^2 + 2av,$$

and

$$k^2 = 1 - \frac{\alpha^2}{\eta^2}.$$

Translational equilibria are identified by finding where both Equations (6.1) and (6.2) are fulfilled in $(\tilde{x}_3, \tilde{x}_2)$. This section finds the translational equilibria and investigates the stability of coils with the same radius ($R_1 = 1, \tilde{R}_2 = 1, \tilde{R}_3 = 1$), then does the same for coils of different radii ($R_1 = 1, \tilde{R}_2 = 1.2, \tilde{R}_3 = 1.5$).

Coils of the Same Radius

Figure 68 shows the equilibria of a system wherein all coils have a radius of 1 and for each of $\frac{\chi}{k^*} = [0.1, 1, 10]$ by plotting red circles for a force balance on coil 2, green circles for a force balance on coil 3, and black circles for a mutual force balance. In order to focus visually on the trends in equilibria as $\tilde{x}_2, \tilde{x}_3$ change (or β_2, β_3 in the next section), rather than going through the full stiffness analysis for every curve in this chapter, static stability is instead determined by observing the shape of the potential energy curve at each equilibrium point.

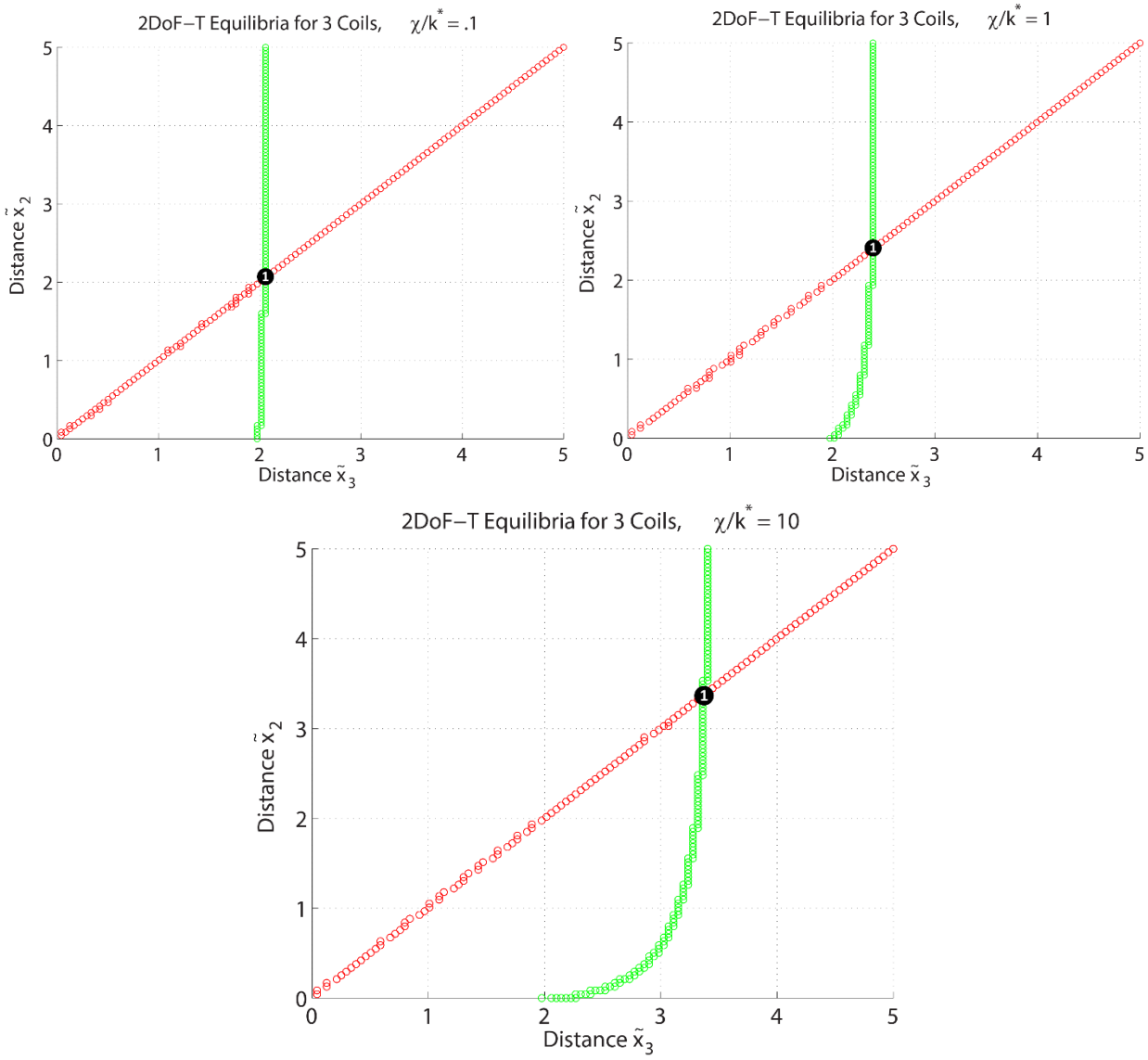

Figure 68: 2DoF-T equilibrium locations for three coils all of radius 1, red being force equilibria on coil 2, green being force equilibria on coil 3, and black being equilibria in both; (a, left) $\frac{\chi}{k^*} = 0.1$, *(b, right)* $\frac{\chi}{k^*} = 1$,*and (c, bottom)* $\frac{\chi}{k^*} = 10$

It can be seen from Figure 68 that as $\frac{\chi}{k^*}$ increases, the equilibrium distance in both $\tilde{x}_2$ and $\tilde{x}_3$ increases. This behavior is intuitive, as is the fact that $\tilde{x}_{2,eq} = \tilde{x}_{3,eq}$, since the coils all have the same radius, meaning that coil 2 will always be centered between coils 1 and 3 at equilibrium. Because of the centering at equilibrium, the red circles in Figure 68 are always along the line $\tilde{x}_2 = \tilde{x}_3$. The green circles start out almost vertical (constant in $\tilde{x}_3$ at the natural length of the spring, 2) for small $\frac{\chi}{k^*}$, but as $\frac{\chi}{k^*}$ increases, the green circles increase in $\tilde{x}_3$ as $\tilde{x}_2$ increases. This curving behavior can be traced back to the initial model as presented in Figure 67; the distance between coils 1 and 3 is equal to $\tilde{x}_2 + \tilde{x}_3$, so when $\tilde{x}_2 = 0$ (coils 1 and 2 collocated), the net magnetic force on coil 3 is zero because coils 1 and 2 cancel each other's force contributions out due to their opposing current directions. As $\tilde{x}_2$ increases, the repulsive force from coil 2 upon coil 3 dominates the attractive force from coil 1 upon coil 3, increasing the distance $\tilde{x}_3$ at which coil 3 is in equilibrium.

-

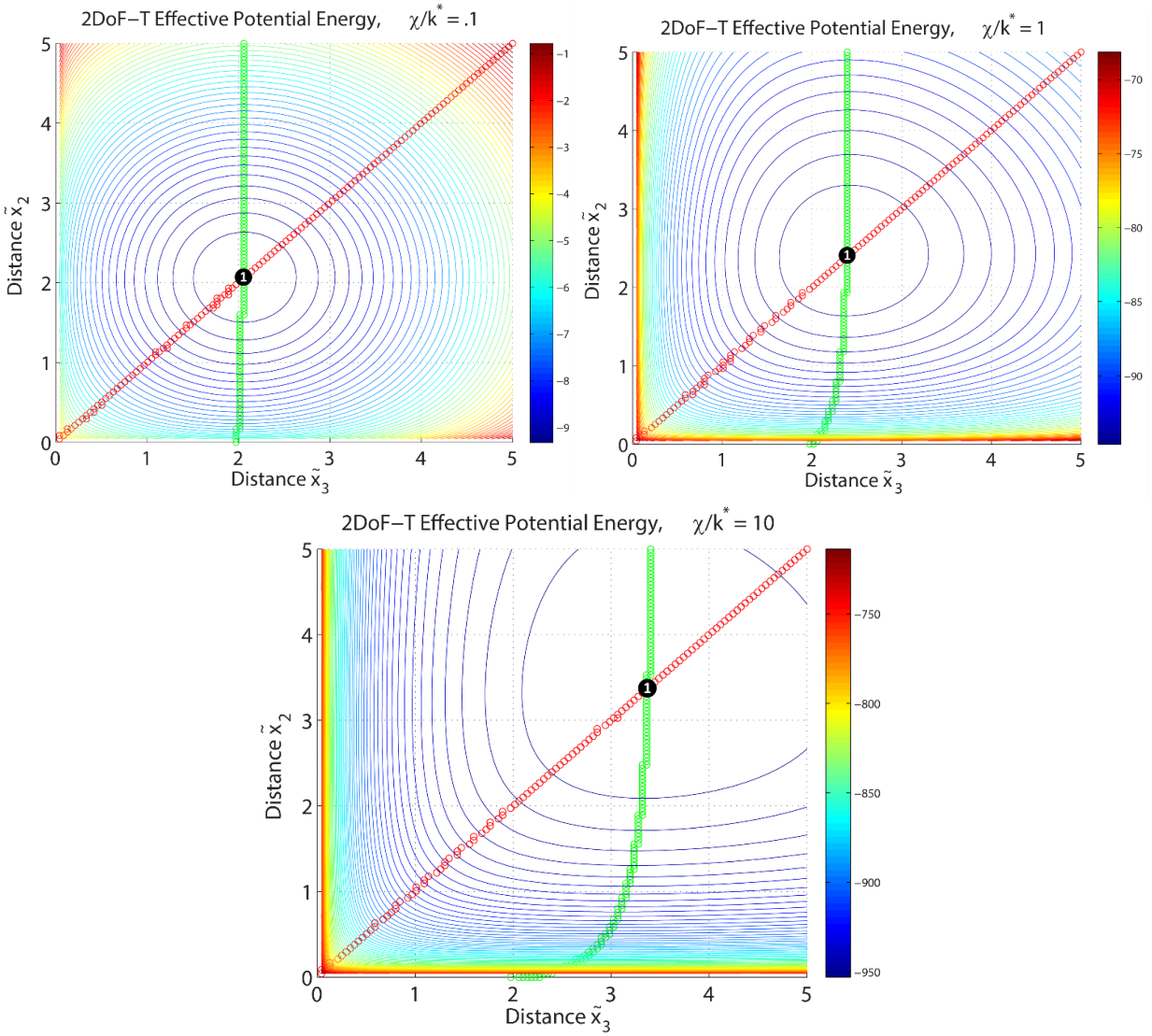

Figure 69: Effective potential energy curves of the 2DoF-T system for three coils all of radius 1, red being force equilibria on coil 2, green being force equilibria on coil 3, and black being equilibria in both; (a, left) $\frac{\chi}{k^*} = 0.1$*, (b, right)* $\frac{\chi}{k^*} = 1$*, and (c, bottom)* $\frac{\chi}{k^*} = 10$

Figure 69 shows the effective potential energy curves for the three-coil identical radius 2DoF-T system, indicating that the equilibria from Figure 68 all occur at a global minimum in the potential energy functional, making them statically and globally dynamically stable (within the boundary conditions that $\tilde{x}_2, \tilde{x}_3 \geq 0$). The next section discusses the rotational equilibria positions and stability of a three coil system with different sized coils.

Coils of Different Radii

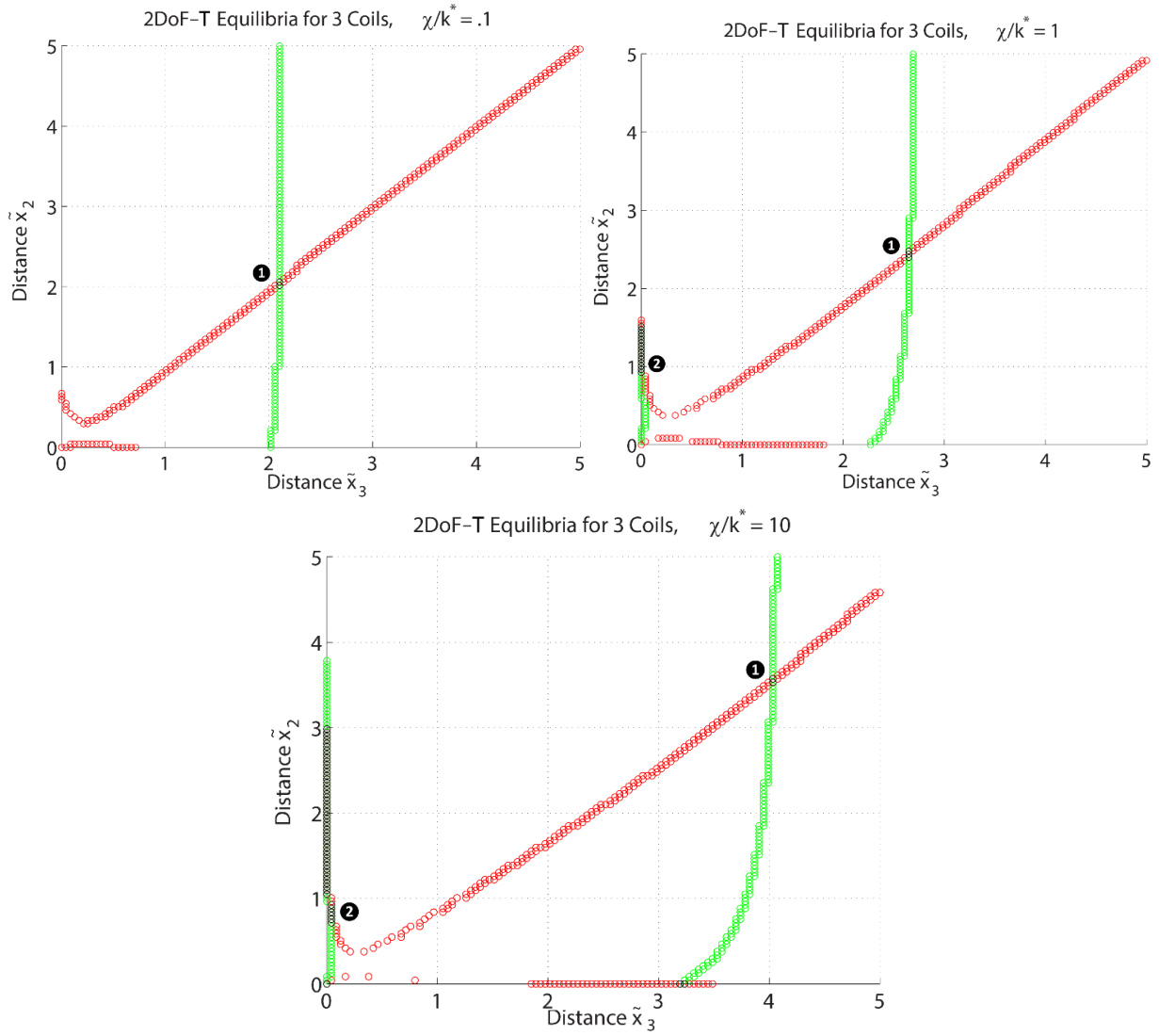

Figure 70: 2DoF-T equilibrium locations for three coils of radius $R_1 = 1, \widetilde{R_2} = 1.2, and\ \widetilde{R_3} = 1.5$*, red being force equilibria on coil 2, green being force equilibria on coil 3, and black being equilibria in both; (a, left)* $\frac{\chi}{k^*} = 0.1$*, (b, right)* $\frac{\chi}{k^*} = 1$*, and (c, bottom)* $\frac{\chi}{k^*} = 10$

When the coils all have different radii (with radius increasing from coil 1 through coil 3), as in Figure 70, the equilibria are similar, with a few notable differences. As $\frac{\chi}{\mathrm{k}^*}$ increases, the red circles no longer follow the line $\tilde{x}_2 = \tilde{x}_3$ but rather an almost-linear curve with a decreasing slope, such that coil 2 is closer to coil 1 than coil 3 at equilibrium. This behavior makes sense because coil 3 exerts a larger repulsive force on coil 2 than on coil 1 because coil 3 is bigger than coil 1.

The equilibria near $\tilde{x}_2 = 0$ occur because when coils 1 and 2 are concentric, they exert no x axis force on one another, and the net force on coil 2 is thus negative, from coil 3 only. As soon as coil 2 moves slightly away from coil 1, coil 1 dominates and the force goes from negative to positive. The same effect occurs

when $\tilde{x}_3 = 0$, such that coils 2 and 3 are concentric with a net negative force from coil 1 on coil 3 and a net positive force from coil 1 on coil 2, both of which change signs soon after coils 2 and 3 move apart, causing the curving behavior of the coil 2 (red) equilibria as $\tilde{x}_2, \tilde{x}_3 \to 0$. The curving effect is due to the resultant force from coil 3 or coil 1 on two not being immediately parallel to the x axis because of the difference in radius between the coils. The mutual equilibria seen along $\tilde{x}_3 = 0$ (numbered with a 2 in Figure 70) are expected to be statically and dynamically unstable as a result of the immediate repulsive forces when $\tilde{x}_3 > 0$.

Figure 71, depicting the effective potential energy of the different-radii system, is very similar to Figure 69; all of the equilibria occur at the global minimum of the system (which is known to be the minimum beyond the bounds depicted, because as the coils all get farther apart, the magnetic potential energy goes to zero, and the elastic potential energy grows as the springs continue to stretch beyond the distances presented in the above plots). Therefore, all of the force equilibria when $\tilde{x}_2, \tilde{x}_3 \geq \tilde{x}_0$ are statically stable and globally dynamically stable. The equilibria near $\tilde{x}_3 = 0$ occur along the top of a ridge in the potential energy functional, making them statically unstable as expected.

In general, the 2DoF-T results for the three coil system are consistent with the 1DoF-T results for two coils: a single statically stable equilibrium in repulsion, with the addition of interesting unstable equilibria in locations where 2 or more of the coils are concentric due to the third coil's influence. In the next section, equilibria in two rotational degrees of freedom (2DoF-R) are discussed, with some less intuitive and more interesting results.

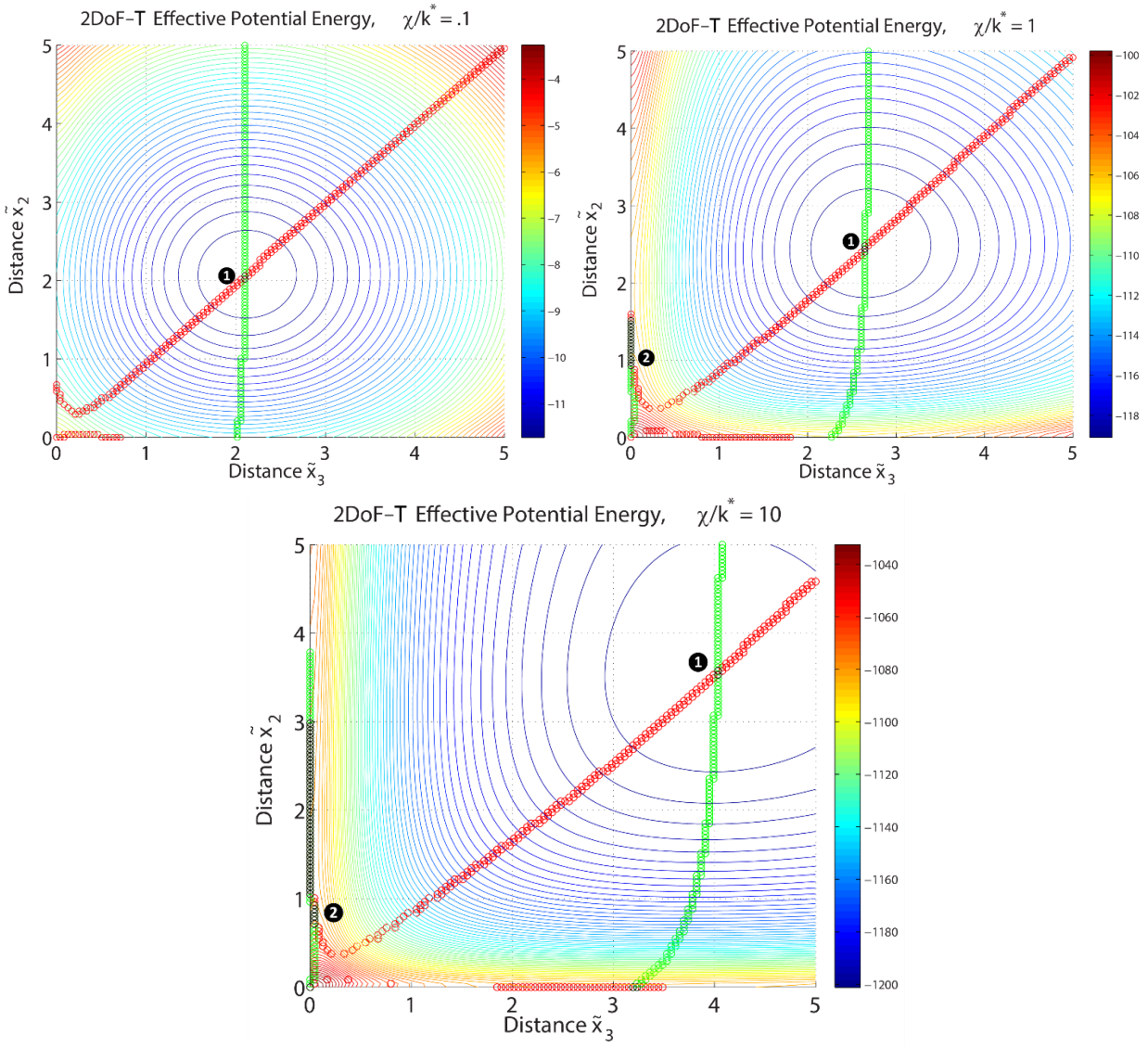

Figure 71: Effective potential energy curves of the 2DoF-T system for three coils of radius $R_1 = 1, \tilde{R}_2 = 1.2,$ *and* $\tilde{R}_3 = 1.5$*, red being force equilibria on coil 2, green being force equilibria on coil 3, and black being equilibria in both; (a, left)* $\frac{\chi}{k^*} = 0.1$*, (b, right)* $\frac{\chi}{k^*} = 1$*, and (c, bottom)* $\frac{\chi}{k^*} = 10$

6.1.2. 2DoF Rotation

Similar to the 2DoF translation case, the 2DoF rotation case requires solving a system of two equations for where both equal zero, except in the rotation case where the equations that are balanced are torques, not forces. Figure 72 shows the 2DoF-R three-coil system being explored in this section, in which the coils have all been fixed in place along the x axis, and coils 2 and 3 are allowed to rotate around the z axis between $\pm\frac{\pi}{2}$.

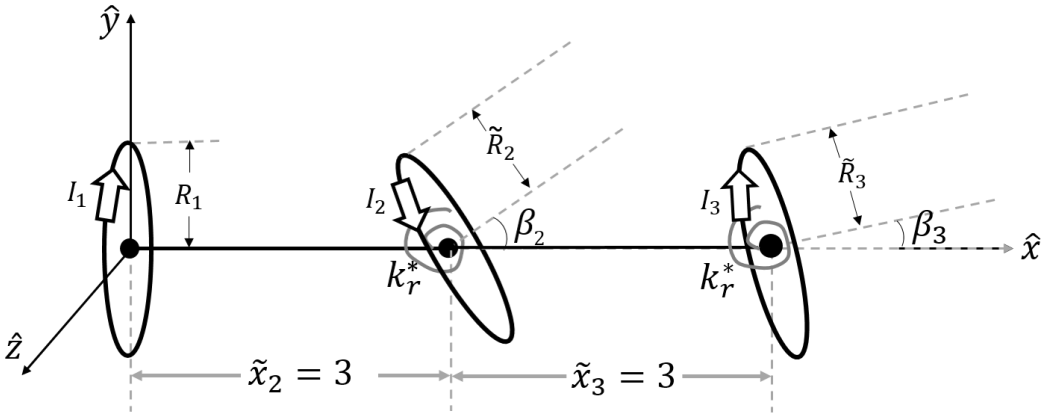

Figure 72: 2DoF-R three-coil system

The separation distances between the coils have been set to 3 such that when the different-radii case is studied, the coils do not overlap at all, even when $\beta_3 = \beta_2 = \pm\frac{\pi}{2}$. Also, as opposed to the 2DoF translation case, each torsional spring just exerts a torque on one coil with respect to the x axis, not both coils, such that combined with the magnetic interactions, the two non-dimensional rotational equations that must be satisfied around the z axis for equilibrium are

$$\tilde{\tau}_{total,2} = \tilde{\tau}_{spring,2} + \tilde{\tau}_{mag,21} + \tilde{\tau}_{mag,23} = 0, \tag{6.6}$$

and

$$\tilde{\tau}_{total,3} = \tilde{\tau}_{spring,3} + \tilde{\tau}_{mag,31} + \tilde{\tau}_{mag,32} = 0, \tag{6.7}$$

or, in which the spring torques are substituted:

$$-k_r^*\beta_2 + \tilde{\tau}_{mag,21} + \tilde{\tau}_{mag,23} = 0, \tag{6.8}$$

and

$$-k_r^*\beta_3 + \tilde{\tau}_{mag,31} + \tilde{\tau}_{mag,32} = 0. \tag{6.9}$$

Rotational equilibria are identified by finding where both Equations (6.6) and (6.7) are fulfilled in (β_3, β_2). This section finds the rotational equilibria and investigates the stability of coils with the same radius ($R_1 = 1, \tilde{R}_2 = 1, \text{and } \tilde{R}_3 = 1$) then proceeds to do the same for coils of different radii ($R_1 = 1, \tilde{R}_2 = 1.2,$ and $\tilde{R}_3 = 1.5$).

Coils of the Same Radius

Figure 73 shows the rotational equilibria of a system wherein all coils have a radius of 1 and for each of $\frac{\chi}{k_r^*} = [1, 2, 3, 4, 5, 10]$ by plotting red circles for a torque balance on coil 2, green circles for a torque balance on coil 3, and black circles for a mutual torque balance. The $\frac{\chi}{k_r^*}$ values were selected to display a range of interesting behaviors.

All of the plots in Figure 73 have equilibria at $\beta_3, \beta_2 = 0$, which is expected when all the coils are parallel to each other and is reflected in the results of the 1DoF-R case in Chapter 5. As $\frac{\chi}{k_r^*}$ increases, the equilibria circles in Figure 73 rotate around the central point $\beta_3, \beta_2 = 0$, a general indication that a coil can rotate more before the torque from its torsional spring (or the influence of coil 1) is large enough to balance with the magnetic torque induced by the other rotating coil. Because there are so many plots in Figure 73, analysis is given for each in order below for clarity.

When $\frac{\chi}{k_r^*} = 1$ (Figure 73a), the net magnetic torque on coil 3 is weak enough from any rotation in β_2 that the equilibrium position (green) of coil 3 is barely perturbed from 0, but positive torque is induced from a positive rotation in β_2 as expected from the tendency of a coil to align with an external magnetic field, in this case the one generated by coil 2. Coil 2 is equidistant from coils 1 and 3, each of which is aligned in the same direction and thus exerts the same direction torque once perturbed so that a positive rotation in β_3 induces a positive rotation in β_2 as well. Because of the equivalent proximity of coils 1 and 3, a larger torque is expected on coil 2 than on coil 1 (which would result in the range of red circles in β_2 to be larger), but since $\frac{\chi}{k_r^*}$ is so small, the spring torque dominates at too small an angle for there to be a noticeable difference in maximum rotation in this torque plot.

When $\frac{\chi}{k_r^*} = 2$ (Figure 73b), however, the difference in maximum rotation of equilibrium is noticeable, with red circles spanning roughly $-0.4 \leq \beta_2 \leq 0.4$ but green circles spanning roughly $-0.25 \leq \beta_3 \leq 0.25$. Also of interest in this plot are the two elliptical paths of coil 2 equilibria (red) that occur when coil 2 rotates beyond about 1 radian in either direction (positive β_2 equilibria happen at positive β_3). Picking the $\beta_3 = 0$ line to examine for simplicity, it can be seen that these equilibria occur because the magnetic torque (coils 1 and 3 exerting torque in the same direction) at a certain angle is strong enough (compared to the previous case) to dominate the torsional spring's resistive torque, causing the region inside the elliptical paths to be a region where the torque on coil 2 has switched signs due to the dominance of the magnets. However, while the maximum magnetic torque on coil 2 from coils 1 and 3 occurs at $\beta_2 = \pm\frac{\pi}{2}$, so does the maximum spring torque, and the spring torque increases linearly whereas the magnetic

torque increases at a decreasing rate, so there's a point near $\beta_2 = \pm\frac{\pi}{2}$ where the spring torque once again dominates over the magnetic torque to change the sign of the torque. The elliptical regions do not extend at both the top and the bottom for all β_3; for $|\beta_3|$>0.6, there only exist these secondary equilibria for coil 2 in the same direction as β_3. This is because when coil 3 is significantly rotated away from coil 1, there is no point in the other direction for which coil 2's magnetic torque in that direction dominates the restorative spring torque.

When $\frac{\chi}{k_r^*} = 3$ (Figure 73c), the elliptical paths of coil 2 equilibria disappear, replaced by a small region from roughly $-0.4 \leq \beta_3 \leq 0.4$ within which three coil 2 equilibria exist versus just one everywhere else. These secondary equilibria exist because the magnetic torque is stronger in this case than the previous one, meaning that a smaller rotation is required to reach a magnetic torque that will dominate the spring torque (recalling that the magnetic torque between two coils goes from a minimum when the coils are parallel to a maximum when one is perpendicular to the other).

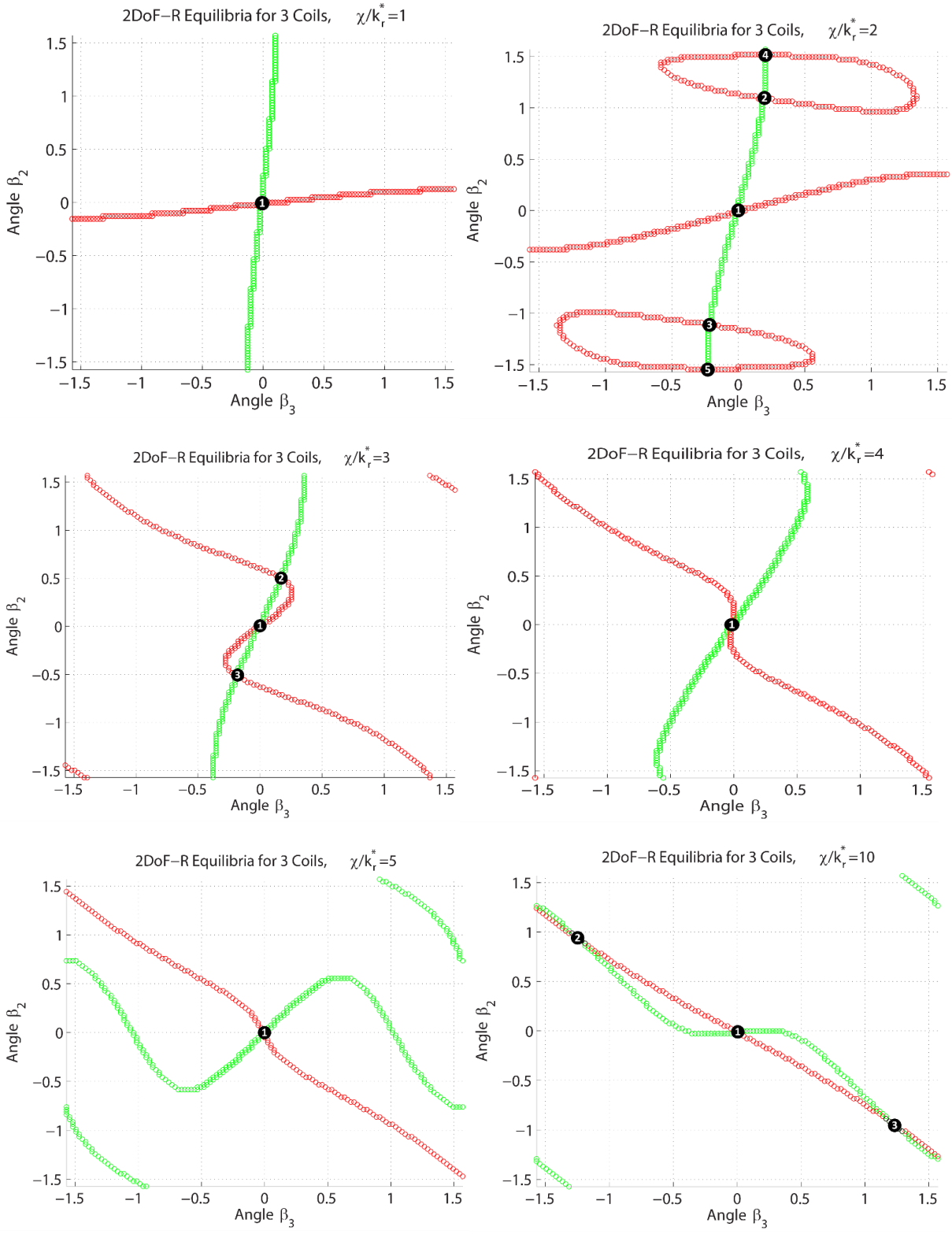

Figure 73: 2DoF-R equilibrium locations for three coils of radius 1, where red is torque equilibria on coil 2, green is torque equilibria on coil 3, and black is equilibria in both; (a, top left) $\frac{\chi}{k_r^*} = 1$*, (b, top right)* $\frac{\chi}{k_r^*} = 2$*, (c, mid left)* $\frac{\chi}{k_r^*} = 3$*, (d, mid right)* $\frac{\chi}{k_r^*} = 4$*, (e, bottom left)* $\frac{\chi}{k_r^*} = 5$*, and (f, bottom right)* $\frac{\chi}{k_r^*} = 10$

When $\frac{\chi}{k_r^*} = 4$ (Figure 73d), the secondary equilibria have disappeared, because now the divergent magnetic torque is strong enough to dominate the restorative spring at even a small rotation from zero. It would therefore be expected that the equilibrium at $\beta_3, \beta_2 = 0$ is now unstable although previously it had been stable. It can be seen that the line of coil 3 (green) equilibria is relatively similar throughout the first four plots of Figure 73, albeit rotating clockwise from plot to plot as the magnetic torque increases, thus increasing the angle at which the magnetic spring torque on coil 3 finally dominates.

When $\frac{\chi}{k_r^*} = 5$ (Figure 73e), the coil 2 curve of equilibria has not changed significantly, since the magnetic torque is already dominating on coil 2; however, the coil 3 curve of equilibria has changed significantly from the previous plot, now having three equilibria for some values of β_2. This is because coil 3 is now going through the same phase that coil 2 did earlier (recalling that coil 3 does not experience as strong an additional contribution from coil 1 as does coil 2), wherein for the same β_2, there is a region of β_3 values for which magnetic torque dominates until the spring torque finally matches it. Outside of that region, the spring torque dominates. For values of β_2 outside of that three-equilibrium region, roughly $-0.6 \leq \beta_2 \leq 0.6$, the only equilibrium for coil 3 is when it twists significantly in the same direction as coil 2. The only reason these equilibria aren't all at $\pm\frac{\pi}{2}$ (at which point coils 2 and 3 would be in a configuration where their magnetic moments are aligned with the external field generated by the other) is that coil 1 exerts a small restorative magnetic torque on coil 3 because they begin in an aligned state at $\beta_3 = 0$.

When $\frac{\chi}{k_r^*} = 10$ (Figure 73f), the two lines of equilibria are far closer together now that the magnetic torque on both coils dominates the spring torque no matter the angle of the other coil (except right at $\beta_2 = 0$). Secondary equilibria appear at roughly $(1.25, -1)$ and $(-1.25, 1)$ and effectively continue out along the joining of the two curves to $\beta_3 = \pm\frac{\pi}{2}$. These secondary equilibria are interesting because if this were a system consisting of just coils 2 and 3, there would never be equilibria near or at $\beta_3 = -\beta_2 = \pm\frac{\pi}{2}$, given that the configuration makes coils 1 and 2 anti-aligned with the other's magnetic field and the influence of the torsional spring, no matter how small compared to the magnetic torque, would make equilibrium impossible. However, because of the influence of coil 1, there exists a very specific orientation of coils 2 and 3 such that both coils 2 and 3 have a net torque of zero in this region of the design space. They are expected to be unstable, due to the general anti-alignment of the system, but these equilibria are still interesting features specific to a three coil system.

Figure 74 shows the potential energy curves of the systems and equilibria depicted in Figure 73.

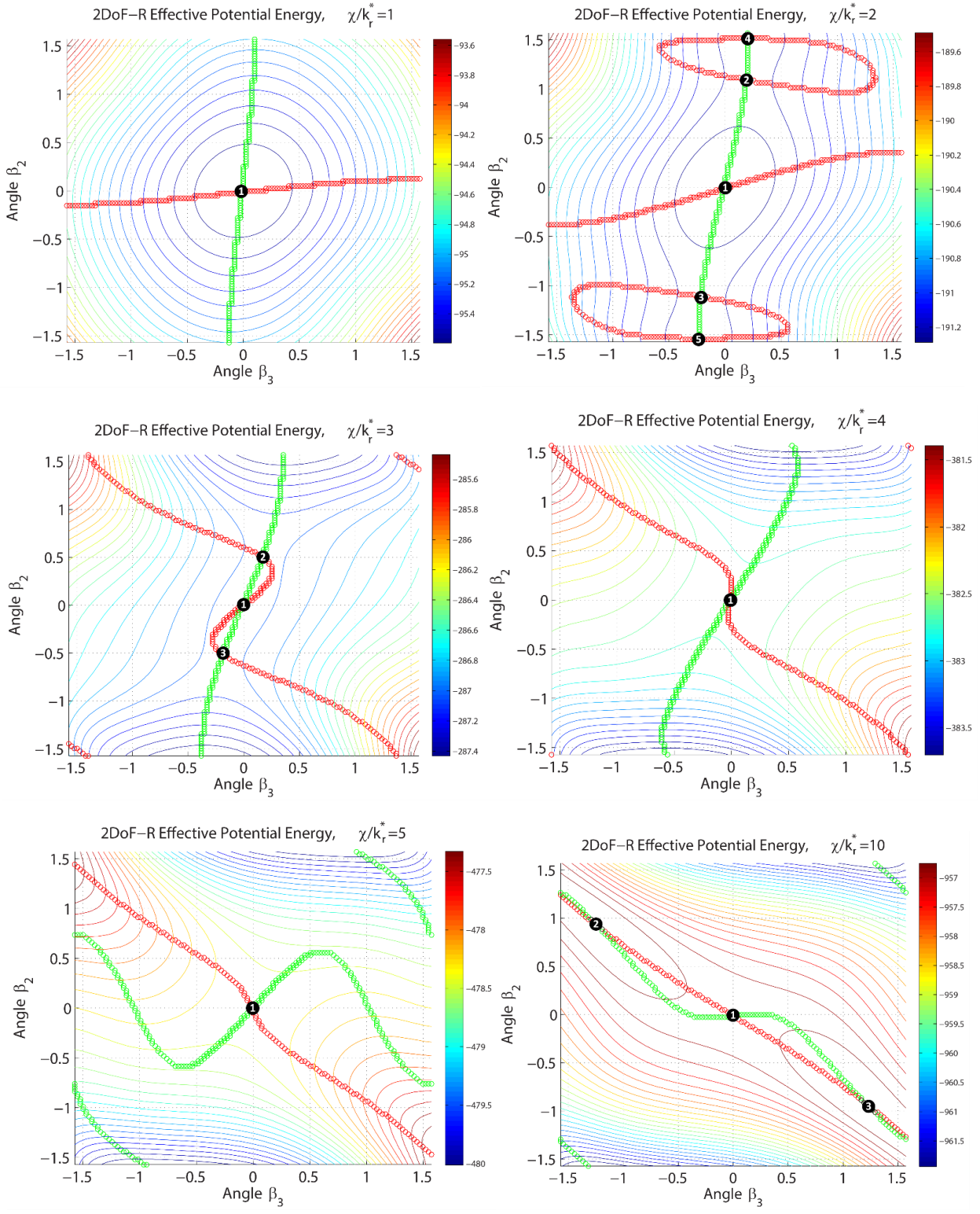

Figure 74: 2DoF-R effective potential energy curves for three coils of radius 1, where red is torque equil. on coil 2, green is torque equil. on coil 3, and black is equil. in both; (a, top left) $\frac{\chi}{k_r^*} = 1$, *(b, top right)* $\frac{\chi}{k_r^*} = 2$, *(c, mid left)* $\frac{\chi}{k_r^*} = 3$, *(d, mid right)* $\frac{\chi}{k_r^*} = 4$, *(e, bottom left)* $\frac{\chi}{k_r^*} = 5$, *and (f, bottom right)* $\frac{\chi}{k_r^*} = 10$

When $\frac{\chi}{k_r^*} = 1$ (Figure 74a), equilibrium 1 clearly occurs at the potential energy minimum within the bounds plotted, making it statically stable. It's possible that there are other minima outside of these bounds (if a coil should rotate beyond $\pm\frac{\pi}{2}$, for instance), so it cannot be said to be globally stable, though there are no other visible minima for equilibrium 1 with which to share metastability. Given the relative weakness of the magnetic torques in this system, the basin-shaped elastic potential energy functional of the torsional springs dominates. The critical initial kinetic energy of this system within the bounds given is therefore determined by the minimum energy along the bounds, which occurs at the top and bottom of the plot where the green curve meets the bounds. $\tilde{T}_{t_0,crit,a1}$= 0.6797.

When $\frac{\chi}{k_r^*} = 2$ (Figure 74b), equilibrium 1 still occurs at the potential energy minimum, making it statically and dynamically stable. Equilibria 2/3 occur at saddle points and thus are statically and dynamically unstable. Interestingly, equilibria 4/5 occur at local minima in the potential energy functional as well, making them statically stable. Equilibria 2/3 dictate the critical initial kinetic energy for equilibrium 1. The value of the potential energy at the bounds determines the critical initial kinetic energy for equilibria 4/5. $\tilde{T}_{t_0,crit,b1} = 0.1285$, and $\tilde{T}_{t_0,crit,b45} = 0.0010$.

When $\frac{\chi}{k_r^*} = 3$ (Figure 74c), equilibrium 1 occurs at a local potential energy minimum, while equilibria 2/3 occur at saddle points. Equilibrium 1 is therefore statically stable and (barely) dynamically stable while equilibria 2/3 are statically unstable and are used to calculate the critical initial kinetic energy of equilibrium 1. $\tilde{T}_{t_0,crit,c1} = 0.0123$.

When $\frac{\chi}{k_r^*} = 4$, 5 or 10 (Figure 74d, e, or f), equilibrium 1 occurs at a saddle point and is thus statically and dynamically unstable. For $\frac{\chi}{k_r^*} = 10$, equilibria 2 and 3 occur at the potential energy maxima in the system and are thus statically and dynamically unstable as well.

Coils of Different Radii

Figure 75 shows the equilibrium curves of three different sized coils ($R_1 = 1, \tilde{R}_2 = 1.2, \text{and } \tilde{R}_3 = 1.5$) for each of $\frac{\chi}{k_r^*} = [1, 2, 3, 10]$. The overall trends are similar to those of the same radius coils in Figure 73, but the larger coils tend to accelerate the convergence of the equilibrium curves to the general shape shown in Figure 73f and Figure 75d, because the larger radius increases the proximity of coil perimeters when one or both of coils 2 and 3 is tilted, increasing the resultant torques as compared to the same size system with the same value of $\frac{\chi}{k_r^*}$. Also, in this asymmetric system, the contributions of coils 1 and 3 on coil 2 are no longer equal. As a result, the rotational symmetry exhibited in Figure 73 persists (because it is rooted in the symmetry of rotation in either direction about the y axis), but some of the general shapes have been skewed or differ in Figure 75 from the general shapes seen in Figure 73.

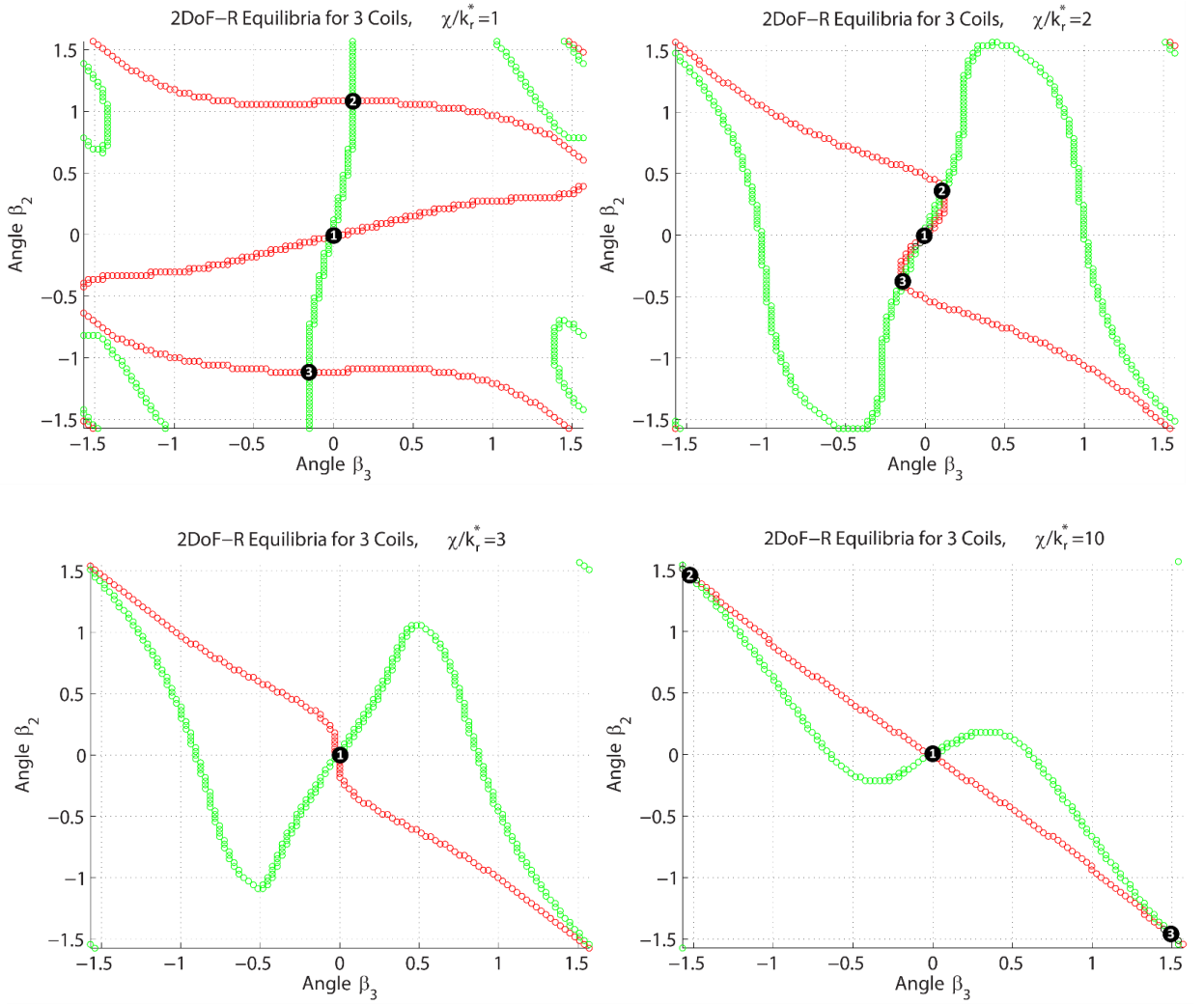

Figure 75: 2DoF-R equilibrium locations for three coils of radius $R_1 = 1, \tilde{R}_2 = 1.2, and\ \tilde{R}_3 = 1.5$, where red is torque equilibria on coil 2, green is torque equilibria on coil 3, and black is equilibria in both; (a, top left) $\frac{\chi}{k_r^*} = 1$, (b, top right) $\frac{\chi}{k_r^*} = 2$, (c, bottom left) $\frac{\chi}{k_r^*} = 3$, and (d, bottom right) $\frac{\chi}{k_r^*} = 10$

When $\frac{\chi}{k_r^*} = 1$ (Figure 75a), secondary equilibria can already be seen in this system as compared to the same radius system. The most interesting thing about this plot is the regions of green equilibria in the corners. Given that both coils 2 and 3 are bigger than coil 1, and thus their interaction dominates these plots, equilibria near the lowest potential energy configuration of coils 2 and 3 ($\beta_3 = \beta_2 = \pm\frac{\pi}{2}$) actually appear in this plot and Figure 75b. There are not mutual equilibria at these points because coil 1 and the springs still exist and contribute torque. The green and red equilibria in the opposing corners will converge as $\frac{\chi}{k_r^*}$ increases to the secondary mutual equilibria seen in the $\frac{\chi}{k_r^*} = 10$ plots.

When $\frac{\chi}{k_r^*} = 2$ (Figure 75b), the plot looks very similar to Figure 73c except that for every value of β_2, there exist three equilibria for coil 3. The three equilibria exist because for each β_2, there is a region in which the magnetic torque on coil 3 dominates and is then matched at the outer equilibria by the restorative spring torque.

When $\frac{\chi}{k_r^*} = 5 \text{ or } 10$ (Figure 75c or d), the shape of the equilibria curves is familiar, converging to the same winding pattern. It can be seen that coil 3 has equilibria at $\beta_3 = \beta_2 = \pm\frac{\pi}{2}$ instead of slightly removed from that point as in Figure 73f, due to the reduced influence of coil 1 on coil 3 as compared to the influence of coil 2 on coil 3.

Figure 76 shows the potential energy curves of the systems and equilibria depicted in Figure 75. The plots in Figure 76 are discussed below.

When $\frac{\chi}{k_r^*} = 1$ (Figure 76a), equilibrium 1 occurs at a local potential energy minimum, while equilibria 2/3 occur at saddle points. Equilibrium 1 is therefore statically stable while equilibria 2/3 are statically unstable and are used to calculate the critical initial kinetic energy of equilibrium 1. $\tilde{T}_{t_0,crit,a1} = 0.1685.$

When $\frac{\chi}{k_r^*} = 2$ (Figure 76b), equilibrium 1 occurs at a local potential energy minimum, making it statically and dynamically stable. It is barely stable, though, as equilibria 2/3 occur at saddle points and have a very small amount more potential energy than equilibrium 1, making the critical initial kinetic energy of equilibrium 1 very small. $\tilde{T}_{t_0,crit,b1} = 0.005.$

When $\frac{\chi}{k_r^*} = 3 \text{ or } 10$ (Figure 76c or d), equilibrium 1 occurs at a saddle point and is thus statically and dynamically unstable. For $\frac{\chi}{k_r^*} = 10$, equilibria 2 and 3 occur at the potential energy maxima in the system and are thus statically and dynamically unstable as well.

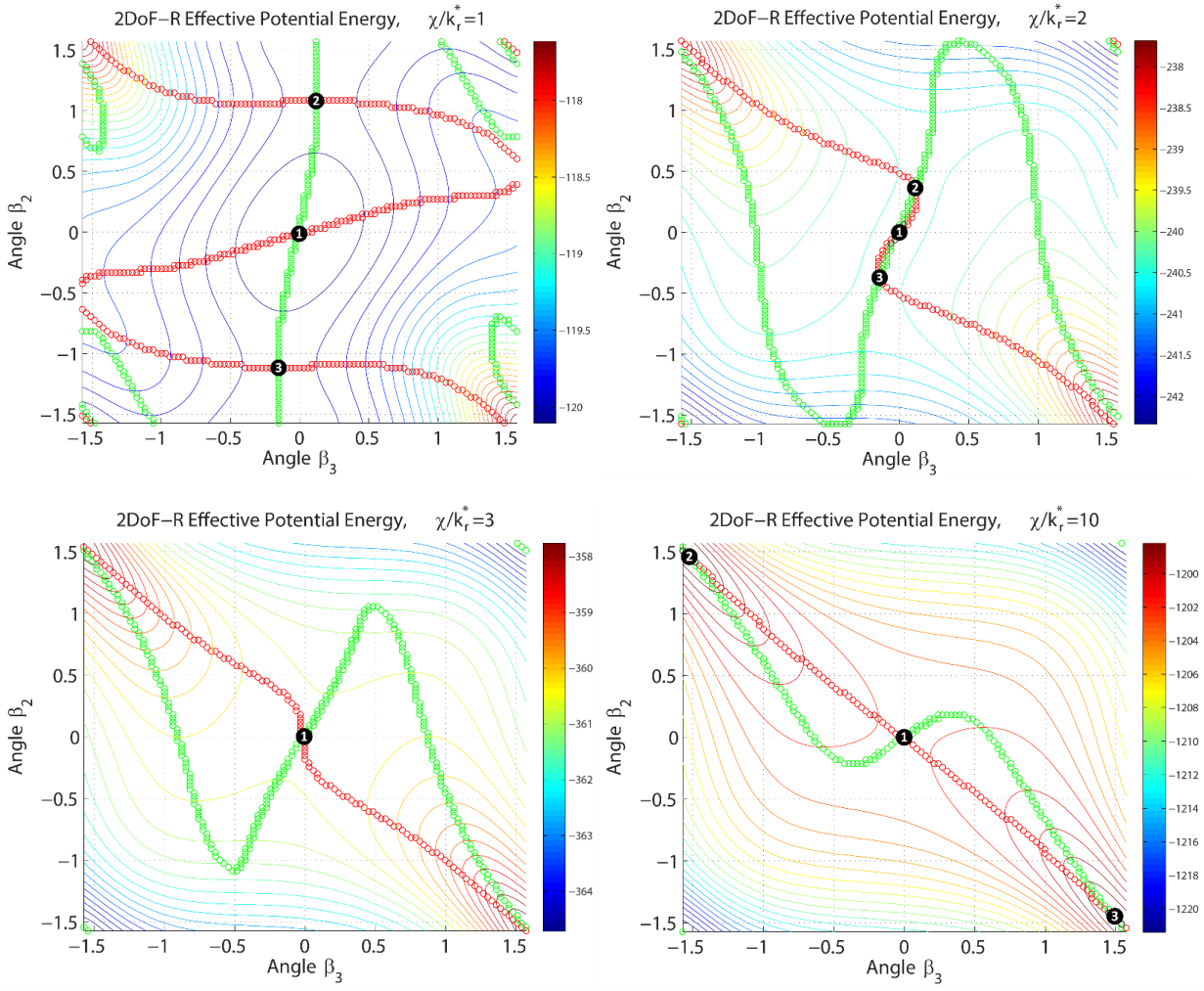

Figure 76: 2DoF-R equilibrium locations for three coils of radius $R_1 = 1, \widetilde{R_2} = 1.2,$ *and* $\widetilde{R_3} = 1.5$, *where red is torque equilibria on coil 2, green is torque equilibria on coil 3, and black is equilibria in both; (a, top left)* $\frac{\chi}{k_r^*} = 1$, *(b, top right)* $\frac{\chi}{k_r^*} = 2$, *(c, bottom left)* $\frac{\chi}{k_r^*} = 3$, *and (d, bottom right)* $\frac{\chi}{k_r^*} = 10$

The analysis done in this section shows that it is possible to have a stable three coil system when two coils are allowed to rotate, but that if the nondimensional coefficient $\frac{\chi}{k^*}$ or $\frac{\chi}{k_r^*}$ is too large (indicating a strong magnetic field), then the system becomes fundamentally unstable. It also proves the extensibility of the approach and model developed in this thesis to more intricate problems than just the two coil interaction.

Future work includes a full 4DoF three-coil system with both of the translational and both of the rotational degrees of freedom studied in this chapter, though effective visualization of that system would be understandably challenging. Additionally, experimentation with the types of connective hardware (various arrays of tethers instead of springs, or torsional springs that act on two coils at once instead of just one coil, as in this chapter) would provide insight to spacecraft designers on how stability is affected by the types of hardware selected. The next section discusses how the type of conductor used for the electromagnetic coils affects stability and the assumptions made thus far in this work.

6.2. Replacing Springs With Tethers

One of the fundamental assumptions made in this work so far is that the electromagnetic coils are connected by elastic hardware capable of exerting forces when compressed; namely, springs. While it is not impossible to have linear springs several coil radii long, at those lengths, buckling of the springs becomes a concern, as well as how the structure still be stowed in a launch vehicle fairing. More likely, coils will be connected by flexible tethers, which exert forces in tension but go slack under compression. Such tethers could be easily coiled when the structure is stowed. This section will explore how changing the elastic hardware assumptions affects the equilibrium and stability conclusions.

6.2.1. Tether Model

In the tether model of a magneto-elastic structure as shown by Figure 77, the single torsional spring and single linear spring have been replaced by two flexible tethers positioned at either side of the two coils (in the positive and negative y extrema of each coil when $\beta = 0$) such that rotation around the z axis causes them to stretch or go slack. As such, the tethers, when stretched, exert torques around the z axis and forces along the x axis in the same way that the spring-based system does. However, when the tethers are less than their natural length, they exert no force or torque at all. The natural length of the spring or tether is $\tilde{x}_0$= 2.5 and $\tilde{R}_2 = 1.2$.

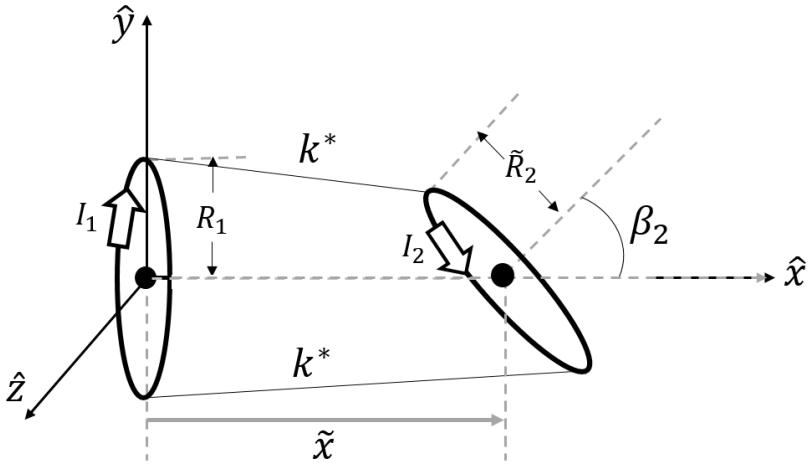

Figure 77: General 2DoF two-coil tether model

Each tether is modeled with the same spring constant as the linear spring in the spring system, meaning that when the coils are parallel to one another and the tethers are stretched, the restorative spring force is double what it was in Section 5.3 because there are two tethers. Therefore, when the 1DoF-T case is considered with tethers, different equilibria are expected as a result. As coil 2 rotates, only one tether exerts a restorative torque (the other going slack), which means that the magnitudes of the spring and tether torques are comparable (and not double as in the force case). However, the magnitude of the torque exerted by a torsional spring and the torque generated by a stretching tether attached at the perimeter of a coil are slightly different, and therefore some differences are expected in torques and potential energy in the 1DoF case with tethers. Finally, the 2DoF case is expected to be more different

with tethers than either of the single degree of freedom cases, given that the tether force is dependent on the angle of the coil, whereas the spring force was not.

Equations (6.10)-(6.12) give the general equations for the spring force and total force on coil 2:

$$\tilde{\vec{F}}_{2,teth1} = \begin{cases} 0, & \tilde{L}_{teth1} - \tilde{x}_0 \leq 0 \\ -k^*[\tilde{\vec{L}}_{teth1} - \tilde{x}_0 \hat{L}_{teth1}], & \tilde{L}_{teth1} - \tilde{x}_0 > 0 \end{cases} \tag{6.10}$$

$$\tilde{\vec{F}}_{2,teth2} = \begin{cases} 0, & \tilde{L}_{teth2} - \tilde{x}_0 \leq 0 \\ -k^*[\tilde{\vec{L}}_{teth2} - \tilde{x}_0 \hat{L}_{teth2}], & \tilde{L}_{teth2} - \tilde{x}_0 > 0 \end{cases} \tag{6.11}$$

and

$$\tilde{\vec{F}}_{total,2} = \tilde{\vec{F}}_{mag,12} + \tilde{\vec{F}}_{2,teth1} + \tilde{\vec{F}}_{2,teth2}, \tag{6.12}$$

where

$$\tilde{\vec{L}}_{teth1} = \tilde{\vec{x}}_{2,teth1} - \tilde{\vec{x}}_{1,teth1}, \tag{6.13}$$

and

$$\tilde{\vec{L}}_{teth2} = \tilde{\vec{x}}_{2,teth2} - \tilde{\vec{x}}_{1,teth2}. \tag{6.14}$$

$\tilde{\vec{x}}_{2,teth1}$ and $\tilde{\vec{x}}_{2,teth2}$ are the vector locations with respect to the system origin of the attachment points of tethers 1 and 2 on coil 2, and $\tilde{\vec{x}}_{1,teth1}$ and $\tilde{\vec{x}}_{1,teth2}$ are the attachment points of the tethers to coil 1. $\tilde{\vec{L}}_{teth1}$ and $\tilde{\vec{L}}_{teth2}$ are thus the vectors along tethers 1 and 2 respectively from where they attach on coil 2 to where they attach on coil 1. As throughout the rest of the thesis, the forces when plotted and balanced are just those in the x direction, but they have been left in vector form here because the torques will be calculated from the force vectors.

Equations (6.15)-(6.17) give the general equations for the spring torque and total torque on coil 2, using the above definitions, and noting that the torque is zero when the force is zero:

$$\tilde{\vec{\tau}}_{2,teth1} = \left[\tilde{\vec{x}}_{2,teth1} - \tilde{\vec{x}}_{2,0}\right] \times \tilde{\vec{F}}_{2,teth1}, \tag{6.15}$$

$$\tilde{\vec{\tau}}_{2,teth2} = \left[\tilde{\vec{x}}_{2,teth2} - \tilde{\vec{x}}_{2,0}\right] \times \tilde{\vec{F}}_{2,teth2}, \tag{6.16}$$

and

$$\tilde{\vec{\tau}}_{total,2} = \tilde{\vec{\tau}}_{mag,12} + \tilde{\vec{\tau}}_{2,teth1} + \tilde{\vec{\tau}}_{2,teth2}. \quad (6.17)$$

All three of these cases will be studied with tethers and compared to their respective spring-based systems in the following sections.

6.2.2. 1DoF-T Tether System

In the 1DoF-T case, coil 2 is not rotated at all, so the tethers remain parallel to and exert forces only along the x axis. Since the coils are in repulsion, all equilibria are at distances greater than the natural length of the tether except the new equilibria which occur when the coils are concentric at $\tilde{x}$=0, since there is no magnetic force *or* elastic force in the tether system at $\tilde{x}$=0 (the spring force is nonzero in the spring model at $\tilde{x}$=0). Figure 78 shows the tether system forces and equilibria in magenta (and green for the negative values of force) plotted over the spring system forces and equilibria in black and grey (for negative values).

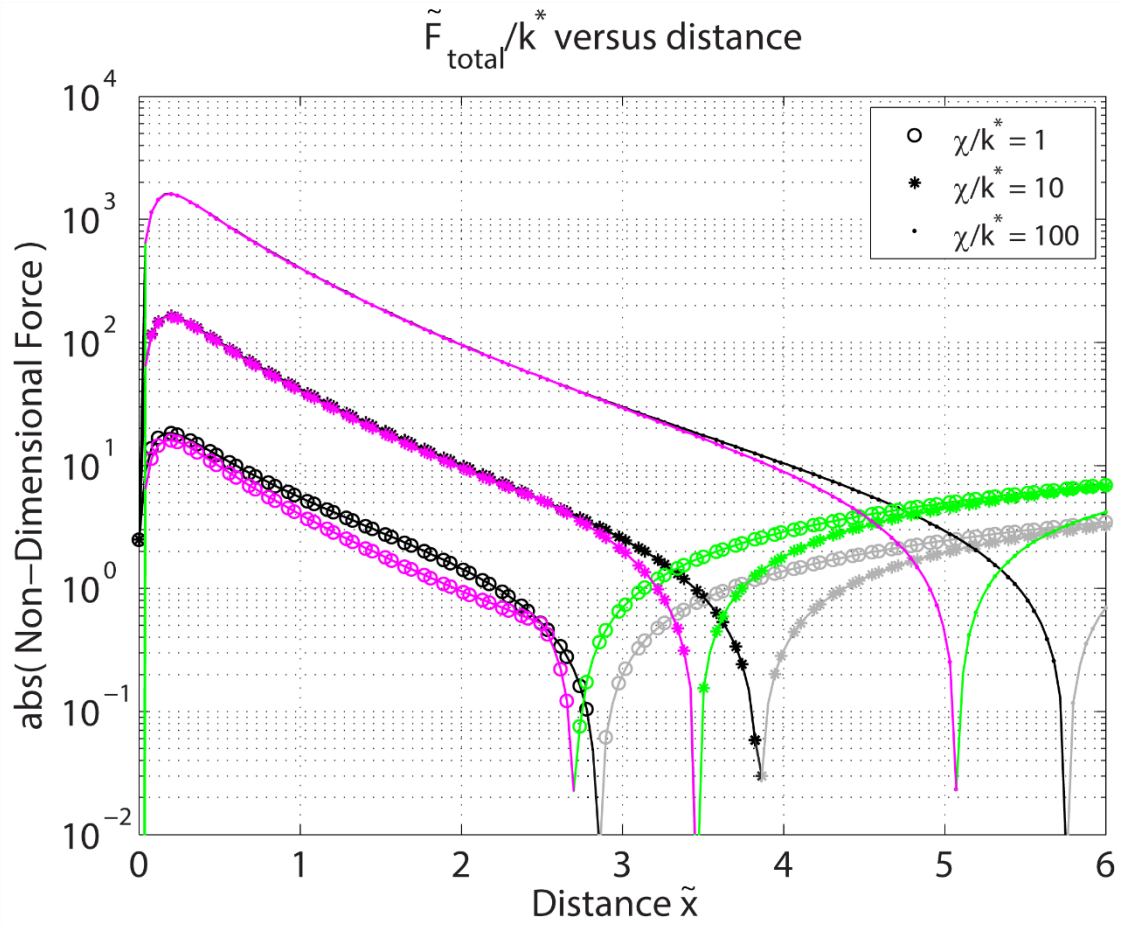

Figure 78: 1DoF-T non-dimensional absolute force versus distance for the spring system (black positive, grey negative) and the tether system (magenta positive, green negative) when $\tilde{x}_0 = 2.5$

It can be seen from Figure 78 that for $\tilde{x} \leq \tilde{x}_0$, the spring system force is greater than the tether system force because the latter falls slack and has no elastic force. When $\tilde{x} > \tilde{x}_0$, the tether system's elastic force is twice that of the spring system and therefore the non-zero equilibrium points for each χ/k^* occur at smaller $\tilde{x}$ than in the spring system. This is as expected from the tether 1DoF-T system. The difference in the spring and tether force curves is most pronounced for smaller χ/k^*, wherein the elastic force makes up a larger portion of the total force.

Figure 79 shows the potential energy curves of the 1DoF-T tether system (magenta) overlaid with the spring system (black). The tether system potential energy is slightly less than the spring system potential energy, though this difference becomes less pronounced as the total magnitude of potential energy increases (since the magnetic potential energy dominates), and the minima are where they are expected to be given the new equilibria. Because there is now an equilibrium point in each curve at $\tilde{x}$=0, the potential energy curves are at a maximum at $\tilde{x}$=0, their rates of change zero.

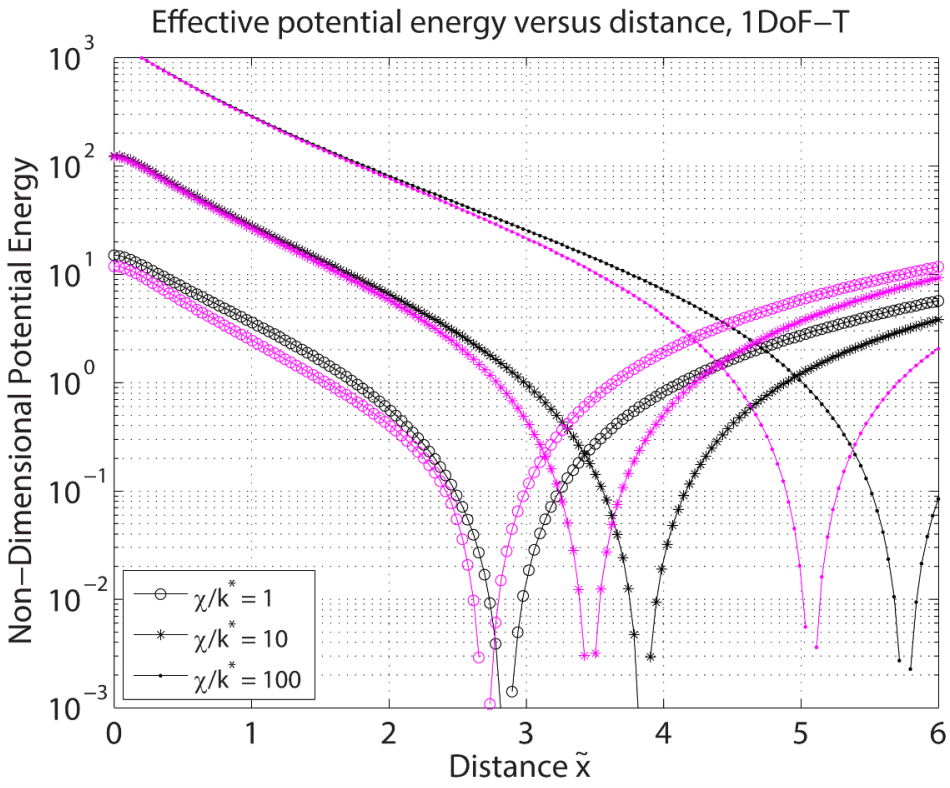

Figure 79: 1DoF-T non-dimensional potential energy versus distance for the spring system (black) and the tether system (magenta) when $\tilde{x}_0 = 2.5$

As is the norm throughout this work, the minimum value of potential energy for each curve has been added to it to place the minimum in potential energy at zero. The non-zero equilibria are all statically stable because they occur at local minima, whereas the zero equilibria are statically unstable because they occur at maxima. Previously, the spring system was defined as globally stable assuming a constraint that did not allow the system to pass through to negative values of $\tilde{x}$. For the sake of comparison, however, that constraint is being relaxed. The critical initial kinetic energies for the spring and tether systems are both determined by the difference in potential energy with respect to $\tilde{x}$=0, since the potential energy increases to infinity as $\tilde{x} \to \infty$. The difference between the spring and tether system potential energies at the origin is just the spring potential energy at that position (3.125); however, the minima occur at different X and thus the minimum in potential energy is of different magnitudes. Table 31 gives the difference in $\tilde{T}_{t_0,crit}$ for each of the statically stable equilibria in Figure 79, which happens to be equal to the elastic potential energy in the spring at zero.

Table 31: Critical initial kinetic energies for the 1DoF-T tether and spring systems

Equilibrium ID	χ/k^*	$\tilde{x}$ value at spring eq	$\tilde{x}$ value at tether eq	$\tilde{T}_{t_0,crit,spring}$	$\tilde{T}_{t_0,crit,tether}$	$\Delta\tilde{T}_{t_0,crit}$
$\tilde{x}_{coil,1}$	1	2.864	2.714	15.04	11.89	3.15
$\tilde{x}_{coil,2}$	10	3.859	3.467	124.2	120.4	3.8
$\tilde{x}_{coil,3}$	100	5.759	5.065	1231	1224	7

6.2.3. 1DoF-R Tether System

The 1DoF-R case assumes $\tilde{x}_0$= 2.5 and $\tilde{R}_2 = 1.2$ as well. Since coil 2's distance from coil 1 is fixed at the natural length of the tethers in the rotational case, one tether is always slack, depending on the sign of β. Figure 80 shows the difference between the torsional spring and the tethers in both torque (Figure 80a) and potential energy (Figure 80b). The spring torque is a linear function of β and its potential energy is simply a quadratic function, but the tether torque is nonlinear and decreases in magnitude as $\beta \to \pm\pi/2$.

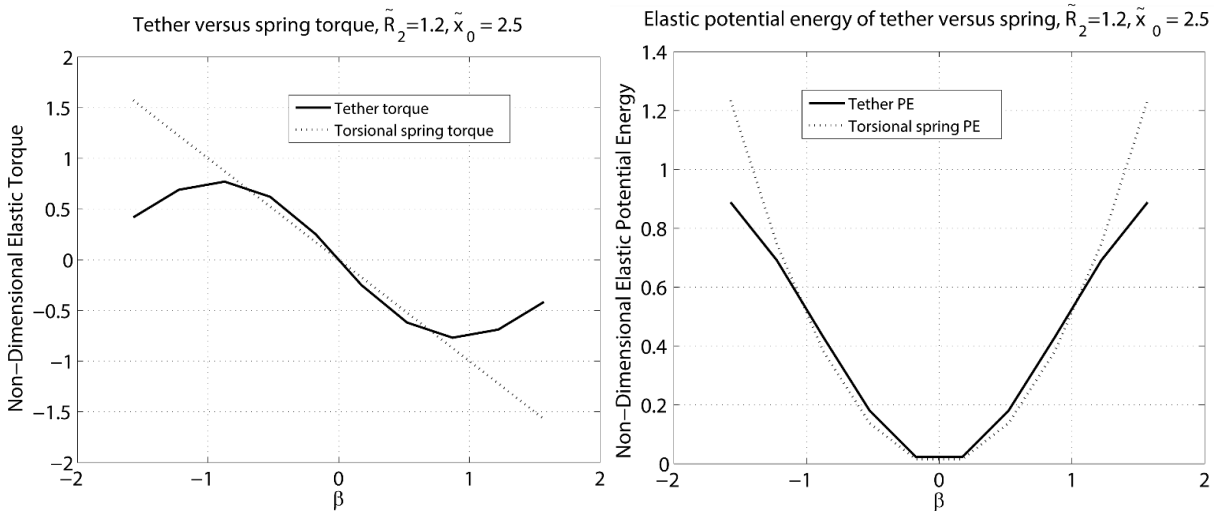

Figure 80: (a, left) Tether versus spring torque over β; (b, right) Elastic potential energy of spring system versus tether system over β

Figure 81a shows all of the tether system torques and equilibria in magenta (and green for the negative values of torque) plotted over all of the spring system torques and equilibria in black and grey (for negative values). Figure 81b-d show the tether and spring systems for each individual value of χ/k^*, for easier observation of the differences between the systems. Because the spring case used χ/k_r^*, that term is used in the legend and titles of these plots instead, but given that k_r^* was taken to be 1, the spring and tether cases are still comparable and χ/k^* and χ/k_r^* are interchangeable in this section.

When $\frac{\chi}{k^*} = 0.1$, the most significant impact of the use of tethers on the torques in the system is to decrease the magnitude of total torque as $\beta \to \pm\pi/2$ because the elastic torques dominate the magnetic torque for a small $\frac{\chi}{k^*}$.

When $\frac{\chi}{k^*} = 10$, the magnitude of total force is actually increased via the use of tethers as $\beta \to \pm\frac{\pi}{2}$ because the magnetic torque dominates the elastic torque in those regions. The secondary equilibria are slightly shifted to higher magnitude βs because the magnitude of the elastic torque is increased in that middle region (also evidenced by the larger magnitude of the total tether torque in between the secondary equilibria, where the elastic torque dominates).

When $\frac{\chi}{k^*} = 100$, the most significant impact of the use of tethers instead of springs is that two secondary equilibria are created on either side of a central equilibrium (the $\tilde{x} = 0$ equilibrium is evidenced by the change in colour; the lack of downward spike at $\tilde{x} = 0$ is due to the resolution of the plot). The increase in magnitude of the elastic torque in the regions between $\beta \sim \pm 0.75$ as shown in Figure 80a is enough to

create secondary equilibria in $\frac{\chi}{k^*} = 100$, which is consistent with the shifting outward of the secondary equilibria in Figure 81c; in systems where the secondary equilibria fall within the range $\beta \sim \pm 0.75$, the use of tethers instead of springs slightly increases the amount the coil has to rotate before reaching a secondary equilibrium (or potentially introduce secondary equilibria from a single zero equilibrium, as in Figure 81d).

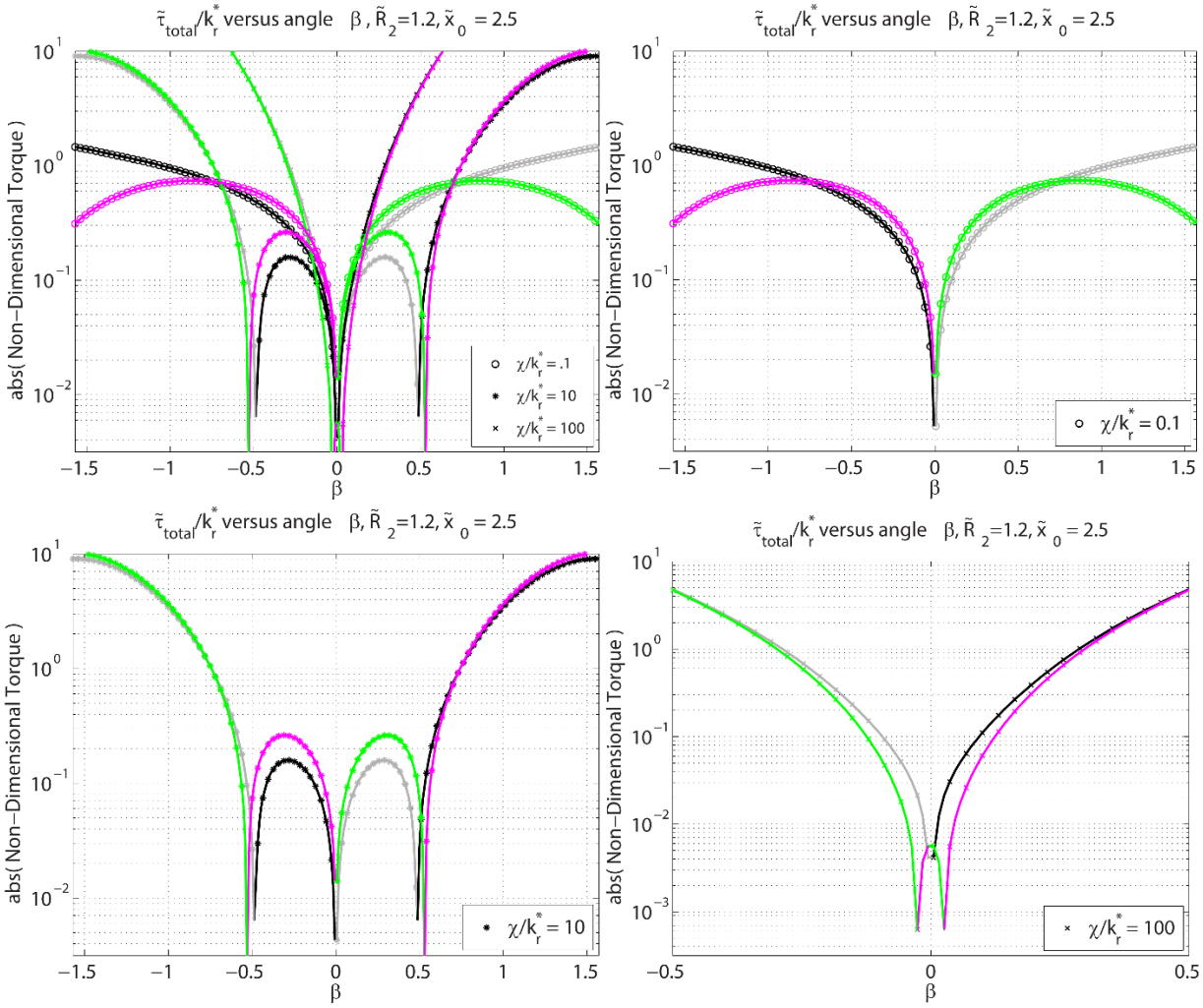

Figure 81: 1DoF-R non-dimensional absolute torque versus distance for the spring system (black positive, grey negative) and the tether system (magenta positive, green negative) when $\tilde{x}_0 = 2.5$; (a, top left) all $\frac{\chi}{k^*}$, (b, top right) $\frac{\chi}{k^*} = 0.1$, (c, bottom left) $\frac{\chi}{k^*} = 10$, (d, bottom right) $\frac{\chi}{k^*} = 100$

Figure 82 shows the potential energy curves of the 1DoF-R tether system (magenta) overlaid with the spring system (black). As expected, the smallest $\frac{\chi}{k^*}$ sees the largest impact of the change in elastic hardware, given that the elastic potential energy is of comparable magnitude to the magnetic potential energy. When $\frac{\chi}{k^*} = 0.1$, the potential energy drops as $\beta \to \pm\pi/2$ compared to the spring case. The medium $\frac{\chi}{k^*}$ sees a small amount of change; the potential energy at each of the secondary equilibria sees a slight increase from that of the spring system. Interestingly, the use of the tethers lowers the critical initial kinetic energy of the statically stable zero equilibrium when $\frac{\chi}{k^*} = 0.1$ but raises the critical initial

kinetic energy of the statically stable zero equilibrium when $\frac{\chi}{k^*} = 10$ because of the way that the tether torque is stronger in the central region but weaker at the boundaries as compared to the spring torque. The $\frac{\chi}{k^*} = 100$ system now has a statically stable central equilibrium due to the introduction of the secondary equilibria, but its critical initial kinetic energy is very small.

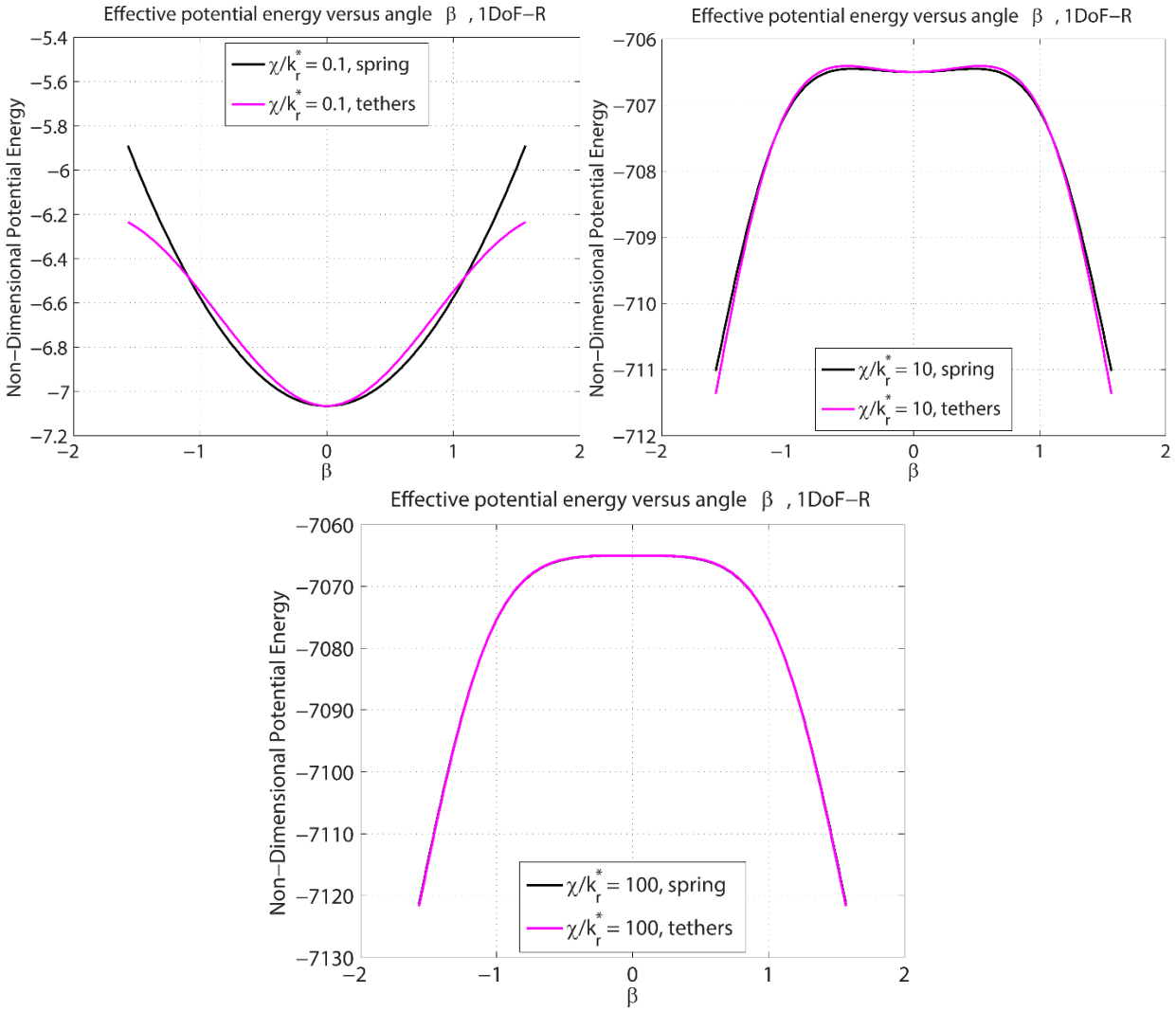

Figure 82: 1DoF-R non-dimensional potential energy versus distance for the spring system (black) and the tether system (magenta) when $\tilde{x}_0 = 2.5$; (a, top left) $\frac{\chi}{k^*} = 0.1$, (b, top right) $\frac{\chi}{k^*} = 10$, (c, bottom) $\frac{\chi}{k^*} = 100$

The critical initial kinetic energy of each of these systems is listed in Table 32 for the tether system and for the spring system. For $\frac{\chi}{k^*} = 0.1$, the critical initial kinetic energy is taken with respect to the values at $\beta = \pm\frac{\pi}{2}$, even though rotation past those bounds may result in a different critical initial kinetic energy; this is because in a tethered system, once coil 2 rotates a small amount past $\beta = \pm\frac{\pi}{2}$, the tethers cannot exert a restorative torque anymore. This can be seen in the way the tether torque approaches zero as $\beta \to \pm\frac{\pi}{2}$ in Figure 80a.

Table 32: Critical initial kinetic energies for the 1DoF-R tether and spring systems

Equilibrium ID	χ/k^*	$\tilde{T}_{t_0,crit,spring}$	$\tilde{T}_{t_0,crit,tether}$	$\Delta\tilde{T}_{t_0,crit}$
$\beta_{coil,1}$	0.1	1.176	0.831	0.345
$\beta_{coil,2}$	10	0.05	0.09	-0.04
$\beta_{coil,3}$	100	0	0.0001	-0.0001

6.2.4. 2DoF Tether System

The 2DoF tether system combines the single rotational and single translational degrees of freedom for $\tilde{x}_0$= 2.5 and $\tilde{R}_2 = 1.2$. This system is expected to have some interesting results compared to the spring system because force changes with angle in the tether system unlike in the spring system. Figure 83 shows the equilibrium positions in β and $\tilde{x}$ for the spring system (the plots on the left) and the tether system (the plots on the right) for each of $\frac{\chi}{k^*} = [0.1, 1, 10]$.

The general features of the 2DoF equilibrium plots have been discussed in previous chapters, so this discussion will focus on the differences between the spring and tether equilibrium plots for the same values of $\frac{\chi}{k^*}$.

The lack of symmetry in force equilibria at the very edges of some of the plots are, as noted in previous chapters, due to the fact that the numerical algorithm for finding equilibria picks the index before the change in sign, and so depending on the search direction, some equilibria are not plotted. The equilibria are in fact symmetric about $\beta = 0$, and if equilibrium occurs on one side, there is also an equilibrium on the other as well. No mutual equilibria are excluded as a result of this effect, so it is of marginal consequence.

For $\frac{\chi}{k^*} = 0.1$, there exists a distinct difference between the spring and tether cases, mostly because the elastic forces and torques are of comparable magnitude to the magnetic forces and torques. Because there are no compressive forces to counter magnetic forces for $\tilde{x} < \tilde{x}_0$, the proximity effect line of equilibria around $\tilde{x} \sim 0.6$ appear in the tether case for smaller $\frac{\chi}{k^*}$ than in the spring case. Also, the red (force) line of equilibria that is relatively flat in the spring case is swept back towards the origin significantly as $\beta \to \pm\frac{\pi}{2}$. This difference is because the tether forces now depend on β and drastically reduce as the coil rotates one way or the other. The magnetic forces are so small in this case, especially when the coil is rotated, that the force equilibrium curve is very similar to the boundary of the values of $\tilde{x}$ for which there is first a nonzero tether force. So, the tether force kicks in at smaller $\tilde{x}$ when $\beta \to \pm\frac{\pi}{2}$ because that is where the maximum extension of one of the two tethers occurs. Also, it can be seen that the torque equilibria curve (green) is more established in the tether case than in the spring case, such that equilibria 2 and 3 along the primary red curve appear even for such a small $\frac{\chi}{k^*}$. This is because of the nonlinearity of the torque as seen in Figure 80a; in the spring case, the magnetic torque is small enough that it only balances with the spring torque when $\tilde{x}$ is small, but in the tether case, the torque decreases in magnitude as $\beta \to \pm\frac{\pi}{2}$, thus allowing the magnetic torque to balance with it at larger values of $\tilde{x}$.

The trends described above persist throughout the $\frac{\chi}{k^*} = 1$ and 10 cases, though the differences between the two cases are less evident as the magnetic effects increase in magnitude. Another interesting note is that equilibria 2 and 3 in the $\frac{\chi}{k^*} = 10$ case occur at larger β values in the tether case. This is again because of the nonlinearity in the spring torque that makes it larger between $\beta \approx \pm\frac{\pi}{2}$.

Figure 84 shows the potential energy contours around the equilibria from Figure 83.

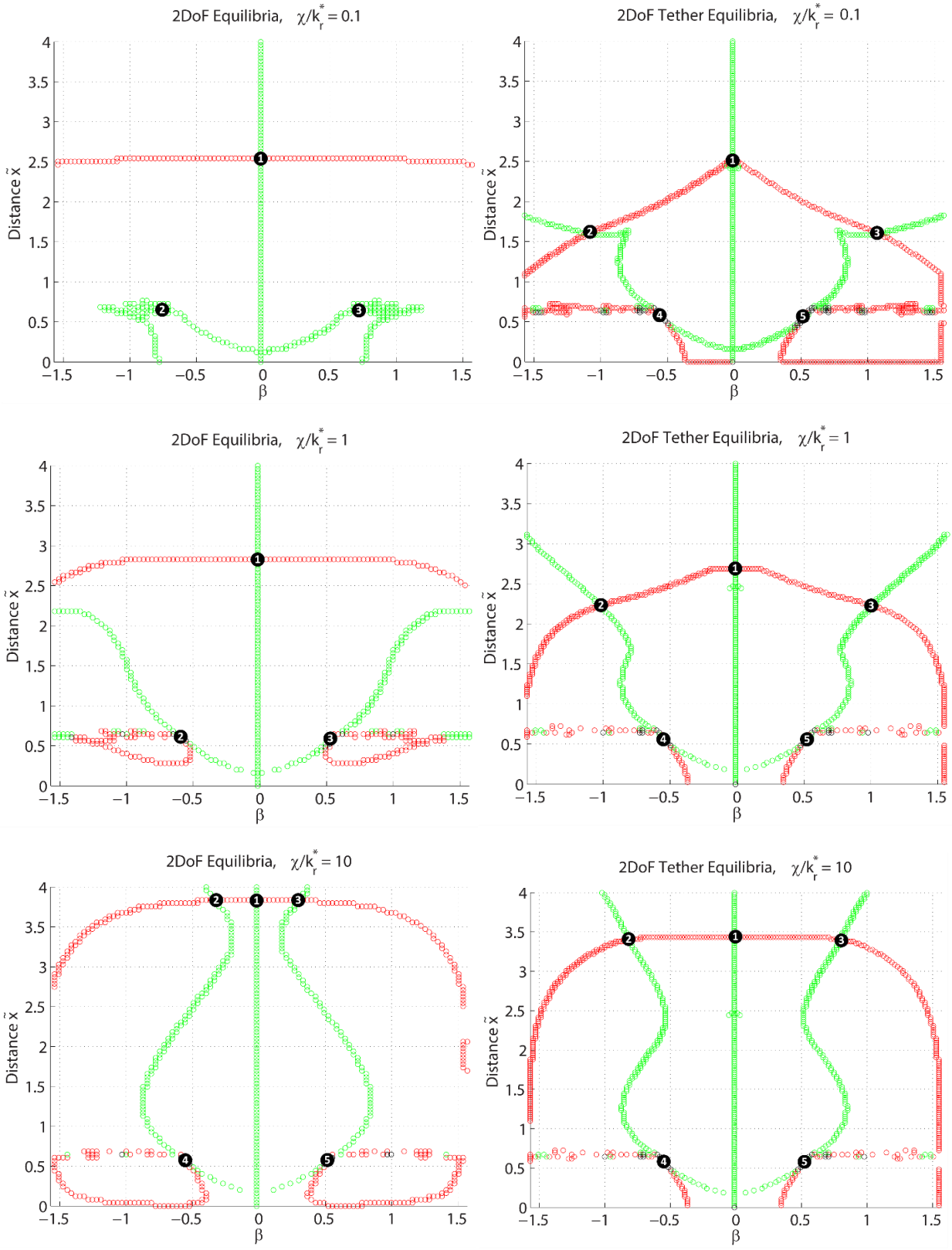

Figure 83: 2DoF equilibria for spring (left, a, c, e) versus tether (right, b, d, f) cases; (a, b, top) $\frac{\chi}{k^*} = 0.1$*, (c, d, middle)* $\frac{\chi}{k^*} = 1$*, (e,f, bottom)* $\frac{\chi}{k^*} = 10$

The potential energy contours and the indicated static stability of the spring and tether systems are much as expected; if there is one equilibrium at $\beta = 0$ and no others along the primary red curve, then it is globally stable within the bounds being studied, and if there are statically unstable secondary equilibria at saddle points along the primary red curve, then the $\beta = 0$ equilibrium is not globally stable and thus has a critical initial kinetic energy which could make it dynamically unstable. The energy levels are rather similar between the spring and tether cases, largely because the elastic potential energy is not a large contributor to the effective potential energy at larger $\frac{\chi}{k^*}$. What is interesting to note is that whereas the first two spring cases have globally stable $\beta = 0$ equilibria, all of the tether cases have unstable secondary equilibria, which indicates that even for weak magnets, there still exist unstable modes in the tether case. As a result, one could make the case that the tether system is "less stable" on the whole than the spring case, which is not surprising given the nonlinearity of its elastic torques.

Also of interest is the difference in shape of the potential energy curve; the low $\frac{\chi}{k^*}$ tether case has a triangular potential energy well as compared to the oval well in the spring case. This observation suggests that different tether designs (potentially crossing from one side to the other, or tied to one another, or asymmetric) could create different potential energy curves which may create statically stable equilibria elsewhere in the $\tilde{\mathrm{x}} - \beta$ space.

6.2.5. Conclusions

Using different connective hardware results in different elastic forces, torques, and potential energy curves, and the methodology presented in this thesis provides a way to visualize the effects of different hardware options or hardware configurations on the equilibrium and static and dynamic stability of a system.

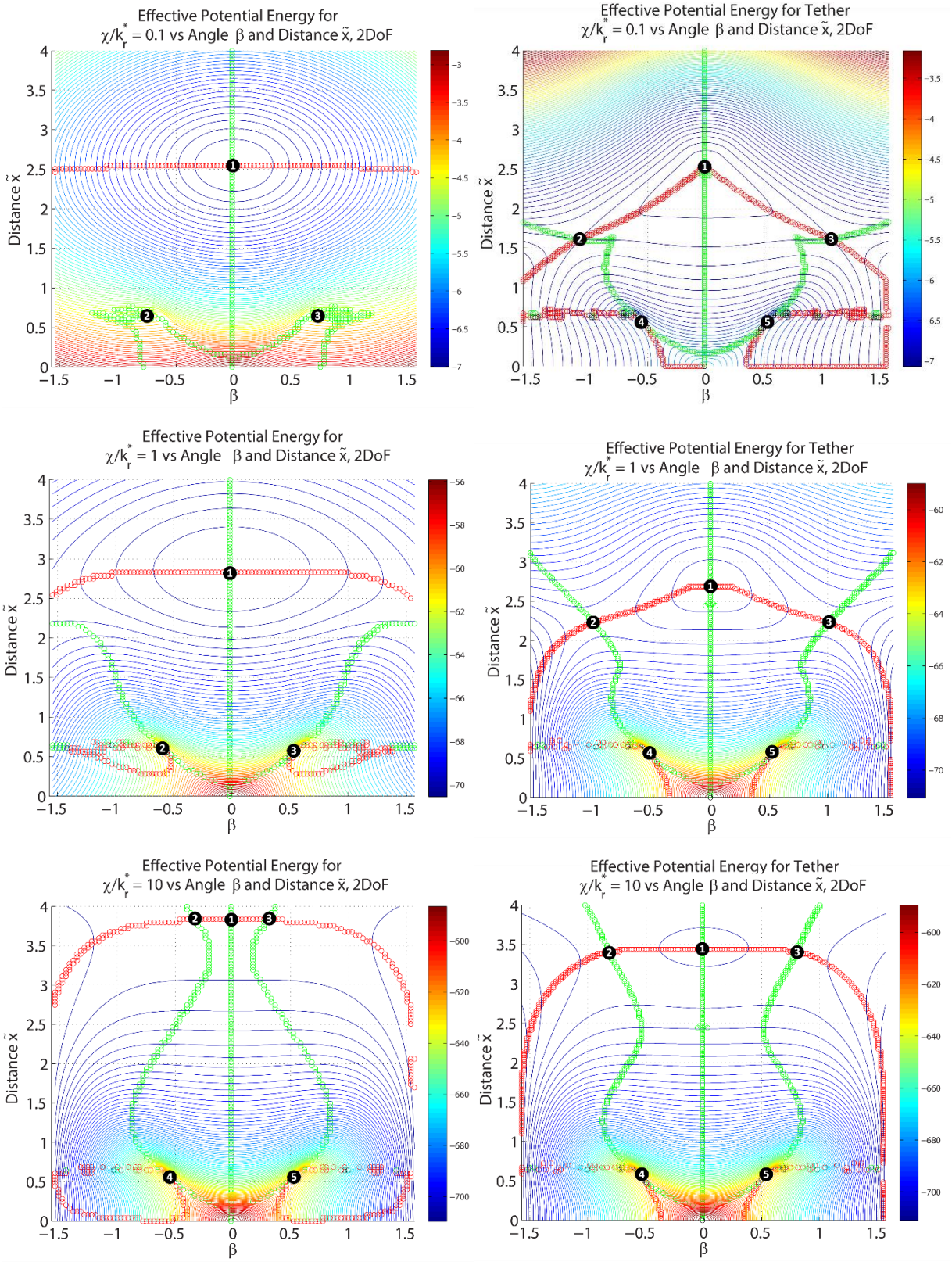

Figure 84: 2DoF effective potential energy curves for spring (left, a, c, e) versus tether (right, b, d, f) cases; (a, b, top) $\frac{\chi}{k^*} = 0.1$*, (c, d, middle)* $\frac{\chi}{k^*} = 1$*, (e,f, bottom)* $\frac{\chi}{k^*} = 10$

6.3. Other Assumptions

Some other assumptions that have been made about the system include the use of superconducting wire and constant currents through the coils. This section briefly discusses how changing these assumptions may affect the stability results.

6.3.1. Type of Conductor

The non-dimensional magnetic coefficients in this thesis have not been limited in range, allowing for any combination of current, number of turns, and radius of coil. However, in a real-world system of electromagnetic coils, the magnetic coefficients are limited to what is physically possible with the conductor used in the coils. As discussed in Chapter 2, a coil wound with copper is capable of carrying roughly two orders of magnitude less current for a given cross-sectional area of wire than a modern second generation HTS-wound coil [31] because of the resistivity of copper. In order to achieve the same current-carrying capacity as an HTS wire, many more turns or larger cross-sections of copper wire are required, which increases the mass of the coil for the same current delivery. The highest values of the nondimensional magnetic coefficients are only obtainable with very high currents or low mass coils, meaning that only superconducting coils can reach those values. This difference in critical current density is the primary difference between regular conductors and superconductors, followed by the necessity to design and implement a cooling system for the superconductors that will add mass and risk to the system over the mission lifetime.

Because a coil wound with superconducting wire has virtually zero resistivity when it is superconducting, it can be operated with a current source or without (called persistent mode) for a long period of time. Persistent mode can be induced in a copper coil, but the current will die off quickly due to the non-zero resistivity of the wire. For both a copper coil and an HTS coil, operating with a constant source results in no difference in current at steady state between a perturbed configuration and its initial configuration (as modeled in this paper so far).

6.3.2. Constant Versus Changing Currents

In terms of how conductor choice affects stability other than in coefficient value, system assumptions must be examined. The current through the coils is assumed to be constant in the thesis up to this point, changing not at all between configurations. This assumption is consistent with a current source that changes to keep the current constant. However, in a system wherein the current sources are not changing to keep the current constant, changing the position of a coil in a multi-coil system would change the magnetic flux through each coil and induce an electromotive force (EMF, $\mathfrak{E}$) around each coil in a direction to oppose the change in flux [49]. The EMF, which in essence is a change in voltage, and the current it thus induces according to Ohm's law ($V_{olt} = IR_{es}$) will either flow in the same direction as the existing current in the coil, increasing the current and magnetic moment, or in the opposite direction, serving to decrease the current and magnetic moment, depending on the direction of the change in flux.

While this different approach for current in the two coil system doesn't impact the location of equilibria, it would affect the stiffness of the system at equilibria as well as the shape of the potential energy curve around the equilibria, since both stability metrics are intended to describe the behavior of a system as it is displaced from equilibrium. Such a displacement would necessarily alter the stiffness and potential energy functional because of the resultant change in current and thus magnetic force, torque and potential energy.

Faraday's law as given by Jackson [49] states that "the induced electromotive force (EMF) around [a] circuit is proportional to the time rate of change of magnetic flux linking the circuit. The sign is specified by Lenz's law, which states that the induced current (and accompanying magnetic flux) is in such a direction as to oppose the change of flux (F_{lux}) through the circuit," where the induced EMF is $\mathfrak{E}$ and k_p is a constant of proportionality that is equivalent to 1 in SI units:

$$\mathfrak{E} = -k_p \frac{dF_{lux}}{dt}.$$

Magnetic flux through an electromagnet is generated by two sources: an external magnetic field such as that created by another coil and/or the internal magnetic field created by current in the magnet itself, such that

$$F_{lux} = F_{lux_{ext}} + F_{lux_{int}},$$

A change in $F_{lux_{ext}}$ resulting from a changing current in the other coil induces an EMF in the coil being studied to resist that change in flux.

The inductive definition of flux [58] says that flux from a given coil is the product of the inductance (self if internal flux, mutual inductance if external flux) and the current (self current if internal, other coil's current if external), such that a time change of flux through a coil establishes a time change of current in that, which in turn establishes a time change of flux through the other coil. Mathematically, for each of coils 1 and 2 respectively,

$$\frac{d}{dt}(L_{12}I_2) = -\frac{d}{dt}(L_{11}I_1)$$

$$\frac{d}{dt}(L_{12}I_1) = -\frac{d}{dt}(L_{22}I_2)$$

In the system considered here, the current is not the initial thing being changed; the mutual inductance term L_{12} changes when the coil is perturbed from equilibrium, which results in a change in flux and induced changes in current as described in the equations above. The initial currents before displacement through both coils are known, and the final currents after displacement are the unknown values of

interest. The initial conditions and constraints on the system, such as conservation of energy, will be important for determining the change in currents for a given initial injection of kinetic energy. Also of interest is whether or not the change in currents becomes time independent in a superconducting system with no energy loss due to resistivity.

Generally speaking, it is expected that with two repelling coils with opposite current directions, the coils being placed closer together (resulting in a larger L_{12}) will result in an increase in magnitude of current in the existing direction of flow, while the coils being moved farther apart will result in a decrease in magnitude of current in each coil. This is because the external magnetic flux is always in the opposite direction in a repelling system from the internal magnetic flux of a coil, so when they are being moved apart, for instance, the external magnetic flux decreases and the internal magnetic flux must also decrease in an effort to keep the same flux. This problem is a very interesting one for future study.

6.4. Conclusions

Addition of a third coil to the validated two coil system exemplifies the extensibility of the methodology to systems with more potential degrees of freedom and more complex interactions. The three coil equilibria and their respective stabilities are in some ways similar to the two coil systems in translation and rotation, but the influence of a third coil results in some new equilibria that do not exist in the two coil system. The use of tethers instead of springs exemplifies the flexibility of the methodology to changing assumptions as well as the plausibility of the system, given that tethers are a more realistic choice of connective hardware than meters-long linear springs or torsional springs.

Chapter 7
Final Words

The fundamental instability of repelling magnets as expressed by Earnshaw's theorem has presented one of the most severe risks to the concept of magneto-elastic space structures since its conception. By focusing not only on identifying statically stable structures but also on how to evaluate their dynamic stability and how much energy the system can handle before becoming dynamically unstable, the work presented in this thesis provides a trustworthy means by which spacecraft designers can investigate the impact of different configurations and connective hardware on stability of systems of the desired size and configuration for their mission concept, thus reducing the risk associated with instability.

7.1. Thesis Summary

This thesis motivated the use of magneto-elastic space structures by first describing the structural and ancillary capabilities that magneto-elastic structures can provide to a spacecraft and then by presenting a pathway to a mature electromagnetic structural technology anchored by several selected example missions. Chapter 2 includes some preliminary analysis of four such missions: superconducting magnetorquers at GEO; an EMIC wave antenna in LEO; a large, fractionated, electromagnetically formation flying observatory at an Earth-Sun Lagrange point, and a magnetic asteroid tug. All were shown to have challenges and risks associated with both the mission in general as well as the technology being used, but the potential for enabling such missions or enhancing the performance of such spacecraft merit further research. Stability was selected as the focus of this thesis due to the likelihood and consequence of instability in an electromagnetic structure.

Chapter 3 introduced a magneto-elastic model using magnetic dipoles such that it could be evaluated using closed-form solutions. Three different combinations of degrees of freedom were studied in this chapter and in the subsequent two chapters: a single translational degree of freedom, a single rotational degree of freedom, and a combination of the two. The equations of motion were nondimensionalized in order to reduce the variable space. It was shown that every system studied had an equilibrium point when $\beta = 0$, its stability in the 1DoF-R and 2DoF cases determined by the non-dimensional ratio of magnetic strength to torsional spring strength, $\frac{\gamma}{k_r^*}$. As $\frac{\gamma}{k_r^*}$ increased from low to high, the $\beta = 0$ equilibrium went from statically stable to statically unstable, an intuitive result, since the magnets create divergent torques and forces and springs create restorative torques and forces. For some intermediate values of $\frac{\gamma}{k_r^*}$ mirrored secondary equilibria appeared at other values of β around a $\beta = 0$ equilibrium, where the secondary equilibria were statically stable compared to a statically unstable $\beta = 0$ equilibrium (as in the 1DoF-R case) or vice versa (as in the 2DoF case).

Chapter 4 used the same dipole model as Chapter 3, but instead of analytical, closed-form solutions, numerical methods were shown to return the same results, thus validating the methods. Also in Chapter

4, the vector potential approach for calculating magnetic potential energy was validated against the analytical magnetic energy formulation from Chapter 3.

Chapter 5 introduced a new, more accurate magnetic coil model to replace the less-accurate but simpler dipole model. Using the now-validated numerical methods, Chapter 5 explored the difference in equilibrium locations and their stabilities between coils and magnetic dipole moments. One of the major findings was the so-called proximity effect, wherein the perimeters of two coils come close together due to rotation, and the high-magnitude forces resulting from that reduced distance dominate the overall trend of magnetic force and torque between two repelling magnets. One of the most interesting consequences of the proximity effect is that in the dipole 1DoF-R case, the central equilibrium for intermediary values of $\frac{\gamma}{k_r^*}$ was unstable with stable secondary equilibria, due to the magnetic torque dominating near $\beta = 0$. In the coil case, however, the central equilibrium is statically stable because the proximity effect actually results in restorative magnetic torques up to a certain rotation angle, at which the magnetic torque becomes divergent, resulting in statically unstable secondary equilibria at those angles. The end result of Chapter 5 was a well-validated model and approach for determining the static and dynamic stability of equilibria in a two-coil spring-based system.

Chapter 6 expanded the applicability of the model to more realistic systems and showed that it was scalable and plausible respectively by investigating the stability of a three-coil system and by replacing the springs with tethers that could go flat and create elastic forces and torques that depend on both of the generalized coordinates of motion rather than one each. The three-coil system, especially the 2DoF-R case, revealed some interesting potential energy curves and coupling between three repelling coils of either identical or different radii, and concurred with the general intuitive finding that stronger magnets as compared to springs result in less stable equilibria. The tether system's coupling of force to angle and torque to distance resulted in the potential energy curve being more interestingly shaped than the analogous spring system and the locations of secondary equilibria changing radically for the same strength magnets and springs or tethers. Both the three-coil and tether systems improved the model in addition to increasing the realism and applicability of the model and approach to real-world systems.

7.2. Contributions

This work has introduced and implemented a validated general methodology for determining the static and dynamic stability of nonlinear magneto-elastic structures in space. In doing so, this thesis has

1. Identified conditions under which elastically connected electromagnetic structures are stable,
2. Located specific passively stable geometries,
3. Defined equilibrium conditions on magneto-elastic structures,
4. Determined the static and dynamic stability of equilibria,

5. Described and depicted how the use of different elastic hardware and different numbers of coils shift stable geometries, and

6. Developed a validated nonlinear, generalizable magneto-elastic dynamics model.

This methodology is intended for use by spacecraft and structural designers to explore the stability of a wide variety of magneto-elastic space structures for use in a number of applications that can benefit from the unique capabilities of electromagnetically-supported structures, many of which have been identified and explored in Chapter 2 of this thesis. This thesis has

1. Enumerated the structural and ancillary capabilities of electromagnets in space,

2. Conducted system trades to quantify electromagnet benefits to spacecraft components and missions,

3. Identified key enabling technologies and feasibility risks for an electromagnetic spacecraft subsystem,

4. Reduced the risk associated with system instability, and

5. Developed a technology maturation pathway for electromagnetic technologies in space, specifically high-temperature superconducting electromagnets.

7.3. Generalization of MAGESTIC

The MAGESTIC methodology and model presented in this work are designed to be broadly applicable and allow for changing of coil orientations and elastic forces and torques, as shown with the addition of a third coil in Chapter 6. However, the model in its current state is still intrinsically limited; for example, it only accepts rigid, circular coils and assumes constant currents and no interaction between individual turns of wire. There are no dynamic effects or energy dissipation mechanisms incorporated yet. To be most useful to system designers, the MAGESTIC model needs to mesh with other engineering tools already designed to analyze structural and dynamic behavior and to allow users to specify material properties and higher-fidelity geometries and systems than the circular electromagnets with uniform current densities studied in this thesis.

There are two primary vectors for improving the MAGESTIC model as it currently stands. The first and most immediate approach is the modification and broadening of the existing quasi-static model to accommodate any arbitrary geometry, material properties, and boundary conditions that a user would like to specify, such as a finite element mesh, rather than just the number and radii of coils and the natural length of the elastic hardware. The model would calculate the magnetic forces, torques, equilibria, and static and dynamic stability for each point within a given configuration space the same as in this thesis but would offload the structural analysis to a solver like NASTRAN that is capable of high-fidelity deformation,

stress, and stiffness calculations. The model would therefore be capable of allowing electromagnets to deform rather than remaining rigid bodies. Figure 85 shows a block model of what such a generalization of the MAGESTIC model would look like.

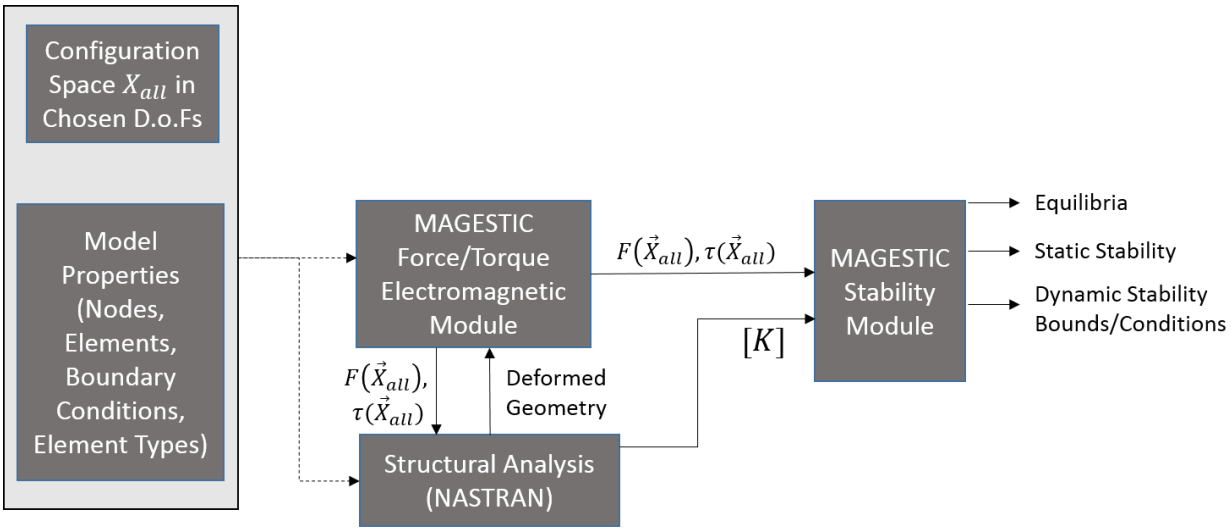

Figure 85: Generalized MAGESTIC model with user-defined inputs and a separate structural analysis tool

The grouped block on the left side of Figure 85 contains the user-defined inputs, both the configuration space (the ranges of the generalized coordinates selected for study) and the model properties, likely in the form of a finite element mesh of the magnetic and elastic hardware for which the user would like to evaluate stability. Both the MAGESTIC magnetic force and torque model and the structural analysis tool take these inputs and use them to calculate the magnetic and elastic forces and torques for each point in the configuration space through an iterative process. The iteration is necessary because structural deformations are caused by magnetic and elastic effects, which in turn are influenced by the deformation of the structure. The stiffness matrix [K] with the forces and torques are then used by the MAGESTIC stability model to locate equilibria in the configuration space and classify their static stability along with the critical initial kinetic energy for dynamic instability. The stability model uses the approach as presented in this thesis but will need to be expanded to find equilibria in more than two degrees of freedom.

This generalization step expands the MAGESTIC model to as many degrees of freedom as are desired in the system and allows users to prescribe whatever configuration of elastic hardware they like. The addition of other degrees of freedom adds to the realism of the simulation. In particular, a shear degree of freedom (translation in the y-z plane) in the systems studied in this thesis would not meet any restorative forces, meaning that different elastic hardware would need to be considered to prevent motion in that plane. Tethers that cross from one side of the x axis to the other diagonally are one such option for resisting motion in the y-z plane. This step also permits the analysis of alternative configurations besides a linear boom, such as configurations with three or more coils where not all coils are aligned along the same axis.

The second step for improving the MAGESTIC model is to position the now-generalized quasi-static model within a broader, multiphysics framework for use in concurrent engineering and optimization. Figure 86 shows the addition of a dynamic timestepper module to the generalized model presented in Figure 85 which takes in a specific set of initial conditions of a user-defined system and models the motion of the system over time as a result of force and torque imbalances. In the diagram, [M] is the mass matrix, and $\vec{X}(t)$, $\dot{\vec{X}}(t)$, $\ddot{\vec{X}}(t)$ are the positions, velocities, and accelerations of the system in the chosen generalized coordinates of motion.

At this point in the model expansion, currents are still modeled as constant, but energy dissipation mechanisms and external disturbances and perturbations are now included in the analysis. Adding dynamic simulation to the model allows a system designer to study deployment dynamics, similar to those examined in Gettliffe 2013 [16] but with added insight into stability and equilibrium positions as well as how added energy impacts dynamic stability. Simulating the dynamic response of a specific system with specific initial conditions and disturbances allows the system to present a conclusive determination of dynamic stability versus just bounds and conditions on dynamic stability. The dynamic response also allows a system designer to test how tweaking initial conditions and model properties affects dynamic stability.

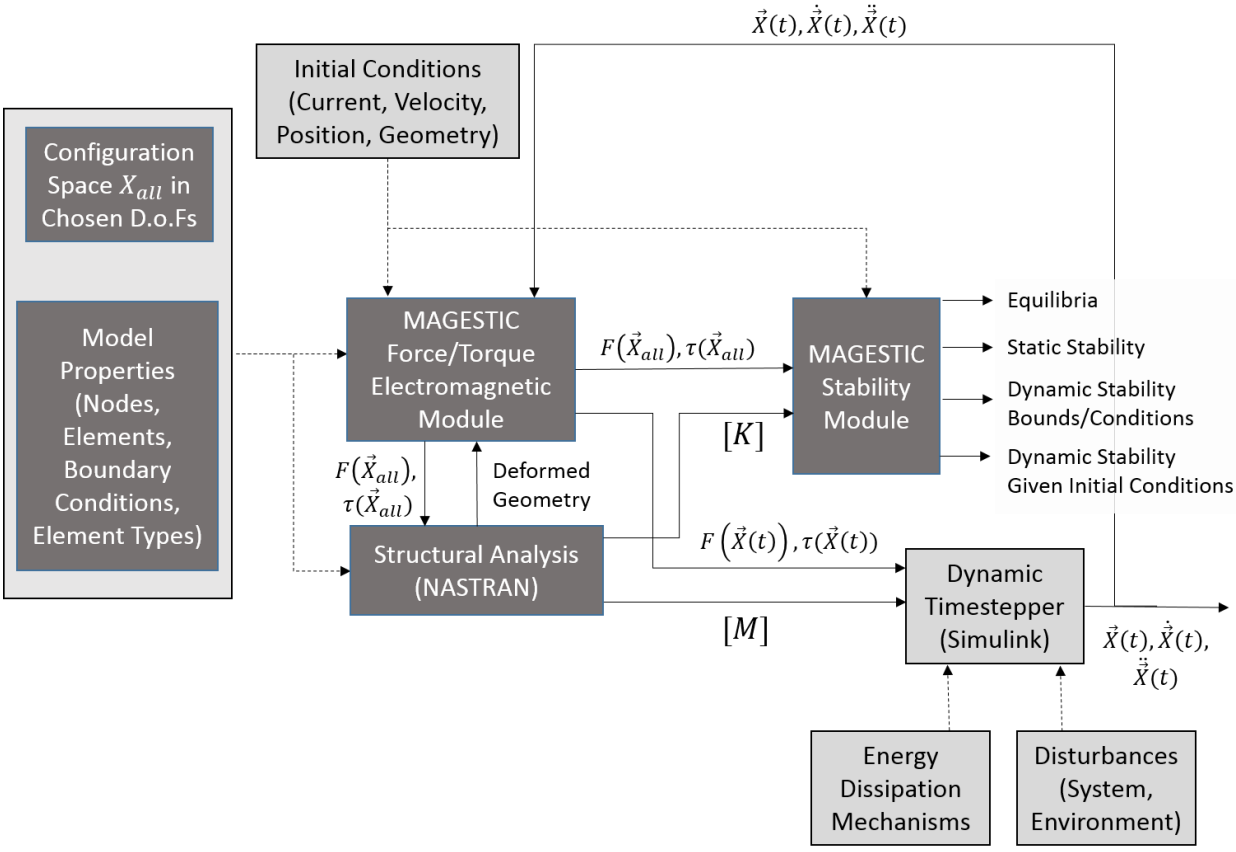

Figure 86: Generalized MAGESTIC model in a dynamic wrapper

Figure 86 represents the structural subsystem mechanics and dynamics. A step beyond the dynamic wrapper is the addition of other multiphysics modules to either add to the realism of the simulation, integrate other closely-coupled subsystems, or both. Figure 87 adds an induced current module to the model. The induced current module changes the currents through the electromagnets in the system in response to changing fluxes through the coils as per the discussion in Section 6.3.2. Other potentially useful modules that can be tied in are thermal and power modules, due to the strong relationship between magnet performance and temperature and the cryogenic requirements for superconductivity, as well as the relatively significant mass and power requirements of cryocoolers. An appendix in the MAGESTIC NIAC Phase II final report [59] presents a multidisciplinary optimization of power, mass, and length in electromagnetic masts like those studied in this thesis. The optimization includes power and thermal modules and also identifies the need for stability conditions for electromagnetic structures as well as a stiffness analog that can be used as a metric to trade against traditional structural technologies.

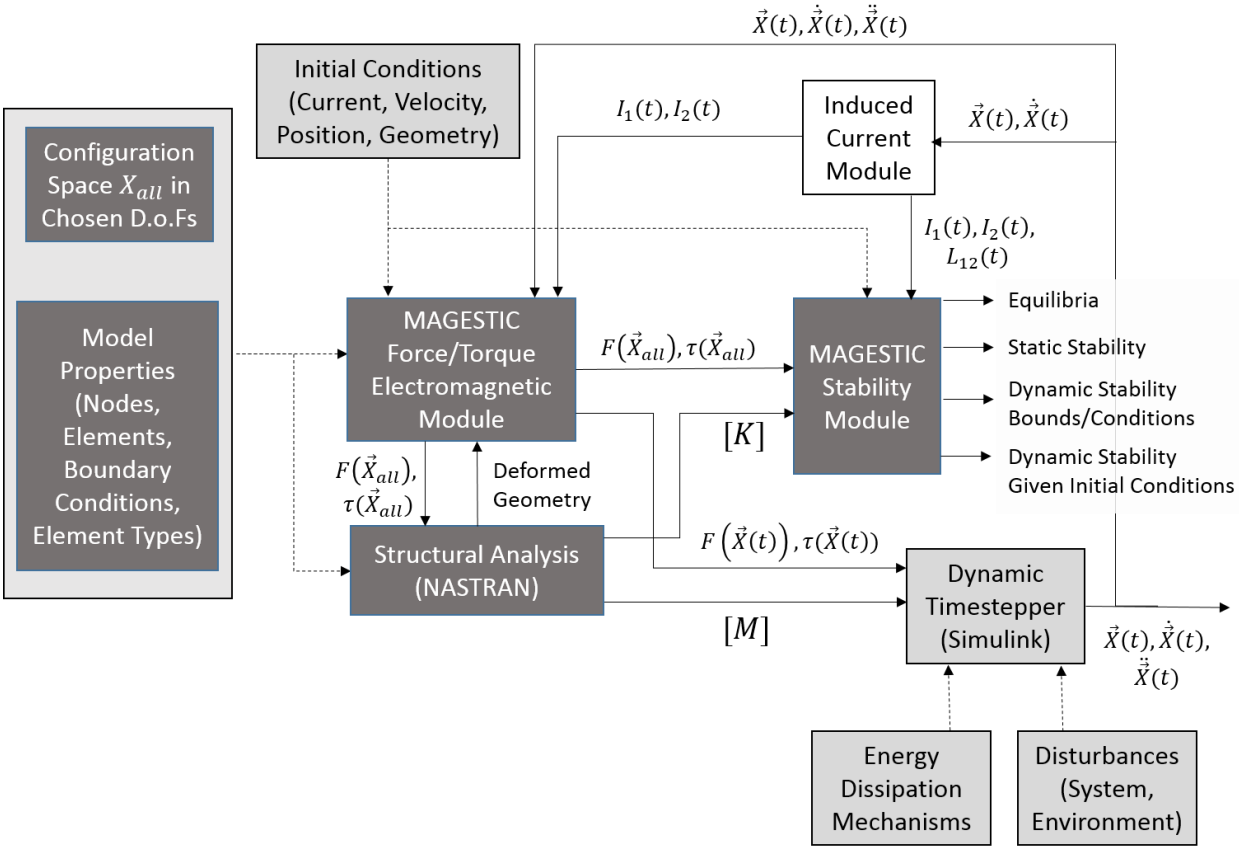

Figure 87: Generalized MAGESTIC model in dynamics wrapper with added induced current module

Once the MAGESTIC electromagnetic structural subsystem model is generalized as discussed above, several other interesting modifications or uses of the model are worth further investigation. These ideas are discussed in more detail as future work in the next section.

7.4. Future Work

There are a number of additional directions in which this work could be taken going forward, depending on the needs of the end user. For instance, an engineer who is interested in how stability changes across a broad range of design variables and choices may want a fast way to explore how stability changes with certain variables. A machine learning approach such as support vector machines could be used to classify equilibria (such as the rotational equilibria at $\beta = 0$) as stable or unstable, train the machine with test data, giving it the ability to estimate the stability of other systems based on the stability of the test points, and then explore how changing different design variables affects stability without having to actually calculate torques and/or forces at every single design point.

A specific mission may present either specific constraints or requirements (or both) on a magneto-elastic structure. There are two main directions in which the generalized module presented in Figure 87 can be used: the system designer can provide budget constraints and objectives, such as achieving the longest mass possible with certain amounts of mass or power, or the system designer can provide requirements on the performance or geometry of the structure. The first direction just requires an optimization wrapper around the methodology presented in this thesis. The second direction requires running the methodology in reverse, starting with positions and required critical initial kinetic energies and stiffnesses, then having to back out the elastic and magnetic strengths that fulfill the requirements. The latter direction will therefore take some effort to develop, but it is worthwhile for designers presented with specific requirements.

The stability results of this thesis have some interesting features, some of which could be exploited by a particularly creative engineer. For instance, the sometimes multiple statically and dynamically stable (metastable) equilibria in a system present the concept of reconfigurability, where an injection of energy in one or more of the generalized coordinates (or a change in current) could induce a switching from one stable configuration to another. Such reconfigurability could be used for applications that require actuation beyond initial deployment of the structure, such as pointing a telescope or an antenna.

7.5. Conclusions

A major takeaway from the analyses presented in this thesis is that there are not so much *regions* of stability within the degrees of freedom being studied as there are individual stable points and then a region surrounding them within which a system may oscillate if the critical initial kinetic energy of that stable point is not exceeded. For a given design vector, the position or positions in the generalized coordinates in which the system is free to move also function as a sort of design variable that determines whether that design vector is stable or unstable.

The concepts of magnetic stiffness and the potential energy functionals used in this work also provide a basis of comparison to other structural technologies besides just the mass of the structure, making trade studies more quantitative and allowing magneto-elastic structures to be considered for those applications which may have strict stiffness requirements. Interestingly, stiffness increases with increasing magnetic strength (larger χ or γ) values, while critical initial kinetic energy (and static stability in general) increases with decreasing magnetic strength, so there is clearly a trade that can be done between stiffness and critical initial kinetic energy, depending on the requirements of an application.

This work presents motivation, maturation and generalization pathways, and a fundamental foundation and lexicon for future studies of electromagnetic space structures. It is the author's sincere hope that such systems will eventually enable new spacecraft missions and one day see flight.

Works Cited

[1] J. R. Wertz, *Space Mission Engineering: The New SMAD,* Microcosm Press, 2011.

[2] F. Moon, Magneto-Solid Mechanics, New York: John Wiley & Sons, Inc., 1984.

[3] "Conservative Systems.," Nonlinear Finite Element Methods (ASEN 6107), University of Colorado at Boulder, 2014. [Online]. Available: http://www.colorado.edu/engineering/CAS/courses.d/NFEM.d/NFEM.Ch06.d/NFEM.Ch06.pdf . [Accessed 15 July 2015].

[4] W.-C. Xie, Dynamic Stability of Structures, Cambridge University Press, 2006.

[5] J. L. Synge and B. A. Griffith, Principles of Mechanics, McGraw Hill, 1949.

[6] H. C. Corben and P. Stehle, Classical Mechanics, Courier Corporation, 1994.

[7] L. D. Landau, General Physics: Mechanics and Molecular Physics, Elsevier, 2013.

[8] A.-R. A. Ragab and S. A. Bayoumi, Engineering Solid Mechanics: Fundamentals and Applications, CRC Press, 1998.

[9] F. Jing and E. Kanso, "Effects of body elasticity on stability of underwater locomotion," *Journal of Fluid Mechanics,* vol. 690, pp. 461-473, 2012.

[10] S. Widnall and J. Peraire, "Lecture L13 – Conservative Internal Forces and Potential Energy," Massachusetts Institute of Technology, 2008. [Online]. Available: http://ocw.mit.edu/courses/aeronautics-and-astronautics/16-07-dynamics-fall-2009/lecture-notes/MIT16_07F09_Lec13.pdf. [Accessed 15 July 2015].

[11] N. J. Hoff, "Dynamic stability of structures," in *Dynamic Stability of Structures*, New York, Pergamon, 1967.

[12] G. J. Simitses, Dynamic Stability of Suddenly Loaded Structures, 2012: Springer Science & Business Media.

[13] A. Joshi and M. Xiao, Controlling Steady-State and Dynamical Properties of Atomic Optical Bistability, World Scientific, 2012.

[14] G. V. Gettliffe, N. Inamdar, R. Masterson and D. W. Miller, "High-temperature superconductors as electromagnetic deployment and support structures in spacecraft: NASA NIAC Phase I Final Report," 2012.

[15] http://www.lhc-closer.es, "Superconductivity in Short," [Online]. Available: http://www.lhc-closer.es/php/index.php?i=1&s=4&p=8&e=0. [Accessed 21 May 2012].

[16] G. V. Gettliffe, High-temperature superconductors as electromagnetic deployment and support structures in spacecraft (SM Thesis), Cambridge: Massachusetts Institute of Technology, 2013.

[17] D. Kwon, *Electromagnetic Formation Flight of Satellite Arrays,* Massachusetts Institute of Technology, 2005.

[18] D. Kwon and R. Sedwick, *Cryogenic Heat Pipe for Cooling High Temperature Superconductors with Application to Electromagnetic Formation Flight Satellites,* Massachusetts Institute of Technology, 2009.

[19] E. Kong, Spacecraft Formation Flight Exploiting Potential Fields, Massachusetts Institute of Technology, 2002.

[20] S. Schweighart, Electromagnetic Formation Flight Dipole Solution Planning, Cambridge: Massachusetts Institute of Technology, 2005.

[21] A. Sakaguchi, Micro-Electromagnetic Formation Flight of Satellite Systems, Massachusetts Institute of Technology, 2007.

[22] R. Zubrin, "NIAC Study of the Magnetic Sail," NASA, 1999.

[23] J. Powell, G. Maise, J. Paniagua and J. Rather, "Magnetically Inflated Cable (MIC) System for Large Scale Space Structures," NASA Institute of Advanced Concepts, 2006.

[24] "Working of MAGLEV Trains," Circuits Today, 16 February 2012. [Online]. Available: http://www.circuitstoday.com/working-of-maglev-trains. [Accessed 11 August 2015].

[25] F. Moon, Superconducting Levitation: Applications to Bearings and Magnetic Transportation, New York: John Wiley & Sons, Inc., 1994.

[26] "ARGOS (Advanced Research and Global Observation Satellite)," Earth Observation Portal, [Online]. Available: https://directory.eoportal.org/web/eoportal/satellite-missions/content/-/article/argos. [Accessed 9 August 2015].

[27] D. Desiderio, M. Lovera, S. Pautonnier and R. Drai, "Magnetic Momentum Management for a Geostationary Satellite Platform," in *47th IEEE Conference on Decision and Control*, Cancun, Mexico, 2009.

[28] N. Tsyganenko, "Modeling the Earth's Magnetosphere Using Spacecraft Magnetometer Data," [Online]. Available: http://geo.phys/spbu.ru/~tsyganenko/modeling.html. [Accessed 10 September 2014].

[29] C. Finlay, "Internation Geomagnetic Reference Field," [Online]. Available: http://www.ngdc.noaa.gov/ IAGA/vmod/igrf.html. [Accessed 10 September 2014].

[30] W. P. Olson, K. A. Pfitzer and G. J. Mroz, "Modeling the Magnetospheric Magnetic Field," in *Quantitative Modeling of Magnetospheric Processes*, Washington, D.C., American Geophysical Union, 1979.

[31] SuperPower Inc., "SuperPower®2G HTS Wire Specifications," [Online]. Available: http://www.superpower-inc.com/system/files/SP_2G+Wire+Spec+Sheet_for+web_2012FEC_v2_0.pdf.

[32] E. B. Inc., "Van Allen Radiation Belt," Encyclopaedia Britannica Online Academic Edition, [Online]. Available: http://www.britannica.com/EBchecked/topic/622563/Van-Allen-radiation-belt. [Accessed 10 September 2014].

[33] R. Reyes, "Charged Particle Motion," Southwest Research Institute, [Online]. Available: http://pluto.space.swri.edu/image/glossary/pitch.html. [Accessed 10 September 2014].

[34] M. de Soria-Santacruz, G. Bautista, G. V. Gettliffe, M. Martinez-Sanchez and D. W. Miller, "Design of a Space-borne Antenna for Controlled Removal of Energetic Van Allen Belt Protons," in *IEEE Aerospace*, 2013.

[35] "Starshades," New Worlds Observer, [Online]. Available: http://newworlds.colorado.edu/starshade/index.htm. [Accessed 10 September 2014].

[36] E. M. Kwon, "Minimum Energy Trajectories for Techsat 21 Earth Orbiting Clusters," in *Space 2001 Conference & Exposition*, Albuquerque, NM, 2001.

[37] J. A. Hoffman, P. Fisher and O. Batishchev, "Use of Superconducting Magnet Technology - NIAC Phase I Final Report," NASA Institute for Advanced Concepts, 2005.

[38] S. C. Westover, R. B. Meinke, R. Battiston, W. J. Burger, S. V. Sciver and S. Washburn, "Magnet Architectures and Active Radiation Shielding Study - NIAC Phase I Final Report," NASA Innovative Advanced Concepts, 2012.

[39] R. R. Fu, B. P. Weiss and D. L. Shuster, "An ancient core dynamo on Vesta," *Science,* vol. 338, pp. 238-241, 2012.

[40] M. Kuzmanoski, G. Apostolovska and B. Novakovic, "The mass of (4) Vesta derived from its largest gravitational effects," *The Astronomical Journal,* vol. 140, no. 3, pp. 880-886, 2010.

[41] M. de Soria, *Controlled Precipitation of Energetic Van Allen Belt Protons by Electromagnetic Ion Cyclotron (EMIC) Waves: Scientific and Engineering Applications,* Cambridge: Massachusetts Institute of Technology, 2014.

[42] R. M. Murray, "Jacobian Linearizations, Equilibrium Points," 2002. [Online]. Available: http://www.cds.caltech.edu/~murray/courses/cds101/fa02/caltech/pph02-ch19-23.pdf. [Accessed 15 July 2015].

[43] O. Bretscher, "Section 8.3 of Linear Algebra with Applications: Nonlinear Systems and Linearization," 2008. [Online]. Available: http://www.math.harvard.edu/~elkies/M21b.08/notes1.pdf. [Accessed 15 July 2015].

[44] D. Katzman, J. Moreno, J. Noelanders and M. Winston-Galant, "Eigenvalue Stability," The Michigan Chemical Process Dynamics and Controls Open Text Book, [Online]. Available: https://controls.engin.umich.edu/wiki/index.php/EigenvalueStability. [Accessed 10 July 2015].

[45] G. F. Franklin, J. D. Powell and A. Emami-Naeini, Feedback Control of Dynamic Systems, Prentice Hall, 2005.

[46] G. Strang, Introduction to Linear Algebra, Wellesley-Cambridge Press , 2009.

[47] "Conservation laws for systems of particles," Brown University School of Engineering, [Online]. Available: http://www.brown.edu/Departments/Engineering/Courses/En4/Notes/particles_work_energy/particles_work_energy.htm. [Accessed 15 July 2015].

[48] Y. C. Wang and R. S. Lakes, "Extreme stiffness systems due to negative stiffness elements," *American Journal of Physics,* vol. 72, no. 1, pp. 40-50, 2004.

[49] J. D. Jackson, Classical Electrodynamics, John Wiley & Sons, Inc., 1999.

[50] S. Brueckner, "crossing.m," MATLAB Central, [Online]. Available: http://www.mathworks.com/matlabcentral/fileexchange/2432-crossing. [Accessed 15 July 10].

[51] M. Iskandarani, "Finite Difference Approximation of Derivatives," [Online]. Available: http://www.rsmas.miami.edu/personal/miskandarani/Courses/MSC321/lectfiniteDifference.pdf. [Accessed 15 July 2014].

[52] N. Ida, Engineering Electromagnetics, Springer, 2015.

[53] B. B. Laud, Electromagnetics, New Age International, 1987.

[54] J. Simpson, J. Lane, C. Immer and R. Youngquist, "Simple Analytic Expressions for the Magnetic Field of a Circular Current Loop," NASA Kennedy Space Center, 2001.

[55] A. Buck, *Path Planning and Position Control and of an Underactuated Electromagnetic Formation Flight Satellite System in the Near Field,* Cambridge, MA: Massachusetts Intitute of Technology, 2013.

[56] A. Fletcher, "Guide to Tables of Elliptic Functions," *Mathematics of Computation - American Mathematical Society,* 1948.

[57] F. W. Grover, Inductance Calculations: Working Formulas and Tables, New York: Dover Publications, Inc., 1962.

[58] S. Liao, P. Dourmashkin and J. W. Belcher, "Visualizing E&M: Inductance and Magnetic Energy," 2004. [Online]. Available: http://web.mit.edu/viz/EM/visualizations/coursenotes/modules/guide11.pdf. [Accessed 15 July 2015].

[59] G. V. Gettliffe, A. Porter and R. Wesenberg, "MAGESTIC: Magnetically Enabled Structures Using Interacting Coils - NIAC Phase II Final Report," NASA Innovative Advanced Concepts, 2015.

[60] J. R. Wertz, Spacecraft Attitude Determination and Control, D. Reidel, 1980.

[61] S. Hahn, *Conversation with Prof. Seungyong Hahn about superconductor inductances,* 2015.

[62] R. W. Chabay and B. A. Sherwood, Matter & Interactions, New York: John Wiley & Sons, Inc., 2011.

[63] G. V. Gettliffe and D. W. Miller, "System Concept Development For Multifunctional Electromagnetically Actuated and Supported Space Structures," in *International Astronautical Congress*, Toronto, 2014.

[64] "Second-order differential equations," The Michigan Chemical Process Dynamics and Controls Open Text Book, 9 February 2012. [Online]. Available: https://controls.engin.umich.edu/wiki/index.php/Second-order_differential_equations. [Accessed 11 August 2015].

Appendix A: Nomenclature

Variable	Section Defined	Definition
$\vec{A}_{rea}$	2.5.1.	Area of coil (m^2)
a_x, a_y, a_z	2.5.1.	Accelerations in x, y, and z directions respectively (subscript p or s referring to primary or secondary mirrors) ($\frac{m}{s^2}$)
α	3.1.	Angle of dipole 1 around the z axis with respect to the x axis (rad)
$\vec{A}(\vec{x})$	4.1.3.	Magnetic vector potential for a current carrying loop at a position $\vec{x}$ from the center of a magnet ($\frac{Vs}{m}$)
$\vec{A}_1(\vec{x})$	4.1.3.	Magnetic dipole vector potential of magnetic dipole moment $\vec{\mu}_1$ ($\frac{Vs}{m}$)
A_{CS}	5.3.4.	Cross-sectional area of the coil through which current flows (m^2)
$A_\phi(r, \theta)$	5.3.4.	The azimuthal component of the magnetic vector potential as a function of distance and angle from coil axis ($\frac{Vs}{m}$)
$\vec{B}, \vec{B}_i$	2.1.	Magnetic field in general and from the ith ($i = 1{:}3$) current-carrying wire, (T)
$\vec{B}_0$	2.5.1.	Earth's magnetic field (T)
$\mathrm{B_{surf}}$	2.5.1.	Mean strength of Earth's magnetic field at surface (T)
$\vec{B}(\vec{r})$	3.1.	Magnetic field at P_{oint} (T)
β	3.1.	Angle of dipole 2 around the z axis with respect to the x axis (rad)
$\beta_{\#a}, \beta_{\#a-\#}$	3.4.2.	Equilibrium angle, attractive case, first # indicates changing β position, second # (if present) indicates which equilibrium at a given β is being referred to
$\beta_{\#b}, \beta_{\#b-\#}$	3.4.2.	Equilibrium angle, repulsive case, first # indicates changing β position, second # (if present) indicates which equilibrium at a given β is being referred to
$\beta_{\#a,ND}$, $\beta_{\#a,ND-\#}$	3.4.2.	Non-dimensional equilibrium angle, attractive case, first # indicates changing β position, second # (if present) indicates which equilibrium at a given β is being referred to
$\beta_{\#b,ND}$, $\beta_{\#b,ND-\#}$	3.4.2.	Non-dimensional equilibrium angle, repulsive case, first # indicates changing β position, second # (if present) indicates which equilibrium at a given β is being referred to
β_{eq}	3.4.3.	Value of β at a particular equilibrium (rad)
$\beta_{\#,-}$	3.5.2.	Equilibrium ID, 2DoF, negative beta
$\beta_{\#,+}$	3.5.2.	Equilibrium ID, 2DoF, positive beta
$\beta_{\#,0}$	3.5.2.	Equilibrium ID, 2DoF, $\beta = 0$

B_x, B_y, B_z	5.1.	Cartesian components of the magnetic field as calculated with the magnetic vector potential
$\beta_{ND,coil,\#-\#}$	5.4.2.	Non-dimensional equilibrium angle in coil moderl, 1DoF-R, first # indicates changing β position, second # (if present) indicates which equilibrium at a given β is being referred to
$\beta_{\#,\#-\#}$	5.5.4.1.	Non-dimensional 2DoF equilibrium angles, first # is the numbered dot in figure, second # is the $\frac{\chi}{k_r^*}$ value, third # (if present) differentiates between equilibra occurring at same β position
β_2, β_3	6.1.	Angle of coil 2 and coil 3 around z axis respectively in three coil system
$\beta_{coil,\#}$	6.2.3.	Equilibrium angle of coil 2 in tether system 1DoF-R, # referring to which statically stable equilibrium it is
CSA	2.5.2.	Cross-sectional area (m^2)
C	3.3.4.	Constant of integration
d	2.5.1.	Distance between primary and secondary mirror (or two coils) or distance between spacecraft and asteroid (m)
δ	3.1.	Angle of dipole 2 about the x axis with respect to the y axis (rad)
E	1.2.2.	Total energy of the system (J)
E_{t_0}	1.2.2.	Total energy at t=0 (J)
ϵ	5.3.4.	Small displacement from exact radius of coil, equal to $\tilde{r}_{CS}$
$\mathfrak{E}$, EMF	6.3.1.	Electromotive force (V)
$\vec{F}_i$	1.2.1.	Force, where $i = 1{:}\,n$, n being the total number of forces (N)
$F_{tot,j}$	1.2.1.	The total force acting in the direction of $x_{t,j}$, where $j = 1{:}\,n_t$ (N)
$\vec{F}_{ij}$	2.1.	Magnetic force from the ith wire on the jth wire (N)
$F_{x,p}, F_{y,p}, F_{z,p}$	2.5.1.	Forces on primary mirror req'd to maintain distance in x, y, z directions (N)
$F_{x,s}, F_{y,s}, F_{z,s}$	2.5.1.	Forces on secondary mirror req'd to maintain distance in x, y, z directions (N)
F_{SP}	2.5.1.	Magnetic force of a coil using SuperPower HTS wire (N)
F_g	2.5.2.	Gravitational force between an asteroid and a spacecraft (N)
F_m	2.5.2.	Magnetic force between two aligned magnetic dipoles (N)
$F_{tot,A}$	2.5.2.	Total force of spacecraft on asteroid (N)
$\vec{F}_{mag,1}$	3.1.	Magnetic force on dipole 1 from dipole 2 (N)
$\vec{F}_{mag,2}$	3.1.	Magnetic force on dipole 2 from dipole 1 (N)
$\vec{F}_{spr,2}$	3.2.	Spring force on dipole 2 (N)
$\vec{F}_{2,rep}$	3.3.1.	Total force on magnet 2 (repulsive case) (N)
$\vec{F}_{2,att}$	3.3.1.	Total force on magnet 2 (attractive case) (N)

$\tilde{\vec{F}}_{2,rep,ND}$	3.3.1.	Total non-dimensional force on magnet 2 (repulsive case)
$\tilde{\vec{F}}_{2,att,ND}$	3.3.1.	Total non-dimensional force on magnet 2 (attractive case)
$F_{spring,x}$	3.3.3.	X component of spring force (N)
$F_{mag,x}$	3.3.3.	X component of magnetic force (N)
$F_{tot,x}$, $\tilde{F}_{tot,x}$	3.3.3.	X component of total force (N), non-dimensional x component of total force
F_{tot}, $\tilde{F}_{tot}$	3.3.3.	Total force (N) and non-dimensional force
$F_{2,rep,x}$	3.3.3.	Magnitude of x component of force on magnet 2 (repulsive case) (N)
$F_{2,att,x}$	3.3.3.	Magnitude of x component of force on magnet 2 (attractive case) (N)
$\tilde{F}_{2,rep,ND,x}$	3.3.3.	Magnitude of x component of non-dim. force on magnet 2 (repulsive case)
$\tilde{F}_{2,att,ND,x}$	3.3.3.	Magnitude of x component of non-dim. force on magnet 2 (attractive case)
f_{rep}, f_{att}	3.3.3.	Dummy function name in state-space representation
$\tilde{\vec{F}}_{2,rep,mag,x}$	3.5.4.	X component of non-dimensional magnetic force, repulsive case
$\vec{F}_{2,mag,coil}$, $\vec{F}_{2,mag,coil,x}$	5.3.1.	Magnetic force on coil 2 from coil 1 and the x component thereof (N)
$\tilde{\vec{F}}_{2,mag,coil}$	5.3.1.	Non-dimensional magnetic force on coil 2 from coil 1
$\tilde{F}_{total,2}$	6.1.1.	Non-dimensional total force on coil 2 in three coil system
$\tilde{F}_{total,3}$	6.1.1.	Non-dimensional total force on coil 3 in three coil system
$\tilde{F}_{spring,21}$	6.1.1.	Non-dimensional force of spring attached to coil 1 on coil 2
$\tilde{F}_{spring,23}$	6.1.1.	Non-dimensional force of spring attached to coil 3 on coil 2
$\tilde{F}_{mag,21}$	6.1.1.	Non-dimensional magnetic force of coil 1 on coil 2
$\tilde{F}_{mag,23}$	6.1.1.	Non-dimensional magnetic force of coil 3 on coil 2, equal and opp. to $\tilde{F}_{mag,32}$
$\tilde{\vec{F}}_{2,teth1}$	6.2.1.	Non-dimensional force on coil 2 as a result of tether 1 (top tether)
$\tilde{\vec{F}}_{2,teth2}$	6.2.1.	Non-dimensional force on coil 2 as a result of tether 2 (bottom tether)
$F(\vec{X}_{all})$	7.3.	Forces of each position in configuration space (N orND)
F_{lux}	6.3.1.	Total flux through a coil (Wb)
$F_{lux_{ext}}$	6.3.1.	Flux through a coil from an external magnetic field (Wb)
$F_{lux_{int}}$	6.3.1.	Flux through a coil from the coil's own field (Wb)
G	2.5.2.	Gravitational constant ($\frac{m^3}{kg-s^2}$)
g_{rep}, g_{att}	3.3.3.	Dummy function name in state-space representation
$\widetilde{H}_{1x}$, $\widetilde{H}_{2x}$	5.3.4.	Non-dimensional grouped terms for vector potential calulations

$\widetilde{H}_{\#\pm\epsilon}$	5.3.4.	Non-dimensional grouped terms for vector potential calculated at $\tilde{r} \pm \epsilon$
I_i, I_j	2.1.	Current through the ith wire, jth wire (A)
I_{eff}	2.5.2.	Effective current (current times number of turns) (A)
I_{turn}	2.5.2.	Current per turn of wire in spacecraft magnet (A)
$[I_n]$	3.3.3.	Identity matrix of dimension n
I_z	3.4.1.	Mass moment of inertia $(kg{-}m^2)$
J	2.1.1.	Current density ($\frac{A}{m^3}$)
J_{rep}	3.3.3.	Jacobian of state-space representation (repulsive case)
$\vec{J}(\vec{x}')$	4.1.3.	The current density of the element at $\vec{x}'$ ($\frac{A}{m^2}$)
$\overrightarrow{J_J}$	5.3.4.	Current density vector in jth $coil$ (A/m^2)
k	3.2.	Linear spring constant (N/m)
k_r	3.2.	Torsional spring constant ($\frac{Nm}{rad}$)
k^*	3.3.1.	Non-dimensional linear spring force coefficient
k_{spring}	3.3.3.	Spring stiffness (N/m)
k_{mag}	3.3.3.	Magnetic stiffness (Ns/m)
κ_{tot}	3.3.3.	Total stiffness (N/m)
$\kappa_{tot,ND}$	3.3.3.	Non-dimensional total stiffness
k_r^*	3.4.1.	Non-dimensional spring torque coefficient
$\kappa_{tot,R}$	3.4.3.	Total rotational stiffness ($\frac{Nm}{rad}$)
$[K_{ND}]$	3.5.3.	Non-dimensional stiffness matrix
$\kappa_{tot,num}$	4.1.2.	Numerical estimation of total translational stiffness (N/m)
$\kappa_{tot,ND}$	4.1.2.	Non-dimensional total translational stiffness
$\kappa_{tot,ND,num,T}$	4.1.2.	Non-dimensional numerical estimation of total translational stiffness
$\kappa_{tot,ND,num,R}$	4.2.2.	Non-dimensional numerical estimation of total rotational stiffness in dipole case
$[K_{tot,ND,num}]$, $[K_{tot,ND}]$	4.3.2.	Numerically estimated non-dimentional total stiffness matrix in 2D0F
$K(k^2), E(k^2)$	5.1.	Complete elliptic integrals of the first and second kind, k^2 being the argument
$\kappa_{tot,ND,coil,T}$	5.3.3.	Non-dimensional total translational stiffness in the coil model
$\tilde{k}_{1x}, \tilde{k}_{2x}$	5.3.4.	Arguments for complete elliptic integrals in $\widetilde{H}_{1x}$, $\widetilde{H}_{2x}$ respectively
$\kappa_{tot,ND,coil,R}$	5.4.3.	Non-dimensional total rotational stiffness in the coil model

k_p	6.3.1.	Constant of proportionality for units in EMF
[K]	7.3.	Stiffness matrix from structural analysis software
$d\vec{l}, d\vec{l}_i$	2.1.	Differential length element along/around a wire in general and around the ith ($i = 1{:}\,3$) current-carrying wire (m)
λ_{rep}	3.3.3.	Eigenvalues of state-space representation (repulsive case)
$\lambda_{\#}$	4.3.2.	Analytically calculated eigenvalues of $\left[K_{tot,ND,num}\right]$
$\lambda_{\#,num}$	4.3.2.	Numerically estimated eigenvalues of $\left[K_{tot,ND,num}\right]$
L_{ij}	5.3.4.	Inductance between ith and jth coils (H); if $i = j$, self inductance, if $i \neq j$, mutual inductance
$\tilde{L}_{teth1}$, $\tilde{L}_{teth2}$	6.2.1.	Non-dimensional length of tether 1,2
μ_0	2.1.	The magnetic constant (vacuum permeability, $\frac{kgm}{s^2A^2}$)
$\vec{\mu}, \vec{\mu}_i$	2.5.1.	Magnetic moment in general and of the ith current carrying coil (Am^2)
μ_A	2.5.2.	Vesta's magnetic dipole moment (Am^2)
μ_1, μ_2	3.1.	Magnetic dipole moments of magnets 1 and 2 (Am^2)
m_p	2.5.1.	Mass of primary mirror (kg)
m_s	2.5.1.	Mass of secondary mirror (kg)
m	2.5.1.	Mass of single coil (kg)
M_A	2.5.2.	Mass of asteroid (Vesta) (kg)
M_{sc}	2.5.2.	Mass of spacecraft (kg)
m_2	3.3.1.	Mass of magnet 2 (kg)
$\widetilde{m}_2$	3.3.1.	Non-dimensional mass of coil/magnet 2
$\widetilde{m}_3$	3.3.1.	Non-dimensional mass of coil/magnet 3
$\vec{M}_2$	4.1.3.	Magnetization of the second dipole ($\frac{A}{m}$)
[M]	7.3.	Mass matrix from structural analysis software
n_t	1.2.1.	Number of translational generalized coordinates in the system
n_r	1.2.1.	Number of rotational generalized coordinates in the system
n	1.2.1.	Total number of generalized coordinates in the system.
N, N_i	2.5.1.	Number of turns in coil in general and of the ith ($i = 1{:}\,3$) current carrying coil
n_{orb}	2.5.1.	Orbital rate (rad/s)
$\hat{n}$	3.1.	Unit normal vector to coil, dictated by direction of current/right hand rule
η	3.1.	Angle of dipole 1 about the x axis with respect to the y axis (rad)

P, $\widetilde{P}$	1.2.1.	Effective potential energy of the system (J) and non-dimensional version
$(dP)_{x_{t,j}}$	1.2.2.	Decrease of the system's potential energy in the direction of $x_{t,j}$ (J)
P_{eq}	1.2.2.	Potential energy at a specified equilibrium (J)
P_C	1.2.2.	Potential energy at point C in ex. problem; the closest unstable equil. (J)
ρ_{HTS}	2.5.2.	Density of HTS wire (kg/m^3)
P_{oint}	3.1.	Point in space where magnetic field is being calculated
ρ	3.3.1.	Mass per unit length of wire (linear density, kg/m)
φ	3.4.2.	Non-dimensional combination of variables, $\frac{\mu_0\mu_1\mu_2}{2\pi k_r x_0^3}$
$P_{rep,T}$	3.3.4.	Potential energy as calculated from $F_{2,rep,x}$ (J)
$P_{att,T}$	3.3.4.	Potential energy as calculated from $F_{2,att,x}$ (J)
$\tilde{P}_{rep,T}$	3.3.4.	Non-dimensional potential energy as calculated from $\tilde{F}_{2,rep,ND,x}$
$\tilde{P}_{att,T}$	3.3.4.	Non-dimensional potential energy as calculated from $\tilde{F}_{2,att,ND,x}$
$P_{rep,R}$	3.4.4.	Potential energy as calculated from $\vec{\tau}_{2,rep,z}$ (J)
$P_{att,R}$	3.4.4.	Potential energy as calculated from $\vec{\tau}_{2,att,z}$ (J)
$\tilde{P}_{rep,R}$	3.4.4.	Non-dimensional potential energy, as calculated from $\tilde{\vec{\tau}}_{2,rep,ND,z}$
$\tilde{P}_{att,R}$	3.4.4.	Non-dimensional potential energy, as calculated from $\tilde{\vec{\tau}}_{2,att,ND,z}$
$\tilde{P}_{mag,T}$	3.5.4.	Non-dimensional magnetic potential energy as calculated analytically from $\tilde{\vec{F}}_{2,rep,mag,x}$
$\tilde{P}_{mag,R}$	3.5.4.	Non-dimensional magnetic potential energy as calculated analytically from $\tilde{\vec{\tau}}_{2,rep,mag,z}$
$\tilde{P}_{2DoF}$	3.5.4.	Total non-dimensional repulsive potential energy in the 2DoF system as calculated analytically
$P_{rep,mag,T}$	4.1.3.	Magnetic potential energy calculated analytically, 1DoF-T (repulsive case) (J)
$\widetilde{P}_{rep,mag,2DoF}$	4.3.3.	Non-dimensional magnetic potential energy calculated analytically, 2DoF (repulsive case)
$\tilde{P}_{tot}$	5.3.4.	Total non-dimensional potential energy in coil system including both translational and rotational degrees of freedom, such as 2DoF
$\tilde{P}_T$	5.3.4.	Total non-dimensional potential energy in translational-only coil system
$\tilde{P}_R$	5.3.4.	Total non-dimensional potential energy in rotational-only coil system
ϕ	5.3.4.	Azimuthal angle (rad)
$\vec{r}_{ij}$	2.1.	Vector from each differential length element $d\vec{l}_i$ to the point where the field is being calculated (m)
$\mathrm{R_E}$	2.5.1.	Radius of Earth (km)

r	2.5.1.	Distance where Earth's magnetic field is being measured (km)
R, R_i	2.5.1.	Radius of coil in general and of the ith ($i = 1{:}\,3$) current carrying coil (m)
r_{ast}	2.5.2.	Radius of asteroid (km, but equation uses m)
$\vec{r}$	3.1.	Vector from the center of a dipole moment to P_{oint} (m)
$\tilde{R}_1, \tilde{R}_2, \tilde{R}_3$	3.3.1.	Non-dimensional radius of coil/magnet 1, 2, or 3
r, $\tilde{r}$	5.3.4.	Magnitude of the distance vector $\vec{r}$ from the center of coil 1 to the point of interest $P(r, \theta, \phi)$ (m) and non-dimensional version
R	5.3.4.	Radius of coil for which magnetic vector potential is being calculated
$\tilde{r}_{CS}$	5.3.4.	Non-dimensional effective cross-sectional radius of the coil bundle
R_{es}	6.3.1.	Resistance (Ohms)
T	1.2.2.	Kinetic energy of the system (J)
T_{t_0}	1.2.2.	Kinetic energy at equilibrium when t=0 (J)
$T_{t_0,crit}$	1.2.2.	Critical initial kinetic energy (J)
T_c	2.1.1.	Superconductor critical temperature (K)
$\mathcal{T}$	3.3.1.	Characteristic time variable
t	3.3.1.	Time (s)
$\tilde{t}$	3.3.1.	Non-dimensional time
$\tilde{T}_{t_0,crit}$	3.3.4.	Non-dimensional critical initial kinetic energy
$\tilde{T}_{t_0,crit,\#\#}$	6.1.2.	Non-dimensional critical initial kinetic energy for 2DoF-R equilibria, first # is the letter of the plot, and second # is the numbered equilibrium in that plot
$\tilde{T}_{t_0,crit,spring}$	6.2.2.	Non-dimensional critical initial kinetic energy of the spring system
$\tilde{T}_{t_0,crit,tether}$	6.2.2.	Non-dimensional critical initial kinetic energy of the tether system
$\Delta\tilde{T}_{t_0,crit}$	6.2.2.	Difference in $\tilde{T}_{t_0,crit}$ between the spring and tether systems
θ	2.5.1.	Co-latitude measured from the Earth's north magnetic pole (rad)
Θ	3.1.	Angle subtended by a coil with respect to a point in space (rad)
θ_m, θ	4.1.3.	Angle between magnetic moment and external field (rad)
$\vec{\tau}_i$	1.2.1.	Torque, where $i = 1{:}\,m$, m being the total number of forces (N-m)
$\tau_{tot,k}$	1.2.1.	The total torque acting in the direction of $x_{r,k}$, where $k = 1{:}\,n_r$ (N-m)
$\vec{\tau}_{mag,i}$	2.5.1.	Magnetic torque on the ith ($i = 1{:}\,3$) current carrying coil (N-m)
$\vec{\tau}_{mag,1}$	3.1.	Magnetic torque on dipole 1 from dipole 2 (N-m)
$\vec{\tau}_{mag,2}$	3.1.	Magnetic torque on dipole 1 from dipole 2 (N-m)
$\vec{\tau}_{spr,2}$	3.2.	Spring torque on dipole 2 (N-m)
$\vec{\tau}_{2,rep}$	3.4.1.	Total torque on magnet 2, repulsive case (N-m)

$\vec{\tau}_{2,att}$	3.4.1.	Total torque on magnet 2, attractive case (N-m)
$\vec{\tilde{\tau}}_{2,rep,ND}$	3.4.1.	Total non-dimensional torque on magnet 2, repulsive case
$\vec{\tilde{\tau}}_{2,att,ND}$	3.4.1.	Total non-dimensional torque on magnet 2, attractive case
$\vec{\tau}_{2,rep,z}$	3.4.4.	Component of total torque around the z axis, repulsive case (N-m)
$\vec{\tau}_{2,att,z}$	3.4.4.	Component of total torque around the z axis, attractive case (N-m)
$\vec{\tilde{\tau}}_{2,rep,ND,z}$	3.4.4.	Component of total non-dimensional torque around the z axis, repulsive case
$\vec{\tilde{\tau}}_{2,att,ND,z}$	3.4.4.	Component of total non-dimensional torque around the z axis, attractive case
$\vec{\tilde{\tau}}_{2,rep,mag,z}$	3.5.4.	Component of non-dimensional magnetic torque around the z axis, repulsive case
$\vec{\tau}_{2,mag,coil}$	5.3.1.	Magnetic torque on coil 2 from coil 1 (N-m)
$\vec{\tilde{\tau}}_{2,mag,coil}$	5.3.1.	Non-dimensional magnetic torque on coil 2 from coil 1
$\vec{\tilde{\tau}}_{2,spring}$	5.4.1.	Non-dimensional elastic torque induced by spring around the z axis on coil 2
$\tilde{\tau}_{2,tot}$	5.4.1.	Non-dimensional total torque on coil 2 around the z axis
$\tilde{\tau}_{total,2}$	6.1.2.	Non-dimensional total torque on coil 2 around z axis in three coil system
$\tilde{\tau}_{spring,2}$	6.1.2.	Non-dimensional spring torque on coil 2 around z axis in three coil system
$\tilde{\tau}_{spring,3}$	6.1.2.	Non-dimensional spring torque on coil 3 around z axis in three coil system
$\tilde{\tau}_{mag,21}$	6.1.2.	Non-dimensional magnetic torque of coil 1 on coil 2
$\tilde{\tau}_{mag,23}$	6.1.2.	Non-dimensional magnetic torque of coil 3 on coil 2
$\tilde{\tau}_{mag,31}$	6.1.2.	Non-dimensional magnetic torque of coil 1 on coil 3
$\tilde{\tau}_{mag,32}$	6.1.2.	Non-dimensional magnetic torque of coil 2 on coil 3
$\vec{\tilde{\tau}}_{2,teth1}$	6.2.1.	Torque from tether 1 on coil 2, non-dimensional
$\vec{\tilde{\tau}}_{2,teth2}$	6.2.1.	Torque from tether 2 on coil 2, non-dimensional
$\vec{\tilde{\tau}}_{total,2}$	6.2.1.	Total torque on coil 2 in tether case
$\tau(\vec{X}_{all})$	7.3.	Torques of each position in configuration space (N-m or ND)
V_R	3.4.4.	Elastic potential energy of a torsional spring (J)
$\widetilde{V}_T$	3.5.4.	Non-dimensional elastic potential energy, linear spring
$\widetilde{V}_R$	3.5.4.	Non-dimensional elastic potential energy, torsional spring
$V_{tot}, \widetilde{V}_{tot}$	5.3.4.	Dimensional (J) and non-dimensional total elastic potential energy
V_{olt}	6.3.1.	Voltage (V)
$W_{t,j}$	1.2.1.	Work done by a component of force $F_{tot,j}$ (J)
$W_{r,k}$	1.2.1.	Work done by a component of torque $\tau_{tot,k}$ (J)

ω	3.3.1.	Natural frequency of magnet 2 on the linear spring (1/s)
W_r	3.4.4.	Work done by the moment due to twisting through a very small angle $d\beta$ about the $+z$ axis (J)
W_{rep}	3.4.4.	Magnetic potential energy, repulsive case (J)
$W_{1DoF,T}$	4.1.3.	The energy associated with magnet 2 in the magnetic field of magnet 1 (or vice versa) in the 1DoF-T case (J)
$\widetilde{W}_{1DoF,T}$	4.1.3.	Non-dimensional magnetic potential energy of one magnet in the field of the other in the 1DoF-T case
$W_{1DoF,R}$	4.2.3.	The energy associated with magnet 2 in the magnetic field of magnet 1 (or vice versa) in the 1DoF-R case (J)
$\widetilde{W}_{1DoF,R}$	4.2.3.	Non-dimensional magnetic potential energy of one magnet in the field of the other in the 1DoF-R case
W_{2DoF}	4.3.3.	The energy associated with magnet 2 in the magnetic field of magnet 1 (or vice versa) in the 2DoF case (J)
$\widetilde{W}_{2DoF}$	4.3.3.	Non-dimensional magnetic potential energy of one magnet in the field of the other in the 2DoF case
W_{tot}, $\widetilde{W}_{tot}$	5.3.4.	Dimensional (J) and non-dimensional total magnetic energy (general formulation w/out specifying DoF)
$\widetilde{W}_{11}$, $\widetilde{W}_{22}$	5.3.4.	Non-dimensional magnetic potential energy due to self inductance term for coils 1 and 2 respectively
$\widetilde{W}_{12}$, $\widetilde{W}_{21}$	5.3.4.	Non-dimensional magnetic potential energy due to mutual inductance, equivalent
$\widetilde{W}_{Grover}$	5.3.4.	Non-dimensional magnetic potential energy due to mutual inductance as per published inductance tables in Grover
$\widetilde{W}_{Jackson,11}$, $\widetilde{W}_{Jackson,22}$	5.3.4.	Non-dimensional magnetic potential energy due to self inductance term for coils 1 and 2 respectively, calculated via estimates in Jackson
X	1.2.1.	Set of generalized coordinates describing system
x_i	1.2.1.	A single generalized coordinate, part of set X
$x_{t,j}$	1.2.1.	A single translational generalized coordinate, where $j = 1{:}\, n_t$
$x_{r,k}$	1.2.1.	A single translational generalized coordinate, where $k = 1{:}\, n_r$
$\vec{X}$	1.2.1.	The position vector of a system in its generalized coordinates
x_I, x_{II}	1.2.2.	Oscillation bounds around equilibrium resulting from T_{t_0} (m)
$x_I(P_c)$, $x_{II}(P_c)$	1.2.2.	Maximum allowable bounds of motion beyond which motion becomes unbounded (m)
x_{cm}	2.5.1.	Position of center of mass
x_p	2.5.1.	Position of primary mirror w.r.t. center of mass (m)

x_s	2.5.1.	Position of secondary mirror w.r.t. center of mass (m)
x_f	2.5.2.	Ratio between magnetic and gravitational forces
$x, \vec{x}$	3.1.	Distance and vector between the magnets along the x axis (m)
Δx	3.2.	Translational displacement along x axis from natural length (m)
x_0	3.2.	Natural length of linear spring (m)
$\tilde{x}$	3.3.1.	Non-dimensional distance from the center of coil 1 to the center of coil 2
$\tilde{x}_0$	3.3.1.	Non-dimensional natural length of the linear spring
$x_{\#a}$	3.3.2.	Attractive equilibrium point (m)
$x_{\#b}$	3.3.2.	Repulsive equilibrium point (m)
$\tilde{x}_{max}$	3.3.2.	Maximum absolute value of $\tilde{x}^4(\tilde{x} - \tilde{x}_0)$ in Figure 30
$\tilde{x}_{\#a}$	3.3.2.	Non-dimensional attractive equilibrium point (m)
$\tilde{x}_{\#b}$	3.3.2.	Non-dimensional repulsive equilibrium point (m)
x_{eq}	3.3.3.	Equilibrium point (m)
ξ	3.4.1.	Non-dimensional magnetic torque coefficient
$\Delta\tilde{x}$	4.1.1.	Non-dimensional displacement along x axis from natural length (m)
$\vec{x}'$	4.1.3.	Coordinates of the current carrying element (m)
χ	5.3.1.	Non-dimensional magnetic coil force coefficient
$\tilde{x}_{coil,\#}$	5.3.2	Equilibrium locations in the 1DoF-T non-dimensional coil model
$\tilde{x}_2, \tilde{x}_3$	6.1.1.	Non-dimensional x locations of coils 2 and 3
$\tilde{x}_{2,eq}$	6.1.1.	Non-dimensional x locations of coil 2 equilibria
$\tilde{x}_{3,eq}$	6.1.1.	Non-dimensional x locations of coil 3 equilibria
$\tilde{\vec{x}}_{2,teth1}$	6.2.1.	Attachment point of tether 1 to coil 2, non-dimensional
$\tilde{\vec{x}}_{2,teth2}$	6.2.1.	Attachment point of tether 2 to coil 2, non-dimensional
$\tilde{\vec{x}}_{1,teth1}$	6.2.1.	Attachment point of tether 1 to coil 1, non-dimensional
$\tilde{\vec{x}}_{1,teth2}$	6.2.1.	Attachment point of tether 2 to coil 1, non-dimensional
$\tilde{\vec{x}}_{2,0}$	6.2.2.	Non-dimensional position of center of coil 2 on x axis
$\tilde{x}_{coil,\#}$	6.2.2.	Equilibrium position in x of coil 2 in tether system 1DoF-T, # referring to which statically stable equilibrium it is
$\vec{X}(t)$, $\dot{\vec{X}}(t), \ddot{\vec{X}}(t)$	7.3.	Position, velocities, and accelerations of coil system over time (ND)
$\vec{X}_{all}$	7.3.	Vector location of every configuration in the configuration space of generalized coordinates (ND)
γ	3.3.1.	Non-dimensional magnetic force coefficient

y	3.3.3.	Dummy variable in state-space representation
Z	2.5.2.	Combination of variables, $\frac{3\mu_0 I_{turn}}{80CSA\rho_{HTS}\pi G}$, $(\frac{kg}{Am})$